



GEOFORSCHUNGSZENTRUM POTSDAM
STIFTUNG DES ÖFFENTLICHEN RECHTS

Scientific Technical Report

ISSN 1610-0956

Scale-related strain evolution at convergent margins and effects due to parameter changes – insights from nature and experiment

Kerstin Schemmann



Dissertation zur Erlangung des Doktorgrades
im Fachbereich Geowissenschaften an der
Freien Universität Berlin

Berlin, September 2007

Erstgutachter: Prof. Dr. Onno Oncken (Freie Universität Berlin)
Zweitgutachter: Prof. Dr. Alexander R. Cruden (University of Toronto)
Tag der Disputation: 06. November 2007

**Eine Wolke zieht vorbei,
der Himmel ist so blau
und klar wie zuvor.**

japanisches Haiku

Summary

Orogens can form at convergent margins by plate subduction or collision. Deformation is hereby accumulated via brittle deformation in the upper crust, controlled by the strength of the lithosphere and therefore linked to the friction coefficients and cohesion of the rocks. Ductile deformation in the lower crust depends on the strain rate and the rock's rheology, which again is controlled by temperature, pressure and mineral composition. Deformation processes and their basic mechanisms are widely understood, whereas the knowledge about the distribution of strain accumulation in space and time on various scales is still insufficient. However, this is crucial for the determination of the dominant deformation frameworks (e.g., continuum-Euclidean model, block model, fractal complexity).

In this thesis, the distribution of strain accumulation on the orogen scale is examined, both in space and in time (geological long-term deformation up to 10^7 a), plus its interaction with the next smaller "regional" scale. Using the existing literature, I compiled a comprehensive data base on deformation activity in the Central Andes (17-27°S and 69-63°W), complemented by artificial data from analogue simulations monitored by a high-resolution system employing "particle imaging velocimetry" (PIV). By means of statistics and geostatistics, I can quantify characteristic scale lengths of active structures and their typical duration for the regional scale, which are on the order of 150-200 km width and 200-300 km length and 2-4 Ma, respectively. On the orogen scale, the scale lengths are multiples of these values, as the orogen scale represents a summary of the active structures on the regional scale, being adjacent and coevally active. These scale lengths are artefacts resulting from the current resolution of the data set.

Furthermore, I analyzed the effect of both system internal and external parameters on the resulting strain pattern for the above mentioned scales. In a first experimental series that simulates only the upper crust using granular media, I show that deformation patterns are controlled by mechanical heterogeneities. Threshold values exist for coupled parameters of both basal (20%) and internal (35%) strength contrasts, which determine if either wedge-like or plateau-style settings will result. These threshold values indicate the absence of gradual transitions between the two endmembers. I was also able to reproduce the spatiotemporal strain evolution of the Central Andean plateau. Yet, the controlling parameter combination in the analogue models is very different from those proposed for the natural example. This indicates that a resulting strain pattern is possibly explained by more than only one parameter combination. Thus, we cannot conclusively infer information from the resulting picture on the controlling factors to relate causes and effects.

A second analogue series simulates the upper crust to the asthenosphere to study the crucial parameters that have to be met in a young system to initiate the plateau formation. A plateau is initiated when two anticlinal hinges enclose an undeformed basin, which is subsequently drained. This is bound to a critical lateral strength contrast within the system combined with a curved geometry. Furthermore, a normal density profile is required, as well as decoupling of the upper crust deformation from layers below.

Comparing three experiments of plateau initiation clearly shows that controlling factors can be of first or second order. The first order parameters actively change the resulting deformation patterns on the orogen scale (e.g., plate geometry) whereas the second order factors become effective only on the next smaller "regional" scale (e.g., additional decoupling horizons), while the orogen scale pattern remains the same. Thus, the effect of controlling parameters is scale-dependent.

In spite of such an unusually well resolved data set on strain accumulation both in space and time from nature, we cannot conclusively distinguish the varying deformation frameworks, possibly due to a still insufficient data resolution. Depending on the applied resolution, we might unintentionally integrate data from different scales, so that their original strain pattern cannot be identified. It is nevertheless likely that dominant frameworks alternate over time. For example, at the beginning of the formation of a deformation system, only a few regional structures are active for the entire orogen scale. Within these active areas, a fractal pattern will establish during an initial stage (e.g., 46-37 Ma). In a subsequent stage,

more regional areas become active that are distributed throughout the orogen. Thus, fractal patterns will be established on the orogen scale within 8-10 Ma as can be observed for the spatial distribution of shortening rates (between 36-16 Ma). Once a rock volume has been saturated with strain, it will accumulate elsewhere. This is true when the plateau interior becomes inactive at 15 Ma, and the system prepares for a transfer of strain accumulation to the Inter/ Subandean after 15 Ma. The development starts again with initial strain accumulation in few areas that eventually develop a fractal pattern.

The strain distribution pattern does not provide conclusive information on the underlying deformation mechanisms. For example, both strain weakening and strain hardening can affect a deformation system that is basically fractal. Such deformation modes can coincide with the different deformation frameworks. Both likely alternate in space and time and so does their effect on different scales. Generally, the lack of highly resolved data precludes the identification of the respective patterns and deformation modes.

Zusammenfassung

An konvergenten Plattenrändern können durch Kollision zweier Platten oder Subduktion Orogene entstehen. Dabei hängt spröde Deformation der oberen Kruste von der Festigkeit des Gesteins, und damit vom Reibungskoeffizienten und der Kohäsion ab. Duktile Deformation in der unteren Kruste ist abhängig von der Strainrate und der Rheologie des Materials, die wiederum von Faktoren wie der Temperatur, dem Druck und der Zusammensetzung des Gesteins bestimmt wird. Deformationsprozesse und die zugrunde liegenden Mechanismen sind weitgehend verstanden. Hingegen ist bis heute noch unzulänglich erklärt, wie die Deformation in räumlicher und zeitlicher Verteilung auf verschiedenen Skalen akkumuliert wird, und welche Faktoren dabei eine bedeutende Rolle spielen. Dies ist jedoch wichtig für das Verständnis der möglichen Deformationsmodelle (Kontinuumsmodell, Blockmodell, fraktale Komplexität).

Diese Arbeit untersucht die Verteilung von Deformation insbesondere auf der Orogenskala, sowohl im Raum als auch in der Zeit (geologische Langzeitdeformation bis 10^7 a) sowie deren Interaktion mit der nächst kleineren „regionalen“ Skala. Die Datengrundlage bildet zum einen eine umfassende Kompilation publizierter Deformationsdaten für die Zentralanden (17-27°S und 69-63°W), sowie experimentelle Daten aus der Analogmodellierung, die aufgrund des gewählten Aufnahmesystems („particle imaging velocimetry“, PIV) sehr hoch aufgelöst sind.

Mittels statistischer und geostatistischer Untersuchungen der räumlichen und zeitlichen Deformationsverteilung kann ich charakteristische Skalenlängen aktiver Strukturen sowie deren Deformationsdauer quantifizieren. Auf der regionalen Skala sind typischerweise Bereiche von 150-200 km Breite und 200-300 km Länge über 2-4 Millionen Jahre aktiv. Auf der Orogenskala haben aktive Strukturen ein Vielfaches dieser Werte, was auf eine räumliche und zeitliche Zusammenfassung benachbarter aktiver Strukturen der nächst kleineren Skala aufgrund der vorliegenden Datenauflösung zurückzuführen ist.

Ferner habe ich systeminterne und externe Parameter auf ihre Wirkung auf das resultierende Deformationsmuster für die oben genannten Skalenbereiche untersucht. In einer ersten Experimentserie, die mit granularen Materialien nur die obere Kruste simuliert, zeige ich, dass mechanische Heterogenitäten das Deformationsmuster bestimmen. Parameter, die laterale (mind. 35%) und basale (mind. 20%) Festigkeitskontraste koppeln, weisen kritische Schwellenwerte auf, die bestimmen, ob ein keilartiges oder plateau-ähnliches Deformationssystem entsteht. Die Existenz dieser Schwellenwerte deutet daraufhin, dass es keine graduellen Übergänge zwischen Systemtypen gibt.

Mit dieser Analogserie konnte ich die räumlich-zeitliche Entwicklung der Deformationsverteilung der Zentralanden reproduzieren, deren Grundlage o.g. mechanische Heterogenitäten bilden, also andere Parameter als für die Natur postuliert wird. Dies weist darauf hin, dass ein Deformationsmuster nicht durch eine einzige Parameterkombination erzeugt und erklärt werden kann, sondern mehrdeutige Schlussfolgerungen zulässt. Mit anderen Worten bedeutet dies, dass ein Deformationsmuster, wie wir es heute vorfinden, keine eindeutigen Rückschlüsse auf seine verursachenden Faktoren ermöglicht.

In einer zweiten Analogserie, in der die obere Kruste bis zur Asthenosphäre modelliert wird, untersuche ich die Parameter, die die Plateauformation initiieren. Diese Initiierung besteht aus der Bildung zweier Gebirgsrücken, die eine flache, relativ undeformierte Ebene einschließen, welche im folgenden von jeglichen Materialzuflüssen abgetrennt wird. Dies geschieht nur, wenn kritische laterale Festigkeitskontraste existieren, die zudem eine gekrümmte Geometrie aufweisen. Außerdem muss ein normales Dichteprofil der Lithosphäre vorliegen, und die Deformation der oberen Kruste von ihrem Unterlager entkoppelt sein.

Der Vergleich von drei Experimenten, in denen es zur Plateauinitiierung kommt, zeigt, dass Einflussfaktoren ersten und zweiten Grades existieren. Die des ersten Grades (z.B. Plattengeometrie) bestimmen das resultierende Gesamtmuster des Systems, wohingegen die Faktoren zweiten Grades (z.B. zusätzliche Entkopplungshorizonte) nicht das Muster der Orogenskala beeinflussen, sondern nur die nächst kleinere „regionale“ Skala. Dies weist darauf hin, dass der Einfluss von verschiedenen

Faktoren je nach Skala unterschiedlich sein kann.

Trotz der einmaligen räumlich und zeitlich hochaufgelösten Datengrundlage aus der Natur ist eine Aussage über die zugrunde liegenden Deformationsmechanismen nicht eindeutig möglich, da die zeitliche und räumliche Auflösung eventuell immer noch nicht hoch genug ist. Je nach verwendeter Auflösung kann es dazu kommen, dass Daten unterschiedlicher Skalen zusammengefasst werden, und damit nicht mehr ihr ursprünglich zugrunde liegendes Muster erkennbar ist.

Es besteht allerdings Grund zur Annahme, dass sich das Muster des betrachteten Systems auch über die Zeit ändert. Zu Beginn der Entwicklung eines Deformationssystems (für die Zentralanden von 46 bis ca. 37 Ma) beschränken sich aktive Strukturen auf einige wenige regionale Bereiche, die intern fraktale Muster aufweisen können. Erst nach einer gewissen Zeitdauer bzw. Deformationsintensität (also einer initialen Phase) hat sich die Aktivität auf regionaler Ebene im Gesamtorogen verteilt (ab ca. 36 Ma), so dass nun das Gesamtsystem eine fraktale Verteilung der Verkürzung aufweist (bis ca. 15 Ma). Sobald die Deformationsakkumulation im Kern des Plateaus abgeschlossen ist, dieser Bereich also inaktiv wird, beginnt erneut eine „initiale“ Phase. Dies könnte dem Transfer von Strainakkumulation aus dem Kern des Plateaus in den Faltenüberschiebungsgürtel des Inter/Subandins ab 15 Ma entsprechen. Das erste fraktale Muster bliebe dabei bestehen.

Ein zugrunde liegendes Verteilungsmuster lässt keine eindeutigen Rückschlüsse auf die dominanten Deformationsmechanismen zu. So können sowohl strain weakening als auch strain hardening Effekte erzeugen, wenn das zugrunde liegende Muster generell fraktal ist. Die verschiedenen Deformationsmodelle und Deformationsmechanismen können also zeitlich und räumlich zusammenfallen und schließen sich dabei nicht aus. Aufgrund mangelnder Datenauflösung kann die genaue Zuordnung in Raum und Zeit jedoch oft nicht quantifiziert werden.

Contents

Abstract	I
Zusammenfassung	III
Contents	V
List of figures	VI
List of tables	VII
1. Introduction	1
2. Frameworks of deformation, scaling relations, dependence on parameter influence	4
3. The Methods	6
3.1. Geostatistics.....	6
3.2. Analogue modelling technique, advantages and limits.....	7
4. Geological Setting - The Central Andean plateau	9
5. Orogen-wide patterns of strain accumulation – the Andean case	12
5.1. Introduction.....	12
5.2. Geological setting.....	12
5.3. Data preparation.....	14
5.4. Statistics.....	15
5.5. Results.....	23
5.6. Conclusions.....	27
6. The effect of mechanical heterogeneity on diversification of deformation patterns – a modelling study with granular media	28
6.1. Introduction.....	28
6.2. Experimental design.....	29
6.3. Experimental results.....	30
6.4. Parameter control.....	32
6.5. PIV monitoring of plateau-style settings.....	35
6.6. Discussion.....	38
6.7. Application to the Central Andean plateau.....	41
6.8. Conclusions.....	43
7. The effect of mechanical heterogeneity on plateau initiation – A modelling study with viscous-brittle media	44
7.1. Introduction.....	44
7.2. Experimental design.....	45
7.3. Experimental results.....	49
7.4. Parameter effect.....	53
7.5. Comparison of three experiments with plateau-initiation.....	55

7.6. Discussion.....	59
7.7. Conclusions.....	62
8. Additional analogue data.....	64
9. Discussion, Conclusions and Outlook.....	71
10. References.....	83
Appendix A-1, Deformation Database.....	1
Appendix A-2, Deformation distribution in 1 Ma steps.....	17
Appendix A-3, Variogram surfaces for deformation activity in 1 Ma steps.....	24
Appendix A-4, Sensitivity analysis.....	31
Appendix B-1, Description of granular experiments.....	36
Appendix B-2, Set-up Sketches (granular experiments).....	42
Appendix B-3, Photographs of analogue devices.....	51
Appendix B-4, Material parameters for vise experiments.....	53
Appendix B-5, Material mixtures for vise experiments.....	55
Acknowledgments.....	59
CV.....	61
List of Figures	
Figure 3.1: Formula semi-variogram.....	6
Figure 3.2: Definition of distance h between two geographical locations.....	6
Figure 3.3: Sample variogram.....	7
Figure 4.1: Topographic map of the Central Andean plateau.....	9
Figure 4.2: Schematic cross section through the Central Andean plateau.....	10
Figure 5.1: Polygons and point grid of the study area.....	13
Figure 5.2: Frequency plots.....	14
Figure 5.3: Frequency plots divided into structural units.....	17
Figure 5.4a: Distribution of mean shortening rates.....	18
Figure 5.4b: Distribution of duration of deformation.....	18
Figure 5.5: Indicator variogram surfaces for deformation activity.....	19
Figure 5.6: Variograms for deformation activity.....	21
Figure 5.7: Kriging maps.....	22
Figure 5.8: Variogram surfaces for shortening rates.....	24
Figure 5.9: Summary of deformation stages.....	25
Figure 6.1: Resulting deformation patterns.....	33
Figure 6.2: Plateau-style vs. wedge-like deformation.....	34
Figure 6.3: PIV strain image of experimental surface.....	35
Figure 6.4a: PIV time series of plateau setting without erosion.....	36
Figure 6.4b: Finite and restored cross section of plateau setting without erosion.....	36

Figure 6.5a: PIV time series of plateau setting with erosion.....	37
Figure 6.5b: Finite and restored cross section of plateau setting with erosion.....	37
Figure 6.6: Topographic map of the Central Andean plateau.....	41
Figure 6.7: Profile at 21°S (Central Andes) and timing of deformation.....	42
Figure 7.1: Stages of plateau initiation and plateau formation.....	44
Figure 7.2: Topographic map of the Central Andean plateau with basin locations.....	45
Figure 7.3: Experimental set-up with analogue and natural dimensions.....	46
Figure 7.4: Strength envelopes of vise and weak lithosphere.....	47
Figure 7.5: Sketches of finite patterns of all experiments.....	50
Figure 7.6: Topographic profiles through experimental settings.....	51
Figure 7.7: Structural evolution of thrust/anticline features.....	53
Figure 7.8: Principal stress trajectories cross-shaped vs. phi pattern.....	54
Figure 7.9a: PIV strain image of finite experimental surface (Exp. 4).....	56
Figure 7.9b: PIV images of strain evolution (Exp. 4).....	56
Figure 7.10: PIV time series for three profiles for each plateau-initiation setting.....	57
Figure 7.11a: Topographic profiles over time (Exp. 4).....	58
Figure 7.11b: Topographic profiles over time (Exp. 5).....	58
Figure 7.12: Finite crustal thicknesses.....	60
Figure 8.1a: Real finite fault pattern.....	64
Figure 8.1b: Incremental velocity field of finite surface (Exp. 4).....	64
Figure 8.2: Incremental velocity field of finite surface (Exp. 6).....	64
Figure 8.3: Comparison of data resolution 1 (incremental vector displacement).....	66
Figure 8.4: Comparison of data resolution 2 (incremental vector displacement).....	67
Figure 8.5: PIV strain image and location of strain profiles.....	68
Figure 8.6: PIV time series with frequent changes in strain accumulation.....	68
Figure 8.7: Incremental vector displacement along one profile.....	69
Figure 8.8: Incremental vector displacement along-strike.....	70
Figure 9.1: Degree of localization and aspect ratios of active structures.....	71
Figure 9.2: Frequency-size distribution of active structures on the orogen scale.....	72
Figure 9.3: Power Spectra of spatial distribution of active structures.....	74
Figure 9.4a: Spatial distribution of earthquakes, Central Andes.....	75
Figure 9.4b: Frequency-size distribution of neighbouring earthquakes, Central Andes.....	76
Figure 9.4c: Magnitude-frequency distribution of earthquakes, Central Andes.....	76
Figure 9.5: Relation of causes and effects.....	79

List of Tables

Table 6.1: Scaling parameters of the granular experiments.....	30
Table 6.2a: Coefficients of Internal Friction, Cohesion, Density.....	31
Table 6.2b: Coefficients of Basal Friction, Cohesion, Density.....	31
Table 6.3: Basal and internal friction coefficients used for Figure 6.2.....	39
Table 7.1: Scaling parameters of the viscous-brittle experiments.....	47
Table 7.2: Initial characteristics and resulting patterns of vise experiments.....	48

1. Introduction

The aim of this dissertation is to quantify scaling relations of strain accumulation in nature on various temporal and spatial scales, in order to characterize the underlying deformation mechanisms, and to answer the questions 1) if strain accumulation is scale-invariant or if it occurs in characteristic patterns with typical structural lengths and durations, and 2) how a deformation system and its strain pattern is influenced by parameter changes (Chapter 2). It hereby focuses on the orogen scale and the next smaller “regional” scale, which includes fault networks as well as single faults and shear zones within geological timespans of millions of years (Ma). To date, these scales representing the upper magnitudes are the least studied in literature.

As a base for (geo)statistical analysis (Chapter 3), I compiled a comprehensive database on deformation activity (published in Oncken et al., 2006) using the natural example of the Central Andean plateau (17-27°S, 69-63°W; Chapter 4). This allows to detect characteristic structural lengths and deformational patterns in time on the above mentioned two scales (Chapter 5). The natural data set is complemented by artificial data sets from two different series of analogue experiments (a granular series and a brittle-viscous series), to cover the “time scales” in between earthquakes and long-term deformation, allowing the analysis of parameter effects on the patterns of strain accumulation.

Hence, I can examine 1) combinations of controlling parameters, that reproduce the spatiotemporal strain distribution observed in the Central Andes (Chapter 6); 2) the effect of parameter changes (in particular mechanical heterogeneities) on the resulting deformational pattern (Chapter 6 and 7); and 3) the effect of parameter changes on the strain pattern of both the orogen and the regional scale and their interaction (Chapter 7).

The experiments were monitored by a special camera system employing “particle imaging velocimetry” (PIV), which allows the calculation of the complete particle displacement field. It provides high resolution of deformation both in space and time. This also allows the quantification of temporal and spatial variation and interaction of strain accumulation within and across structures of the analogue data (Chapter 8). Placing the results

for the upper scales in the context of general scaling relations, I discuss their significance for the underlying deformation mechanisms, comment on potential consequences for geological studies, and give an outlook on future research (Chapter 9).

STRUCTURE OF THESIS

Apart from the introduction (Chapter 1), the dissertation is divided into eight further chapters: a review of the common deformation frameworks, scaling relations and their dependence on parameter changes (Chapter 2); a description of the applied methods (Chapter 3); a description of the tectonic setting of the Central Andean plateau (Chapter 4); three scientific manuscripts for publication in international peer-reviewed journals (Chapter 5, 6, 7); additional analogue data (Chapter 8); and conclusions with outlook on future research (Chapter 9). The appendix includes all references used in any of the chapters, the deformation database used in Chapter 5, more geostatistical data, data for the sensitivity analysis, a short documentation on all performed granular experiments with set-up sketches, material properties of visc experiments, acknowledgments, and a CV.

DESCRIPTION OF CHAPTERS

Chapter 1 presents the main objective and structure of the thesis and the topics of the following eight chapters.

Chapter 2 reviews the main deformation frameworks and their characteristic structures. It is likely that not a single framework is dominant for strain accumulation at a given time, but that more than one are either coinciding (both in a spatial and temporal sense) or alternating. Previous studies have either focused on spatial scales on or below the regional scale excluding the orogen scale, or are only applicable to plate margins. More research has been done on the comparison of displacement rates on the geological timescale vs. seismic events (Friedrich et al., 2003; 2004), which often does not cover the intermediate time scales (Leffler et al., 1997; Liu et al., 2002; Klosko et al., 2002). However, the given examples suggest the existence of deformation patterns in time, probably overprinting each other and therefore not to be discriminated in the field. Scaling relations are further complicated by the effect of both internal

and external parameters and their changes over time, which do not necessarily occur on the same scale.

Chapter 3 introduces the applied methods, i.e., (geo)statistics and analogue modelling with the particle imaging velocimetry (PIV) technique. I present the advantages of these methods, but also point out the technical limitations confining the data interpretation.

Chapter 4 provides an overview on the geodynamic setting of the Central Andean plateau, the characteristics of the Altiplano and Puna plateaux and their differences.

Chapter 5 is the first in the series of scientific manuscripts and examines if critical spatial and temporal patterns are present in the distribution of strain accumulation in the Central Andes (17°-27°S) on the orogen scale, and how these patterns are influenced by active deformation on the smaller regional scale. The analyzed deformation data were compiled from literature and are included in the appendix A (database was previously published in Oncken et al., 2006). The data are rearranged into one million year steps (comprising a total of 46 million years) and further analyzed by means of frequency statistics and geostatistics including variogram analysis.

Chapter 6 shows results from the first analogue series, in which the upper crust is modelled with granular materials. In two set-ups of different dimensions (and therefore different geometric scaling factors), numerous parameters were tested on their influence on the resulting strain accumulation pattern. They included system internal factors, namely horizontal and lateral mechanical heterogeneities, and external parameters such as erosion and indentation by a curved plate.

Chapter 7 discusses results from the second analogue series (“vise models”), where brittle material is used for the upper crust and viscous materials are employed for the lower crust and mantle lithosphere (these layers rest isostatically on the asthenosphere). With this series I studied the initial conditions that have to be met in a system to initiate plateau formation.

Chapter 8 provides additional PIV analogue data, that have the potential for quantification of variation and interaction of strain accumulation both within and across active structures, including their changes over time. Also, PIV data of incremental velocity fields allow the comparison to their natural

analog: GPS data.

Chapter 9 links previous chapters 5, 6, 7, and 8, and puts their main conclusions in the broader context of deformation frameworks. I illustrate the dissertation’s contribution to the ongoing scientific debate, present consequences and drawbacks for the geoscientific community and discuss open questions for future research.

SCIENTIFIC MANUSCRIPTS

Chapter 5, 6, and 7 are scientific manuscripts that will be submitted to peer-reviewed journals, or are already under review. K. Schemmann is responsible for the scientific content and has written all of them. The contribution of co-authors is stated below.

Chapter 5 is titled “Orogen-wide patterns of strain accumulation – the Andean case” by K. Schemmann, O. Oncken and A. Levander and will be submitted to *Geochemistry, Geophysics, Geosystems* in a revised form including data from Chapter 5 and 9. K. Schemmann is responsible for scientific ideas, the choice and implementation of methods and the scientific content of the manuscript. O. Oncken helped to improve the readability of the manuscript. A. Levander provided input and programming codes for the computation of data (cf. Chapter 9).

Chapter 6 bears the title “The effect of mechanical heterogeneity on diversification of deformation patterns - A modelling study with granular media” by K. Schemmann and O. Oncken. The first author carried out all analogue experiments and is responsible for the scientific content, ideas and interpretation. O. Oncken provided useful feedback and helped to strengthen the manuscript. The manuscript is submitted to *Tectonophysics*.

Chapter 7 is called “The effect of mechanical heterogeneity on plateau initiation - A modelling study with viscous-brittle media” by K. Schemmann, D. Boutelier, O. Oncken and A.R. Cruden. The analogue experiments were carried out at the *Tectonophysics Laboratory*, University of Toronto, with which D. Boutelier and A.R. Cruden are affiliated. These authors shared their experience with viscous analogue modelling and previous vise models (Cruden et al., 2006), and discussed the experimental results. All co-authors reviewed earlier versions of the manuscript to increase its coherence and strength. The manuscript is submitted to *Tectonophysics*.

FUNDING

Funding for the thesis was provided by a 33 months dissertation grant of the “Studienstiftung des deutschen Volkes” (German National Merit Foundation). They also financially supported K. Schemmann’s research stay at the Tectonophysics Laboratory, University of Toronto, where the viscous-brittle analogue experiments were carried out. Granular analogue experiments were performed in the Analogue Laboratory, GeoForschungsZentrum Potsdam. The attendance of conferences and a field-trip to Chile was funded by CSAG (Center for System Analysis of Geoprocesses) and the GFZ.

2. Frameworks of deformation, scaling relations and dependence on parameter influence

The imbalance between a) tectonic forces that are characterized by convergence and coupling between upper and lower plate or the coupling between the lithosphere and the underlying mantle, and b) buoyancy forces that are caused by the lateral and vertical density contrasts within the lithosphere, is often held responsible for orogen dynamics (e.g., McKenzie, 1969; Forsyth and Uyeda, 1975; Chapple and Tullis, 1977; Richardson et al., 1979; Dewey, 1980; Ranalli, 1987), more references in Sengör, 1990). The resulting force first drives the activation of faults in the upper brittle crust that deforms according to Byerlee's law (Byerlee, 1978); the remaining force is then released as deformation of the ductile lower lithosphere, depending on rheology (and therefore temperature) and strain rate (e.g., Ranalli, 1987; Thatcher, 1995; Royden, 1996; Zoback and Townsend, 2001).

These features are subject to the three common deformation frameworks (summarized by Ben-Zion and Sammis, 2003), which differ according to the mode of strain accumulation and their dominant structures. The first is the "continuum-Euclidean" framework, in which the effect of strain softening decreases the yield strength of the upper brittle crust and strain localizes at fault planes that have simple "Euclidean", i.e., planar geometries. These faults are evenly distributed in an elastic continuum accumulating different amounts of strain (Thatcher, 1995; Behn et al., 2002; Ben-Zion and Sammis, 2003). The continuum has been approximated by the simplified "thin viscous sheet model" (England and McKenzie, 1982), assuming the lithosphere to be viscous, rheologically homogeneous and isostatically compensated (Thatcher, 1995; Townsend and Sonder, 2001).

The second deformation framework is the "block model", describing strain accumulation at the margins of rigid blocks that do not deform internally (e.g., Jackson, 2002). Strain accumulation is diffuse and occurs in broad shear zones (King et al., 1994), where faults are numerous, but small. This is further reinforced by the effect of strain hardening, which is characteristic for the block model.

In the third model, strain accumulates along complex structures that follow fractal patterns and/

or power law relationships (e.g., Turcotte, 1992; Bak, 1996). The processes of strain softening and strain hardening balance each other so that the system is in a "critical state". Deformation structures are scale-invariant and self-similar (e.g., Turcotte, 1992; Bak, 1996), so that the structures show neither spatial nor temporal patterns (be it regional fault networks, single faults or any other structures within fault zones) (e.g., Ben-Zion and Sammis, 2003).

One good example for a power law relation is the Gutenberg-Richter relation, in which the frequency of seismic events correlates with their magnitude (Bak and Chang, 1989; Kagan and Jackson, 1991; Bak, 1996). Similarly, the particle size in shear zones correlates with the duration of fragmentation processes (Billi and Storti, 2003), whereas the displacement of faults in analogue models correlates with their size, and the size of faults with slip frequency (Bellahsen et al., 2003). Fractal patterns exist for particle size in fault cataclases (Billi and Storti, 2003), length of fault segments (Okubo and Aki, 1987; Marrett and Allmendinger, 1994), and size of crustal blocks of the block model (Gallagher, 1981; Nur et al., 1989).

Ben-Zion and Sammis (2003) argue that fractal patterns and power law relations are not exclusively indicative of complex structures, as they can also be found when structures generally have Euclidean geometries. In a similar fashion, Turcotte and Glasscoe (2004) point out that deformation in the crust is not linearly viscous according to the "viscous sheet model" (England and McKenzie, 1982), but according to a power law relation which correlates stress and strain rate, and that faults of various sizes equally accumulate strain. However, they concede that these arguments do not preclude the "continuum model".

Zoback et al. (2002) give another example in which various models occur in close spatial proximity, namely along the North American plate margin (fore-arc and adjacent foreland basin). High heat flow is responsible for low viscosities in the lower crust supporting ductile deformation. When heat flow is high, only small stresses are necessary to cause brittle deformation at the same time, which is consistent with the continuum model. In contrast, the heat flow in the adjacent foreland basin is very low, causing the crust to behave as a rigid block, not deforming internally.

This is characteristic for the block model.

Given these examples, it is likely that models co-exist both in space and time, and that characteristic structures overprint each other. Ben-Zion and Sammis (2003) argue that strain initially accumulates in diffuse shear zones during a period of strain hardening or along complex structures. Subsequently, characteristic structures are dominantly strain softening and strain localizes along structures. Complex structures that have played an important role in the initial stage become more and more planar with increased slip.

Changes from initially diffuse strain distribution in broad shear zones to strain localization along planar faults have been demonstrated in analogue models with granular media like sand (Adam et al., 2004). Simulations by Tchalenko (1970) show that deformation initially accumulates along Riedel shears, then along P- and Y-shears, and eventually forms narrow shear zones.

To date, the spatial distribution of characteristic structures has been better examined on various scales (from millimeter scale to fault networks up to plate margins) than the temporal pattern. This is due to the fact that different stages, during which characteristic deformation structures are formed, cannot be easily differentiated in the field, as structures overprint each other. Therefore, we lack the details of the deformational patterns over time, e.g., regarding the number of deformation stages and their duration, which again depends on the spatial scale of the observed structures. In contrast, sedimentary patterns and stratigraphic sequences have been studied with much higher temporal resolution in the outcrop and in seismic sections.

As far as the temporal aspect of strain accumulation is concerned, previous studies mainly focused on the comparison of deformation rates on the geological long-term scale of several million years and current GPS rates. In this regard, Leffler et al. (1997) and Liu et al. (2000) have shown that, e.g., for the Central Andes, shortening rates of both scales are different. Klosko et al. (2002) note that such a comparison is not straightforward, because GPS rates also include the elastic component. The works of Friedrich et al. (2003, 2004) in the Basin and Range province, USA, additionally cover time scales over four orders of magnitude in between and can therefore quantify the duration of deformation activity from sudden seismic events

over kiloyears, to millions of years. Their results also show that displacement rates are different for each of the studied scales. This suggests the existence of characteristic deformation patterns in time. Yet, the characteristics of such patterns remain to be identified over the scales.

Further complications result from the diverse impact of parameters that are either 1) intrinsic such as rheological properties with lateral and vertical mechanical anisotropies (e.g., Thatcher, 1995; Townsend and Sonder, 2001; Jackson, 2002; Pysklywec et al., 2002; Klepeis et al., 2004); buoyancy effects caused by density and viscosity contrasts (Townsend and Sonder, 2001; Jackson, 2002); coupling effects between upper and lower crust or between lithosphere and mantle (Vanderhaeghe and Teyssier, 2001; Klepeis et al., 2004); and thermal effects (e.g., a. heat flow, Zoback et al., 2002; b. delamination processes, Corti et al., 2003; Babeyko et al., 2004a; c. magmatism, Corti et al., 2003; Klepeis et al., 2004; Trumbull et al., 2006), or 2) influenced by external factors on the deformation system including convergence rate, subduction angle, degree of coupling between the upper and the lower plates, effect of an indenter during collision (Pysklywec et al., 2002), and climatic effects (Schlunegger and Willett, 1999; Zeitler et al., 2001; Hoth et al., 2004).

Each of these parameters acts on a particular scale or range of scales in time as well as in space. However, their impact is likely to extend to other scales as well. Additionally, parameters are coupled variously to each other, changing their influence on a system and thus leading to an increased complexity of the relation between causes and effects, both in time and space.

3. The Methods

3.1. Geostatistics

Geostatistical methods (e.g., Matheron, 1962; 1970; Journel, 1977; Deutsch and Journel, 1992) are applied to analyze the distribution of a variable in space (2D), or in space and time (3D). Variography is one of them, examining the correlation of variable values across space, i.e., the spatial change of the variable value in the resulting variogram. These variograms are approximated by mathematical models that form the base for interpolation techniques (e.g., kriging). This allows filling unknown spaces with probable values, but is only valid, if the analysed variable is continuous over space and several other conditions are met (e.g., Matheron, 1962; 1970; Journel, 1977; Deutsch and Journel, 1992).

This study analyses the distribution of strain in the Central Andes. The original deformation data (database compiled from literature, Appendix A) includes geographical coordinates of the study areas as well as the beginning and end of deformation in the respective areas. Only those references were included that precisely documented the geographical location of the study area and the samples used for dating, as well as the dating method. In the original format, the data plot as polygons of various sizes and shapes.

I initially reorganized the data into a grid of points covering the entire area. To each of these points information is assigned on beginning and end of deformation for the given geographical position, so that the duration of deformation at each point can be calculated. Additionally, I included shortening estimates derived from balanced cross sections (compilation from Oncken et al., 2006), to gain shortening rates for every data point with a spatial resolution of 40 km, and a temporal scale of 1 Ma steps. These lower cut-off values represent the upper boundary of the error of the data, meaning that the data are not solid below these values.

For both the deformation activity and shortening rates the variables are continuously distributed in space, as they will only have positive values or be zero. However, I could not use our variogram models for interpolation as we do not precisely know which of the natural boundaries (e.g., faults) have to be accounted for dividing the entire area into subareas. For the same reason, we did not use 3D models: it is hard to distinguish

the limits of the correlation between points that are at a distance, spatially and temporally. Therefore, we only employ spatial 2D analysis for each time window of 1 Ma.

Variogram analysis requires that variables are given with geographical coordinates (x/y) and individual values. The variation in variable values from one point to another separated by a distance h (lag spacing) is calculated according to this formula (Fig. 3.1):

$$\gamma^*(h) = \frac{1}{2 N(h)} \sum_{i=1}^{N(h)} [z(x_i) - z(x_i + h)]^2$$

Fig. 3.1: Formula for semi-variogram

This is done for every distance h and in all possible directions (Fig. 3.2).

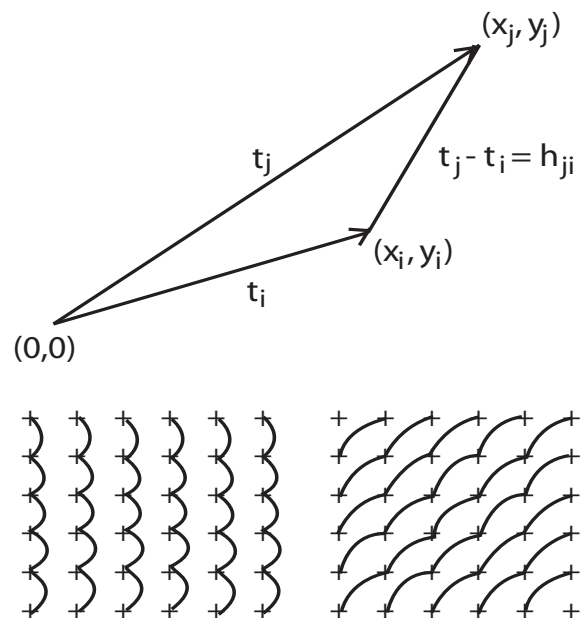


Fig. 3.2: Graphical representation of the distance h between points. " h " is calculated for all possible directions.

All distances h are plotted on the x-axis against the variation (y-axis).

The omnivariogram includes all directions at once, whereas directional variograms can be calculated for a given direction, which is necessary when the data show anisotropies, i.e., pronounced differences in some directions. Directions are given in degrees: East is 0, North is 90, West is 180 etc., counting counterclockwise. Such anisotropies can be easily detected on variogram surfaces, which display the variation over the entire area at once.

Several features exist that characterize the spatial distribution (Fig. 3.3): 1) the sill is the nominal value of variation beyond which the curve of the variogram reaches a plateau and becomes stable; 2) the range is the nominal value for the

distance “ h ” beyond which the variation does not increase any further, i.e., when the curve reaches the sill; 3) the hole effect occurs when the variation decreases for higher “ h ” to increase again, i.e., the curve drops down and goes up again, indicating a recurrent pattern or a periodicity; 4) the nugget value is present when the curve has an initial variation, i.e., originates at a value >0 of the y -axis,

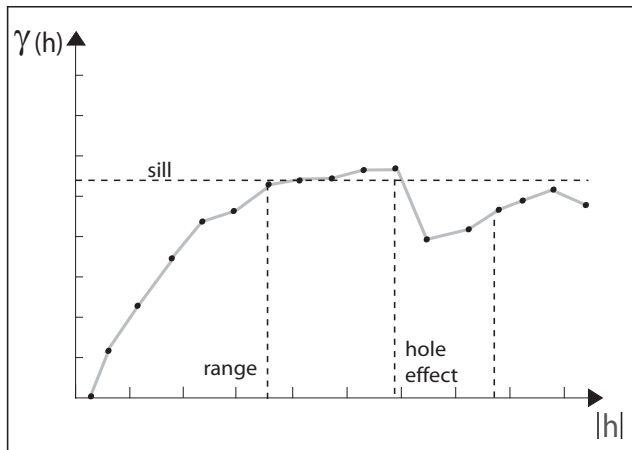


Fig. 3.3: Sample variogram with sill, range, and hole effect

which is due to a random component within the data (e.g., due to a measurement error). None of our fitted variogram models required a nugget.

3.1.1. Other approaches

The better quantification of deformation on a scale spatially smaller than the entire region requires the knowledge of fault displacements. The displacement can be derived from the length of a fault according to a power law that relates displacement and length (e.g., Watterson, 1986; Walsh and Watterson, 1988; Cowie and Scholz, 1992; Davy et al., 1992; Dawers et al., 1993; Scholz et al., 1993; Wojtal, 1994).

However, the exact power law exponent of d - l ratios is still under debate, as it might vary e.g., for extensional and compressional structures, for single faults and those that are interconnected (e.g., Dawers and Anders, 1995; Cartwright et al., 1995; Wojtal, 1996; Cladouhos and Marrett, 1996), for faults in homogeneous or inhomogeneous material (Fossen and Hesthammer, 1997; Gross et al., 1997) etc (cf. Bonnet et al., 2001 for a thorough review). The resulting uncertainty in displacement estimates leaves a range of values that is too big to be used. This uncertainty is even higher when the available digitized geological maps are not very accurate.

3.2. Analogue modelling technique, advantages and limits

In analogue experiments every parameter can be studied separately and in combination, and can directly be related to its effect on the resulting pattern of strain accumulation. All experiments were monitored with a special camera system using the “particle imaging velocimetry” technique (PIV), which allows high resolution of the complete particle displacement fields of strain in time and space. Thus, the effect of every parameter can be studied in detail on e.g., the orogen scale and the next smaller regional scale.

The cameras are to be calibrated before each experimental run. This is particularly important when two cameras are in stereoscopic view for 3D resolution. The calibration yields a mapping function accounting for any distortion, and was applied to the recorded sequential pairs of stereoscopic images. For 3D experiments, digital elevation models were additionally calculated for every stereo image pair by cross-correlation, which were further used for the calculation of the vector fields.

A special algorithm employing Fast Fourier Transformation was executed with the commercial software DaVis by LaVision. Thus, the complete particle displacement field with all components of the strain gradient tensor is resolved with an accuracy of 0.33 mm (viscous-brittle experiments) and 0.38 mm (granular experiments) for every pixel. The pixel error is one order of magnitude lower than its resolution, which is below the scale of a single grain of sand ($\sim 400\mu\text{m}$). For the granular series, images were sampled every second, rendering 24 images per centimeter of convergence at a motor speed of 2.5 cm/min. For the brittle-viscous experiments, image pairs were taken every five minutes, i.e., every 0.6 mm of shortening at a motor speed of 7 mm/h.

The pixel resolution is limited by the size of the recorded area. A bigger experimental surface requires the cameras to be at a larger distance, thus reducing the resolution. This constraint precludes the high resolution of structures below the fault-scale (e.g., stick-slip behaviour of single grains of sand), when the orogen-scale is to be recorded at the same time. Therefore it can be said that the changes in the velocity fields suggesting deformational stages (cf. Chapter 8) are real and not due to the stick-slip behaviour of grains. However, materials need to have a high elastic

component and to be velocity-strengthening for real analogue earthquakes to occur (Rosenau et al., 2006); also, the normal load has to be higher. Further, the temporal resolution (in the viscous-brittle experiments) has to be much higher to record this instantaneous motion, which occurs within seconds.

All granular materials used in our experiments were tested in a ring shear device. Shear stresses were measured for known applied normal loads. Regression analysis then was used to determine the coefficients of friction and cohesion (according to the Coulomb failure criterion: $\tau = c + \mu \sigma$) for peak, static-stable, and dynamic-stable frictions (e.g., Lohrmann et al., 2003; Hampel et al., 2004), which correspond to the frictional strength until failure, the strength of fault reactivation, and the strength of actively deforming material (Byerlee, 1978). The rheological properties of the viscous mixtures were measured with a TA Instruments AR1000 rheometer under applied shear rates on the order of 10^{-5} s^{-1} .

The viscosities had power law relations with exponents close to 1, classifying them as quasi-Newtonian materials. They are not sensitive to changes in convergence rate, i.e., motor speed. Only non-Newtonian materials show time-dependence, so we created different time scales artificially by leaving out some of the recorded time steps.

All experiments are dynamically scaled. The scaling procedures are described in detail in Chapter 6 (granular series) and Chapter 7 (viscous-brittle series). This allows the comparison of strain evolution in the models to that in the natural example. As we are interested in the general nature of deformation processes, the exact geometric and kinematic similarity and the precise deformation activity over time of single faults is not aimed for.

On these lines, the reproducibility of experiments does not require a precise one-to-one, i.e., the same structures do not need to have exactly the same position with identical geometries and the same timing of strain localization and duration of deformation activity. Instead, the strain pattern, the general strain evolution and resulting deformational system had to be reproducible, including the same aspect ratios.

The cross-shaped pattern (Fig. 7.5, 7.8, cf. Chapter 7 for details) in some of my vise experiments is the same as in some experiments from Cruden et al. (2006), even though the initial

model set-up is not the same: experiments by Cruden et al. (2006) allow lateral extrusion, which was not possible in our vise set-up. Similarly, the pattern shape of experiments by Cagnard et al. (2006) resembles the plateau-initiation settings (Fig. 7.5, 7.8, cf. Chapter 7 for details), even though strain localization is initiated in the center of their set-up by a velocity discontinuity.

The preparation of the viscous-brittle experiments set-up requires a special technique. When the the viscosity contrast of the lithosphere (upper crust, lower crust, and mantle lithosphere) and the asthenospheric mantle is low, the asthenosphere affects deformation of the lithosphere. To minimize this effect, the viscosity of the asthenosphere was chosen to be very low. Low-viscosity silicone is an expensive option; water is a good alternative, as long as all layers above have densities below 1.

However, it is not easy to place the viscous layers in the tank without spilling water on top, in which case the layers would immediately sink down. Freezing the water together with the plexiglass tank is not an option as the screws in the plexiglass tank are not made for temperatures of -60°C (the temperature of the freezer was not to decrease). Instead, the layers were frozen themselves.

Therefore, all layers are allowed to float into contact as one big block comprising all viscous parts of the experiment and are frozen thereafter. Such a frozen block can easily be put on the water in the tank. Water, accidentally spilled on the viscous block, will freeze instantaneously without imprinting on the viscous layers. When the viscous block has reached ambient room temperature and is fully settled, the brittle upper crust with a mixture of sand and ceramic beads (Z-lights) is sieved on top.

The calibration of the PIV cameras has to be carried out before the model is fully set up. This means that none of the camera appliance (including the carrying poll and the camera cables) must be touched at any instant after the calibration has been finished. Otherwise the calibration has to be redone.

In total, ten vise experiments were carried out, all but one documented in Chapter 7 (cf. Appendix B). For the granular series, more experiments were performed than are described in Chapter 6. They are documented in Appendix B.

4. Geological setting – the Andean plateau

The Tibetan Plateau in the Himalayas and the Altiplano-Puna Plateau in the Central Andes are the only two examples of active plateau orogens worldwide. They are both characterized by a very large area that is hardly internally deformed and has an elevation of more than 4000 m for the Andean plateau and more than 5000 m for the Tibetan example. These flat areas are bounded to both sides by mountain ranges which have an extent of several hundred kilometers.

The Andean Cordillera stretches all along the western margin of South America, but only from $\sim 17^{\circ}\text{S}$ - 27° the mountain range is developed as a plateau orogen. The Altiplano lies north of 24° , the Puna south of it; together they form the Altiplano-Puna plateau, in the following referred to as the orogen (excluding parts of the Andes that have no plateau). In this thesis, I focus on the Central Andean Altiplano (Fig. 4.1).

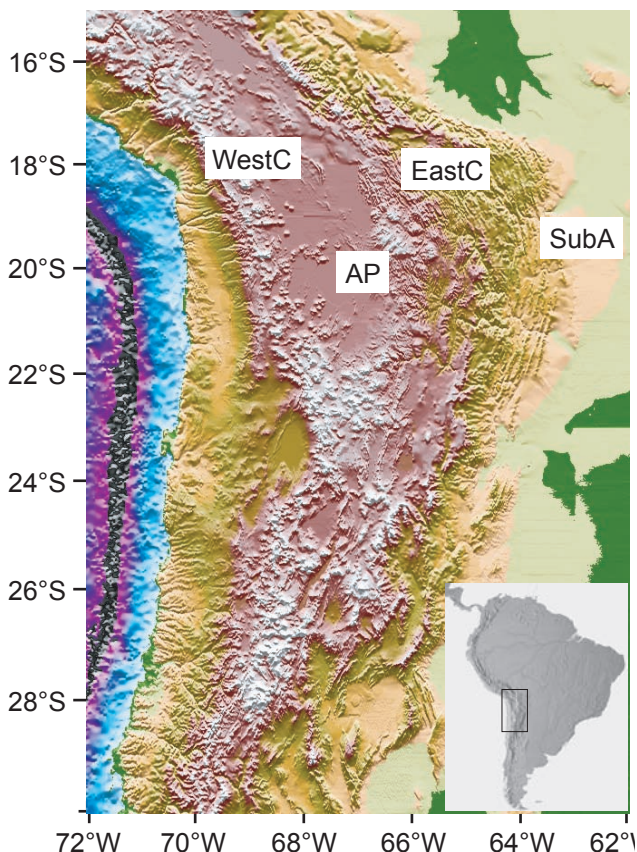


Fig. 4.1: Topographic map of the Central Andean plateau. The following abbreviations are used: WestC – Western Cordillera, AP – Altiplano, EastC – Eastern Cordillera, SubA – Subandean fold-and-thrust belt.

The orogen exhibits a symmetric oroclinal bend (Gephart, 1994) with its symmetry axis coinciding with the current direction of plate

convergence. Both paleomagnetic data within the forearc (e.g., Macedo-Sánchez et al., 1992; Butler et al., 1995; Somoza et al., 1999; Roperch et al., 1999; 2000; Rousse et al., 2005) as well as differential shortening indicate counterclockwise rotation (up to 45°) north of the symmetry axis and clockwise rotation south of it explaining the oroclinal bending of the Andes (Isacks, 1988). This is supported by balanced cross sections (Kley, 1999). The convergence rate for relative motion between the Nazca plate and South America can be averaged to 7 cm/a for the last 30-40 Ma (Silver et al., 1998). At the largest distance (from forearc to foreland) of the orogen between 18°S - 20°S , 280 km of shortening have been accumulated within the last 40 Ma (e.g., Kley, 1999).

The studied region within the Central Andes comprises the five major units from west to east: a) the fore-arc, b) the Western Cordillera (magmatic arc), c) the Altiplano plateau, d) the Eastern Cordillera, and e) the Subandean fold-and-thrust belt.

Both Cordilleras formed at positions of inherited structures: a Permian rift in the Eastern Cordillera (Sempere et al., 2002), and the magmatic arc in the Western Cordillera (Oncken et al., 2006), both operating as weakness zones where strain localized. A low-velocity zone at a depth of 20 km is imaged in seismic sections. It can be interpreted as a zone of partial melt possibly decoupling deformation of the upper crust from that of the lower crust (Yuan et al., 2000), which has probably developed since about 30 Ma ago (Babeyko et al., 2002). This horizon possibly extends to the east connecting with the detachment of the Subandean fold-and-thrust which is located in Ordovician shales (Kley et al., 1996); the Subandean might be underthrust by the cold Brazilian Shield (Babeyko and Sobolev, 2005). To the west of the Western Cordillera, the little internally deformed forearc might have acted as a “pseudo-indenter” pushing into the comparably weaker orogen during subduction (Victor et al., 2004; Tassara, 2005). Thus, the orogen would have been squeezed between two relatively stronger units: the forearc and the Brazilian Shield. I used the mentioned characteristics (cf. Fig. 4.2) as analogies to develop the experimental set-ups, which are described in detail in Chapter 6 (granular series) and Chapter 7 (viscous-brittle series).

Shortening estimates based on balanced cross sections (for all relevant latitudes) have been

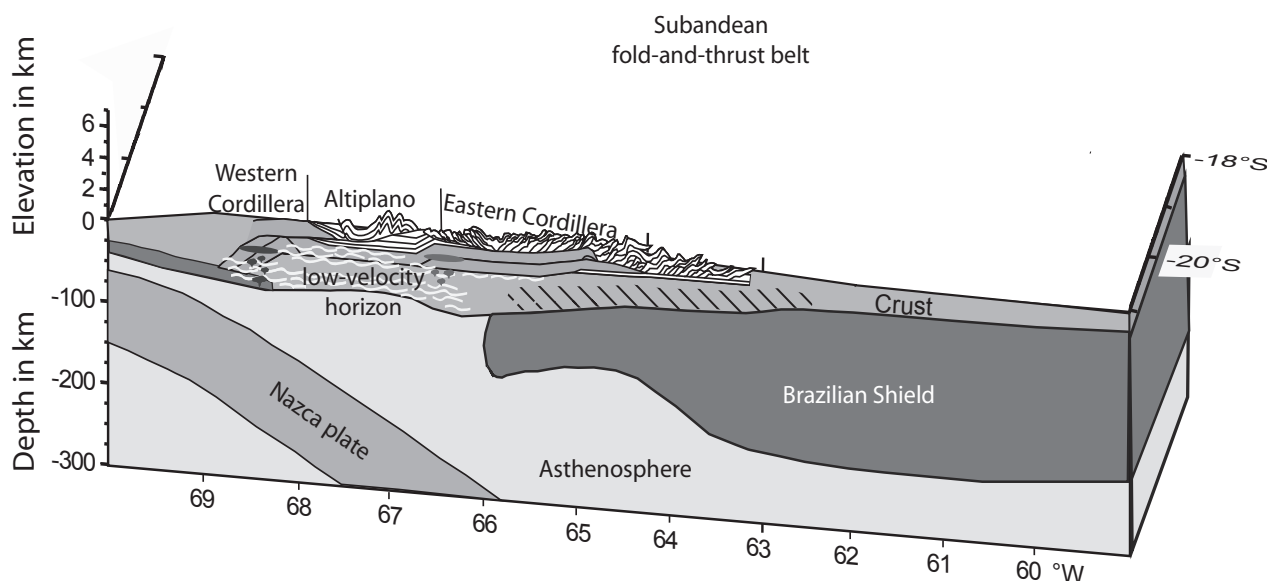


Fig. 4.2: Schematic cross section through the Central Andean plateau with the characteristics used as analogies for the experimental set-up. Further description in-text. Modified from Beck and Zandt (2002).

summarized in Oncken et al. (2006).

Deformation activity has been grouped into five main time windows by Oncken et al. (2006). The beginning of deformation in both Cordilleras (West: 46 Ma, East: 40 Ma) falls within the first window (46-37 Ma), the intramontane basin of the plateau area between these Cordilleras (Elger et al., 2005) has started to deform in the second time window (36-30 Ma) with the Cordilleras remaining active. Subsequent windows (29-20 Ma and 19-8 Ma) are marked by the north-south extent of deformation activity and the last (7-0 Ma) is characterized by transfer of the active deformation away from the plateau into the Subandean fold-and-thrust belt (e.g., Allmendinger and Gubbels, 1996). Responsible for this spatiotemporal strain distribution was a special combination of parameters including differential trench-upper plate velocity evolution, high plate interface coupling from low trench infill, and the lateral distribution of weak zones in the upper plate (Oncken et al., 2006).

Several separate mechanisms have been previously suggested to be responsible for the plateau formation and its uplift, but they cannot explain the strain evolution in space and time. The following mechanisms have been proposed: a) changes in plate convergence (e.g., Pardo-Casas and Molnar, 1987; Coney and Evenchick, 1994; Scheuber et al., 1994; Silver et al., 1998; Somoza, 1998); b) changes in the properties of the downgoing slab (e.g., Gephart, 1994; Giese et

al., 1999; Gutscher et al., 2000a,b; Yanez et al., 2001); c) mantle processes (e.g., Isacks, 1998; Wdowinski and Bock, 1994a; Allmendinger et al., 1997; Kay et al., 1999; ANCORP-Working Group, 2003; Garzzone et al., 2006); d) intra-plate strength variations (e.g., Allmendinger and Gubbels, 1996; Hindle et al., 2002; Lamb and Davis, 2003); and e) climate-related variations (e.g., Masek et al., 1994; Horton, 1999; Montgomery et al., 2001; Lamb and Davis, 2003; Sobel et al., 2003).

The two plateau areas, Altiplano and Puna, differ in many aspects. The Altiplano accumulates more shortening, deforms thin-skinned, is underthrust by the cold Brazilian Shield (Babeyko and Sobolev, 2005), and thus has a thicker crust. In contrast to this, the Puna accumulates less shortening, and has a less wide plateau area, which attains higher elevations than the Altiplano. It deforms thick-skinned and has a thinner lithosphere; this is probably due to mantle delamination (Kay and Kay, 1993; Sobolev and Babeyko, 2005), as the Brazilian Shield does not underthrust the Santa Barbara fold-and-thrust belt (which is the southern equivalent to the Subandean fold-and-thrust, that belongs to the Altiplano region).

Allmendinger and Gubbels (1996) have classified two different deformation modes for the two areas: the Altiplano deforms in a simple shear mode, meaning that localization of deformation in the upper crust does not occur in the same vertical column as the lower crust. This "pure shear" mode

is true for the Puna plateau. In addition, the Puna plateau is still actively deforming and uplifting, while the Altiplano has already attained its final elevation.

Most of these characteristics can readily be explained by along-strike variations in the initial system: the location and type of sedimentary deposits, which determine the style of thrusting in the fold-and-thrust belt, the boundaries of a continental shield, or the fact that delamination of the lithospheric mantle affects the thermal state of the system and therefore its strength (e.g., Allmendinger and Gubbels, 1996). Thus, some characteristics in our models are rather true only for the Altiplano, like the fact that two stronger blocks compress a weaker orogen, analogue to the indenting forearc to the west (Victor et al., 2004; Tassara, 2005) and the strong Brazilian Shield to the east. The natural counterpart of the decoupling horizon is the layer of partial melt beneath the Altiplano (Yuan et al., 2000).

The Andean plateau is the natural example for my study, as the resolution of strain data is very high. This is due to unique outcrop exposures as a result of the arid climate, and also to the preservation of datable syntectonic deposits in intramontane basins. Therefore, the area is extensively studied and deformation is dated very well and highly resolved. All available data compiled from literature yield a comprehensive deformation database (Appendix A, previously published in Oncken et al., 2006). These data form the base for further analysis (Chapter 5).

5. Orogen-wide patterns of strain accumulation – the Andean case

To better understand and quantify deformation frameworks on multiple spatial and temporal scales, the attempt is often made to find scaling laws of strain accumulation for the comfortable extrapolation of data to all scales. However, scale invariance vs. characteristic lengths of structures and deformation in stages has not yet been studied in detail on the orogen scale in relation to the next smaller regional scale. By means of (geo)statistical methods we examine the strain evolution on the orogen scale for the Central Andean plateau (17-27°S and ~69-63°W) for the last 46 Ma based on a comprehensive literature compilation of all available deformation data. Thus, we are able to detect typical lengths of structures and characteristic temporal patterns of strain accumulation on both the regional and the orogen scale. Regionally active areas commonly have widths of 150-200 km and along-strike extents of 200-300 km. On the orogen scale however, they are coevally active over lengths of 600-800 km. This is true for all deformation stages which are typically 2-4 Ma long. Therefore, we propose the following temporal pattern for the Central Andean plateau, which is refined compared to previous estimates: 46-43 Ma, 42-41 Ma, 40-34 Ma, 33-29 Ma, 28-18 Ma, 17-13 Ma, 12-11 Ma, 10-9 Ma, and 8 Ma to present.

5.1. Introduction

Extensive work has been done to detect critical scaling laws that relate e.g., the frequency of seismic events with their magnitudes (Gutenberg-Richter, e.g., Bak and Chang, 1989; Kagan and Jackson, 1991; Bak, 1996), the displacement of faults with their length (e.g., Watterson, 1986; Walsh and Watterson, 1988; Sornette and Davy, 1991; Dawers and Anders, 1995; Wojtal, 1996; Nicol et al., 1996), the length of a fault with its slip frequency (Scholz et al., 1993; Bellahsen et al., 2003), or the length of fault segments with their frequency (Okubo and Aki, 1987; Wojtal, 1994). Such scaling relations follow power laws that are practically valid on all scales, so that data from one scale could be extrapolated to another, e.g., bigger scale like the orogen itself, which cannot easily be studied in detail.

However, not all deformation processes underlie this “fractal” deformation framework, but rather follow the continuum-Euclidean view, in which strain localizes along some faults or fault systems (strain weakening); or the granular view, in which strain accumulation is diffuse (strain hardening). It has been suggested that deformation frameworks alternate over time (cf. Ben-Zion and Sammis, 2003), and characteristic patterns exist. Unfortunately, characteristic structures superpose each other, so that they can hardly be attributed to the respective deformation framework and thus, deformation patterns cannot easily be detected in the field. In addition to this difficulty, temporal

patterns on one spatial scale need not be the same on another, unless strain accumulation was scale-invariant.

In this study we aim to examine the strain pattern on the orogen scale for the Central Andean plateau (17-27°S and ~69-63°W) on the base of a thorough literature compilation of all available deformation data, and to detect typical lengths of structures and characteristic duration of strain accumulation on both the regional scale (e.g., fault systems and networks) and the orogen scale by means of (geo)statistical methods. By comparing the two, we are able to examine the effect of spatially smaller scales on the next bigger scale over time, and to elaborate on the permissibility of extrapolating data from one scale to another.

5.2. Geological setting

The Central Andes are the result of the last ~46 Ma of subduction of the oceanic Nazca plate beneath the South American continent, and bear one of only two active plateau orogens worldwide. The studied region comprises four major units (excluding the fore-arc region), which are from west to east: a. the Western Cordillera (magmatic arc), b. the Altiplano plateau, c. the Eastern Cordillera, and d. the Subandean fold-and-thrust belt (cf. Fig. 5.1). This is true for the plateau north of 24°S; south of 24°S, the plateau is called the Puna.

In the Central Andes, the amount of shortening varies along-strike and reaches a maximum of 260-280 km at 21°S (summary of

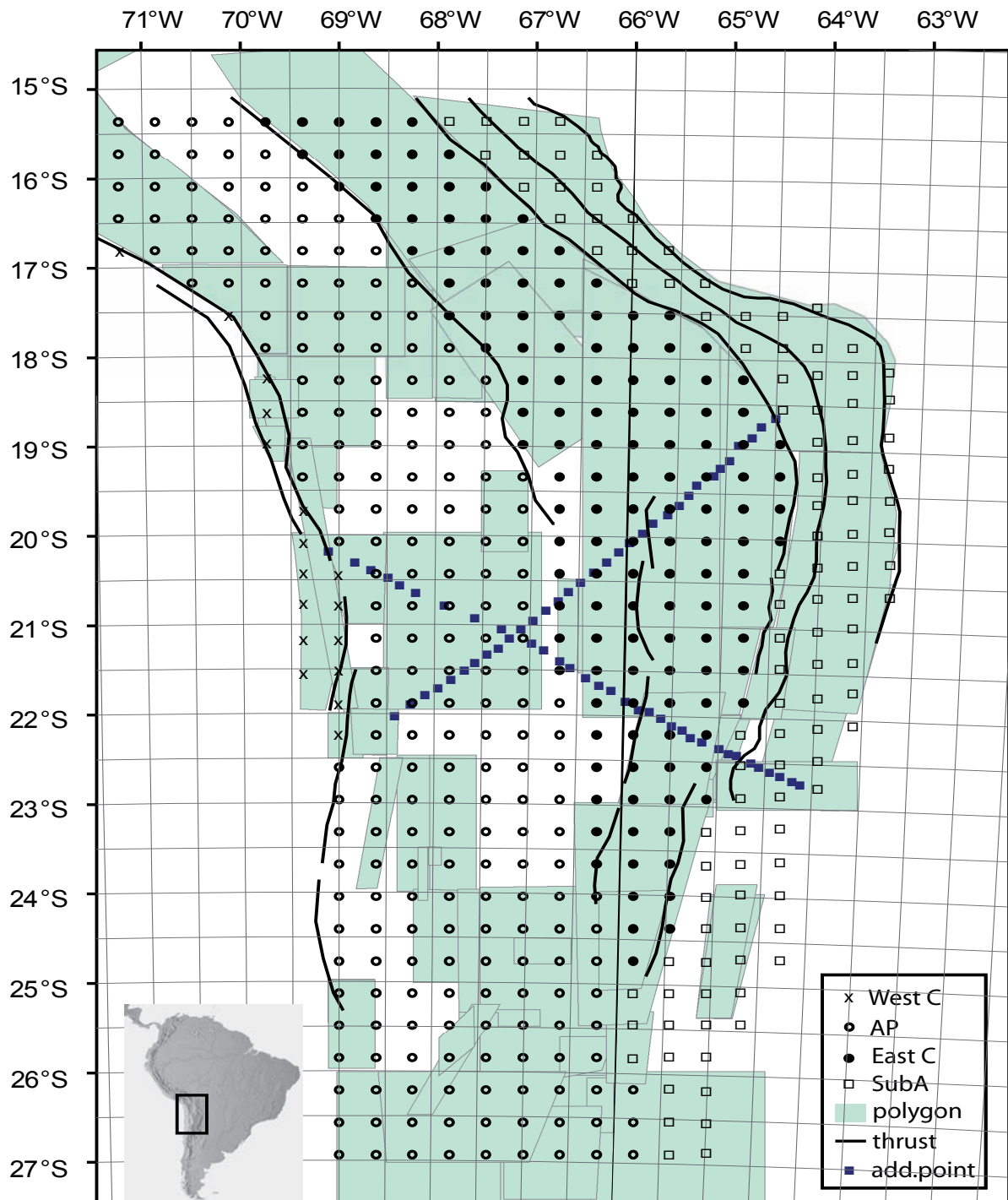


Fig. 5.1: The study area of the Central Andes comprises the four structural units from west to east, which are separated by major thrust faults (black lines): Western Cordillera (crosses), Altiplano-Puna plateau (points), Eastern Cordillera (solid points), and Subandean fold-and-thrust belt (squares). Each of these points is part of the point grid that overlies the polygons (grey area), for which deformation data are given. Areas for which no appropriate data exist are left white. To the lower left a small map of South America shows the location of the study area (black box).

shortening estimates in Oncken et al., 2006). Deformation has commonly been divided into three main orogenic pulses (45-30 Ma, 30-10 Ma, and 10-0 Ma) of which each has an established shortening rate (0-8 mm/yr; 6-10 mm/yr; and 8–14 mm/yr respectively with 9-15 mm/yr as the present-day value, summary in Oncken et al., 2006). Due to numerous datable syntectonic deposits

like volcanic ash horizons and little erosion, the deformation activity in the Central Andes is highly resolved both in space and time.

On the basis of a thorough literature compilation of all available deformation data, Oncken et al. (2006) were able to refine these pulses into five main deformation stages (46-37 Ma: deformation in both Cordilleras; 36-30 Ma:

5. Orogen-wide patterns of strain accumulation - the Andean case

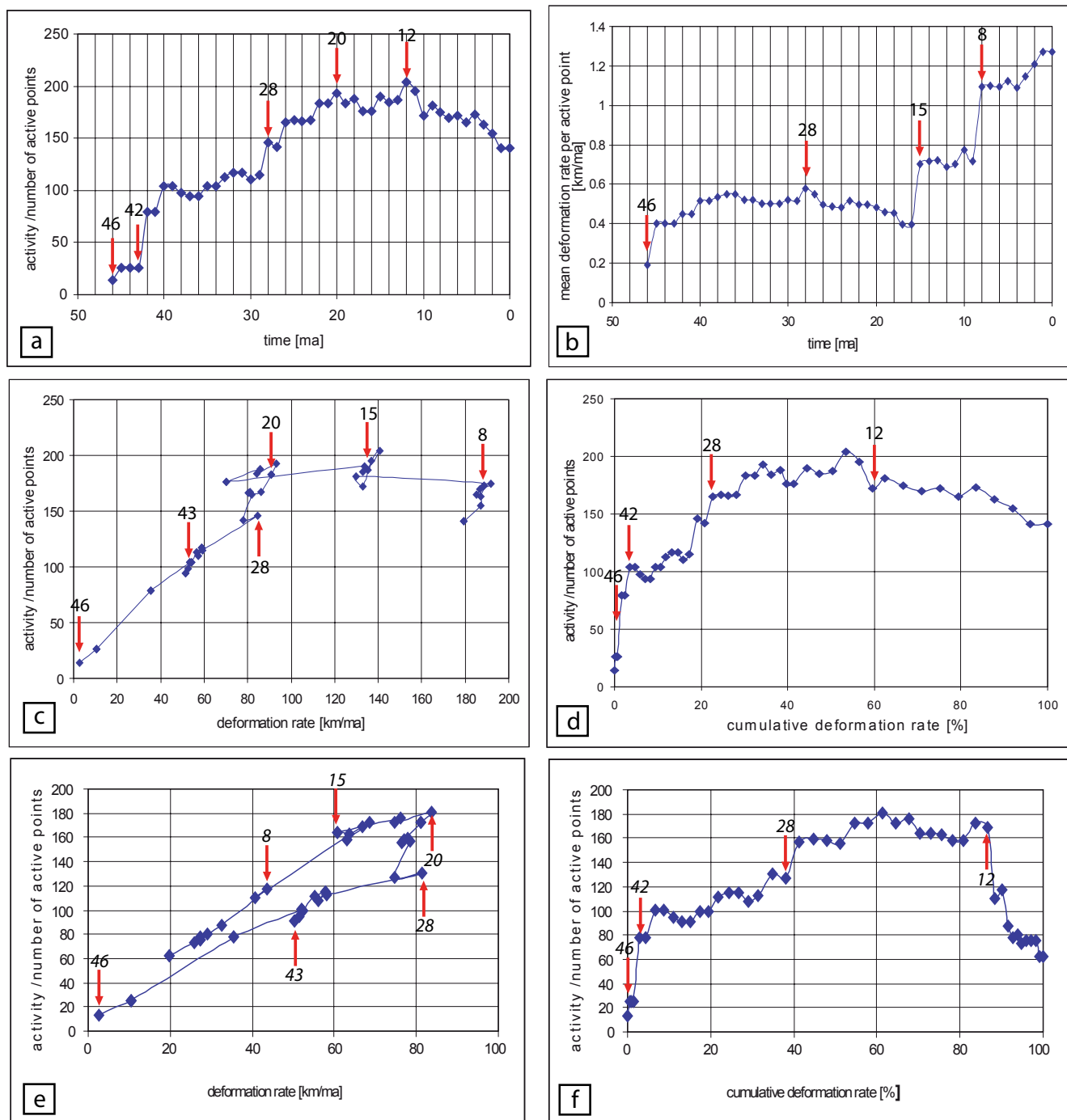


Fig. 5.2: Plots of frequency statistics, for which we mark the beginning of major deformation stages with red arrows: a. the number of active points over time shows how many points, i.e., how much of the total area has actively undergone deformation for a given million year from 46 Ma to the present; b. the mean deformation rate per point (points of all structural units) over time; c. the number of points vs. the cumulative deformation rate (in km/Ma); d. the number of points over cumulative deformation rate (in %); e. is similar to c. but without data points of the Subandean fold-and-thrust belt; and f. is similar to d. but without the Subandean. Stages inferred for e. and f. are in italics to show that the “stages” would be similar to the other stages a.-d., but they are not included in the summary.

deformation in the intramontane basin of the plateau area; also 29-20 Ma and 19-8 Ma, and 7-0 Ma: transfer of the active deformation away from the plateau into the Subandean fold-and-thrust belt). These times are characterized by coeval strain accumulation within the main structural units of the Central Andean plateau along-strike for several hundred kilometres. The authors suggest that these characteristics are only observed when

deformation data are examined on time scales of >5 Ma.

5.3. Data preparation

The databank published in Oncken et al. (2006) includes a compilation of the existing literature on deformation activity for our study area for the last 46 Ma (appendix A). Each data set includes the start and end of deformation

activity in millions of years (Ma) inferred for the geographic area given with exact coordinates by the respective authors. We take into account only those references that precisely document the location of the study area, the position and processing of samples, and the used method for dating. We further weight the data according to the accuracy of the sample coverage (e.g., how many samples, dating error), the number of available references for an area, and the age of publication. The data cover almost the entire area, except for some regions within the Altiplano (between 18.5-19.5°S and 22.5-23.5°S) for which the field exposure is not good for deformation quantification.

All data were then plotted as deformation polygons in an ArcGis project, as given by the geographic coordinates of the study areas (Fig. 5.1). Each polygon has been attributed the start and end of deformation. Instead of continuing the analysis with irregularly shaped polygons, we convert the data into a regular grid of points (spacing is 40 km). We chose this distance as the smallest study areas given from literature have widths of slightly more than 40 km, which still allows two grid points to be located within it. However, most study areas are several hundred kilometers in length, for which there is no variation between the grid points. Therefore, a higher resolution, i.e., a smaller distance than 40 km between grid points is not useful. To cover the values below the grid steps for geostatistical analysis, it is common practice to include some additional points with a smaller but random distance.

Next, each of these points is assigned the information of the polygon in which it plots, namely the geographic coordinates (x, y), the start and end of deformation, and the respective structural unit of the Central Andes in which the point is located. In case a point plots in several polygons, it is assigned the information of each.

5.3.1. Deformation activity

As we know the beginning and end of deformation for each point, we can calculate the duration of deformation activity for each point. For each time step of 1 Ma out of the 46 million years, we assign every point either activity for a given Ma (nominal value of 1), or inactivity for a given Ma (value is 0). We chose time steps of 1 Ma as the error for the deformation ages are commonly on the order of 1 Ma. Therefore, it does not make

sense to use smaller time steps, which are not reliable due to this constraint. The resulting data set of deformation activity includes a total of ~440 nominal values of 0 and 1.

5.3.2. Shortening rates

Additionally, we determined the shortening rate for each point of the grid (or deformation rate). Oncken et al. (2006) compiled published shortening estimates inferred from balanced cross sections, which exist for all latitudes of the study area and in between; and mostly include estimates for each of the structural units individually. The amount of shortening known from this compilation is divided by the number of points that lie in the respective balanced cross section according to our grid. This gives us the shortening estimate for an area that is located between two neighbouring points. As we also know how long each point was actively deforming, we can further divide these estimates by the duration of deformation and obtain shortening rates. Shortening rates for small areas (40 km) for 1 Ma tend to be rather low compared to big areas, and therefore strain rates would be better as they can be used irrespective of the initial length. As we do not know the initial length of each of the 40 km areas, we cannot calculate strain rates.

We acknowledge that this procedure is only valid under the assumption that strain accumulates homogeneously and if all faults in a polygon have equally accommodated strain. We will discuss this issue at a later stage.

5.4. Statistics

For the frequency statistics, different deformation times are differentiated according to breaks in lines from one million year to the next million year, when one of the following criteria is met: 1. the number of active points changes by ~50 or more, 2. the difference in nominal values between two points makes up ~50% of the smaller value or more, or 3. the slope of the curve from one point to the next is higher than ~60° (i.e., increase of the nominal values when the slope goes up, or decrease when the slope goes down).

For the geostatistics, temporal patterns are differentiated when a spatial variation of the data exists from one million year to the next, depending on 1. the value of variation, 2. the direction of highest variation, or 3. the characteristics of the sill (i.e., highest value of variation), the range (i.e., the distance beyond which the variation becomes

stable) or the hole effect (which indicates a correlation between points at a higher distance). All of these characteristic features are further described below. We also carried out a sensitivity analysis (cf. section 5.5.1. and Appendix A), in which we weighted the significance of each of the time steps.

5.4.1. Frequency of deformation activity

We plotted the frequency of deformation activity of all units against time, i.e., the number of active points for each million year (Fig. 5.2a). Depending on the breaks of the line, the following deformation stages can be detected: 46-43 Ma, 42-29 Ma, 28-21 Ma, 20-13 Ma, and 12-0 Ma.

5.4.2. Frequency of shortening rates

We plot the mean shortening rates (i.e., for distances of 40 km) for each Ma, which is a value averaged for all points over all structural units (Fig. 5.2b). Another plot includes the number of active points vs. the cumulative deformation rate, which shows how much area is involved in each 1 Ma to account for the given deformation rate (values in Fig. 5.2c include all structural units, whereas Fig. 5.2e excludes the Subandean fold-and-thrust belt). When two consecutive points are far apart and its slope is zero or negative, the shortening rate per point has increased from one million year to the next (as fewer points are active). On the other hand, if the slope increases, more points have become active suggesting that the shortening rate decreases for each point. When figures 2c) and 2e) are compared, it becomes obvious that when the Subandean is not included in the plot (Fig. 5.2e), the deformation rate decreases drastically for the last 15 Ma, as the fold-and-thrust belt in the Interandean/ Subandean has accumulated most of the shortening for the last 15 Ma. This can also be seen in figures 5.2d) and 2f), which depict the number of active points over the percentage of cumulative deformation rate, again for all units and without the Subandean respectively.

In general, each of the following times indicates the beginning of a deformation period: 46 Ma, 43 or 42 Ma, 28 Ma, 20 Ma, 15 or 12 Ma, and 8 Ma.

Figure 5.3 shows data for each of the structural units individually, namely the deformation rate and the mean deformation rate per active point over time. Thus we can detect characteristic patterns of each structural separately. In figures

5.3a) and b) it becomes clear, that the Western Cordillera is active from 46-38 Ma with very low shortening rates, after which strain accumulation in the Western Cordillera practically ceases.

The Altiplano plateau (Fig. 5.3c-d) shows dominant deformation activity between 33-12 Ma for which the shortening rate constantly increases. The mean deformation rate per active point however experiences fluctuations with an increase from 33-27 Ma, and a subsequent decrease to a lower but constant value.

The Eastern Cordillera (Fig. 5.3e-f) shows a constant deformation rate from 40-29 Ma, followed by a peak at 28 Ma and a subsequent steady decrease until 17 Ma, with another drastic decline until 10 Ma, after which the shortening rate is comparatively small. Similar fluctuations can be observed for the mean deformation rate per active point.

In contrast, the fold-and-thrust belt does not accumulate shortening in the Interandean until after 15 Ma, and in the Subandean until after 10 Ma.

5.4.3. Other patterns

Figure 5.4a shows the deformation rate for each point of the grid averaged over the last 46 Ma. In general one can say that the Western Cordillera has the lowest shortening rates, followed by the plateau area that has also experienced lower deformation rates than the Eastern Cordillera and the Subandean. The latter two structural units have lower shortening rates towards the northern and southern boundaries of the study area, which can be explained by the oroclinal bend.

Figure 5.4b shows the duration of deformation activity for each point of the grid. Except for the Subandean belt, there is a correlation between the duration and the deformation rate: the higher the deformation rate for an area, the longer it was active. This correlation is partly due to the assumption of homogeneity, which was necessary to obtain shortening rates (cf. section 5.3.2.).

5.4.4. Geostatistics

Variogram analysis is a common method to analyse the variation (i.e., the inversion of correlation) of a variable in a temporal, spatial, or spatiotemporal context (e.g., Matheron, 1962; 1970; Journel, 1977; Deutsch and Journel, 1992). The variable is defined by spatial coordinates (x, y) and a nominal value. Variogram analysis

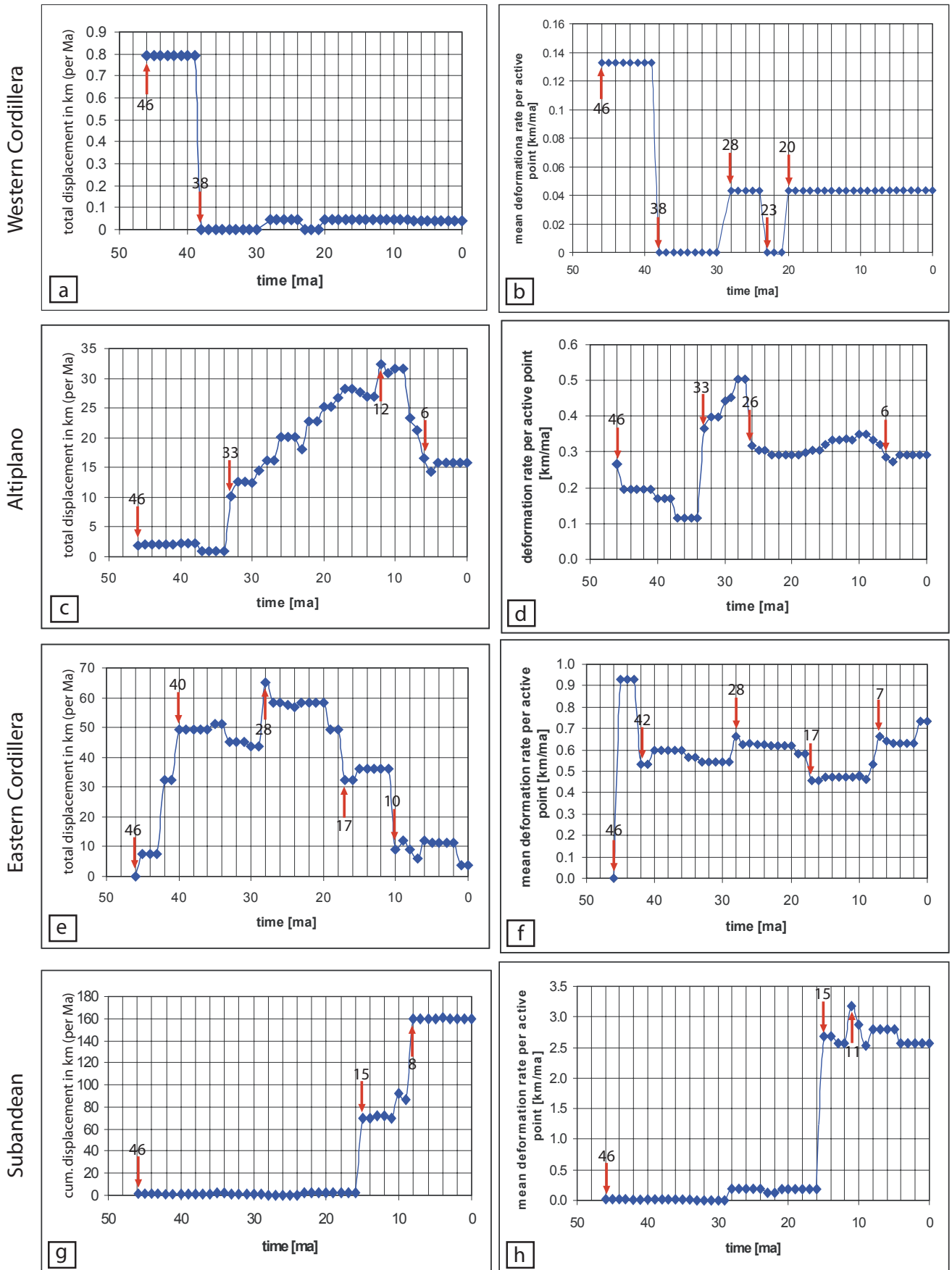


Fig 5.3: Plots of frequency statistics for each of the four units (arrows mark the beginning of major deformation times), namely the displacement over time (left column) and the mean deformation rate per active point over time (right column).

can only be implemented when the variable is continuously distributed in space. This is true for

both deformation activity, which is either 0 or 1 at every location, and shortening rate, which is 0 or a

5. Orogen-wide patterns of strain accumulation - the Andean case

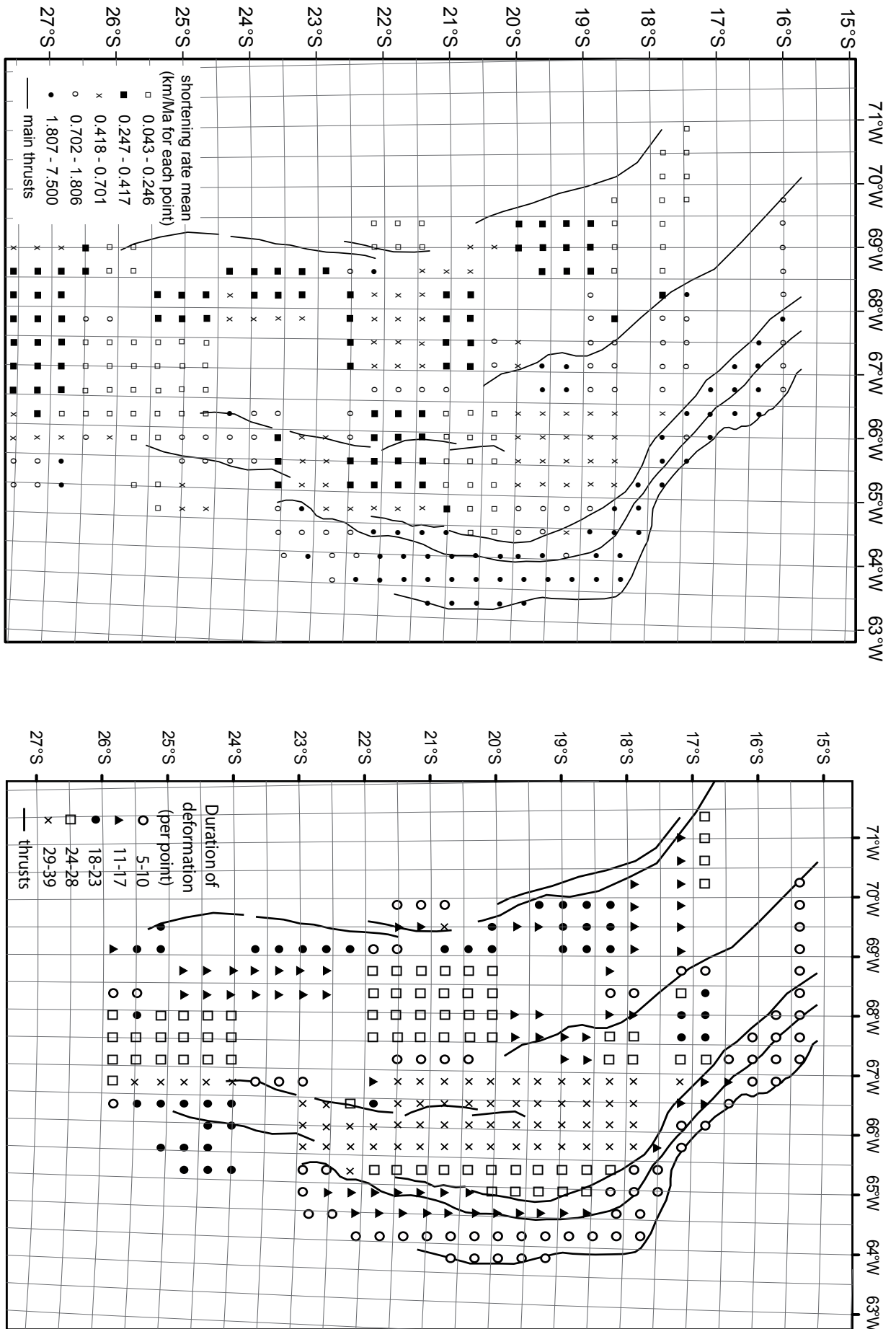


Fig. 5.4 a (left), b (right): The points carry information on their a) mean shortening rate in km/Ma and b) duration of deformation in Ma (refer to legend for nominal values). The values in a) represent the average over 46 Ma, yet there is a clear difference in values over the structural units.

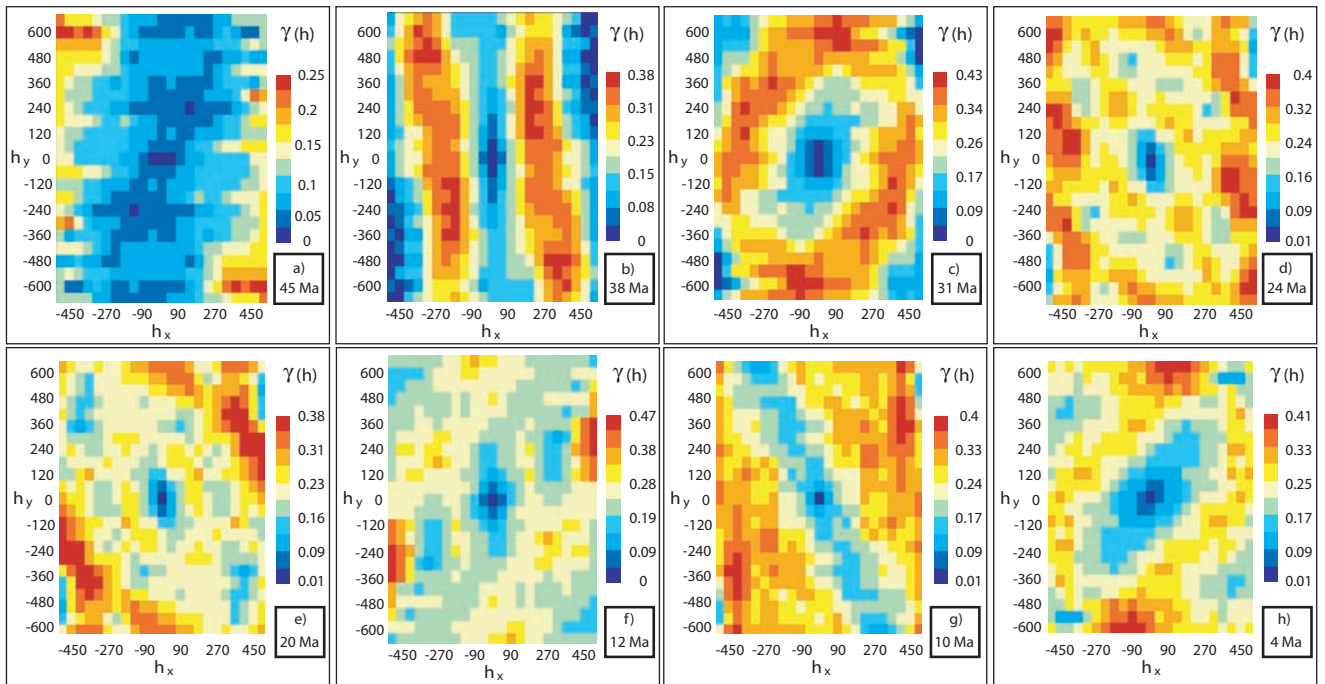


Fig. 5.5: Indicator variogram surfaces are shown for eight different time windows (1 Ma), each representing the spatial variation of deformation activity for a significant deformation period. The data are described in more detail in-text.

positive integer. The main objective of the analysis is to calculate the differences in value of the variable at spatial positions that are separated by a distance “h”. This difference between values is calculated for all possible “h” and in all possible directions, and forms the major part in the formula of variation with $z(x_i)$ and $z(x_{i+h})$ being the values of the variable at position (x_i) and (x_{i+h}) respectively, $N(h)$ is the number of pairs of points (x_i) and (x_{i+h}) that are separated by a distance h (in km):

For example, if we have one active area of the extent “y”, then “h” will be low for all $h < y$,

$$\gamma^*(h) = \frac{1}{2N(h)} \sum_{i=1}^{N(h)} [z(x_i) - z(x_{i+h})]^2$$

as then the distance is calculated for two points that are both located within the same deformation area. For larger ranges “h” between two points, the points are likely to fall within different deformation areas, or one is active and the other is not, and the variation becomes higher. The advantage of the method is its ability to a. quantify the degree of spatial correlation of strain accumulation (e.g., over the entire orogen vs. the next smaller scale) for a given direction, also b. in a temporal context. Thus, it enables us to detect scale invariance vs. characteristic lengths of actively deforming regions and correlation of different structural units.

5.4.4.1. Indicator variogram surfaces

Indicator variogram surfaces are maps

of the spatial variation of a variable (Fig. 5.5). The variation is colour coded, and is given for all distances “h”, namely for both positive and negative x-directions (h_x) and y-directions (h_y). Thus, the spatial position is not directly given in geographic coordinates, but via the distances “h” (in km) between geographic coordinates. This is the reason why the variation is point-symmetrical about the origin in the center of each map (Fig. 5.5). The pattern of these maps indicates the directions of anisotropy, i.e., the direction for which the minimum and maximum variation is most persistent in space. The maximum extent of the active areas can be identified from the maps when clear anisotropy directions are present. For Fig. 5.5b) this is 200 km in width and 600 km in length, for Fig 5.5c) about 400 km both in width and length, for Fig. 5.5f) 200 km in width and 600 km in length, for 5.5g) 200 km in width and 600 km in length, and for Fig. 5.5h) 200 km in width and up to 600 km in length. The upper cut-off is 600 km for the indicator variogram surfaces, so potential length higher than 600 km were not resolved.

The following major stages with their respective main anisotropy directions (and orthogonal to them) can be summarized (Fig. 5.5 a-h): a. 46-43 Ma (NNW-SSE), b. 42-34 Ma (N-S), c. 33-29 Ma, d. 28-21 Ma (NNW-SSE), e. 20-13 Ma (NW-SE), f. 12-11 Ma (NNE-SSW), g. 10-9 Ma (NNW-SSE), and h. 8-0 Ma (NE-SW).

5.4.4.2. Indicator variograms

Indicator variograms (Fig. 5.6) are another way of depicting the spatial variation of the variable. The distance “h” between two points (x-axis) is plotted against the variation of deformation (y-axis). The resulting curves have several characteristic features. The distance “h”, for which the curve does no longer increase, which means that there is no more variation for larger “h”, is called the “range”. Beyond the range, the value for variation remains stable and is called the “sill”. A third characteristic feature of variograms is the “hole effect”, occurring when the curve slopes down (i.e., decreases in variation) to increase in slope again (i.e., increases in variation) with higher “h”. Such hole effects are present, e.g., when a small inactive deformation area is embedded between two actively deforming areas. Thus, the active areas would have a “hole” of inactivity in between. Variograms can include all directions at once (omnidirectional), or a range of specific directions, which are given by numbers: 0 indicates E(ast), 90 is N(orth), 180 is W(est) and so on. In Figure 5.6, we can differentiate the following significant time windows with average extents of actively deforming areas (e.g., the range commonly indicates the minimum extent of an active area as the sill becomes stable, i.e., no more variation occurs for longer ranges “h”, which is the maximum extent):

- a) The first stage 46-43 Ma is determined by the omnidirectional variogram, as only few points are active. This is also the reason for the low value of the sill (~0.1), which means that almost no variation is present for either small or large distances “h”. A range of about 90 km can be inferred from the first slope, which decreases thereafter to increase again slightly after ~450 km. The first value reflects the width of the active units, the second gives their maximum along-strike extent. The sill is stable at 200 km, which indicates the general length of the active units.
- b) The stage between 42-34 Ma has a clear anisotropy along-strike of the units, namely to ENE-WSW (20) and perpendicular to it NNW-SSE (110). In the first anisotropy direction, the range yields ~200 km reflecting the maximal width of the active units. A hole effect is present between 400 km and 750 km

in the same direction. This explains that inactive areas can be found in between active areas. In the second direction, no more variation exists beyond the range of ~200 km, which means that the along-strike extent of deformation areas is 200 km or larger (for which case there is no more variation within one deformation area), and can be active along-strike for up to ~800 km.

- c) Stage 33-29 Ma is characterized by deformation within the center of the study area (namely Eastern Cordillera and Southern Altiplano). The variation is similar in all directions for the same distances “h”. The inferred range of ~400 km reflects the maximum diameter of a continuously active area. A hole effect between 400 and 800 km is related to the regions beyond this active area up to the boundaries of the study area.
- d) Stage 28-21 Ma has no clear anisotropy in any direction, because the active areas are partly turning around the oroclinal bend. However, a range of 180-270 km in the E-W direction reflects the E-W extent of the active areas. The strong hole effect at 600 km for the E-W direction can be explained by the limited extent of the study area in this direction. The range in NNW-SSE direction is 240 km. A slight hole effect between 360 and 600 km can be attributed to the bending of some of the active areas. The maximum length of structural units beyond the hole effect is ~700 km. This illustrates the possible minimum and maximum along-strike extents of the active units.
- e) Stage 20-13 Ma is similar to the previous stage, with the range for the ENE-WSW direction being ~150-200 km reflecting the widths of the active areas. The hole effect in this direction between 200 and 400 km reflects the variation between active and inactive areas perpendicular to their strike. The range for the NNW-SSE direction is at 270 km, which is the minimum length of active units along-strike. The sill is stable up to 600-800 km which is the

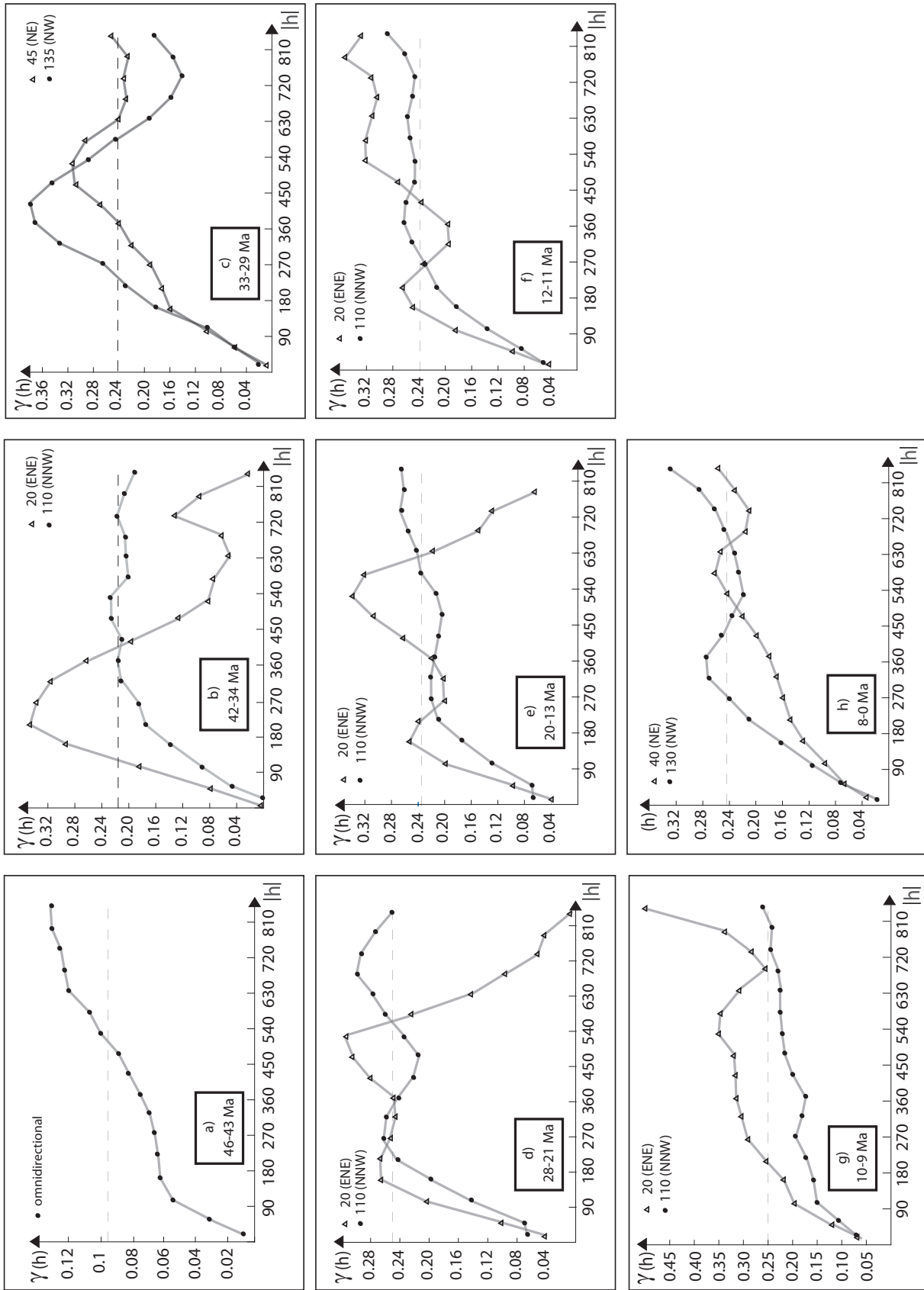


Fig. 5.6: Indicator variograms show the variation of deformation distribution ($\gamma(h)$ over distances h (x-axis). Two different curves are given in parts b) to h), which represent the variation in the directions specified in the upper corner of each plot. Only a) shows an omnidirectional variogram, which means that variation was not studied in a specific direction. Further description of the plots in-text.

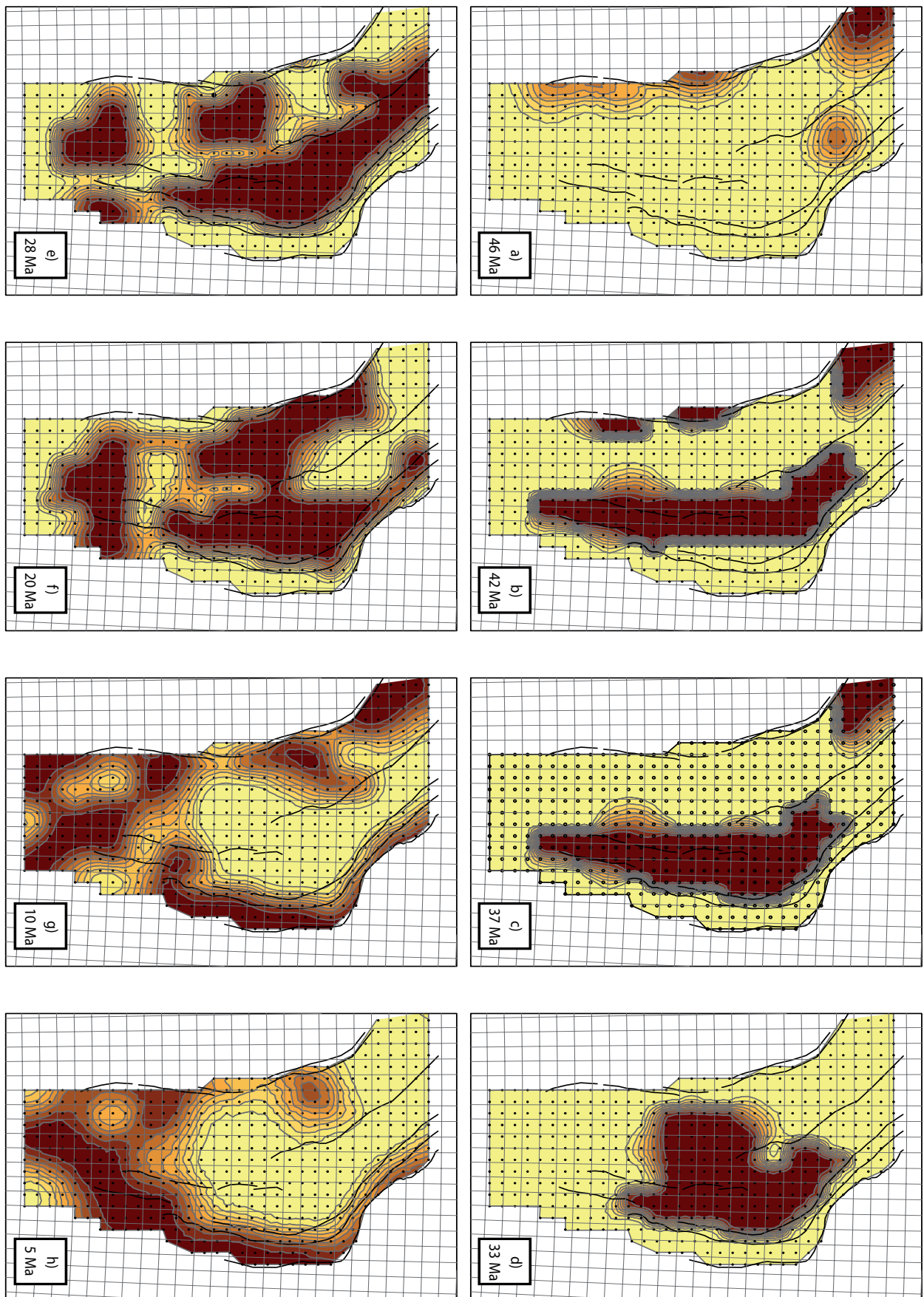


Fig. 5.7: Each of the eight maps a) to h) shows a contour plot of active deformation (brown colours) and inactive regions (yellow) interpolated by kriging. Further description of each of the plots in-text.

- maximum along-strike extent.
- f) Stage 12-11 Ma shows clear anisotropy directions to the NNW-SSE and orthogonal to it with ranges of ~400 km (minimum length) and ~150-200 km (width) respectively. However, active areas attain length up to 800 km. The smaller value is caused by the oroclinal bend region, which separates one long active unit into areas of different characteristic strike/ anisotropy.
 - g) Stage 10-9 Ma is again characterized by a slight anisotropy in the NNW-SSE direction reflecting active areas north of the oroclinal bend (namely the northern part of the Western Cordillera, the Peruvian Altiplano, and the northern Subandes). The generally low variation indicates the long spatial continuity along-strike of active units up to 800 km. The range is ~270 km indicating the along-strike extent of smaller areas. The range for the ENE direction is about 100-200 km indicating the width of the deformation areas.
 - h) The final stage 8-0 Ma is once more characterized by anisotropies to the NW-SE and NE-SW. The range is ~300 km in the first direction and ~150-200 km in the second. This reflects the minimum widths of the units. Active areas in the NW-SE direction attain length of up to 600 km (with a hole effect from 400 km to ~600 km, which reflects the inactive areas in between the still active margins. In the NE-SW direction, the sill steadily increases showing that active areas wider than 200 km are present.

Active areas around the oroclinal bend will not entirely be resolved in the analyzed directions. In fact, the maximum extent of ~600-800 km as in stages f), h), g) in the NNW direction can also be found in other directions, e.g., to the NW. Thus, the entire length of active areas can increase up to almost the total extent of the study area.

5.4.4.3. Kriging plots

Modelled indicator variograms are the base for kriging (e.g., indicator kriging or ordinary kriging), which are interpolation algorithms. They allow the smooth display of our point data for every

million year in space. The following eight stages are most prominent (Fig. 5.7): a. 46-43 Ma, b. 42-38 Ma, c. 37-34 Ma, d. 33-29 Ma, e. 28-21 Ma, f. 20-11 Ma, g. 10-6 Ma, and h. 5-0 Ma.

5.4.4.4. Variogram surfaces: shortening rates

Similar to the diagrams in Figure 5.5, we also performed variogram analysis on the spatial variation of the shortening rate, of which eight variogram surfaces are prominent (Fig. 5.8). The following time windows can be differentiated according to the variations from one million year to the next and with their respective main anisotropy directions (Fig. 5.8 a-h): a. 46-41 Ma (NNW-SSE), b. 40-34 Ma (NNW-SSE), c. 33-29 Ma, d. 28-24 Ma (NW-SE), e. 23-18 Ma (NW-SE), f. 17-11 Ma (NNE-SSW), and g. 10-0 Ma (N-S).

5.5. Results

5.5.1. Sensitivity analysis

All inferred deformation stages from the above described methods are summarized in Figure 5.9. Next, we have to determine which of the time steps causes a major change in the spatial variation of deformation (either activity or shortening rate), defining a significant deformation stage for the orogen. The different results are alternately coloured dark grey and light grey, and each of these “stage” changes are marked with a stippled yellow line.

Time steps (1 Ma to the next 1 Ma) for which more than three stippled yellow lines are present are further investigated in the sensitivity analysis. Following the sensitivity analysis described below, the “significant” time windows are highlighted by a through-going solid yellow line; insignificant time steps are marked by a through-going yellow stippled line.

We evaluated the boundaries between two consecutive time steps according to the following impact factor: $(\text{points}_{\text{changed}} * 10 / \text{points}_{\text{active}}) / (12 - \text{areas}_{\text{active}})$ including the number of changed points from one time step to the next, the number of active points, and the number of active areas. This formula is designed to equally weight these factors, so that significant time windows occur only when a critical amount of active points and active areas changes. For example, when only one or two big areas are active in the first 1 Ma (i.e., data from one or two different authors) and change, then a lot of points are active that can change, but the error can be comparatively large when the original

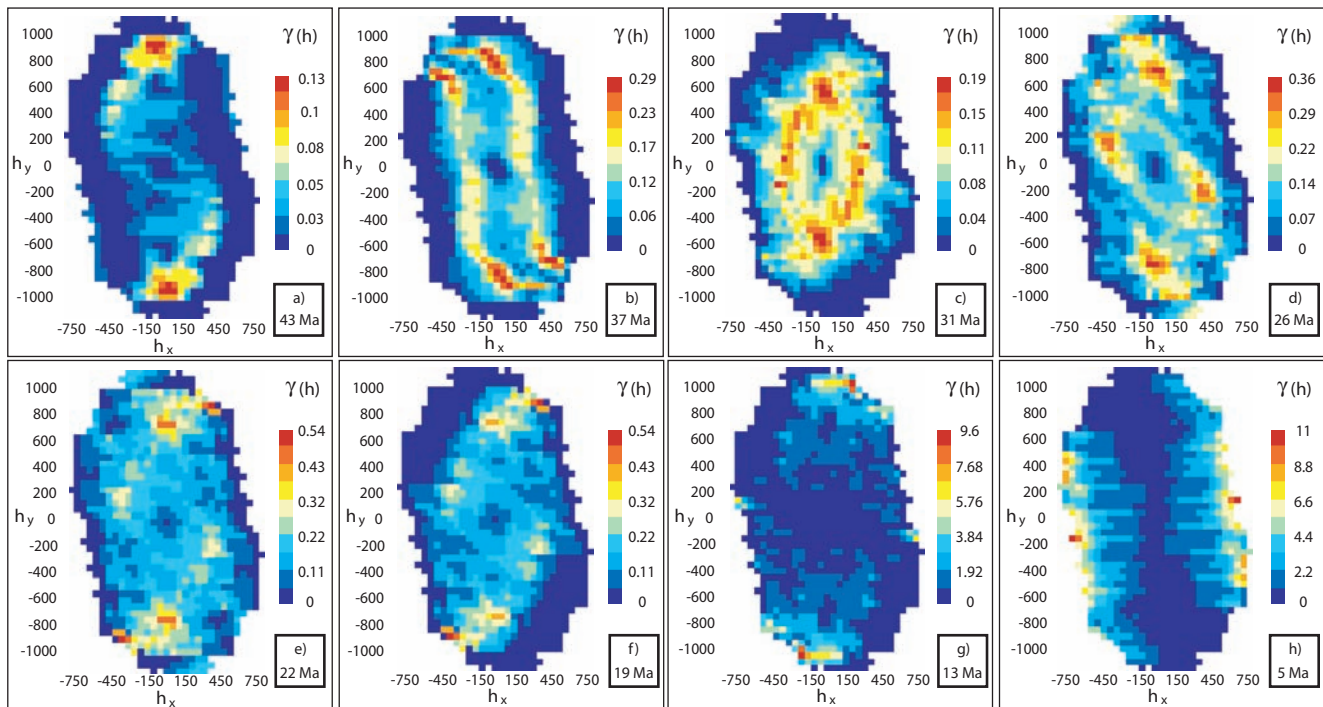


Fig. 5.8: Each of the eight plots a) to h) shows a variogram surface depicting the variation of shortening rates in space. Further description of each plot in-text.

data have an error. On the other hand, when a lot of active areas change but only a small number of points, because the areas are small, it can still be a significant change.

We allowed one additional Ma in our calculation to account for the general area that might result from the original data (e.g., some dating errors do not allow pinpointing deformation with an accuracy of 1 Ma). The result of the impact formula yields values between 0.8 and 9. When they are above 1, we define the stage to be significant. If the value is <1 , it is not. Results of the sensitivity analysis are summarized in Appendix A.

5.5.2. Summary

The following deformation time windows appear to be significant with characteristic associated lengths of active structures/ areas, which take the oroclinal bend into account:

- 1) 46-43 Ma (the Western Cordillera starts to deform), 90 km width and 200 km length;
- 2) 42-41 Ma (the Eastern Cordillera becomes active), 200 km width and 200 km to 800 km length;
- 3) 40-34 Ma (the shortening rates of the active areas increase), also 200 km width and 200 km to 800 km length;
- 4) 33-29 Ma (activity in the Altiplano area begins), 400 km in width and \sim 400 km in length;

- 5) 28-18 Ma (more points become active especially in the Eastern Cordillera, but generally local fluctuations of strain distribution occur), 180 km to 270 km in width and 240 km to 800 km in length (up to 21 Ma);
- 6) 17-13 Ma (the system prepares for a general change in location of strain accumulation), 150 to 200 km in width and 270 km to 800 km in length (already starting from 20 Ma on);
- 7) 12-11 Ma (the Eastern Cordillera ceases activity, and strain transfers to the Interandean), 150-200 km in width and 400 km to 800 km in length;
- 8) 10-9 Ma (activity in the Interandean becomes less, but takes up in the Subandean), 100-200 km in width and 270 km to 800-1000 km in length;
- 9) 8-0 Ma (Subandean shortening remains active until now), 150-200 km but also more than 200 km in width and 300 km to 800-1000 km in length.

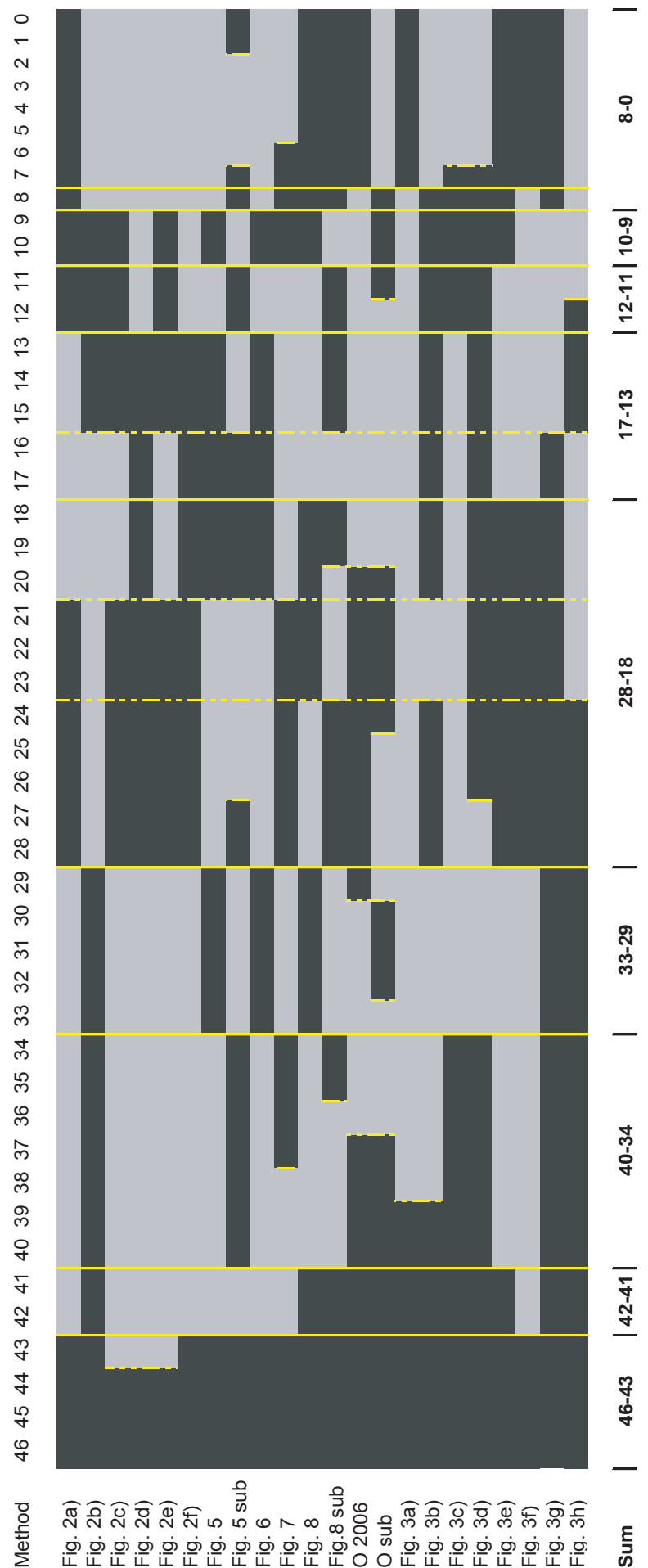
In general, the numbers given for the length mean that the two values (minimum and maximum) co-exist, but no values in between the estimates. It seems as if two characteristic lengths exist for the along-strike extents of active areas (namely about 200-300 km for the smaller extent and 600 km for

the large extent up to 800-1000 km when taking the oroclinal bend into account), whereas the width generally yields an estimate of 150-200 km (with deviations of 90 km and up to 270 km). The only exception from these values is the time from 33-29 Ma in which deformation is limited to a rather central cluster that has similar extents along-strike of the units and orthogonal to it.

This allows the conclusion that the width of the active units generally is about 20-50% of the length of active units. The longer length values are 2-5 times the smaller length values. This further suggests that the smaller of the values reflects the extent of a single active area, whereas the larger value represents several active areas, that are coevally active, spatial neighbours. This also explains that the first stage has a width that is half of the common value of stage 2 and stages thereafter, as in the initial time window, no coeval areas seem to have been active, which only begins in the later time windows. The same is true for the along-strike extent, which only yields a value of 200 km, i.e., the length of one active area. A multiple of this length occurs only from the second stage on. However, another difference is striking: before the time of 33-29 Ma in which the plateau interior is active, the common length scale of one area was closer to 200 km, which extends more to 300 km in the time windows after 33-29 Ma.

The characteristic lengths for structures of ~200 km and multiples

Fig. 5.9: This table is a summary of all deformation stages inferred from the different methods (frequency statistics (Fig. 5.2), indicator variogram surfaces (Fig. 5.5) with substages (termed "Fig. 5.5 sub", not depicted), variograms (Fig. 5.6), kriging plots (Fig. 7), variogram surfaces of shortening rate (Fig. 5.8) and substages (termed "Fig. 5.8 sub", not depicted), deformation periods from Oncken et al. (O 2006) with substages ("O sub"), and more data from frequency statistics (Fig. 5.3). The solid yellow lines indicate major deformation changes over time (from one Ma to the next), whose results are significant, whereas the stippled yellow lines mark stages that are not significant and could rather be interpreted as substages. The row at the bottom shows the resulting deformation time windows when summarized.



thereof suggest that the common structures, e.g., faults in a fault network, have the same scale lengths, irrespective of their position within a structural unit. Each of these smaller areas, probably representing fault systems, can be regarded as a coherent unit, which is independent at first. Their eventual coeval activity causes the multiple lengths (i.e., the larger values) maybe due to an interlinkage between faults. The only exception is the plateau interior: the characteristic length only grows up to ~400 km maximum length.

5.5.3. Discussion

By means of frequency- and geostatistics we studied the spatial pattern of deformation for the Central Andes over the last 46 Ma. By resolving these data down to one million year steps, we are able to detect significant temporal deformation patterns: each deformation stage lasts between 3 and 10 Ma. We have to note that we would not be able to resolve stages below the duration of or with a greater accuracy than 1 Ma, as the error for dating deformation in the initial data is on the order of 1 Ma. All of these stages are driven by the deformation activity in regional areas, which are much smaller in spatial extent than the orogen itself. Thus, the deformation pattern we detect on the orogen scale is solely driven by variations on the next smaller scale, which imprints its effect on the orogen scale.

The smaller scale variations occur on temporal scales that are shorter than some of the deformation stages of the orogen scale mentioned above, namely on the order of 2-4 Ma. Such variations can certainly be ascribed to the different fault systems or faults that are active, to strain transfer between systems and faults, and also to changes in strain accumulation mode. Characteristic lengths of structures for the respective time windows are summarized above, yielding average extents of 150-200 km in width and 200-300 km for along-strike length. When neighbouring structures are coevally active, the characteristic along-strike length increases by a multiple of the characteristic length of one active area, up to 600-800 km (and even 1000 km), as the faults of the smaller scales interconnect.

The shortening rates that we calculate are very small (cf. mean values in Fig. 5.2, 5.3, and 5.4), unlike commonly used values for the past (5-15 mm/yr, e.g., Klosko et al., 2002; Liu

et al., 2002). Certainly, our values are minimum estimates (sometimes below mm/yr) and probably not realistic, when compared to other local estimates (1-8 mm/yr, e.g., Elger et al., 2005) as they are calculated under the assumption that strain was distributed homogeneously over the entire area and over time. Thus, as the resulting data are actually “too” low, we could therefore in turn infer and conclude that accumulation of fault slip must be heterogeneous in space and time.

Unfortunately, attributing strain rates for an entire orogen and dividing the formation of an orogen in phases of up to 15-20 Ma during which the entire orogen was actively deforming is often our only option when studying the deformation history of orogens, as better resolved data -both in space and time- are usually not available (due to lack of field exposure).

Strain accumulation exhibits characteristic spatial and temporal structures on the orogen and the next smaller regional scale, and higher data resolution on all scales is needed for the deduction of deformation processes. However, we can compare the regional scale of ~150-200 km in width and 200-300 km in length to the orogen scale pattern which yields up to five times the amount of the length, whereas the width remains about the same. These characteristic scale lengths are the same for all significant time windows, which are themselves commonly on the order of 2-4 Ma, but also twice as much. It remains to be analyzed if the characteristic lengths on the regional scale are real or due to the lack of data resolution below the regional scale. Thus, within the regional area, some parts might actually be inactive, dividing the larger regional area into smaller areas. The characteristic regional scale length would again be merely a summary of lengths found on the smaller scale. Chapter 9 discusses such artefacts resulting from lack of resolution and their implications that strain accumulation can still be scale-invariant.

Characteristic sedimentary sequences, i.e., temporal patterns, have also been suggested for erosional responses to deformation cycles, which are on the order of 2-3 Ma as inferred from sedimentary basin infill in the Central Andes (Elger, 2003; Echavarría et al., 2003); therefore similar to our results for strain accumulation on the regional (fault system) scale.

5.6. Conclusions

With a multitude of both frequency and geostatistics of deformation activity and shortening rates, we examined the spatial strain accumulation pattern on the orogen scale for the last 46 Ma of Central Andean plateau formation, with the goal to identify characteristic temporal and spatial scale lengths on the regional and the orogen scale. We observe the unsystematic way of strain accumulation for the Central Andean plateau orogen, which is in contrast to strain propagation inherent to fold-and-thrust belts.

We were able to calculate shortening rates that are resolved down to a spatial scale of 40 km for time steps of one million year within an orogen of several hundred kilometers extent. The rates are simplified due to the assumption that strain is distributed homogeneously, and therefore merely represent minimum estimates. As they are very low, we propose that strain accumulation does not occur in a homogeneous but a heterogeneous fashion, and varies from one fault system or fault to another. Also, strain accumulation is not continuous over time, but follows a temporal deformation pattern (probably with varying deformation intensities and resulting shortening). As previously suggested by Oncken et al. (2006), these deformation times do not always pertain to along-strike coeval activity, but exhibit regional scale events (2-4 Ma duration). When analyzing deformation activity, these regional scale events have typical scale length of 200-300 km in along-strike extent and 150-200 km in width. As several of these regional areas are active at the same time, the along-strike extent increases to a multiple on the orogen scale, i.e., up to 600-1000 km (cf. Chapter 9 for further discussion).

Most of the regional deformation stages on the order of 2-4 Ma significantly affect the orogen scale pattern, so that we propose the following main deformational stages for the Central Andean plateau: 46-43 Ma, 42-41 Ma, 40-34 Ma, 33-29 Ma, 28-18 Ma, 17-13 Ma, 12-11 Ma, 10-9 Ma, and 8-0 Ma.

Acknowledgments

This work is part of KS' PhD thesis, funded by a stipend from the "Studienstiftung des deutschen Volkes" (National Merit Foundation). Martina Böhme double-checked the accuracy of the data and helped with the preparation of figures and diagrams.

6. The effect of mechanical heterogeneity on diversification of deformation patterns - A modelling study with granular media

The evolution of a deformation system is driven by a multitude of both intrinsic and external parameters that may generate e.g., simple fold-and-thrust belts or plateau-style settings. We explore the distribution of mechanical properties on the development of different deformation patterns in granular analogue models monitored by high-resolution particle imaging velocimetry. This allows us to address the question which mechanical parameters may cause plateau-style deformation patterns. We show that plateau-style settings indeed only form when critical strength contrasts are present within the initial system, both laterally in the crust and with respect to its base. Threshold values for these parameters exist (at 20% lateral strength contrast and 35% basal contrast), which determine the style of the brittle analogue strain pattern: taper-like or plateau-style, without any transitional stages in between. Our models are able to reproduce the spatial and temporal distribution of strain accumulation as observed on the orogen scale of the Central Andean Altiplano. The driving factors that can explain the deformation pattern of this plateau orogen are still under debate. The fact, that the pattern of a complex natural system can be approximated by a simple model, implies that the pattern cannot be caused by only one parameter combination, and thus has no unique explanation. This ambiguity in turn precludes the possibility to conclude the responsible driving mechanisms from the respective strain patterns.

6.1. Introduction

A variety of parameters have been shown to influence the balance between plate boundary and buoyancy forces in controlling the evolution of orogens (e.g., McKenzie, 1969; Forsyth and Uyeda, 1975; Chapple and Tullis, 1977; Richardson et al., 1979; Dewey, 1980; Ranalli, 1987, more references in Sengör, 1990). More particularly, the resulting orogenic system and its internal deformation patterns depend on the impact of a. internal factors such as rheological heterogeneities within the plates (due to e.g., differential temperature, density properties, rock composition, inherited weaknesses, presence of fluids, etc.), crust-mantle interaction (decoupling, delamination, magmatism), and strain weakening; as well as on b. external factors like plate geometry, convergence kinematics, subduction angle, coupling along the plate interface, and climate.

The specific contribution of these individual parameters to and their role in the evolution of a particular deformation system is usually a matter of debate. Different strain accumulation patterns, e.g., plateau-style or wedge-like deformation (narrow single- or bivergent) etc., may grade into each other along-strike in spite of similar plate tectonic settings and also appear to exist

in quite diverse tectonic settings. This becomes particularly clear when observing the lateral variability of the subduction-related Andes or of the collisional Himalayan-Alpine system. The spatial and temporal strain accumulation is extremely diverse and suggests complex system behaviour from interaction of a multitude of processes and properties.

Although a large number of controlling parameters have been proposed for the formation of the Andean Altiplano-Puna plateau (e.g., mantle-driven processes like delamination (e.g., Kay and Kay, 1993; Allmendinger et al., 1997); crustal channel flow (e.g., Wdowinski and Bock, 1994a;b; Yuan et al., 2000; Husson and Sempere, 2003); strength variations in the plates and their interface (e.g., Allmendinger and Gubbels, 1996; Lamb and Davis, 2003); climate (e.g., Lamb and Davis, 2003; Masek et al., 1994; Horton, 1999; Sobel et al., 2003); changes in plate/indenter geometry (e.g., Gephart, 1994; Tassara, 2005; Giese et al., 1999); and convergence kinematics (e.g., Pardo-Casas and Molnar, 1987; Somoza, 1998; Silver et al., 1998)); they so far do not account for the observed spatial and temporal evolution of the orogen-internal deformation pattern. With a correlation analysis of time series data of various processes

suggested for these deformation patterns for the Andean plateau, Oncken et al. (2006) have shown that only a special combination of parameters can explain the spatiotemporal strain distribution (namely differential feedback of trench infill, plate interface coupling, associated shortening transfer and slab rollback, as well as the position of inherited structures of crustal weakness). This strategy, however, hinges on the assumption that temporal and spatial correlation of coupled processes and strain accumulation provides a unique explanation for the observations. By the same token, numerical modelling of multiply coupled (mostly non-linear) processes often allow only the identification of one controlling mechanism, but not a distinct hierarchy of interdependent controlling mechanisms (cf. studies by e.g., Wdowinski and Bock, 1994a, b; Royden, 1996; Sobolev and Babeyko, 2005; Vietor and Oncken, 2005).

This ambiguity of interacting processes does not only preclude the understanding of what might stipulate complex system behaviour, which is neither easily identified from the rock record, nor in standard modelling approaches. The difficulty in demonstrating the uniqueness of parameter combinations also restrains the possibility to in turn use the resulting strain pattern of a structural system, leading to e.g., plateau-style or wedge-like deformation, to infer the key driving factors responsible for their formation.

In this paper we single out the individual role of mechanical heterogeneity, which is itself characterized by multiple factors, and systematically investigate its contribution in controlling both the spatial distribution and timing of deformation. To address this question we perform analogue experiments in which we successively implement and change single mechanical properties and combinations thereof, so that initially simple systems become more complex. All experiments are monitored by particle imaging velocimetry permitting high resolution of resulting strain patterns in space and time (cf. Adam et al., 2004). This enables us 1) to explore and determine the effect, stability and uniqueness or non-uniqueness of mechanical heterogeneity driven by certain parameter combinations for their ability to develop plateau-style vs. wedge-like deformation systems, and 2) to contrast analogue strain patterns of model and nature caused by dissimilar parameter combinations.

6.2. Experimental design

6.2.1. Scaling analysis

The brittle crust is modelled by granular materials which show similar frictional-plastic behaviour as natural rocks, with a strain hardening phase until failure followed by a phase of strain weakening and localization (Byerlee, 1978; Mandl, 1988; Krantz, 1991; Marone, 1998; Schellart, 2000; Lohrmann et al., 2003). Thus, material is characterized by the coefficient of friction (internal and basal), cohesion, and density. Granular experiments are scaled to nature according to: $\sigma^* = C^* = \rho^* \lambda^* g^*$ (asterisk indicates ratios of model to nature, σ is tectonic stress, C is cohesion, ρ is density, λ is the geometric length, and g is gravity) (e.g., Hubbert, 1937; Koyi, 1997; Schellart, 2000). The geometric scaling factor is given by: $\lambda^* = \rho_{\text{nat}} C_{\text{mod}} g_{\text{nat}} / \rho_{\text{mod}} C_{\text{nat}} g_{\text{mod}}$. Using typical density values for upper crustal rocks of about 2700 kg/m³ with cohesion being on the order of <10⁰-10² MPa; and density values of about 1700 kg/m³ for the granular material, with cohesion being on the order of 10⁰ Pa-10² Pa at natural gravity of $g = 9.81$ m/s², our geometric scaling factor ranges between 10⁻⁴ to 10⁻⁸ (Table 6.1).

6.2.2. Materials and model construction

In granular set-ups, the strength of a material is mainly characterized by the coefficient of friction. We determine these coefficients using a ring shear device: shear stresses are measured for given normal loads and the appropriate values of coefficients of friction and cohesion for the peak, static-stable, and dynamic-stable frictions are thereafter determined by means of regression analysis (e.g., Lohrmann et al., 2003; Hampel et al., 2004). These are equivalent to the frictional strength until failure, the strength of fault reactivation, and the strength of actively deforming material respectively (Byerlee, 1978). Properties of materials used are summed up in Table 6.2.

The measurements yield absolute values with which we obtain the applied normal and shear stresses within the experiments by means of the Coulomb failure criterion: $\tau = c + \mu \sigma$. Thus for 0.018 m of model crust, a density of 1700 kg/m³ and natural gravity, a typical normal stress σ_{mod} at the base of the analogue layer is 300 Pa. For a basal coefficient of friction of 0.5 with cohesion being negligible, the shear stress τ_{mod} at the base is 150 Pa, above which the material will fail.

In the following we will refer to the

Table 6.1. Scaling parameters

Parameter	Equation	Nature	Model	Scaling factor
<i>Thickness</i> <i>upper crust</i>	$\sigma^* = \delta^* g^* L^*$	20 km	1.8 cm	$L^* = 9.1 \times 10^{-7}$
<i>Density</i>	$\delta_{\text{mod}}/\delta_{\text{nat}}$	2700 kg/m ³	1700 kg/m ³	$\delta^* = 0.63$
<i>Gravity</i>	g	9.81 m s ⁻²	9.81 m s ⁻²	$g^* = 1$
<i>Cohesion</i>	C^*	10 ⁰ - 10 ² Pa	10 ⁻⁴ - 10 ⁻⁸ Pa	
<i>Stress</i>	σ^*			$\sigma^* = 5.74 \times 10^{-7}$

coefficients of friction for materials as the value of the dynamic-stable friction. Two simplifications have to be noted: we neglect cohesion, which is approximately one order of magnitude below the resulting stresses, and we neglect that the normal stress in the model is lower closer to the surface.

All materials are sieved into the model set-up. Vertical or inclined material boundaries are established by thin metal boards separating units during sieving, which are later removed. To obtain a plane surface, material is slightly compressed after sieving. If cohesion is to be kept low, barium sulphate must not be compressed at all. Finally, a marker grid of coloured sand is sieved on top of the experimental set-up with squares of 5 cm x 5 cm.

6.2.3. Dimensions of the experimental set-up

We carried out experiments with a scaling factor of 9.1×10^{-7} as well as with 4.55×10^{-7} for comparison. The experimental dimensions of 60 cm x 84.2 cm x 1.8 cm (width x length x height) respectively 30 cm x 42.1 cm x 0.9 cm equal 660 km x 925 km x 20 km in nature. We chose these values close to the natural analogue of the Central Andean plateau. The dimensions thus cover the area of the Altiplano plateau (17°-23°S) within the upper crust down to the decoupling horizon at 20 km depth (e.g., Yuan et al., 2000), adding the amount of shortening that has been accumulated (~265 km, e.g., Kley, 1999). The system is closed to the sides by glass panels to prohibit lateral extrusion of the material.

6.2.4. Monitoring technique

Most of the experiments were monitored by a special camera system using the technique of particle imaging velocimetry (PIV), which allows the quantification of instantaneous velocities and

displacements of particles (e.g., sand grains) during the experimental run (cf. Adam et al., 2004). One PIV camera is employed which monitors the 2D strain surface from above. The calibration of the camera before an experiment is used for the calculation of a mapping function, which accounts for image distortion. The calibration error for the experiments is on the order of 10^{-1} pixel, which equals 0.038 mm, therefore being one order of magnitude smaller than the size of a single sand grain.

Sequential images are cross-correlated by the commercial software DaVis (e.g., adaptive multipass pattern cross-correlation employing Fast Fourier Transformation, for details refer to Adam et al., 2004). The observed velocity field can be decomposed into all components of the strain gradient tensor.

Additionally, digital images are sampled every second, which gives 24 images per centimeter of convergence at a motor speed of 2.5 cm/min.

6.3. Experimental results

We performed a series of more than 40 experiments (Appendix B), in which a piston compresses the initial set-up from one side (back wall) to the other (front wall) (cf. Fig. 6.1). The initial set-up generally consists of four structural units (termed unit 1, 2, 3, and 4) which are characterized by different material properties and therefore exhibit lateral strength contrasts (sand, glass beads, barium sulphate, salt, grains of rice pudding, grains of corn meal, starch, sugar).

Additional weak zones were introduced in units 1 and 3 (glass beads, salt, fine sand) as vertical columns (cf. Fig. 6.1). The position of the shear horizon is at the bottom of the experimental set-up, either “fixed” to the table (glass beads,

6. The effect of mechanical heterogeneity on diversification of deformation patterns

Table 6.2a. Coefficients of Internal Friction, Cohesion, and Density, as measured with the Ring shear apparatus

Density (g/m ³)	Peak friction μ_{peak}	Static-stable friction μ_{static}	Dynamic-stable friction μ_{dynamic}	Cohesion, Pa
<i>Sifted Dry Quartz Sand (Grain Size <0.63 mm)</i>				
1.73	0.70	0.60	0.54	140-90
<i>Glass Beads (Grain Size <0.4 mm)</i>				
1.55	0.50	0.46	0.41	60-40
<i>Barium Sulphate</i>				
1.26	0.82	0.79	0.76	460-360
<i>Sifted Z-lights Ceramic Beads (Grain Size <0.4 mm)</i>				
0.65	0.48	0.46	0.43	60-35
<i>Corn Meal</i>				
Density (g/m ³)	0.71	0.89	1.49	1.01
<i>Rice Pudding</i>				
Friction (range)	0.85-0.65	0.87-0.71	0.70-0.55	0.67-0.6
<i>Salt</i>				
<i>Starch</i>				
<i>Sugar</i>				

Table 6.2b. Coefficients of Basal Friction, Cohesion, and Density, as measured with the Ring shear apparatus

Peak friction μ_{peak}	Static-stable friction μ_{static}	Dynamic-stable friction μ_{dynamic}	Cohesion, Pa
<i>Sifted Dry Quartz Sand (Grain Size <0.63 mm) vs. teflar foil</i>			
0.32	0.23	0.23	103-160
<i>Glass Beads (Grain Size <0.4 mm) vs. teflar foil</i>			
0.19	0.11	0.11	150-200
<i>Barium Sulphate vs. teflar foil</i>			
0.41	0.27	0.26	90-160
<i>Barium Sulphate vs. alcor foil</i>			
0.53	0.5	0.5	74-33
<i>Sifted Dry Quartz Sand (Grain Size <0.63 mm) vs. alcor foil</i>			
0.36	-	0.30	-
<i>Sifted Dry Quartz Sand (Grain Size <0.63 mm) vs. sand paper</i>			
0.63	0.58	0.55	66-62
<i>Glass Beads (Grain Size <0.4 mm) vs. sand paper</i>			
0.5	0.49	0.46	21-1

fine sand, Teflon foil or alcor foil) on which the experiments were run, or “loose” with additional material (glass beads, fine sand, salt) between the units and the fixed foil on the table. Depending on the implemented parameter characteristics and combinations, five different deformation systems

evolve, which we describe in order of increasing complexity. All five types generally follow either a “wedge-like” or “plateau-style” deformation. A summary of the initial set-up, structural evolution and final results are summarized for each experiment in Appendix B.

6.3.1. Single “wedge-like” setting, (Fig. 6.1a)

The taper configuration represents the classical wedge (Fig. 6.1a), which increases in taper angle and sheds sediments over its slope with continuing compression until a certain point when it becomes stable. All structural units (1-4) are involved in its formation.

6.3.2. Bivergent “wedge-like” setting, (Fig. 6.1b)

This set-up produces a peak ridge in the center (unit 2) which has symmetric slopes verging to both sides (Fig. 6.1b). Sediments shed down these slopes on both sides.

6.3.3. Low-angle “wedge-like” setting, (Fig. 6.1c)

One peak ridge develops close to the moving piston in unit 1, followed by uplift of the area adjacent to this peak ridge (unit 2), which itself is only little deformed. This area has the same elevation as the peak ridge. Thrusts form subsequently in units 3 and 4 (Fig. 6.1c). The resulting taper has a rather low angle, as most units have the same elevation.

6.3.4. High “plateau-style” setting, (Fig. 6.1d)

This setting is similar to c), but after the first peak ridge has formed in unit 1, another peak ridge develops in unit 3, adjacent to unit 2. Unit 2 has been uplifted to approximately the same elevation as both peak ridges, but in contrast, has not been highly deformed. Again, additional thrusts develop further away from the piston in unit 4 (Fig. 6.1d).

6.3.5. “Plateau-style” setting, (Fig. 6.1e)

This deformation system (Fig. 6.1e) is characterized by the development of two peak ridges (units 1 and 3), both adjacent to unit 2, which itself forms a plateau area. The plateau area lies at a higher elevation than the initial surface, but remains at a lower elevation than the peak ridges. The peak ridges shed sediments on top of the plateau surface. Thrusts develop in unit 4 as soon as deformation in both peak ridges and the plateau area becomes inactive.

6.4. Parameter control

The five described settings develop in response to two main controlling parameters: a. the basal detachment, and b. the lateral strength

variation between structural units. Both parameters can be expressed in terms of strength contrasts, which yield dimensionless ratios: a. “basal contrast”: basal friction (with respect to unit 2)/ internal friction (of unit 2), and b. “lateral contrast”: internal friction of stronger unit/ internal friction of adjacent weaker unit. In some experiments, weak zones are implemented in units 1 and 3, which allow further variation with respect to the units' strength.

6.4.1. Basal strength contrasts

The basal detachment is positioned beneath the set-up as a foil fixed to the table, which is characterized by the basal coefficient μ of the foil with respect to the material above (we use unit 2 as reference material, here baryte) which ranges from 0.26 for teflar foil, 0.45 for alcor foil, 0.55 for glass bead foil, up to 0.65 for sand paper. In some experiments, an additional material layer of sand, salt, or glass beads is implemented between the foil and the set-up (with internal coefficients of friction of 0.54, 0.55, and 0.41 respectively). The respective value for basal friction depends on the thickness of the additional layer. If it is ~3 mm or thicker, the effect of the foil becomes minimal and we take the internal value of the material. If the thickness is lower, we take the mean value of both the basal friction of the foil and the internal friction of the additional material.

The basal strength contrast is the ratio between the mean basal friction with respect to the material of unit 2 and the internal friction coefficient of unit 2. This ratio has a threshold value close to 0.67, which determines if the deformational style is wedge-like (>0.67 ; a, b, c) or plateau-like (<0.67 ; d, e) (Fig. 6.2).

The presence and properties of the additional layer determines the type of plateau-style setting. Setting d) requires additional material beneath the set-up, as it supports the uplift of a plateau surface, whereas type e) only develops, when no additional material is present. Setting c) of the wedge-like systems also requires additional material below the set-up, but with a higher basal friction than d).

We further have to note that in some experiments we varied the properties of the basal horizon along-strike (Appendix B, Exp. 35, 43, 45). It then depends on the position of the piston (i.e., amount of convergence), which of the basal properties are effective. Thus, the basal

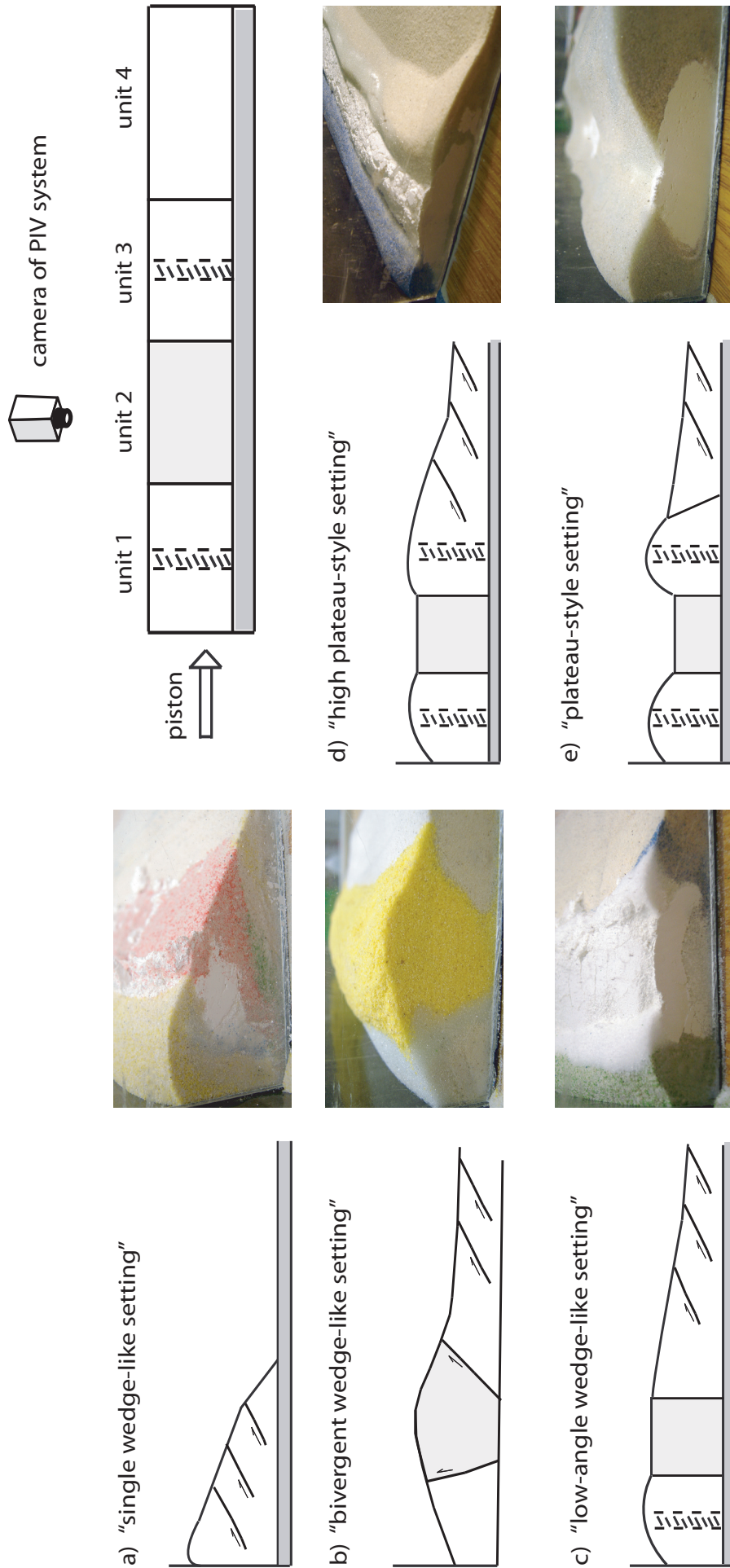


Fig. 6.1: The initial set-up (upper right) results in settings a. to e. depending on the mechanical properties of the system. The five types can be grouped into two main deformational types: wedge-like (on the left) and plateau-like (on the right). Threshold values exist for both the basal and the lateral strength contrasts determining if either the one type or the other evolves. For each of the settings a sketch and a photograph of the final set-up are shown. Further explanations in-text.

effect on the deformation system changes over time, and the plateau-style setting might become taper-like at a later stage.

6.4.2. Lateral strength contrasts

Lateral strength contrasts are defined as the ratio of the internal friction coefficient of the strongest unit (unit 2) and the mean internal friction of the weaker unit adjacent to the strong unit (units 1 and 3). If no lateral variation is present, the ratio is 1. It becomes greater than 1 with increasing lateral strength contrast, i.e., the strong unit becomes stronger or the weak unit weaker. Internal friction coefficients of the materials used for the four structural units range from 0.38 (glass beads 40-70 µm) to 0.76 (baryte). In some experiments, we put additional weakness zones within units 1 and 3

to localize deformation in these units and to initiate their uplift. The value for the mean internal friction is calculated depending on the percentage of the widths of the weakness zones.

Again, a threshold value for the minimum contrast exists laterally, that has to be overcome to develop a plateau-style rather than a taper-like setting (Fig. 6.2). When the contrast is 1 or slightly higher, the resulting system will be taper-like (a.). If the ratio is about 1.2 or higher, a taper-like setting (both a. and c.) only develops when the basal contrast is higher than ~0.35 at the same time. Else, the setting will be plateau-like (Fig. 6.2).

This is only true for materials that have similar densities. For instance, when the material in unit 2 has a much lower density than materials of adjacent units 1 and 3 (e.g., ~600-900 kg/m³

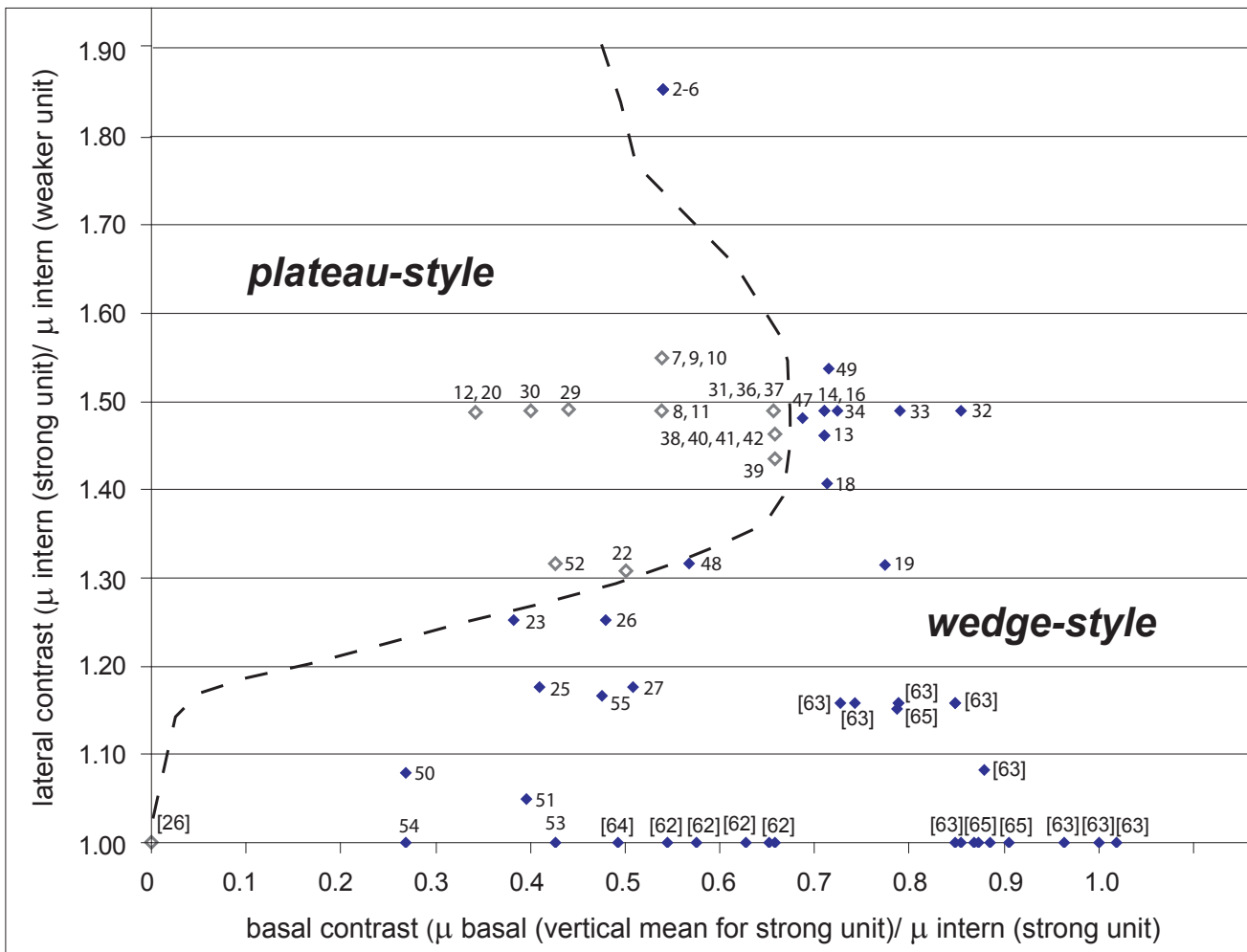


Fig. 6.2: This plot shows the dependence of the deformation style (taper- or plateau-like) on the basal strength contrast (x-axis) and the lateral strength contrast (y-axis) within the system. The basal contrast is defined as the ratio of the basal coefficient of friction (with respect to the strongest unit) and the internal friction coefficient of the strongest unit. The lateral contrast is defined by the ratio of the internal friction of the strongest unit and the internal friction of the weaker material adjacent to the strong unit. Both ratios are dimensionless. Plateau-style settings plot as outlined diamonds (including settings d. and e.), taper-like settings plot as solid diamonds (settings a., b., and c.). The dashed line separates the two fields. The numbers indicate the experiment numbers summarized in Appendix B. Numbers in brackets indicate the following references: [26] Vietor, pers.comm., 2007; [62] Schreurs et al., 2006; [63] Lohrmann, 2002; [64] Marques and Cobbold, 2002; [65] Hoth, 2005. Values for each of the points are summarized in Table 6.3. Further explanation in-text.

vs. $\sim 1500\text{-}1800\text{ kg/m}^3$), the resulting setting is bivergent (b), as material is squeezed upwards during compression.

6.4.3. Shape of the indenting piston

If the curvature angle was low ($<20^\circ$) and already attained before convergence, the effect of the bent indenter is not very strong compared to the boundary effect of side wall friction (cf. Schreurs et al., 2006). If the indenter is initially straight and highly gains in curvature during convergence (up to $>45^\circ$), the material is moving parallel to the direction of convergence only in the center point of the indenter and has a higher translational component towards the sides.

6.4.4. Effect of strong lithosphere on the backside of the orogen

We modelled a strong lithospheric block or mass by placing a wooden plate with a slope at the back of the experimental set-up, so that material of the fold-and-thrust belt can thrust on top of it. For angles of less than 10° there is no distinction within the general setting. If the angle was higher, material would not overcome the boundary to thrust on top, but rather piles up in front.

6.4.5. Internal geometries and symmetries

When the structural units are wider, more

thrusts can take up more bulk shortening. If the crust is thicker, the spacing of thrusts will increase, and the peak ridges can uplift higher. The additional weakness zones in units 1 and 3 allow the localization and uplift initiation of the peak ridges, when they make up at least 6% or more of the initial width of the structural unit. If weak zones are wider than necessary, more material is squeezed or thrust, which subsequently falls down the slopes onto the plateau.

If the strength contrasts from units 1 and 3 to unit 2 are not the same on either side, both peak ridges form, but the plateau surface in between has a dip towards the peak ridge with the lower strength, producing an asymmetric setting.

We also tested vertical material boundaries vs. boundaries at an angle, for which we did not see any differences in outcome.

6.5. PIV monitoring of plateau-style settings

6.5.1. Plateau without erosion

We monitored the plateau-style setting e) with the PIV technique described above to obtain the displacement field for every single time step (one image every second, convergence rate: 2.5 cm/min , about 40 cm of total convergence). Figure 6.3 shows a PIV image from the surface of the experiment showing incremental strain in the direction of convergence (E_{xx} in %). It depicts

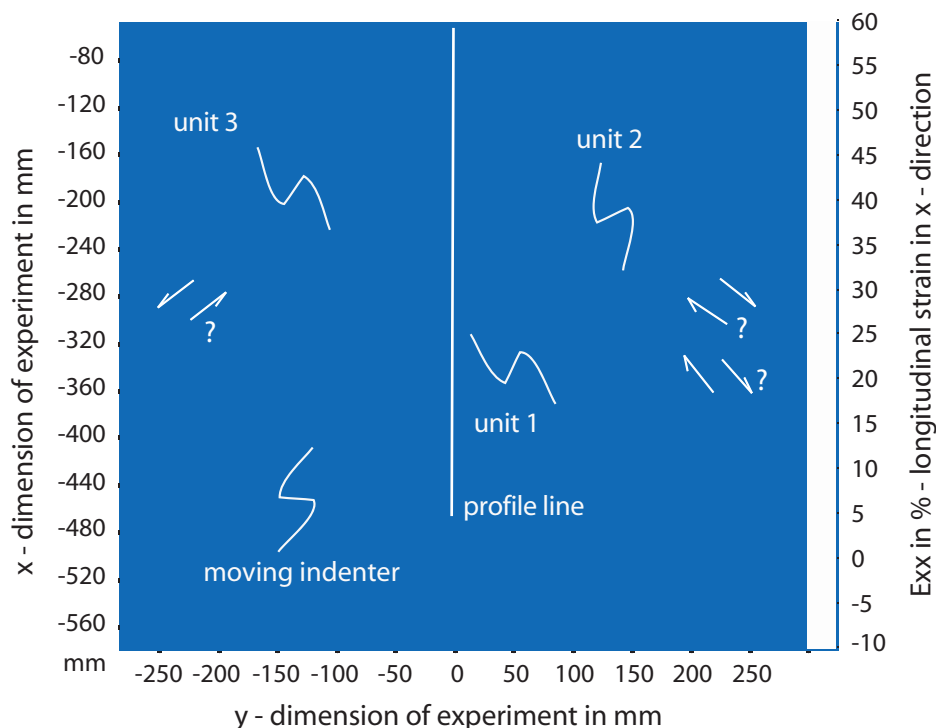


Fig. 6.3: PIV strain image of experimental surface after 12 cm of convergence. Lighter colours indicate zones of incremental strain in the x-direction (direction of convergence); here three thrusts are currently active in three different units. Also visible are potential strike-slip components close to the sides, and the outline of the indenter. The white vertical line marks the position of the profile shown in Figure 6.4a and Figure 6.5a.

localized deformation along the two peak ridges as well as one thrust within the plateau area. The curved indenter might have caused transpressional structures close to the sides of the set-up, but as these structures are not well defined, they probably result from side wall friction (cf. Schreurs et al., 2006).

We extract the strain data along one profile crossing the surface area for each image to obtain a time series of strain accumulation in space (Fig. 6.4a). Structures develop first in the upper left and move down to the lower right, as time increases from top to bottom and convergence is from left to right. The black areas represent zones of high strain accumulation. First, the peak ridge close to the piston develops with three thrusts (marked 1 to 3), representing the initial uplift within the weak zone. The white colour to the left of the structure indicates avalanches from the peak ridge. In this

initial phase, avalanches occur away from the plateau interior towards the indenter. The fourth thrust of peak ridge 1 is coevally active with the initiation of thrusting within the plateau area, which is directed towards the foreland (marked 4 and 5).

While the second thrust within the plateau is still active, and uplift of the first peak ridge is ongoing, the uplift of the second peak ridge starts (5), again within the weak zone. Avalanches become stronger (from both thrusts 5 and 6) and thrusting within the plateau dies out. Unlike the initial phase, avalanches from both peak ridges are directed towards the plateau interior. As directions of avalanches typically correlate with the direction of thrust motion, we gain information on the internal structures from surface data and are able to reconstruct a cross section (Fig. 6.4b). Here, the avalanches indicate that the vergence of thrusts within the first peak ridge has changed

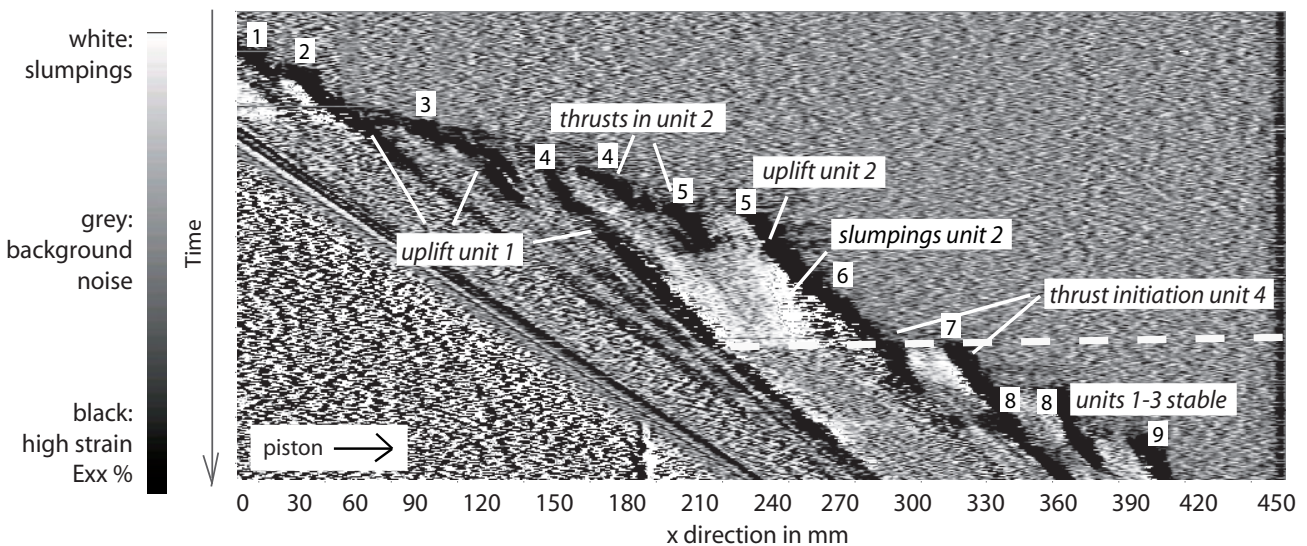
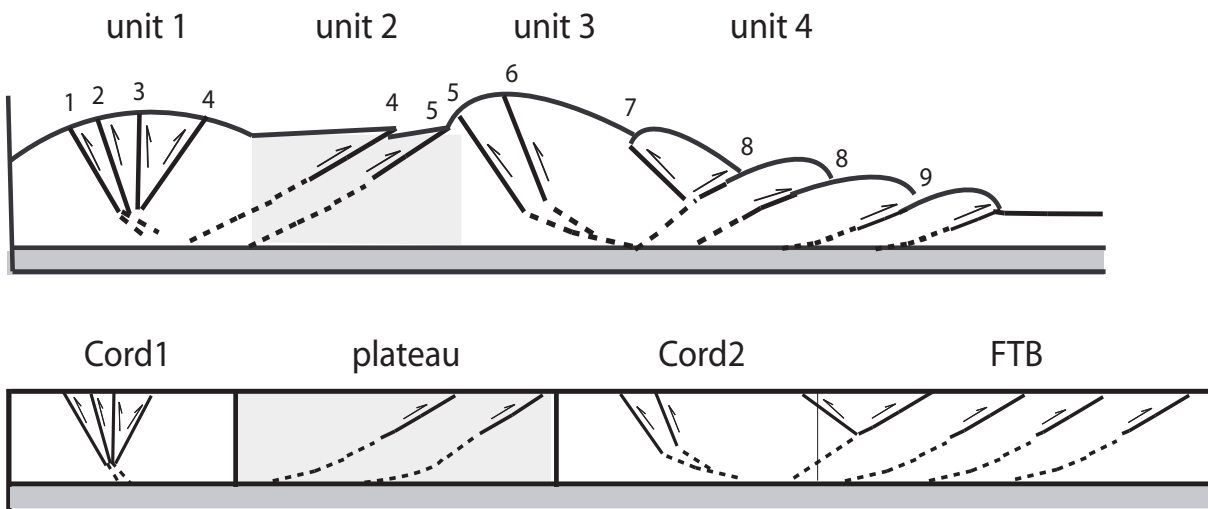


Fig. 6.4a (top) + b (bottom): a) Strain data along profile through center of experiment “plateau-style setting without erosion” (cf. Fig. 6.3) for all time increments. Active thrusts are black, avalanches are white, and background noise is grey. Active thrusts are chronologically numbered, the structural units are also marked. Further explanation in-text; b) Sketch of cross section of the finite (top) and balanced (bottom) plateau-style setting. Thrusts are chronologically numbered as in a).



towards the foreland (4), and backthrusts are no longer active (1 to 3). Backthrusts are only active within the second peak ridge (5, 6).

The white dashed line in Figure 6.4a marks the time increment when the first thrust of the wedge-like part (unit 4) becomes active, coeval with the halt of avalanches from both peak ridges, which means that deformation is no longer active. Thus, plateau-style deformation stops, and wedge-like deformation becomes dominant in unit 4. Avalanches of thrust 7 towards the piston die out and thrusts with opposite vergence (to the foreland) become active (8). From that point on, thrusts propagate towards the front wall.

6.5.2. Plateau with erosion

We eroded along peak ridge 1 close to the

piston for the first time after 4 cm of convergence, when it had already attained some elevation and then every 4 cm until peak ridge 2 started to develop, which we eroded every 4 cm from 29 cm onwards (constant erosion approach). The combined strain profile through time in Figure 6.5a shows that the relative chronology of activity within the units is the same as in Figure 6.4a. However, the number of faults is less in units 1 and 3 (three instead of four thrusts in unit 1, and one instead of three in unit 3), but higher in the plateau area (three instead of two). Avalanches are smaller as sediment supply is less, but they are of longer duration.

Each of the thrusts in the peak ridges and the plateau region is active for a longer period of time, with faults being reactivated (e.g., in the plateau region). In contrast, faults within the

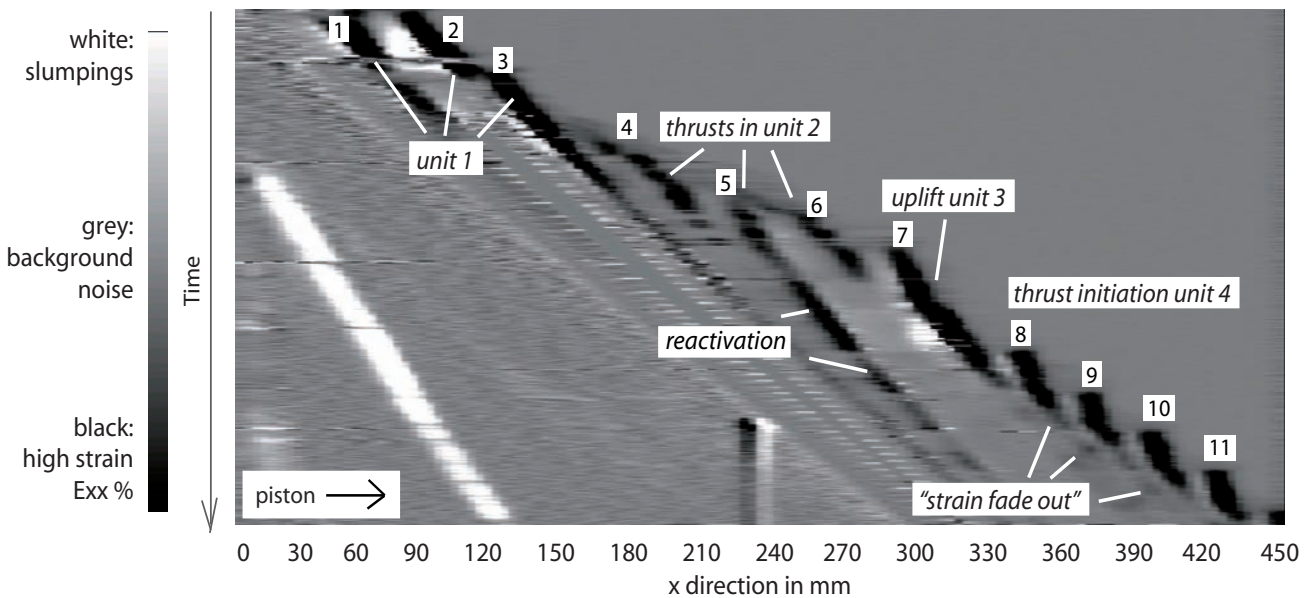
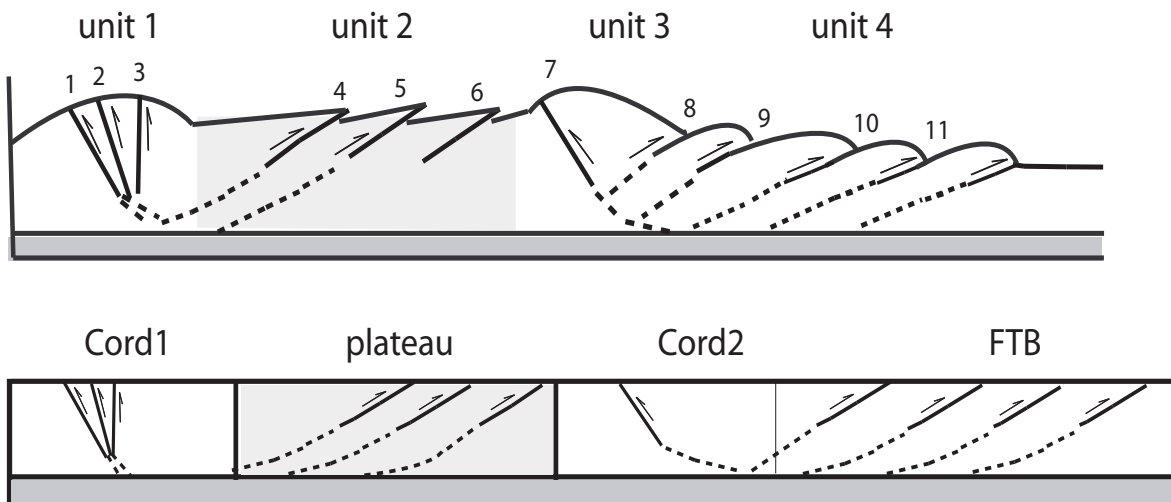


Fig. 6.5a (top) + b (bottom): a) Strain data along profile through center of experiment “plateau-style setting with erosion” (cf. Fig. 6.3) for all time increments. These profiles are taken from an experiment in which material of unit 1 is eroded every 4 cm of convergence up to 29 cm of shortening, after which unit 3 is eroded. Active thrusts are black, avalanches are white, and background noise is grey. Thrusts are numbered according to their start of activity. Further explanation in-text; b) Sketch of cross section of the finite (top) and balanced (bottom) plateau-style setting with erosion. Thrusts are chronologically numbered as in a).



wedge-like part (unit 4) accumulate strain for a shorter period of time. Towards the end of a thrust's activity, strain accumulation "fades out" to almost zero, which is indicated by the faint black tail (Fig. 6.5a). The direction of avalanches indicates that faults in the peak ridges are all backthrusts (Fig. 6.5b).

6.6. Discussion

6.6.1. Internal parameter control

Despite being a rather simple model of the upper crust, the granular set-up is able to show that certain parameters in combination are responsible for the evolution of two prominent types of strain accumulation. These parameters comprise two internal parameters that are coupled to each other: basal strength contrasts (including basal detachments) and lateral strength contrasts (including inherited structures). Thus, rheological properties of the system causing mechanical heterogeneity are first order factors controlling the style of strain accumulation. Figure 6.2 shows that two domains exist: one for plateau-like patterns and one for taper-like deformation (including both single- and bivergent settings), which can be separated from each other by a sharp line. This means that no gradual transitions exist from one type to the other, but that critical threshold values are present for both the lateral and the basal strength contrast, which determine if either the one or the other deformational setting develops.

The threshold value for lateral strength contrasts between adjacent units has to be higher than ~ 1.2 (or $\sim 20\%$ lateral strength contrast) for the formation of a plateau-style setting, which converges towards 1 when the basal contrast approaches 0 (no frictional coupling at the base). Numerical experiments have shown that as soon as the slightest basal friction is present (Vietor, pers. comm. 2007), deformation will be in a wedge-like rather than a plateau-style fashion, irrespective of lateral strength contrasts. Therefore we assume that the lower end of the line separating the two deformational settings will draw near to this point at 0 (basal contrast) and 1 (lateral contrast) (Fig. 6.2). At the same time, this means that without the lateral strength contrast the resulting strain pattern will always be wedge-like for any basal contrast > 0 .

The threshold value for the basal contrast is ~ 0.67 (or $\sim 35\%$ basal strength contrast) beyond which the strain pattern will be wedge-

like, irrespective of lateral strength contrasts. If the value for the basal strength contrast is lower than the respective threshold value, the style of deformation will be plateau-like independent from any increase of the lateral strength contrast beyond the above mentioned value (~ 1.2). However, some experiments (1-6, Fig. 6.2) indicate that if the lateral strength contrast will be very high (more than 50%) the plateau-style settings only develop when we again decrease the basal contrast.

Certainly, these values might shift depending on the aspect ratios of the initial system. This means, that with increased thickness of the upper crustal layer (but constant width of the units), the normal stress increases, and a higher shear stress or a lower basal friction is required for yielding (according to the Mohr-Coulomb criterion). The contrary is true for higher lateral widths with the same thickness, as the normal force is lower (i.e., the force acts on a bigger surface), and therefore the yield strength can be overcome at lower shear stresses or comparably higher basal friction. With respect to this issue, the line separating both fields might shift slightly to the left or right depending on the scaling ratio. However, the two different scaling ratios tested in our experiments have very similar threshold values.

We also conclude that plateau-style settings require more mechanical heterogeneity (complexity), as they develop only when both the basal and the lateral strength contrasts exist. In contrast, taper- or wedge-like systems already develop when only a basal contrast is present, but no lateral variation.

We can show that a hierarchy exists for all parameters. The controlling first order factors are basal and lateral strength contrasts. But, as taper-like settings already develop with only the basal contrast and do not necessarily require a lateral strength contrast, we interpret the basal contrast to be more important than the lateral contrast. The other tested internal parameters did not have any influence on the resulting deformation style, and are therefore only second order factors.

6.6.2. Effect of external parameters

In our experiments, the external parameters such as shape of the indenter, the effect of a backstop or erosion merely cause a system to react to imposed changes, which can go as far as putting a system into a supercritical or subcritical state.

Table 6.3. Basal and internal friction coefficients used for the calculation of values for basal and lateral contrasts (cf. Figure 6.2)

No	Basal friction (foil)	Basal friction (additional material)	Basal friction (average)	Internal friction (strong unit)	Internal friction (weak unit)	Basal contrast	Lateral contrast	Deformation type
02		0.41		0.76	0.41	0.54	1.85	a)
03		0.41		0.76	0.41	0.54	1.85	a)
04		0.41		0.76	0.41	0.54	1.85	a)
05		0.41		0.76	0.41	0.54	1.85	a)
06		0.41		0.76	0.41	0.54	1.85	a)
07		0.41		0.76	0.49	0.54	1.55	d)
08		0.41		0.76	0.51	0.54	1.49	d)
09		0.41		0.76	0.49	0.54	1.55	d)
10		0.41		0.76	0.49	0.54	1.55	d)
11		0.41		0.76	0.51	0.54	1.49	d)
12	0.26			0.76	0.51	0.34	1.49	e)
13		0.54		0.76	0.52	0.71	1.46	c)
14		0.54		0.76	0.51	0.71	1.49	a)
15			viscous	0.76	0.52	-	1.46	e)
16		0.54		0.76	0.51	0.71	1.49	c)
18		0.55		0.76	0.54	0.72	1.41	c)
19		0.55		0.71	0.54	0.77	1.31	b)
20	0.26			0.76	0.51	0.34	1.49	e)
22	0.28			0.76	0.58	0.5	1.31	d)
23	0.25	0.5	0.38	0.65	0.52	0.58	1.25	b)
25	0.25			0.6	0.51	0.41	1.18	b)
26	0.25	0.41	0.305	0.65	0.52	0.47	1.25	b)
27	0.25	0.41	0.305	0.59	0.51	0.51	1.18	b)
29	0.26	0.41	0.335	0.76	0.31	0.44	1.49	d)
30	0.3			0.76	0.51	0.40	1.49	e)
31	0.5			0.76	0.51	0.66	1.49	e)
32	0.65			0.76	0.51	0.86	1.49	a)
33	0.6			0.76	0.51	0.79	1.49	a)
34	0.55			0.76	0.51	0.72	1.49	a)
35	0.5/0.65		0.66/0.86	0.76	0.51	0.66/0.86	1.49	e), then a)
36	0.5			0.76	0.51	0.66	1.49	e)
37	0.5			0.76	0.51	0.66	1.49	e)
38	0.5			0.76	0.52	0.66	1.46	e)
39	0.5			0.76	0.53	0.66	1.43	e)
40	0.5			0.76	0.52	0.66	1.46	e)
41	0.5			0.76	0.52	0.66	1.46	e)
42	0.5			0.76	0.52	0.66	1.46	e)
43	0.5/0.65		0.66/0.86	0.76	0.52	0.66/0.86	1.46	e), then a)
44	0.5			0.76	0.52	0.66	1.46	e)
47	0.55			0.8	0.54	0.69	1.48	a)
48	0.3			0.54	0.41	0.56	1.32	a)
49	0.45			0.63	0.41	0.71	1.54	a)
50	0.11			0.41	0.38	0.27	1.08	b)
51	0.17			0.43	0.41	0.4	1.05	b)
52	0.23			0.54	0.41	0.43	1.32	d)
53	0.23			0.54	0.54	0.43	1	a)
54	0.11			0.41	0.41	0.27	1	a)
55	0.3			0.63	0.54	0.48	1.17	b)
61	0.3	0.37	0.335	0.62	0.62	0.54	1	a)
62	0.3	0.49	0.385	0.67	0.67	0.57	1	a)
62	0.3	0.41	0.355	0.63	0.63	0.63	1	a)

Such a parameter influence becomes most obvious when comparing a system that has undergone erosion to one that has not been eroded. In general, erosion prolongs the activity of each thrust as well as the general uplift activity within the plateau-like part of the system, and therefore avalanches take place for a longer time than without erosion, but are small as sediment supply is scarce. Strain seems to be more localized in space and along fewer faults in the experiment with erosion, as thrusts are reactivated more often. Also, the deformation transfer from the stable plateau-style system (units 1-3) to the "external" wedge-like part (unit 4) can only be clearly observed without erosion. This is due to the fact, that the system does not become critical under the continued influence of erosion, an influence to which the system has to react and to adjust. Models by Babeyko et al. (2006) show that the effect of low to moderate erosion rates are negligible, but that high erosion rates at the plateau margin result in strain weakening of the lithosphere, which in turn leads to an increase of shortening rate within the plateau.

In general we can say that the spatiotemporal strain partitioning mode on the orogen scale resulting from internal parameter control cannot be affected by external parameters. Only minor changes on a sub-orogen scale can occur both in time (prolonging deformation activity in one unit) and space (number of faults) with some external parameters (e.g., erosion).

6.6.3. Limitations of the set-up

We are able to show the importance of the effect of basal contrasts by means of varying the frictional properties analogue to mechanical properties of natural systems. However, modelling only the brittle upper crust and decoupling it from a stiff base implies an important limiting boundary condition, unless layers down to the asthenosphere are incorporated. Also, isostatic effects (e.g., buoyancy) are not taken into account. We assume that isostatic effects have an influence on the general crustal thickness, the topographic elevation, and also on the spatiotemporal pattern of strain accumulation because of the different role of body forces. But as we suspect that isostatic effects would vary locally in response to rheological and therefore mechanical heterogeneities, it would further support our conclusion, that mechanical heterogeneities are first order factors in determining

63	0.33	0.43	0.365	0.56	0.56	0.56	0.65	1	a)
63	0.35	0.43	0.33	0.52	0.52	0.52	0.57	1	a)
63	0.47	0.43	0.52	0.66	0.66	0.66	0.79	1.16	a)
63	0.61	0.43	0.49	0.66	0.66	0.66	0.72	1.16	b)
63	0.91	0.43	0.49	0.66	0.66	0.66	0.84	1.16	b)
63	0.59	0.43	0.49	0.66	0.66	0.66	0.84	1.16	b)
63	0.58	0.43	0.49	0.66	0.66	0.66	0.88	1.08	a)
63	0.56	0.43	0.49	0.66	0.66	0.66	0.85	1.16	a)
63	0.48	0.43	0.49	0.66	0.66	0.66	0.73	1.16	b)
63	0.52	0.43	0.49	0.66	0.66	0.66	0.96	1	a)
63	0.45	0.43	0.49	0.66	0.66	0.66	0.85	1	a)
63	0.53	0.43	0.49	0.52	0.52	0.52	1.02	1	a)
63	0.48	0.43	0.49	0.55	0.55	0.55	0.87	1	a)
64	0.36	0.43	0.49	0.73	0.73	0.73	0.49	1	a)
65	0.55	0.43	0.49	0.53	0.53	0.53	0.91	1	b)
65	0.52	0.43	0.49	0.53	0.53	0.53	0.87	1	b)
65	0.52	0.43	0.49	0.53	0.53	0.53	0.98	1.15	b)
65	0.52	0.43	0.49	0.61	0.61	0.61	0.98	1.15	b)

Table 6.3. A description of each of the experiments (with corresponding numbers) is found in Appendix B. Values are determined on the base of basal and internal coefficients of friction (Table 6.2 a+b). In some cases the basal friction of only the foil or only the material was used, in other cases we used the average of both of these values (more details in-text). The values from Schreurs et al., 2006 [62], Lohrmann, 2002 [63], Marques and Cobbold, 2002 [64], and Hoth, 2005 [65] were partly reinterpreted to fit the value format that is used for Figure 6.2. Values from three experiments were not used in the plot, either because the material strength cannot be expressed in terms of friction coefficients (Exp. 15), or because the resulting deformation type changes during the experiment, as the basal friction varies laterally (Exp. 35, 44) (more details in-text).

the resulting strain pattern and deformation style.

6.7. Application to the Central Andean plateau

Today's Central Andes (17-23°S) have developed since the Paleogene due to the convergence between the Nazca plate and South America. From west to east they comprise four main structural units: the Pre- and Western Cordillera, the Altiplano plateau, the Eastern Cordillera, and the Subandean fold-and-thrust belt (Fig. 6.6). The plateau itself has an average elevation of 4000 m and is bounded by two Cordilleras with average elevations of about 5000 m (Lamb et al., 1997). The Pre- and Western Cordillera represent a former and the recent magmatic arc, and formed since about 46 Ma ago involving <2 % of shortening; the Eastern Cordillera developed as a fold-and-thrust belt since c. 40 Ma with some 30% of shortening, and the plateau has developed as an intramontane basin that has undergone deformation (<20% shortening) since 30 Ma (Elger et al., 2005). Deformation became inactive in all of these units c. 7-10 Ma ago, when active deformation was transferred to the Subandean fold-and-thrust belt (Allmendinger and Gubbels, 1996: "simple shear"

mode for the Altiplano), that has accumulated most of the shortening (~100 km, or 50%).

Both Cordilleras formed at positions of inherited structures: a Permian rift in the Eastern Cordillera (Sempere et al., 2002), and the magmatic arc in the Western Cordillera (Oncken et al., 2006), which act as zones of weakness. A low-velocity zone at a depth of 20 km as imaged in seismic sections can be interpreted as a zone of partial melt possibly decoupling deformation of the upper crust from that of the lower crust (Yuan et al., 2000), which has probably developed since about 30 Ma ago (Babeyko et al., 2002). This horizon possibly extends to the east connecting with the detachment of the Subandean fold-and-thrust belt, which is located in Ordovician shales (Kley et al., 1996), and might be underthrust by the cold Brazilian Shield (Babeyko and Sobolev, 2005). To the west of the Western Cordillera, the little internally deformed forearc might have acted as a "pseudo-indenter" pushing into the comparably weaker orogen during subduction (Victor et al., 2004; Tassara, 2005). Thus the orogen would have been squeezed between two comparably stronger units: the forearc and the Brazilian Shield.

The orogen exhibits a symmetric oroclinal bend (Gephart, 1994) with its symmetry axis coinciding with the present direction of plate convergence. Both paleomagnetic data within the forearc (e.g., Macedo-Sánchez, 1992; Butler et al., 1995; Somoza et al., 1999; Roperch et al., 1999; 2000; Rousse et al., 2005) as well as differential shortening indicate counterclockwise rotation north (up to 45°) of the symmetry axis and clockwise rotation south of it explaining the oroclinal bending of the Andes (Isacks, 1988). This is supported by balanced cross sections (Kley, 1999).

The convergence rate for relative motion between the Nazca plate and South America can be averaged to 7 cm/a (Silver et al., 1998) for the last 30-40 Ma. At the largest width of the orogen between 18-20°S (e.g., Kley, 1999), 280 km of shortening have been accumulated within the last 40 Ma.

The general characteristics of the Andean Altiplano that have been considered as major contributors to the plateau evolution can also be found in our experiments: the compressing piston represents the indenting forearc, our basal detachment simulates a zone of partial melt, which is present beneath the plateau, and the amount of shortening is the same. When comparing the

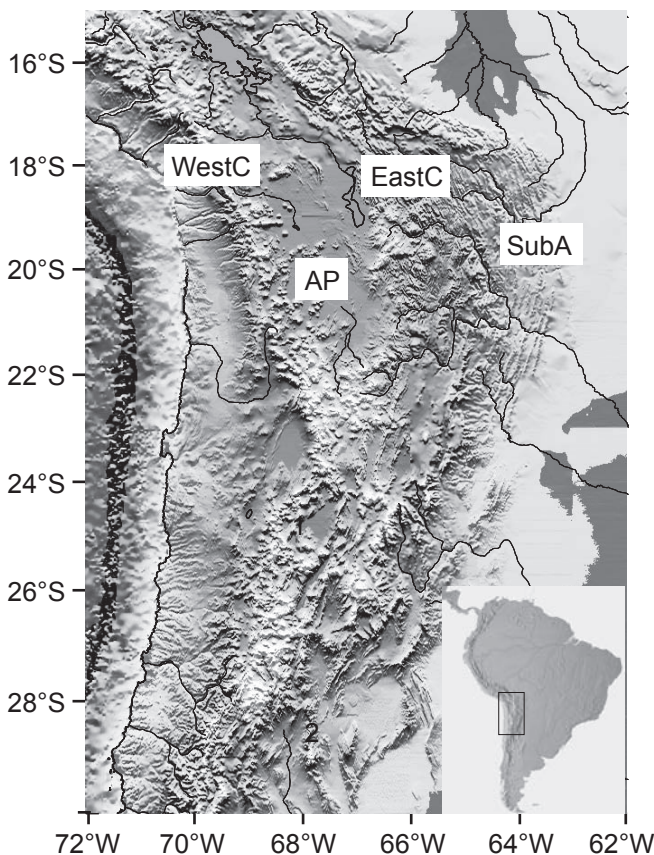


Fig. 6.6: Topographic map of the Central Andean plateau. The following abbreviations are used: WestC – Western Cordillera, AP – Altiplano, EastC – Eastern Cordillera, SubA – Subandean fold-and-thrust belt.

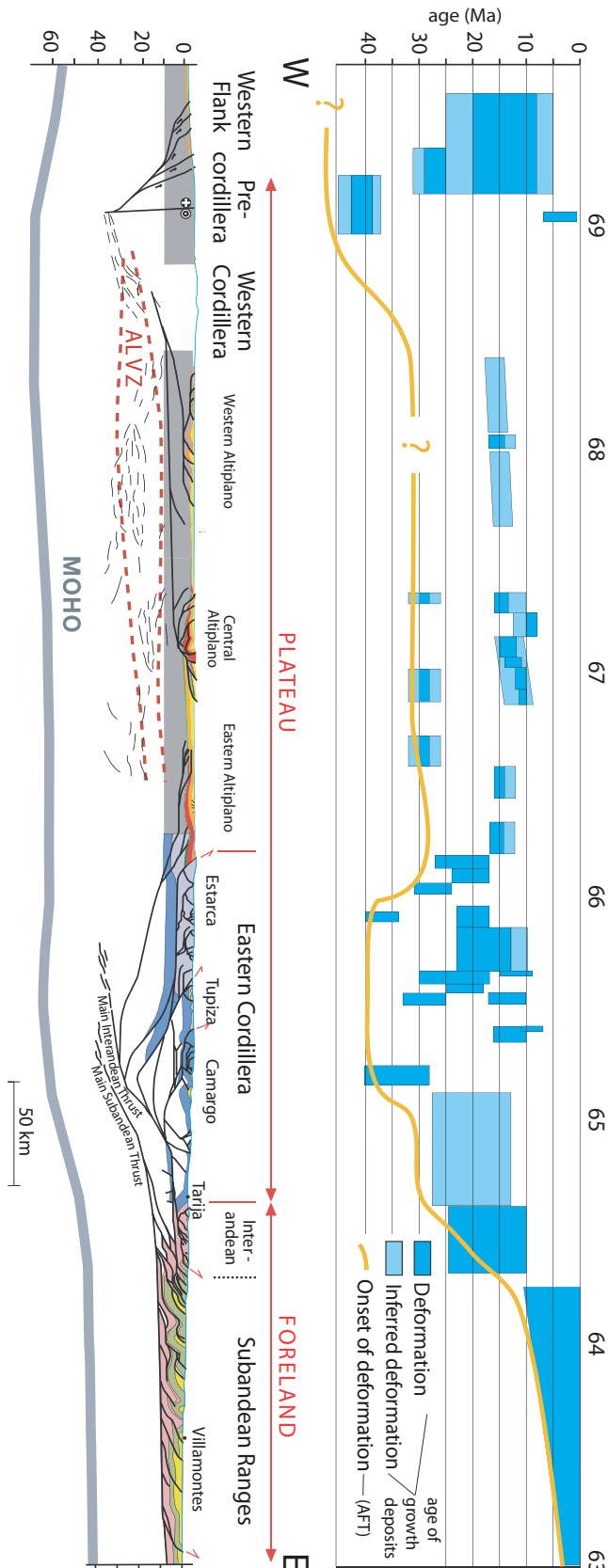


Fig. 6.7: Top: Deformation timing and duration for each structural unit (from Oncken et al., 2006; data compiled from Gubbels et al., 1993; Kley, 1996; Mueller et al., 2002; Haschke and Guenther, 2003; Silva-Gonzalez, 2004; Victor et al., 2004; Elger et al., 2005; Ege et al., 2007) Bottom: Balanced cross section through the Central Andean Plateau at 21°S (from Oncken et al., 2006; data compiled from Yuan et al., 2000; Mueller et al., 2002; ANCORP-Working Group, 2003; Victor et al., 2004; Elger et al., 2005).

cross section of our analogue experiments (Fig. 6.4b) with that of the Central Andes at 21°S (Fig. 6.7), we observe that the structural inventory of each of the units is strikingly similar.

Oncken et al. (2006) have attributed the temporal evolution to a special combination of parameters that initiated and controlled the evolution of the Altiplano and the associated strain pattern as well as the amount of strain: feedback of trench infill, plate interface coupling, and associated shortening transfer and slab rollback; changes in relative velocities of trench and upper plate, as well as the position of inherited structures. Certainly we are not able to examine all potential factors that have contributed to the formation of the Central Andes. We also cannot explain why and when the plateau surface has been uplifted to an elevation close to the peak elevation of the Cordilleras, which is still strongly debated (e.g., Gregory-Wodzicki, 2000; Elger, 2003; Garzzone et al., 2006; Ghosh et al., 2006; Rech et al., 2006; Eiler et al., 2006).

But we are able to reproduce not only the relative timing of strain accumulation in the Central Andes, but also the spatial deformation pattern. Our Andean-type plateau is solely driven by mechanical heterogeneity and yet shows the same strain partitioning mode as the natural example. The analysis by Oncken et al. (2006) has revealed that only a special combination of driving factors can explain the observed strain pattern. These two very different parameter conditions lead to the formation of a strikingly similar pattern, once in a simple model and in the complex natural example. This means that the strain pattern can be caused by more than one parameter combination and explained by various controlling mechanisms. Therefore, strain patterns should not be used to infer the key controlling factors responsible for the formation of a deformation system.

6.7.1. Comparison to other modelling studies

Previous modelling studies on plateau orogens (especially the Central Andean example) mainly focused on the effect of only one parameter: the role of a. thermal perturbation within the lithosphere (Wdowinski and Bock, 1994a; b), b. crustal flow (Royden, 1996), c. gravity-driven channel flow (Husson and Sempere, 2003), d. flow indentation of the lower crust (Gerbault and Willingshofer, 2005), and e. mass flux along a detachment, which caused the formation of the

plateau (Vietor and Oncken, 2005). Only Sobolev and Babeyko (2005) investigated coupled parameters, namely the combined influence of crustal thickness and interplate friction. Certainly, it is highly probable that several parameters in combination affect the formation of a natural system, of which one of the crucial parameters is related to decoupling at the base of the crust.

However, none of these studies was able to explain the spatiotemporal strain pattern as presently observed for a plateau orogen, as most of the studies were not able to reproduce more than a. the final stage of a plateau orogen (Gerbault and Willingshofer, 2005), b. the present-day topography of the Central Andean plateau (Wdowinski and Bock, 1994b; Royden, 1996), or c. the present crustal thickness (Husson and Sempere, 2003).

In contrast, Vietor and Oncken (2005) were already able to reproduce the orogen scale deformation in time and Sobolev and Babeyko (2005) even the timing of topographic development and the approximate amount of shortening over time on the orogen scale. However, being 3D, our study is the first that can reproduce the relative Andean-type distribution of strain accumulation in both space and time on the orogen scale and provides information on the sub-orogen scale as single faults of the structural units are resolved.

Also, we achieve this not only by one single parameter, but we detect the interdependence of two parameters of mechanical heterogeneity. We can pinpoint critical threshold values for these two coupled parameters, which determine the first-order deformational style: wedge- or plateau-like.

6.8. Conclusions

In our granular models of the upper crust we can show that a special combination of both basal and lateral strength contrasts determines the style of the resulting deformation system. Depending on critical threshold values for both of these mechanical parameters, either a plateau-style or a wedge-like setting (single- or bivergent) develops. This means that, in the brittle field, the change from one deformation setting to another is not gradual but abrupt, and no transitional deformation types exist in analogue experiments. Being above or below the threshold value exactly determines if either the one setting or the other forms (Fig. 6.2). Finally, we speculate that the deformation modes with distinct thresholds

observed in our brittle analogue experiments also pertain to natural orogens exhibiting more complex rheologies.

Our analogue plateau-style settings are able to reproduce a strikingly similar spatial and temporal mode of strain partitioning to the one revealed by the patterns of the Central Andean plateau. Further, we can produce the same strain pattern both on the orogen scale and the sub-orogen scale, although driving factors for the natural example are likely to have been more complex than in our simple models. We conclude that strain patterns are not unique, as various combinations of processes and parameters seem to be able to explain one strain pattern. Therefore, strain patterns should not be used to infer their controlling factors.

Acknowledgments

M. Böhme was of great help during performance of the experiments and data logging. N. Kukowski, M. Rosenau, and J. Lohrmann are thanked for discussion and/or assistance with the PIV software. G. Tauscher built the experimental set-up. The friction measurements were carried out and made available by various scientists of the Analogue Laboratory at the GFZ.

This work is part of KS' PhD thesis, funded by a scholarship from the "Studienstiftung des deutschen Volkes" (German National Merit Foundation).

7. The effect of mechanical heterogeneity on plateau initiation - A modelling study with viscous-brittle media

Viscous-brittle analogue vise models, comprising two strong blocks that compress a weaker deformable domain, are employed to investigate critical factors for initiation of plateau-style tectonic deformation. The experiments focus on the role of mechanical heterogeneities in the lithosphere and specifically: 1) a critical lateral strength contrast between the strong “vises” and the intervening domain (e.g., more than twice the strength); 2) the presence of a decoupling horizon within the lower crust of the weak domain; 3) the degree of buoyancy of the lower crust; and 4) oroclinal bending. These parameters are shown to be first order features, which result in the formation of mountain ranges that enclose a flat basin, similar to geometries observed in nature (e.g., Andean and Tibetan plateaux). By further varying these parameters, for example by introducing additional decoupling horizons or decreasing the strength contrast between the strong blocks and the weak domain, the strain pattern at the surface remains that of a plateau-initiation setting, but has pronounced along-strike differences. Thus, some first order parameters have additional second order influence.

7.1. Introduction

Many driving factors are likely to play a role in the development of plateau orogens including crustal channel flow (e.g., Wdowinski and Bock, 1994a,b; Yuan et al., 2000; Husson and Sempere, 2003), climate (e.g., Masek et al., 1994; Horton, 1999; Lamb and Davis, 2003; Sobel et al., 2003), strength variations within the plates and their interface (e.g., Allmendinger and Gubbels, 1996; Lamb and Davis, 2003; Sobolev and Babeyko, 2005), mantle-driven processes (e.g., Kay and Kay, 1993; Allmendinger et al., 1997), changes in plate/indenter geometry (e.g., Gephart, 1994; Giese et al., 1999; Tassara, 2005), and convergence kinematics (e.g., Pardo-Casas et al., 1987; Somoza, 1998; Silver et al., 1998; Sobolev and Babeyko, 2005). Most of these studies on plateau formation focused on one potential driving factor that is able to account for the present-day strain pattern or the general orogen scale configuration. We suspect that several key conditions must be met early on in the initial system to allow the initiation of plateau growth (Oncken et al., 2006).

For the Tibetan plateau, Meyer et al. (1998) summarize the following conditions necessary for successful initial basin capture and subsequent plateau formation: 1) decoupling of crust and mantle produces a décollement, in which, 2) large, interconnected, coevally active thrusts root to produce, 3) broadly spaced parallel ranges that separate wide basins, 4) tectonic cut-off of river catchments that allows internal drainage of these basins, and 5) sedimentary infill from adjacent ranges, which finally leads to the smoothing of

relief and surface uplift (cf. Fig. 7.1).

The development of distinctly spaced high ranges that entail basin capture when supported by arid climate preventing the export of material have also been suggested to be crucial points for the Andean plateau (Sobel and Strecker, 2003; Sobel et al., 2003). Interestingly, the formation of spaced ranges entrapping a basin occurs on various length scales, from ~10 km in the Sierras Pampeanas and the Santa Barbara domain (Sobel et al., 2003; Mortimer et al., 2007) to the entire Altiplano (Elger et al., 2005) (Fig. 7.2).

The conditions for basin capture can be met by lithospheric buckling, where the wavelength of the periodic instabilities or buckle folds is determined by the vertical strength contrasts within the crust (e.g., Biot, 1961; Fletcher, 1974; Smith, 1975; Martinod and Davy, 1994; Burg and Podlachikov, 1999; Cagnard et al., 2006). However, previous

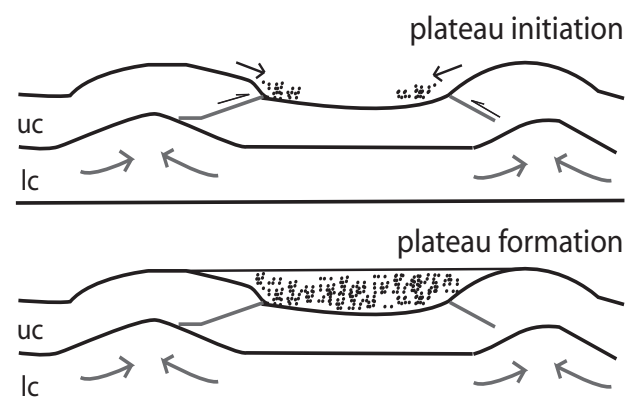


Fig. 7.1: Two evolutionary stages of plateaux include the plateau initiation, in which a basin is captured by two bounding ranges, and the plateau formation, which is successful when the basin has been drained, filled with sediments and uplifted.

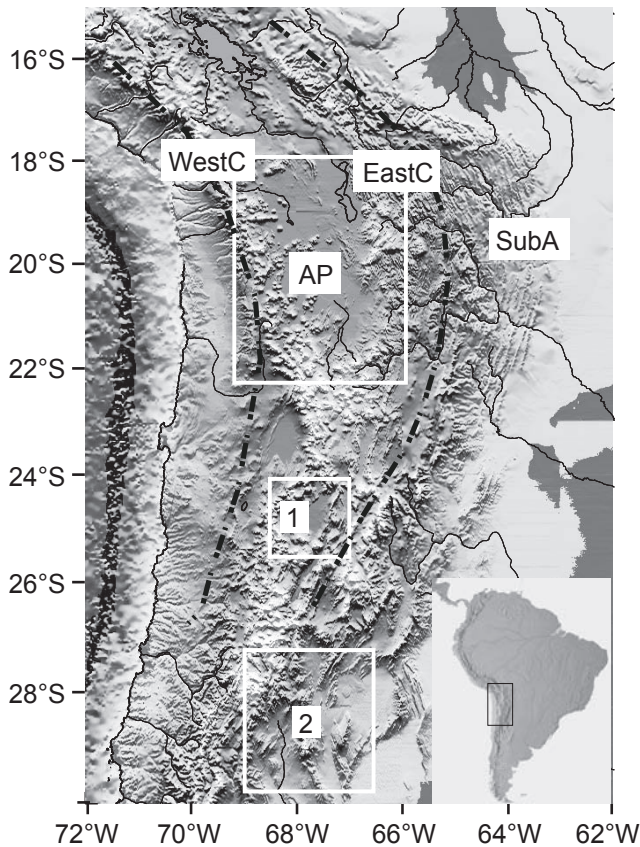


Fig. 7.2: Topomap of the study area of the Central Andes with main structural units; WestC: Pre- and Western Cordillera, AP: Altiplano plateau, EastC: Eastern Cordillera, SubA: Subandean fold-and-thrust belt (inset shows location in South America). Black dashed lines outline “vise” boundaries. White frames show locations of basins that have been preserved in between mountain ranges and internally drained (AP: Altiplano, 1: Puna, 2: Sierras Pampeanas).

studies have several limiting factors with respect to natural examples of plateau initiation: 1) the crust is horizontally homogeneous and strength contrasts exist only vertically, 2) strain localization does not occur in a similar fashion to that in nature, where it is guided by weak zones that are more prone to strain accumulation than others, 3) lithospheric buckles often occur instantaneously and coevally, and cannot explain the chronological evolution of mountain ranges and entrapped basins observed in natural systems, and 4) they cannot account for processes operating at distinctly different spatial length scales.

In this paper we investigate the role of mechanical heterogeneity in the lithosphere on basin capture and the initiation of plateaux, consisting of a combination of both vertical and horizontal physical contrasts (strength and density). Thus we aim to address some limitations of previous models, and to investigate the role of coupled parameters that can explain the initiation of plateaux, which are both comparable to nature and

have the potential to develop a plateau thereafter. These include lateral strength contrasts between the strong “vises” and the intervening domain, decoupling horizons within the lower crust of the weak domain, degrees of buoyancy of the lower crust, and oroclinal bending.

We accomplish this by viscous-brittle analogue experiments following previous numerical and laboratory vise simulations (Ellis et al., 1998; Cruden et al., 2006), in which a weak domain is compressed in between two strong blocks. Particle imaging velocimetry (cf. Adam et al., 2004) enables high-resolution monitoring of the evolution of strain in space and time, and the development of 3D topographic relief. Thus we can compare our models to natural examples at the orogen scale, and are also able to detect variations on smaller scales.

7.2. Experimental design

7.2.1. Experimental procedure

The model set-up is similar to previous analogue vise models (Cruden et al., 2006), in which two strong blocks (“vise 1” attached to the advancing piston, and “vise 2” on the opposite immobile side) compress a weak domain. Both the vises and the intervening domain are composed of brittle upper crust, a viscous lower crust and a viscous mantle lithosphere floating isostatically on the asthenosphere (Fig. 7.3). The boundaries to the sides of the box are closed to avoid lateral extrusion of the model.

One piston is advanced into the model at a constant rate during the experiment. The contacts of vise and piston, vise and weak domain, vise and tank wall, and weak domain and tank wall are no-slip boundaries. The upper boundary is a free surface.

7.2.2. Scaling

All scaling factors are dimensionless ratios of model to nature (Table 7.1). The length scale ratio yields $L^* = l_{\text{mod}}/l_{\text{nat}} = 3.75 \times 10^{-7}$, as we use a model crustal thickness $l_{\text{mod}} = 1.2$ cm, which corresponds to 32 km in nature. The density ratio $\rho^* = \rho_{\text{mod}}/\rho_{\text{nat}}$ is 0.326 given by a mantle lithosphere density of 3000 kg/m³ and a model density of 980 kg/m³. The gravity for the models is the same as in nature, so that g^* is 1. Thus, the stress scaling factor $\sigma^* = L^* \rho^* g^*$ yields 1.2225×10^{-7} .

The viscosity ratio $\eta^* = \eta_{\text{mod}}/\eta_{\text{vat}}$ yields a factor of 5×10^{-18} Pa s, if we assume 5.9×10^{21} Pa

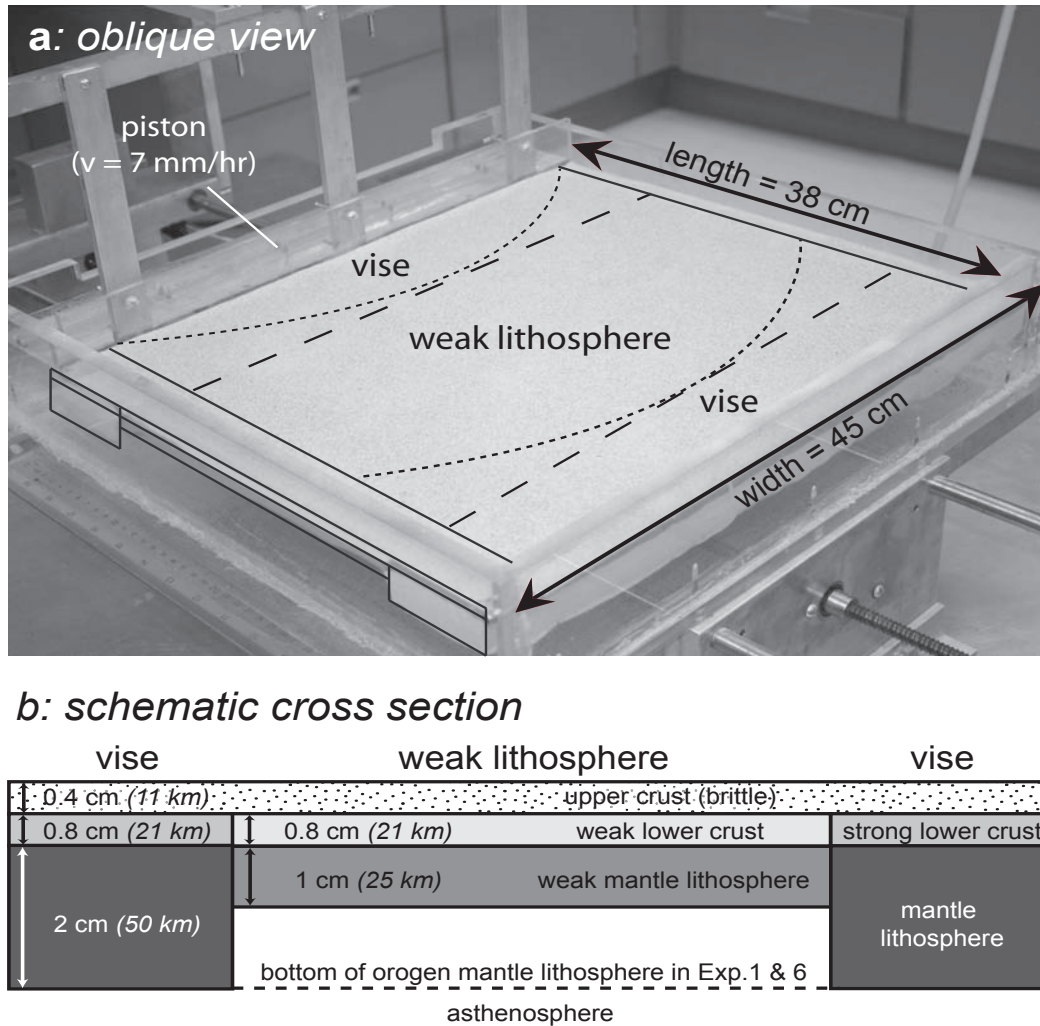


Fig. 7.3: a) Photograph of experimental set-up. The shape of the “vises” is either curved or straight. Tank dimensions are 46 cm x 45 cm x 10 cm, but the experimental set-up surface is only 38 cm (length) x 45 cm (width).

b) The thicknesses for each layer are given with the natural equivalents (in italics). In two experiments (Exp. 1 and Exp. 6), the mantle lithosphere of the weak domain has the same thickness as the vise mantle lithosphere (both 2 cm).

s as viscosity for the natural mantle lithosphere of the weak domain, which we model with material that has a viscosity of 2.95×10^4 Pa s at an experimental strain rate of $2.44 \times 10^{-5} \text{ s}^{-1}$. Further, we obtain the duration of our model runs $t^* = \eta^* / \sigma^*$ with $t_{\text{mod}} / t_{\text{nat}} = 5 \times 10^{-18} / (0.326 \times 3.75 \times 10^{-7}) = 4.1 \times 10^{-11}$. For our deformational system to develop we assume a duration of $t_{\text{nat}} = 40 \text{ Ma} (= 3.504 \times 10^{11} \text{ h})$ which gives $t_{\text{mod}} = 14.3 \text{ h}$.

Of further interest is $\varepsilon^{\text{dot}*} = \sigma^* / \eta^*$ which results in 2.44×10^{10} , where $\varepsilon^{\text{dot}*}$ is the dimensionless ratio for strain rate. Therefore natural strain rates on the order of 10^{-15} s^{-1} are scaled with model strain rates of $\varepsilon^{\text{dot}}_{\text{mod}} = 2.44 \times 10^{-5} \text{ s}^{-1}$. Velocities are scaled by $V^* = \varepsilon^{\text{dot}*} L^*$. Thus $V_{\text{mod}} / V_{\text{nat}}$ is given by $2.44 \times 10^{10} \times 3.75 \times 10^{-7}$ which yields $V^* = 9146.3$. Assuming an average amount of shortening in nature of about 280 km over 40 Ma, the shortening rate is 7 km/Ma ($8 \times 10^{-4} \text{ mm/h}$), and we obtain $V_{\text{mod}} = 7 \text{ mm/h}$. To verify the values for velocity and time, we use

$V^* = L^* / t^*$, which is $3.75 \times 10^{-7} / 4.1 \times 10^{-11} = 9146.3$. A total experimental run of 14.3 hours results in about 10 cm of piston convergence and a bulk shortening of 27.7 %. All scaling parameters are summarized in Table 7.1.

7.2.3. Materials and model construction

Variations in viscosity and density of viscous laboratory materials are accomplished by adding Harbutt’s plasticene, bouncing putty, low-viscosity silicone or granular fillers like 3M Z-lights ceramic microspheres, and 3M Scotchlith Glass Bubbles to transparent Polydimethylsiloxane (PDMS) (for details refer to Cruden et al., 2006). The rheological properties were measured for all viscous mixtures using a TA Instruments AR1000 rheometer over a broad range of stresses at ambient room temperature. Strength profiles of both weak lithosphere and strong vises are presented in Figure 7.4.

Table 7.1. Scaling parameters

Parameter	Equation	Nature	Model	Scaling factor
<i>Initial Thickness</i>				
	L_{mod}/L_{nat}			$L^* = 3.75 \times 10^{-7}$
upper crust		10.7 km	0.4 cm	
lower crust		21.3 km	0.8 cm	
mantle lith. (weak)		(26.7 km or) 53.4 km	(1 cm or) 2 cm	
mantle lith. (vise)		53.4 km	2 cm	
mantle asthenosphere		120.2 km	4.5 cm	
<i>Density</i>				
	ρ_{mod}/ρ_{nat}			$\rho^* = 0.326$
upper crust		2600 kg/m ³	850 kg/m ³	
lower crust (weak)		2480 kg/m ³ ; 2900 kg/m ³	810 kg/m ³ ; 950 kg/m ³	
lower crust (vise)		2900 kg/m ³	950 kg/m ³	
mantle lith. (weak)		3000 kg/m ³	980 kg/m ³	
mantle lith. (vise)		3030 kg/m ³	990 kg/m ³	
mantle asthenosphere		not scaled	1000 kg/m ³	
<i>Viscosity</i>				
	η_{mod}/η_{nat}			$\eta^* = 5 \times 10^{-18} \text{ Pa s}$
lower crust (weak)		3 - 4.2 x 10 ²¹ Pa s	1.5 - 2.1 x 10 ⁴ Pa s	
lower crust (vise)		9 x 10 ²¹ Pa s	4.5 x 10 ⁴ Pa s	
mantle lith. (weak)		5.9 x 10 ²¹ Pa s	2.95 x 10 ⁴ Pa s	
mantle lith. (vise)		3.6 x 10 ²² Pa s	1.83 x 10 ⁵ Pa s	
mantle asthenosphere		not scaled	0.89 x 10 ⁻³ Pa s	
low-viscosity layer		~10 ¹⁶ -10 ¹⁷ Pa s	10 ¹ -10 ² Pa s	
<i>Gravity</i>				
	g	9.81 m s ⁻²	9.81 m s ⁻²	$g^* = 1$
<i>Strain rate</i>				
	$\dot{\epsilon}^{dot*} = \sigma^*/\eta^*$	10 ⁻¹⁵ s ⁻¹	2.44 x 10 ⁻⁵ s ⁻¹	$\dot{\epsilon}^{dot*} = 2.44 \times 10^{10}$
<i>Time</i>				
	$t^* = \eta^*/\sigma^*$	40 Ma	14.3 h	$t^* = 4.1 \times 10^{-11}$
<i>Convergence rate</i>				
	$V^* = L^*/t^*$	7 mm/yr	7 mm/h	$V^* = 9146.3$
<i>Stress</i>				
	$\sigma^* = \rho^* g^* L^*$			$\sigma^* = 1.2225 \times 10^{-7}$

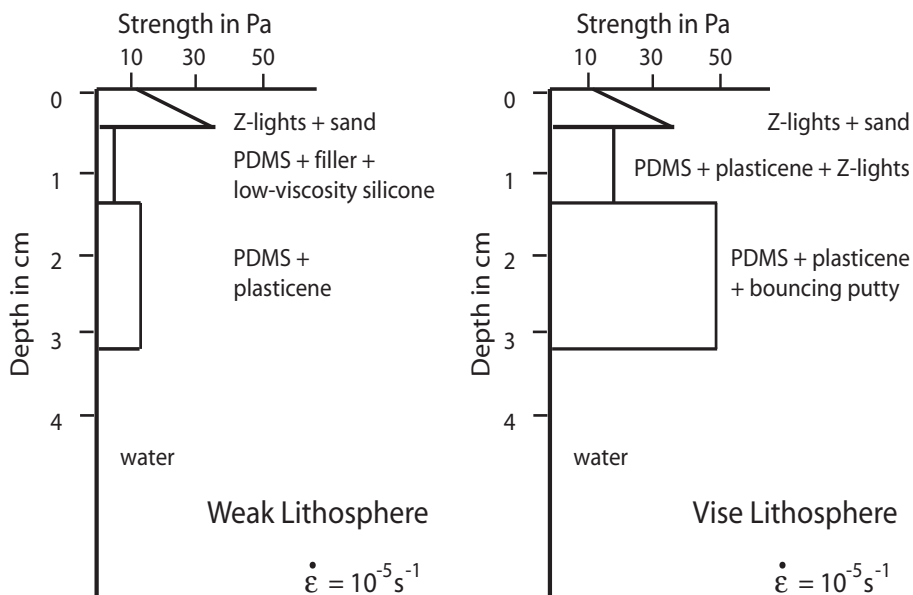


Fig. 7.4: Strength profiles for material mixtures used in both the “weak” lithosphere (left) and the strong “vise” lithosphere (right). For densities and viscosities of materials confer Table 7.1.

7. The effect of mechanical heterogeneity on plateau initiation

Table 7.2. Initial characteristics and resulting patterns of experiments.

	Initial Characteristics	Resulting pattern	Strain localization at % of bulk shortening
Exp. 1	Straight vises, non-buoyant lower crust, 2 cm mantle lithosphere in weak domain	cross-shaped (broad)	10 %
Exp. 2	Straight vises, buoyant lower crust, 1 cm mantle lithosphere in weak domain	cross-shaped (narrow)	4-6 %
Exp. 3	Curved vises, buoyant lower crust, 1 cm mantle lithosphere in weak domain	horizontal Phi (narrow)	5 %
Exp. 4	Curved vises, non-buoyant lower crust, 1 cm mantle lithosphere in weak domain	horizontal Phi (broad)	11.5 %
Exp. 5	Curved vises, non-buoyant lower crust, 1 cm mantle lithosphere, additional low-viscosity horizon	horizontal Phi (broad)	11.5 %
Exp. 6	Curved vises, non-buoyant lower crust, 2 cm mantle lithosphere in weak domain	horizontal Phi (broad)	11.5 %
Exp. 7	Curved, small vises, non-buoyant lower crust, 1 cm mantle lithosphere in weak domain	other	11 %
Exp. 8	Curved, small vise 1, straight vise 2, non-buoyant lower crust, 1 cm mantle lithosphere	mix of cross-shaped and horizontal Phi	12 %
Exp. 9	Curved vises, buoyant domain within non-buoyant domains, 1 cm mantle lithosphere	other	13 %

To ensure that the system is not coupled to mantle flow (e.g., by drag from below), we use water as our model asthenosphere. The viscosity of the asthenosphere is therefore underestimated, but the role of this layer in our experiments is solely to provide isostatic equilibrium.

After thorough mixing, each layer is allowed to relax in a frame to remove air bubbles. Layers of the mantle lithosphere, both of the vises and the weak domain, are later assembled together in a larger frame and allowed to flow into contact. Next, the layers of the lower crust are placed on top and allowed to settle. Finally, the large frame containing all the viscous units is put into a freezer, so that the layers can be placed on the water as one solid block.

After warming up to ambient room temperature and isostatic readjustment, a granular upper crust composed of sand and Z-lights is sieved on top of the model. To minimize boundary effects within the system, an additional buffer layer of pure PDMS is introduced along the sides orthogonal to the piston, on which no granular material is placed.

7.2.4. Dimensions of the experimental set-up

The experimental tank is 46 x 45 x 10 cm³ (length x width x depth) (Fig. 7.3). Convergence is in the direction of length. Due to the position of

the piston, the total length of the experiment is 38 cm, of which each vise makes up 7 cm and the weak domain has a length of 24 cm. The width of each unit is 41 cm with an additional 2 cm on each side to avoid boundary effects. The depth of the piston corresponds to the bottom of the mantle lithosphere, thus only the viscous layers are pushed, and the asthenospheric mantle flows freely below the piston. Thicknesses for the vise are the following: 2 cm of mantle lithosphere, 0.8 cm of lower crust and 0.4 cm of upper crust; and for the weak domain: 1 cm of mantle lithosphere, 0.8 cm of lower crust and 0.4 cm of upper crust (Table 7.1). In two experiments, the mantle lithosphere of this domain is also 2 cm (Exp. 1, 6, Table 7.2).

For experiments with curved vises, the one attached to the piston has a maximum length of 7 cm at its center point decreasing to the sides, whereas the vise on the other immobile side has a minimum length of 7 cm in its center point increasing in length towards the sides to reach 14 cm. The curvature angle is about 20° (Fig. 7.3).

7.2.5. Monitoring technique

In order to quantify the instantaneous horizontal velocities and vertical displacements of the model surface, all experiments are monitored by “particle imaging velocimetry” (PIV) (cf. Adam et al., 2004). The surface is imaged by two

stereoscopic cameras, which are calibrated (3D volume calibration) before each experiment to obtain a mapping function. This function is used for the error evaluation, which is on the order of 10^{-1} pixel. One pixel equals 0.33 mm, so the error is one order of magnitude smaller than the size of a single sand grain ($\sim 400 \mu\text{m}$). Digital images are taken every five minutes, which equals 0.6 mm of shortening at a motor speed of 7 mm/h.

Data processing further includes the calculation of digital elevation models for each of the stereo image pairs, which serve as the base for the subsequent computation of the observed velocity field. This is achieved by cross-correlation of sequential images by the commercial software LaVision DaVis (for details refer to Adam et al., 2004). The velocity field is then used to compute incremental and cumulative strain gradients in multiple directions (e.g., in E_{xx} , E_{yy} , E_{xy}).

7.3. Experimental results

7.3.1. Tested parameters

The initial set-up generally follows the model in Figure 7.3 depending on the implementation of the following parameters, which are based on features of the Central Andes: a) the geometry of the vises (oroclinal bend of the Central Andes, cf. Fig. 7.2), b) an additional low-viscosity horizon in the lower crust (zone of partial melt beneath the Andean plateau), c) lateral strength contrasts between two stronger units compressing a weaker domain (vises: the Andean forearc as the “pseudo-indenter”, Victor et al., 2004; Tassara, 2005; and the strong Brazilian Shield, e.g., Sobolev and Babeyko, 2005), and d) the density profile (studying the two possible end members of density variations due to, e.g., the presence of partial melt or delamination processes).

Figure 7.5 presents the resulting strain patterns of all nine experiments depending on the changed parameter combinations. The upper row shows the different tested geometries of the vises, which are combined with various characteristics given on the left hand side (buoyancy, decoupling layers, and mantle lithosphere thickness). The initial characteristics and the resulting strain patterns are also summarized in Table 7.2 and are described in more detail below.

7.3.2. Strain patterns

The resulting finite strain patterns can be grouped into 1) “cross-shaped” patterns (Exp. 1,

2); 2) “horizontal phi”-patterns (Exp. 3, 4, 5, 6); and 3) other patterns (Exp. 7, 8, 9).

7.3.2.1. Cross-shaped pattern

The first group (Exp. 1 and 2) is characterized by a final strain pattern that resembles a saltire, as the structures cross in the center of the weak domain at a very low angle, and move outwards to both sides (Fig. 7.5a+b). No plateaux are initiated, as the anticlinal hinges do not capture an undeformed area in between (Exp. 1, 2, Fig. 7.5a+b). This is possibly due to the limiting effect of the side walls of the tank, which might not happen when the experimental set-up was larger.

Both experiments have straight vises on both sides; the lower crust in Exp. 1 (Fig. 7.5a) is non-buoyant with respect to the upper crust, and buoyant in Exp. 2 (Fig. 7.5b). In Exp. 1, the first thrust develops about 2 cm inward from vise 1 in the weak domain after about 10% of bulk shortening. At about 13% of bulk shortening eight thrusts begin to develop coevally, and are distributed within the weak domain with a spacing of 2-6 cm. Localization mostly initiates in the center of the model, from where thrusts propagate laterally closer to the vises. With increased shortening, thrusts develop hanging wall anticlines that gain in elevation. Strain is accumulated solely within these structures.


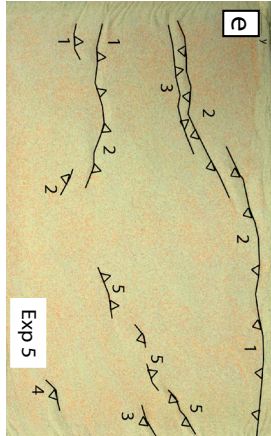
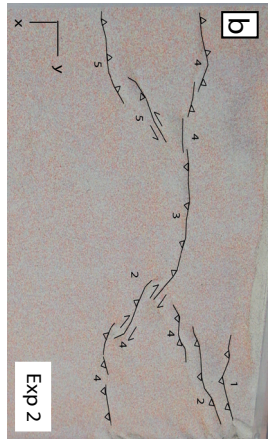
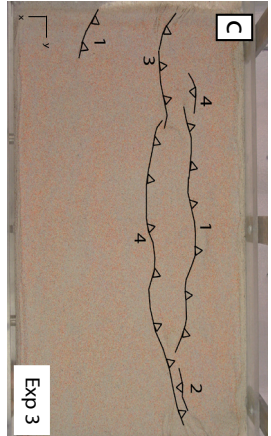


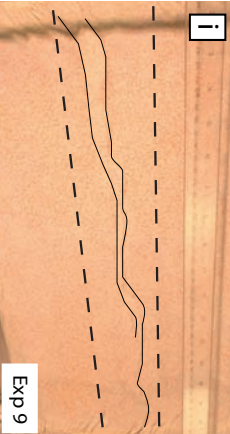
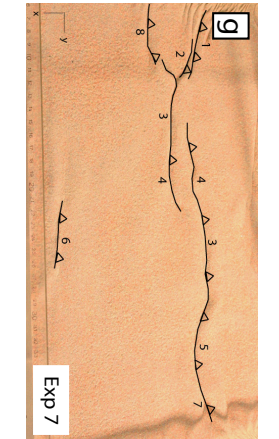
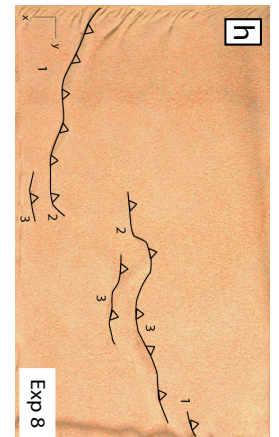
In Exp. 2, a first set of three en-echelon structures develops from the piston close to the side walls inwards towards the front wall at 4-6% of bulk shortening. Subsequently, a major structure develops within the center, coevally with another set of en-echelon faults that localizes from the center outwards towards the first en-echelon set. After 9% of bulk shortening, the main structure in the center extends towards the sides near the back wall, followed by another en-echelon set towards the front wall. After about 14% of bulk shortening, the cross-shaped strain pattern remains unchanged and accumulates all subsequent strain.

Figure 7.6 shows topographic profiles across the system for experiments 1 and 2. They do not exhibit flat and relatively undeformed areas that are entrapped by anticlinal hinges.

7.3.2.2. Phi pattern (plateau-initiation)

Characteristic for the plateau-initiation settings is the development of two anticlinal

7. The effect of mechanical heterogeneity on plateau initiation

Thick mantle lith	LVL	Buoyant lc	Non-buoyant lc	
 <p>Exp 6</p>	 <p>Exp 5</p>	 <p>Exp 2</p>  <p>Exp 3</p>	 <p>Exp 1</p>  <p>Exp 4</p>	<div style="display: flex; justify-content: space-around; align-items: center;"> <div style="border: 1px solid black; padding: 5px; text-align: center;"> vise 1 weak lithosphere vise 2 </div> <div style="font-size: 2em;">↑</div> <div style="border: 1px solid black; padding: 5px; text-align: center;"> vise 1 weak lithosphere vise 2 </div> </div> <p style="text-align: center; font-weight: bold;">convergence</p>
 <p>Exp 9</p>	<p style="text-align: center;">other (cf. text)</p>		 <p>Exp 7</p>  <p>Exp 8</p>	<div style="display: flex; justify-content: space-around; align-items: center;"> <div style="border: 1px solid black; padding: 5px; text-align: center;"> vise 1 weak lithosphere vise 2 </div> <div style="border: 1px solid black; padding: 5px; text-align: center;"> vise 1 weak lithosphere vise 2 </div> </div>

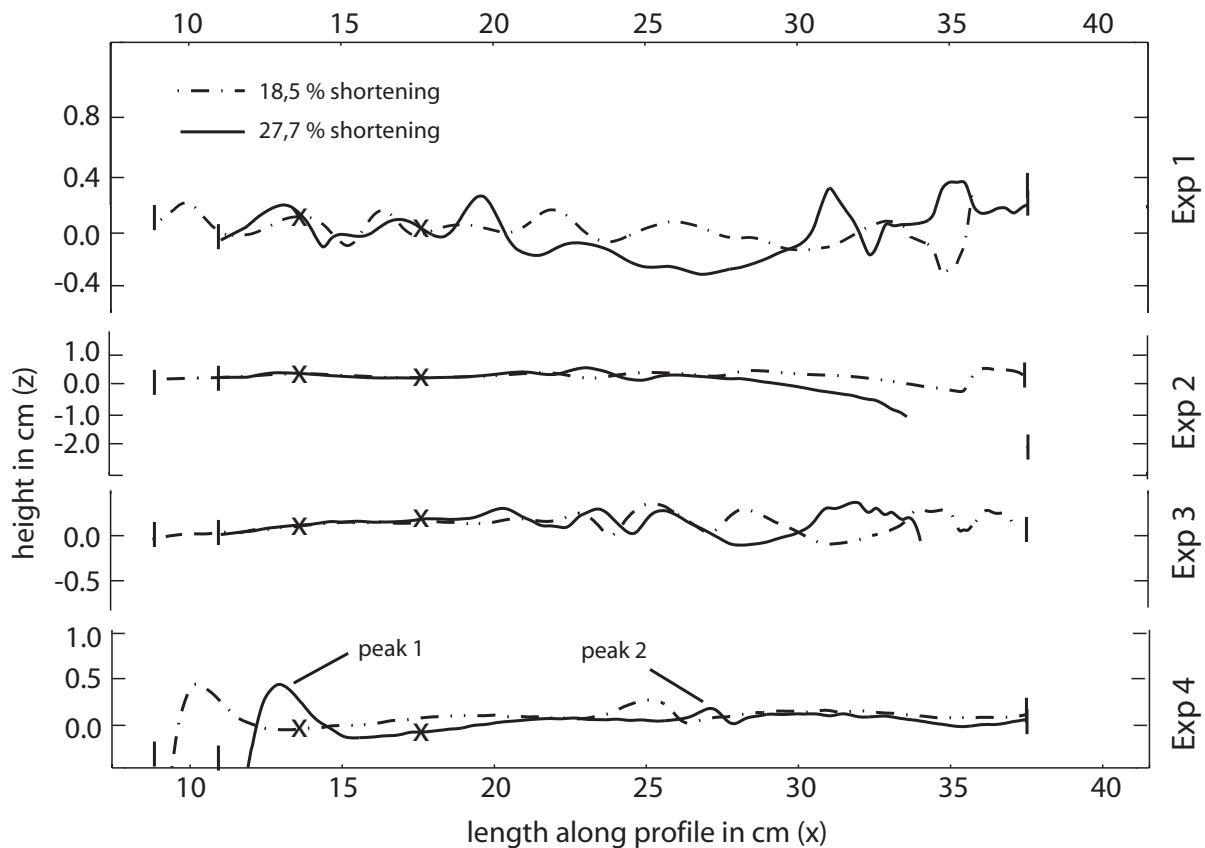


Fig. 7.6: Topographic profiles of Experiments 1, 2, 3 (non-plateau style) vs. Experiment 4 (plateau-initiation setting). For each of the experiments the elevation is plotted of one central profile (location: profile 2, Fig. 7.9a) after 18.5% shortening (stippled line), and 27.7% shortening (total amount, solid line). The plateau-initiation setting (basic setting, Exp. 4) is characterized by two final peak ridges (at 13 cm and at 27 cm) which bound a wide, flat area. Note the breaks on the y-axis, and the differences in vertical exaggeration. Crosses mark the approximate position of the boundary of vise 1 and the weak domain.

hinges with a general strike orthogonal to the direction of convergence with a slight concave curvature that bound a flat and undeformed area. This area will subsequently be part of the plateau formation process including internal drainage, uplift and sedimentary infill. The final strain pattern resembles a “phi” turned 90°.

All experiments (Exp. 3-6, Fig. 7.5c-f) have curved vises on both sides, with a convex shaped vise 1 (attached to the piston wall) and a concave shaped vise 2. Apart from Exp. 3 (Fig. 7.5c), the lower crust is non-buoyant with respect to the upper crust (Table 7.2). Exp. 4-6 (Fig. 7.5d-f) further differ from each other due to the presence of a low-viscosity silicone layer in the lower crust (Exp.

Fig. 7.5 (left): Photographs of the experimental surfaces after 27.7% of bulk shortening (convergence from top to bottom). The final area has a size of 27.5 cm (x-direction) and 45 cm (y-direction). Thrusts are partly numbered according to their appearance. The upper row of experiments shows the configurations with non-buoyant lower crust and the respective geometry of the vises (curvature and size) visible above. Rows below show experiments with a buoyant lower crust, a low-viscosity layer and a thick mantle lithosphere (a. to i. mark Experiments 1 to 9). Further details on experimental set-up and structural development in-text.

5, Fig. 7.5e), ~2 mm below its surface, simulating a zone of partial melt. This position at a depth of ~6 mm corresponds to a zone of partial melt a depth of ~16 km in nature. The weak mantle lithosphere in Exp. 6 (Fig. 7.5f) has the same thickness as that of the vises (2 cm).

In the experiment with buoyant lower crust (Exp. 3, Fig. 7.5c) strain localization begins already at 5% of bulk shortening, when the first structure develops in the center of the weak lithosphere, ~4 cm from the boundary of vise 1. The fault extends to the sides up to a distance of about 10 cm. Another fault develops on both sides 3 cm further towards vise 2, and extends from the tip of the first fault closer to the sides. Another main structure develops in the center of the weak domain, at a distance of about 8 cm from the first main feature. This last structure develops after 7% of bulk shortening, and has a similar lateral extent as the first thrust.

In contrast, strain localization in experiments with non-buoyant lower crust begins much later (e.g., after 11.5% of bulk shortening, cf. Table 7.2). In Exp. 4 (Fig. 7.5d) strain first localizes

along faults close to the piston within the weak domain both in the center and from the sides towards the center. These faults later interconnect. More thrusts develop, which extend across to the other side wall (until 27.7% of bulk shortening). The timing of strain localization and the position of both the thrusts and the undeformed area in Exp. 5 and 6 is similar to Exp. 4. However, instead of forming a more or less continuing range with a slight curvature, the curvature becomes much more pronounced as the faults form step-over zones instead of interconnecting with each other in Exp. 6 (Fig. 7.5f). They curve strongly inwards towards the side walls, so that the two ranges almost merge. The area that has been left undeformed in between these two features is wider than in Exp. 4 (Fig. 7.5d) and Exp. 5 (Fig. 7.5e).

The topographic profile of Exp. 4 (Fig. 7.6) clearly shows that plateau-initiation settings are characterized by anticlinal hinges that bound a flat and undeformed area in between. This is less obvious for the profile of Exp. 3, in which the basin area is very narrow.

7.3.2.3. Other patterns

The other experiments do not develop either of the two patterns (Exp. 8, 9, Fig. 7.5h+i), or display both patterns at the same time (Exp. 7, Fig. 7.5g).

Exp. 7 (Fig. 7.5g) has a curved vise 1 that is 30 cm wide (about 50°), and a straight vise 2 that extends all across the width of the box. Lower crust is non-buoyant. Thrusts develop at ~12% of bulk shortening (from one side towards the middle in the center of the weak domain), at ~18% of bulk shortening (in the center of the weak domain develops closer to the piston), and thereafter (extending further to the sides connecting to previous faults to form a small step-over zone). The final pattern resembles a mixture of the cross-shape and “phi”-pattern: along-strike of the set-up, the cross-shape pattern dominates from the sidewalls to the boundaries of vise 1, whereas a very narrow “phi” pattern occurs from one vise boundary to the other (Fig. 7.5g).

Exp. 8 (Fig. 7.5h) has a convex vise 1 and concave vise 2, but vises do not extend to the sides as they are only 30 cm wide (instead of 41 cm). Lower crust is non-buoyant. After ~11% of bulk shortening, thrusts localize strain in the center close to the front wall, and about ten faults of various sizes extend to the sides in en-echelon

patterns that step back close to the back wall. The final pattern therefore resembles a single curve (Fig. 7.5h).

Exp. 9 (Fig. 7.5i) has a convex vise 1 and a concave vise 2. Its lower crust is non-buoyant with respect to the upper crust for the first 7 cm inwards from vise 1, followed by 10 cm of buoyant crust, and another 7 cm of non-buoyant crust, so that two lateral density contrasts are present within the lower crust (with the two end member densities of 0.81 and 0.94 g/cm³). Strain localizes in the center of the experiment in the middle of the buoyant domain after ~13% of bulk shortening. These thrusts subsequently interconnect and develop step-over zones (Fig. 7.5i).

7.3.3. Deformation mode

The deformation modes within the viscous layers (pure shear, homogeneous thickening) are different to that observed in the granular upper crust (strain localized along faults). However, faults in the brittle crust localize within the same vertical column as lower crustal antiform-synform structures.

Based on the analysis of subsequent PIV images and the finite deformation of the viscous layers observed in model cross sections, we propose the following sequence of structural evolution (Fig. 7.7): 1) strain accumulates by pure shear of the viscous layers while deformation of the upper crust is restricted to the piston and back walls of the box; 2) strain eventually localizes as thrusts in the upper crust; 3) thrusting then creates accommodation space, so that the ductile lower crust can thicken below; and the upper crust further bulges above the thickening lower crust; 4) sedimentation from the hanging wall onto the footwall results in a sedimentary load that causes formation of footwall synclines in the lower crust; and 5) the lateral strength contrast between the sediment filled syncline and adjacent viscous crust causes thrusting on the other side of the syncline (viz., Cagnard et al., 2006).

Newtonian viscous layers (or nearly Newtonian fluids) deform homogeneously and therefore do not exhibit strain localization. It could be argued that if random heterogeneities were present within the viscous layers, they could be responsible for the formation of anticlines (by upward bulges of the lower crust), which would in turn cause strain to localize in the upper crust directly above the bulges. However,

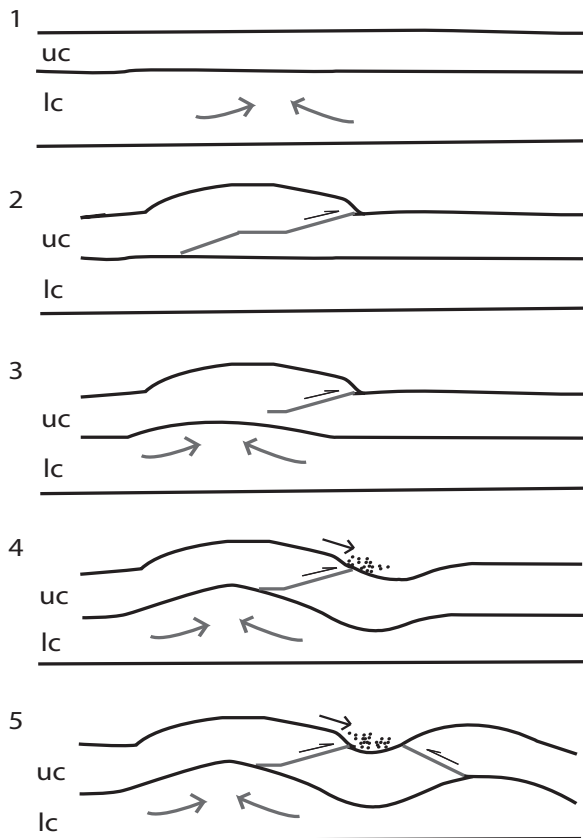


Fig. 7.7: Evolution of structures within the upper (uc) and lower crust (lc) indicates decoupling of deformation of both layers. See text for further explanation.

such a mechanism relies solely on the random distribution of heterogeneities (possibly due to mixing of material), which in turn would not be expected to develop the recurrent patterns in our experiments (e.g., the cross-shaped or “phi” patterns in Experiments 1, 2, (9) and Experiments 3-6, (9), respectively). Therefore, we conclude that the strain distribution in recurrent patterns does not result from material heterogeneities due to the model set-up, but that strain localization in the brittle layer controls the strain pattern and that deformation in the upper crust is effectively decoupled from the lithospheric mantle. Although the anticlines do not resemble periodic instabilities such as buckle folds, the driving mechanism may be similar; insofar that it is the strong brittle layer that controls and initiates the structures (e.g., Martinod and Davy, 1994).

The decoupling layer in the models is usually the lower crust; in experiments with a low-viscosity layer decoupling takes place higher up in the lower crust, along this additional horizon. Decoupling occurs only within the weak domain and not within the vises, as they do not deform significantly internally.

7.3.4. Reproducibility of experiments

The general evolution of the strain pattern can be reproduced when the same experiment run is repeated or even when second order features are varied (i.e., an additional decoupling horizon or a different strength contrast), as it is the case for experiments 4, 5, and 6. Yet, they have a comparable aspect ratio of structures. In this regard, the general distance between e.g., the anticlinal hinges is alike. Experiments also bear a close resemblance when compared with results from other analogue studies. In general, we do not aim to reproduce the exact position of every single thrust, the number of thrusts or the same timing of deformation, but the orogen scale pattern and associated aspect ratios of structures.

The cross-shaped pattern occurs in experiments by Cruden et al. (2006), in which case the system has open sides to allow for lateral extrusion. Yet, the aspect ratios and angles between structures of the “cross” are very similar. Also, experiments by Cagnard et al. (2006) exhibit a “phi” pattern, although they use a velocity discontinuity to localize strain in the center of the model. Still, the final pattern exhibits curved structures (anticline/syncline structures), that leave an undeformed area in between.

7.4. Parameter effect

7.4.1. Vise geometry

We tested both straight and curved vises (convex vise at the piston wall, concave vise on the opposite side) with a curvature angle of 20°. This curvature determined both the location and orientation of the faults, which typically form step-over zones. With straight vises, strain localizes along faults that develop from the boundaries close to the piston further inwards to the center, and moves again to the sides close to the opposite wall. The resulting pattern is “cross-shaped” (e.g., Exp. 1 and 2, Fig. 7.5a+b). With curved vises, the orientation of the step-over zones is inverted: strain localizes first in the center close to the moving vise 1, then along faults stepping over to the sides, which step in again towards the center. This pattern resembles a horizontal “phi” (e.g., Exp. 3, 4, 5, 6). Figure 7.8 shows the relation between the finite strain pattern and the approximate stress field, that we assume for the corresponding geometries (cf., e.g., Eisbacher, 1996). The structures of the upper crust are

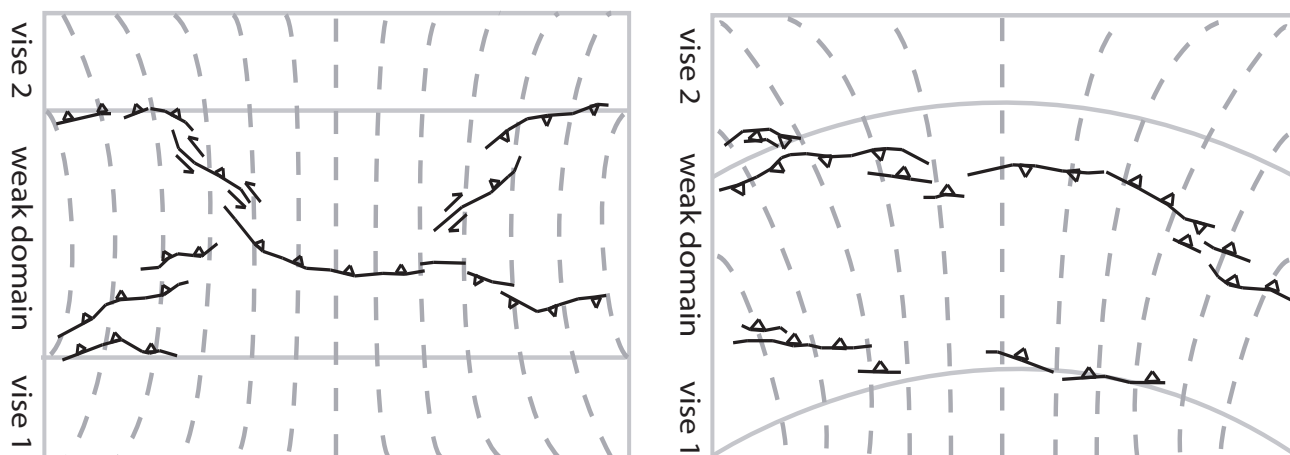


Fig. 7.8: Principal stress trajectories (dashed grey lines) approximately match the position of thrust/anticline structures in the upper crust (solid black lines), and thus explain the observed finite strain pattern: cross-shaped pattern for straight vise geometry (left) and “phi” pattern for curved vise geometry (right).

roughly perpendicular to the stress trajectories, so that the position of strain localization can readily be explained by the geometry of the vises.

If the geometry of the vises on either side of the weak domain is dissimilar/ asymmetric, both the position and orientation of faults change along-strike. Along the width of the small curved vise 1 in Exp. 7, the strain pattern resembles the “phi”-pattern. Beyond its width, the pattern is influenced by the straight geometry of vise 2, and changes from the “phi”-pattern to the “cross-shaped” pattern (Fig. 7.5g).

7.4.2. Strength contrasts

7.4.2.1. Horizontal strength contrasts

The lower crust is weaker than the mantle lithosphere, both within the vises and the weak domain. However, in most of our experiments the mantle lithosphere of the weak domain is thinner than the mantle lithosphere of the vises. Only in Exp. 1 and Exp. 6 do the weak and the strong mantle lithosphere have the same thickness (2 cm instead of 1 cm). The thickness of the layers has an influence on the integrated strength and therefore on the lateral contrast.

Experiments with relatively thick mantle lithosphere result in a wider final deformation pattern than other experiments. The anticlines are spaced much farther apart in Exp. 6 (Fig. 7.5f), than for instance in Exp. 4 (Fig. 7.5d) and Exp. 5 (Fig. 7.5e). Thus, the thickness (Exp. 1, 6) or in turn an increased horizontal strength contrast controls the spacing of the deformed zones, changing the pattern and position of strain localization, which becomes more widely distributed with increasing lithospheric thickness.

An additional low-viscosity layer enables decoupling (Exp. 5, Fig. 7.5e) at a higher level than in experiments without this layer, in which decoupling occurs in the weaker lower crust (e.g., Exp. 4). Depending on the position of the decoupling horizon, the crust below it undergoes pure shear, and does not participate in the anticline formation. Interestingly, the final orogen scale strain pattern is very similar, either with or without an additional decoupling horizon. This suggests that decoupling effectively takes place at similar depth in the lower crust when no additional decoupling horizon is introduced.

7.4.2.2. Lateral strength contrasts

In order to accumulate strain solely within the weak part of the lithosphere rather than within the vises, the vises must be stronger than the weak domain. Viscosity ratios between the strong and the weak equivalents in our experiments have values of about 2.2 for the lower crust, and 6.2 for the mantle lithosphere. These ratios are rather low, as the viscosities for both the weak domain and the vises are on the same order of magnitude, indicating a relatively small strength contrast between the weak domain and the strong vises. Yet, these ratios are sufficient to accumulate strain within the weak domain and not to deform the vises.

If no strength contrast is present between the vises and the intervening domain, the homogeneous material of the weak lithosphere should deform similarly to the experiments of Martinod and Davy (1994), in which periodic instabilities (buckling) occurred simultaneously throughout the model. The thrust pattern observed

in experiments by Cagnard et al. (2006) also resembles ours, although they used a velocity discontinuity to initiate strain localization in the center of their experiments.

7.4.2.3. Length of structural units

If the length of the weak domain is reduced, the potential area for strain accumulation becomes smaller, and it is likely that only one structure will develop in the center, even with non-buoyant crust (cf. Section 7.4.2.2.). Sufficient initial space is therefore needed to accommodate at least two anticlinal hinges that can preserve a basin, which is necessary for plateau initiation. Willingshofer et al. (2005) included a weak zone that had a length/thickness ratio of 3.34 (10:3) and 4 (10:2.5). In neither case was a basin captured for plateau initiation. In our experiments, the length/thickness ratio for the buoyant area in Exp. 9 (Fig. 7.5i) was 4.54 (10:2.2). In all other experiments, the length/thickness ratio was much higher, between 7.5 (24:3.2, Exp. 1+6, Fig. 7.5a+f) and 10.9 (24:2.2, all other experiments). The critical length of the structural unit is dependent on the thickness, which determines the integrated strength of the weak domain. The critical length/thickness ratio for the weak unit must be above a value that lies between ~5 and 7.5. We cannot exclude that, for basin capture to occur, this value is further coupled to the ratio of total length of the set-up and to the width of the units. In our experiments, the weak domain makes up 63% of the total length of the set-up, compared to 100% in Cagnard et al. (2006), who did not employ stronger vise blocks. In contrast, the weak zones in Willingshofer et al. (2005) comprised only 25% of the total length.

If the accommodation space is too small, material could also thrust over the vise blocks (“water bed effect”, Cruden et al., 2006), which themselves would bend downwards beneath the weak domain.

7.4.3. Buoyancy

Two strong end members are used for the density of the lower crust to better evaluate the effect of buoyancy. We are aware of the fact that their densities are rather high (non-buoyant case) or rather low (buoyant case), when scaled back to nature (cf. Table 7.1).

When the lower crust is buoyant it tends to bulge upwards due to density inversion. This behaviour promotes strain localization in the

upper crust, which occurs at early stages of convergence (e.g., after 5% of bulk shortening, Exp. 2, 3), whereas strain localization in the upper crust typically does not start until about 12% of bulk shortening in non-buoyant experiments (with 27.7% being the total amount). Also, the mode of strain accumulation within the viscous layers is different: with a buoyant crust, homogeneous thickening dominates in the mantle lithosphere, whereas with non-buoyant crust thickening occurs in the weak lower crust.

In general, the effect of a buoyant lower crust is to enhance strain localization in fewer structures, which are positioned within the center of the weak domain. Non-buoyant crust tends to localize strain along numerous thrusts, which are more distributed and have wider spacing (viz., Cruden et al., 2006). This is particularly well observed in Exp. 9 (Fig. 7.5i), where one area of buoyant lower crust is located in between two non-buoyant lower crustal domains. Here, the structure develops in the middle of the buoyant area. It extends almost perfectly perpendicular to the direction of compression, thereby remaining in the buoyant domain. Similarly, the cross-shaped pattern in Exp. 1 (non-buoyant lower crust, Fig. 7.5a) occurs over a wider area than for example in Exp. 2 (buoyant lower crust, Fig. 7.5b), in which deformation localized on a smaller area.

In order to initiate the formation of a plateau, deformation must localize not only at one dominant structure in the center, but along two or more structures that entrap an intervening basin. This is only possible when the crust is non-buoyant. This counterintuitive result reflects the importance of the buoyancy on the timing and location of strain accumulation for plateau initiation.

7.5. Comparison of three experiments with plateau-initiation

In the following, we compare characteristics of the three experiments that exhibit basin capture and plateau initiation (Exp. 4, 5, 6), and examine the along-strike variation of the orogen scale pattern, i.e., differences on the suborogen scale.

In all plateau-style settings (Fig. 7.9a+b), the model possesses a non-buoyant, weak lower crust and a sufficient strength contrast between the curved vises and the weak domain (viscosity ratios between the strong and the weak mantle lithosphere are around 6). Exp. 4 (Fig. 7.5d) is referred to as the “basic setting”, Exp. 5 (Fig.

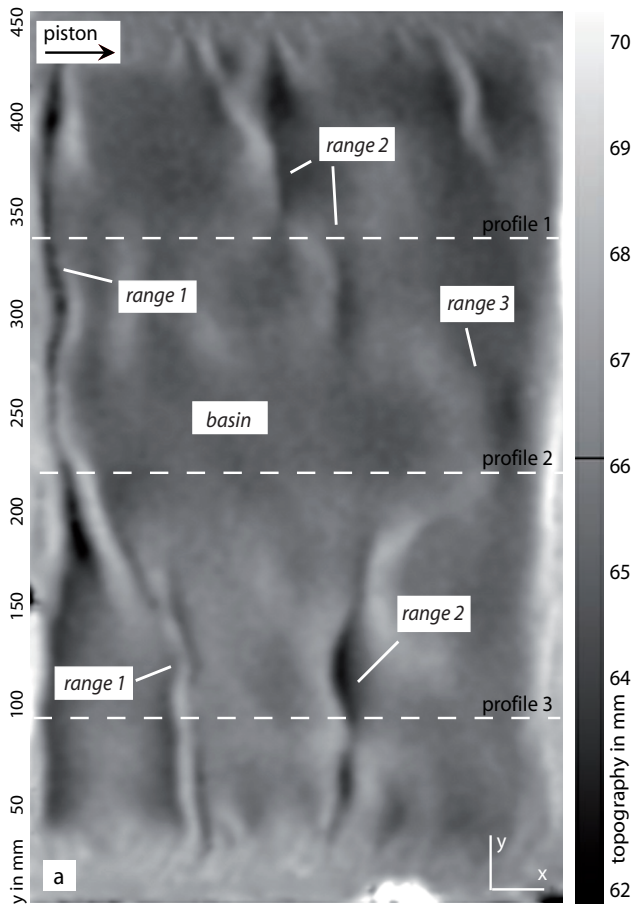


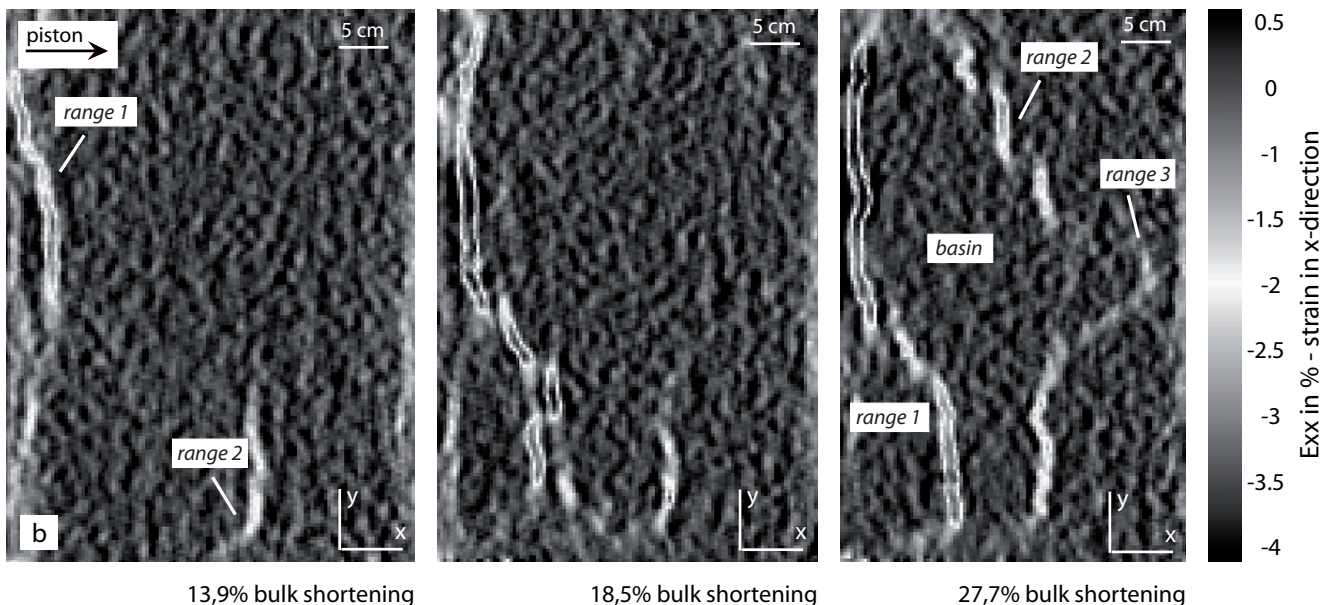
Fig. 7.9a (top), b (bottom): a) Topography of the final surface of Exp. 4 after 10.5 cm of convergence as recorded by PIV. Light colours indicate high elevation, dark colours subsided areas. Both anticlinal ranges (range 1 and range 2) bounding the basin area are delineated by elevated thrusts/anticlines (white). The initial surface was at a height of 63 mm. White dashed lines depict location of three profiles. b) Strain accumulation (% of strain in x-direction) of Exp. 4 as recorded by PIV. Light colours outline regions of high strain. Thrusting in the upper crust starts at ~11.5% of bulk shortening, and two peaks (range 1 and range 2) develop that bound an undeformed area (basin).

7.5e) has an additional low-viscosity layer (“LVL setting”), and Exp. 6 (Fig. 7.5f) has a thick weak mantle lithosphere (“thick setting”).

In all three settings strain is accumulated by thrusts within the upper crust, cusp-shaped hanging wall anticlines bounded by deep synclines in the weak lower crust (Fig. 7.7), as well as thickening of both the lower crust and the mantle lithosphere. The vises themselves remain undeformed. For the three plateau-initiation settings, we further describe differences in 1) time series of strain accumulation at the surface (Fig. 7.10), 2) topographic profiles orthogonal to the weak domain (Fig. 7.11a+b), and 3) the finite strain accumulation within the viscous layers (Fig. 7.12). The location of the profiles is marked in Figure 7.9a, and is the same for each of the three experiments.

7.5.1. Differences in plateau style: strain distribution profiles

The three plateau-initiation settings display pronounced differences in strain evolution. High strain accumulation is coloured black. Thrusts are pointed at by little arrows. Fault zones in the “basic setting” are narrow and discrete, with a spatially homogeneous strain accumulation (Exp. 4, profiles 1 to 3, Fig. 7.10). In contrast, the “LVL setting” has wide fault zones, which have a diffuse margin around a dominantly accumulating core (Exp. 5, profiles 1 to 3, Fig. 7.10). Even more diffuse are the fault zones of the “thick setting”, with small dominant cores that are surrounded by areas of reduced strain accumulation (Exp. 6, profiles 1 to 3, Fig. 7.10). This probably occurs because more strain can be accumulated within the thicker



13,9% bulk shortening

18,5% bulk shortening

27,7% bulk shortening

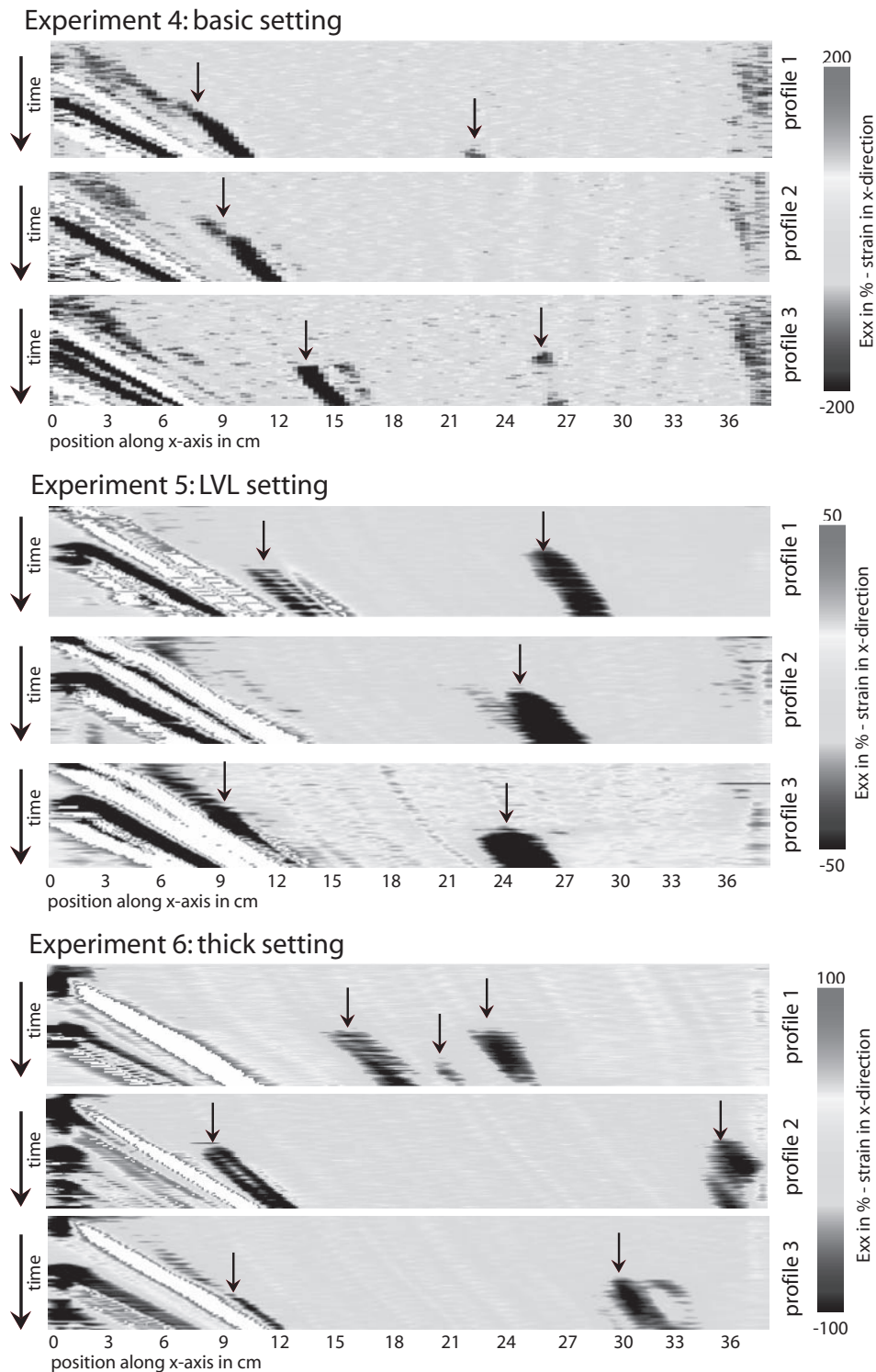


Fig. 7.10: These time series through plateau-initiation settings (Exp. 4, 5, 6) show strain data along profiles crossing the surface area similar to the strain surfaces of Figure 7.9b. The profiles for each time step are plotted below each other, so that the figures are read from top to bottom as time increases. Convergence increases from left to right; thus the motion of the piston is reflected by the oblique white patch with respect to the position along the x-axis. Dark colours depict fault zones with very high strain accumulation (Exx), indicated by small arrows. Depending on the position of structures, we can infer both the temporal and spatial (along a profile) strain accumulation within one experiment. Further explanation in-text.

mantle lithosphere.

In general, all of these settings develop two main thrusts (which bound the basin area) in which strain accumulates. In the basic setting, the first thrust close to the piston accumulates more strain than the second. The latter accumulates

strain in discontinuous pulses (interruption of “black” high strain periods by “light” low strain periods). A similar but less pronounced effect can be observed in the LVL setting, in which the second thrust is more dominant. The thick setting does not contain a dominant structure, but strain

7. The effect of mechanical heterogeneity on plateau initiation

accumulation switches back and forth between the two main thrusts. In general, both thrusts appear to accumulate the same amount of strain (e.g., Fig. 7.10, profile 1, Exp. 6).

“Secondary” faults also occur in both the basic (Exp. 4, profile 2) and the thick setting (Exp. 6, profiles 1 to 3). These are faults that are located “behind” another fault and accumulate less strain

than the main faults closer to vise 1. In the thick setting secondary faults are more pronounced and also more diffuse in both geometry and timing of strain accumulation.

The spacing of the main thrusts differs along-strike. In general, the spacing is narrower in the basic setting than in the LVL setting. This can be attributed to the fact that the LVL is a

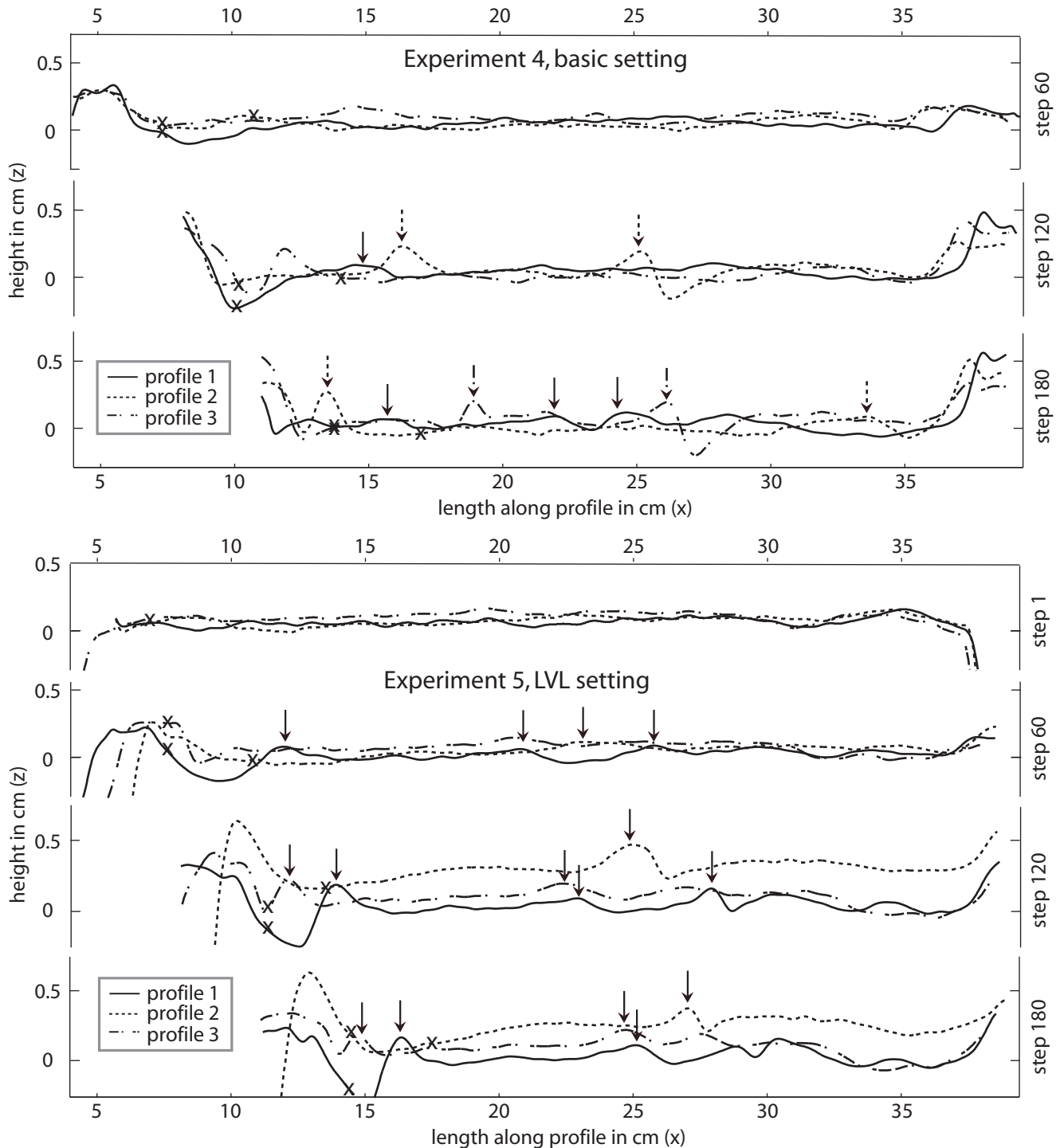


Fig. 7.11a (top), b (bottom): a) Topographic profiles of the basic setting. For each of the three profiles of Exp. 4 (location in Fig. 7.9a), three time steps are shown (60, 120, and 180 equaling 9.2%, 18.5% and 27.7% of bulk shortening). Further explanation in-text.

b) Topographic profiles of the LVL setting (Exp. 5). The four time steps (60, 120, and 180 equaling 9.2%, 18.5% and 27.7% of bulk shortening) are depicted together for all three profiles (profiles 1, 2, 3; location in Fig. 7.9a). Crosses indicate the approximate position of the boundary between vise 1 and the weak domain. Arrows point to the main anticlinal hinges.

decoupling horizon weaker than the “basic” lower crust allowing coherent displacement of wider thrust sheets towards the foreland.

Pronounced differences do not only occur from one experiment to the other, but within one setting. In this regard for example, both the number and position of primary and secondary faults change along-strike in the “thick setting”, and thus also the spacing and the amount of strain accumulated by individual faults. The spacing is either very small (Exp. 6, Fig. 7.10, profile 1) close to the sides, or very large in the center (Exp. 6, Fig. 7.10, profile 3).

7.5.2. Differences in plateau style: topography

The topographic evolution is strongly linked to the strain evolution, as thrusts and anticline-syncline structures typically represent areas of local relief. Thus, the above differences in strain evolution along-strike within one experiment also apply to the development of topographic relief. Figure 7.11a plots differences in topography for the basic setting; in profiles 1, the main ridges are widely spaced whereas they are closer together in profile 3.

The initiation of topography development coincides with strain localization. The spacing of topographic features in the LVL setting (Fig. 7.11b) is more or less constant along-strike. This occurs although the elevation of the area between the main ridges differs. The undeformed areas crossed by profiles 2 and 3 (Fig. 7.11b) have experienced uplift, whereas profile 1 has experienced subsidence with respect to the initial surface. In general, subsidence of the undeformed areas is common, which is part of the plateau-initiation process.

7.5.3. Differences in plateau style:

3D thickening of the lithosphere

About ten cross sections were made of each experiment (five inward from each side in 2-3 cm steps) and the thicknesses of both the lower crust and the mantle lithosphere of the weak domain were measured. The change in thicknesses are plotted and contoured in Figure 7.12. When plotted on top, structures in the upper crust roughly bound areas of homogeneously thickened viscous layers. In general, the location of pronounced thickening is similar in both the lower crust and the mantle lithosphere, with local deviations where a low in the mantle lithosphere coincides with a region of increased thickness of the lower crust (e.g., Fig.

7.12, Exp. 5, LVL setting).

The amount of strain that is accumulated in the different layers varies: in the basic setting (Fig. 7.12, Exp. 4), depending on the location, the initial thickness of the mantle lithosphere increases by 50-100%, and of the lower crust by 10-20%. This is similar in the thick setting (Fig. 7.12, Exp. 6), where the mantle lithosphere has increased by 50% and the lower crust by 10-20%. In contrast, the LVL setting (Fig. 7.12, Exp. 5) has experienced only a 25-50% increase in mantle lithosphere thickness, and between 10% of thinning (first half of the weak domain, closer to vise 1) to 10% of thickening in the lower crust (in the second half towards vise 2). This can be attributed to the fact that the LVL acts as a decoupling horizon at a high level within the lower crust. The material within the lower crust below this horizon does not accumulate much strain. Therefore, the volume of material that can thicken is less than in the other plateau-initiation settings, and is mainly restricted to the volume above the decoupling horizon.

The location of crustal thickening is also dissimilar for the three models. In the basic setting (Exp. 4), the thickness decreases away from the piston. In the LVL setting (Exp. 5), strain is accumulated in the far half of the weak domain, closer to vise 2, which again can be explained by the decoupling layer within the lower crust.

In the mantle lithosphere of the thick setting (Fig. 7.12, Exp. 6), strain accumulation is most pronounced at the boundaries with the vises. This suggests that the lithosphere is likely to thicken closer to the boundary of the weak domain and the vises, i.e., the mechanical anisotropy, when the strength contrast is low. When it is high, viscous layers thicken more homogeneously in the center of the weak domain, as is the case for the LVL setting.

7.6. Discussion

7.6.1. Parameter control

Plateau initiation includes the formation of at least two mountain ranges that are separated by an undeformed area (e.g., Fig. 7.9a+b), which is a basin prone to undergo sedimentary infill due to internal drainage resulting in surface uplift (e.g., Meyer et al., 1998; Sobel and Strecker, 2003; Sobel et al., 2003) (cf. Fig. 7.1). Typically, such mountain ranges do not form in fold-and-thrust belts where one range develops close to and after another as strain and evolving thrusts propagate

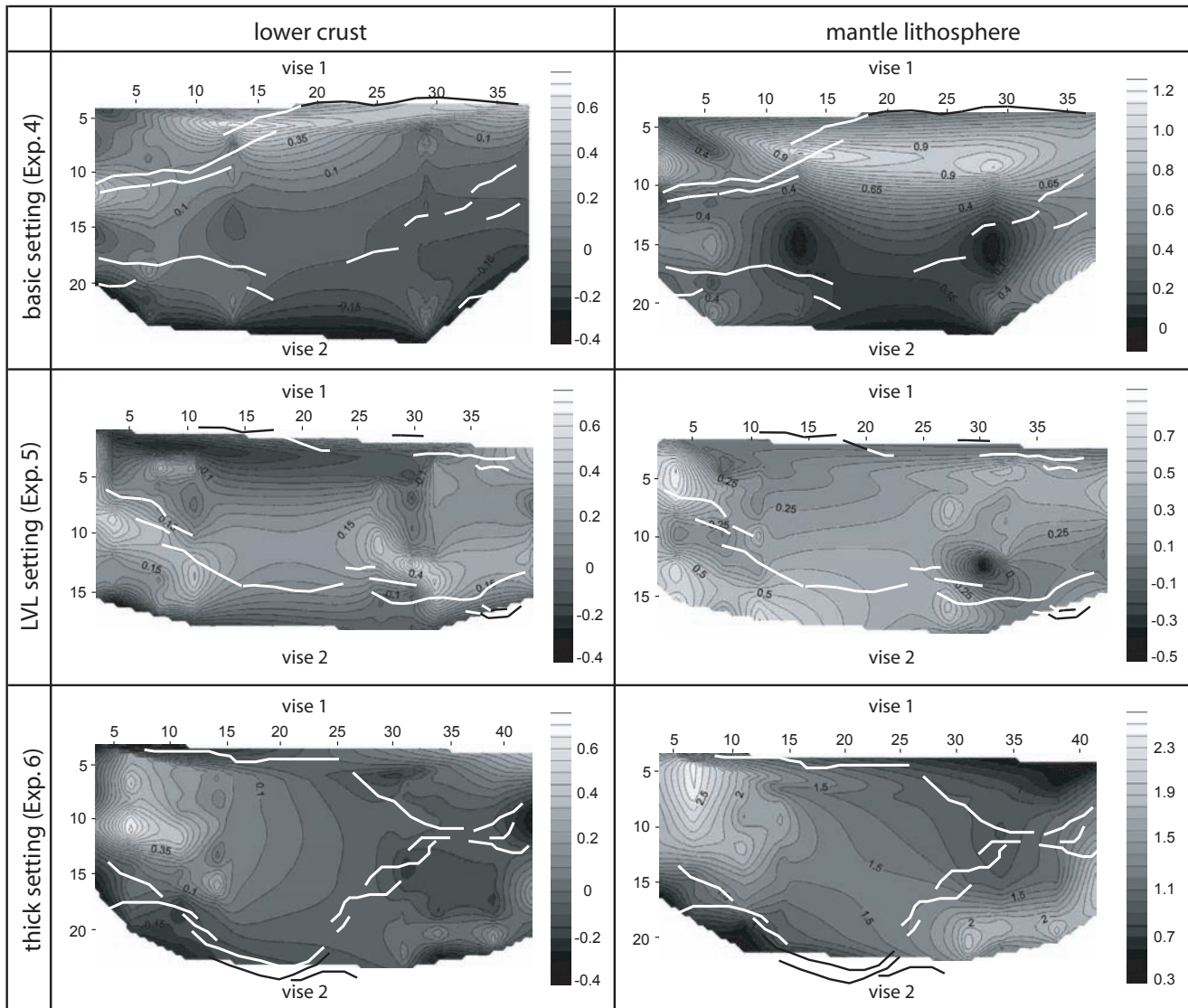


Fig. 7.12: Increase in thicknesses of viscous layers in centimetres (left: lower crust, right: mantle lithosphere) for the three plateau-initiation settings (top: basic setting (Exp. 4), centre: LVL setting (Exp. 5), bottom: thick setting (Exp. 6)). Note that colour palettes differ slightly for each of the figures. Structures (thrust/anticlines) of the upper crust are marked with white and black lines. Further description in-text.

towards the foreland, and hence do not leave enough accommodation space for basin infill and do not in general produce plateaux. In contrast, decoupling of deformation in the upper crust from the lower crust or the upper mantle reduces frictional resistance at the base of the upper crust and, hence, allows displacing longer coherent slabs before their strength limit is reached, which is the key prerequisite for plateau initiation.

The initial strain pattern required for subsequent plateau growth only occurs when all of the following parameter conditions are met:

1. The vertical layer density stratification must be gravitationally stable (non-buoyant crust with respect to the upper crustal parts) to enable strain localization with spacing several times the thickness of the upper crust.

2. A lateral strength contrast between the

strong portions of lithosphere enclosing a weaker part must be present.

3. The lateral contrast between the weak domain and the vises must be sufficient to localize strain solely in the weak domain. If it is too strong the whole weak domain buckles at once, with the first buckle localizing close to vise 2, in which case only one anticlinal range develops with no entrapped proto-basin (see Willingshofer et al., 2005).

4. The weak domain must be long enough to allow strain accumulation in two locations. The critical threshold for the length/thickness ratio is above a value between ~ 5 and 7.5.

5. The geometry of the strength contrast must be curved for both vises (convex vise 1, concave vise 2) to enable the localization of two laterally linked anticlinal ranges that enclose

accommodation space for an intervening basin. With reduced curvature and in an open system, the width of the deformational system could in principle grow to very large values, precluding the trapping of closed basins. This probably occurs with length-width ratios <0.6 (e.g., Exp. 1 and 2, and experiments by Cruden et al. (2006), which allow lateral extrusion).

Although a lack of buoyancy of the lower crust appears as a necessary condition (1. point) for a basin area to be entrapped between the anticlines, such an area also develops with buoyant lower crust and curved visé shape (Exp. 3), but it is very narrow. The next three points above (2-4.) hold for all of the experiments. Yet, two different strain patterns (the “cross-shaped” and the “phi”) can be distinguished, which depend solely on the geometry of the lateral strength contrast. As it has not been demonstrated if the cross-shaped pattern can develop captured basins in a larger experimental set-up, we assume that the most crucial parameter in our experiments for the development of a strain pattern that enables subsequent plateau initiation is the curvature of the visés. The geometry of the visés changes the corresponding stress field, whose stress trajectories roughly match the position of structures of the upper crust (which are perpendicular to the trajectories, Fig. 7.8) and can therefore explain the resulting finite strain patterns.

The spacing between anticlinal hinges is influenced by the thickness of the weak domain. If the lithosphere is thicker (e.g., similar thickness of weak and strong crust, Exp. 6), fold hinges are farther apart than when the lithosphere is only half the thickness of the visés. This effect is similar to spacing relations in the upper crust (e.g., Mulugeta and Koyi, 1992; Koyi, 1995; Morellato et al., 2003), which depend on the thickness of the deformed layer, and also on the basal and internal friction of the layer. The latter can be regarded equivalent to the integrated strength of the units. Unlike typical fault spacing in e.g., fold-and-thrust belts, the spacing between the anticlinal hinges in plateau initiation settings varies along-strike: the maximum distance between the anticlinal hinges is typically in the center, which decreases towards the sides, so that the captured basin is “closed off” (cf. Fig. 7.5d-f).

7.6.2. Application to the Andean plateau

The Central Andean plateau comprises

four main structural units from west to east: the Western Cordillera, the highly elevated plateau area (Altiplano-Puna), the Eastern Cordillera and the Subandean fold-and-thrust belt (Fig. 7.2). The main characteristics on the orogen scale are two mountain ranges (the Cordilleras) that bound the flat and rather undeformed plateau area in between (e.g., Isacks, 1988). External to this “orogenic system” is the fold-and-thrust belt, which formed once the plateau had become stable (e.g., Allmendinger and Gubbels, 1996).

When looking at scales smaller than the orogen itself, we observe flat and undeformed areas that are bounded by adjacent ranges (Fig. 7.2) similar to our experiments. These undeformed areas are not necessarily plateau areas yet, but rather marginal basins that are in the process of being internally drained (e.g., in the Puna: Sobel and Strecker, 2003; Sobel et al., 2003). After “regional” plateau initiation, these features are incorporated into the “orogenic-scale” plateau (e.g., Mortimer et al., 2007). Thus, some of these basins are not yet at the stage of attaining a highly-elevated plateau region, but are still in the plateau-initiation phase, as e.g., for the Sierras Pampeanas region. Subsequently, the area will internally drain, uplift and be filled with sediments, and thus be incorporated as “regional” plateau areas in the orogenic plateau of the Puna.

Our experiments resemble these plateau initiation settings, in which two ranges allow the preservation of a peneplain, which may undergo basin-like subsidence or uplift. The topographic relief in our models is unrealistically high when scaled back to nature, but this is due to the lack of erosion. Therefore it is likely that significant amounts of debris from adjacent ranges can produce the infill for the initial basin in our models as observed in the northern Sierras Pampeanas in Argentina (Sobel and Strecker, 2003), if we were to model erosional processes with tectonic river cut-off and internal drainage.

Critical parameter combinations must be met early on in the system for a plateau-style system initiation, which includes a normal crustal density profile, a lateral strength contrast with a critical curvature (the hot back-arc region is compressed between the strong and cold “pseudo-indenting” fore-arc to the west (Victor et al., 2004; Tassara, 2005) and the thick cold Brazilian shield to the east (e.g., Sobolev and Babeyko, 2005), both with curved in-plane geometries, see Fig.

7.2), a decoupling horizon within the lower crust (a zone of partial melt or weak lower crust beneath the Altiplano-Puna plateau; Yuan et al., 2000), and a sufficient initial width. Isacks (1988), Kay and Kay (1993) and Allmendinger et al. (1997) have all proposed that thermal weakening of the crust or delamination of the mantle lithosphere are necessary prerequisites of plateau formation.

The fact that we observe variations in strain partitioning mode, topographic relief and the extent of peneplains on several scales below the orogen scale in our models, emphasizes the observation that internal basin drainage and plateau initiation occurs on scales ranging between 400 km (e.g., for the Altiplano basin) down to scales <100 km (e.g., smaller basins in the Puna and the Sierras Pampeanas, cf. Fig. 7.2). Also, it reproduces local along-strike differences in, for example, elevation or spacing of structures.

7.6.3. Previous modelling studies

Most modelling studies focus on the effect of one parameter on the formation of a plateau -and not the plateau initiation- (e.g., thermal perturbation within the lithosphere (Wdowinski and Bock, 1994a+b); crustal flow (Royden 1996), gravity-driven channel flow (Husson and Sempere, 2003), flow indentation of the lower crust (Gerbault and Willingshofer, 2005), mass flux along a detachment (Vietor and Oncken, 2005)), rather than the influence of coupled parameters (e.g., the combined influence of crustal thickness and interplate friction, Sobolev and Babeyko, 2005). Analogue experiments by Schemmann and Oncken (under review) are the first to reproduce not only e.g., the final stage of the plateau-style setting, the finite strain pattern or the topographic evolution, but the development of orogen scale deformation in time and space for the Central Andean plateau, as well as the strain evolution of single faults of the structural units. This requires that two parameters of mechanical heterogeneity are coupled (namely internal and basal strength contrasts), for which Schemmann and Oncken (under review) pinpoint critical threshold values. These determine the deformational type that will form, i.e., a plateau-style or a wedge-like system.

One of the advantages of their analogue set-up is the implementation of granular media. This allows the successive test of different materials to precisely set the limits for critical threshold values without changing the stress scaling factor. At the

same time, modelling only the brittle upper crust without taking isostatic effects (e.g., buoyancy) into account, as well as decoupling the crust from a stiff base, imply limiting boundary conditions.

This study compensates for previous shortcomings by employing viscous and brittle media in a 4-layer set-up that accounts for more complexity similar to nature, dynamic scaling, pure and simple shear, and more effects such as strain rate and isostasy etc. Thus, more parameters than only two can be coupled (e.g., strength contrasts (internal and basal), buoyancy effects, lithospheric thickness, and plate geometry).

Schemmann and Oncken (under review) are able to resolve below the orogen scale, namely single faults in each structural unit. However, plateau formation was active only on the orogen scale. In contrast, this study can show that the same process, namely plateau initiation, is active on the orogen scale but at the same time also on scales below. In addition, we can examine the effect not only of first order features on scale related deformation and its variation but of second order parameters as well. These variations can be analyzed in the strain evolution, the development of topography and the finite crustal thickness.

7.7. Conclusions

Through 4-layer brittle-viscous analogue experiments, we conclude that the development of plateau-style settings only begins when the starting conditions follow a parameter combination that includes a critical lateral strength contrast between the strong bounding blocks and the intervening weak domain (the strength of the strong units should be at least twice the strength of the weak equivalent, but likely not more than ten times), a curved geometry of the vise blocks (convex vise 1 and concave vise 2), a decoupling horizon within the lower crust of the weak domain, and a non-buoyant lower crust.

Anticline-syncline structures and thrust faults that develop at their inflection points occur in all experiments. However, the necessary distance between the structurally controlled topographic ranges required for the preservation of an enclosed peneplain is only possible under the above conditions. This scenario can subsequently be subject to internal drainage, which is the next condition to the formation of a plateau. If we increase the thickness of the mantle, the surface pattern predicts even wider spacing of active

structures bounding basins and hence wider plateaux.

Along-strike of the main ranges, variations in strain evolution, topography and finite crustal thickness occur not only within one experiment, but also when comparing the three different plateau-initiation settings. This suggests that basin capture between tectonically active structures occurs at several scales, similar to small-scale basins in the Sierras Pampeanas (e.g., Sobel and Strecker, 2003, Mortimer et al., 2007) or larger basins like the Altiplano basin.

Acknowledgments

This work is part of KS' PhD thesis, funded by a grant from the "Studienstiftung des deutschen Volkes" (National Merit Foundation), who additionally sponsored her research visit to the Tectonophysics Laboratory at the University of Toronto. ARC acknowledges funding from the National Sciences and Engineering Research Council of Canada.

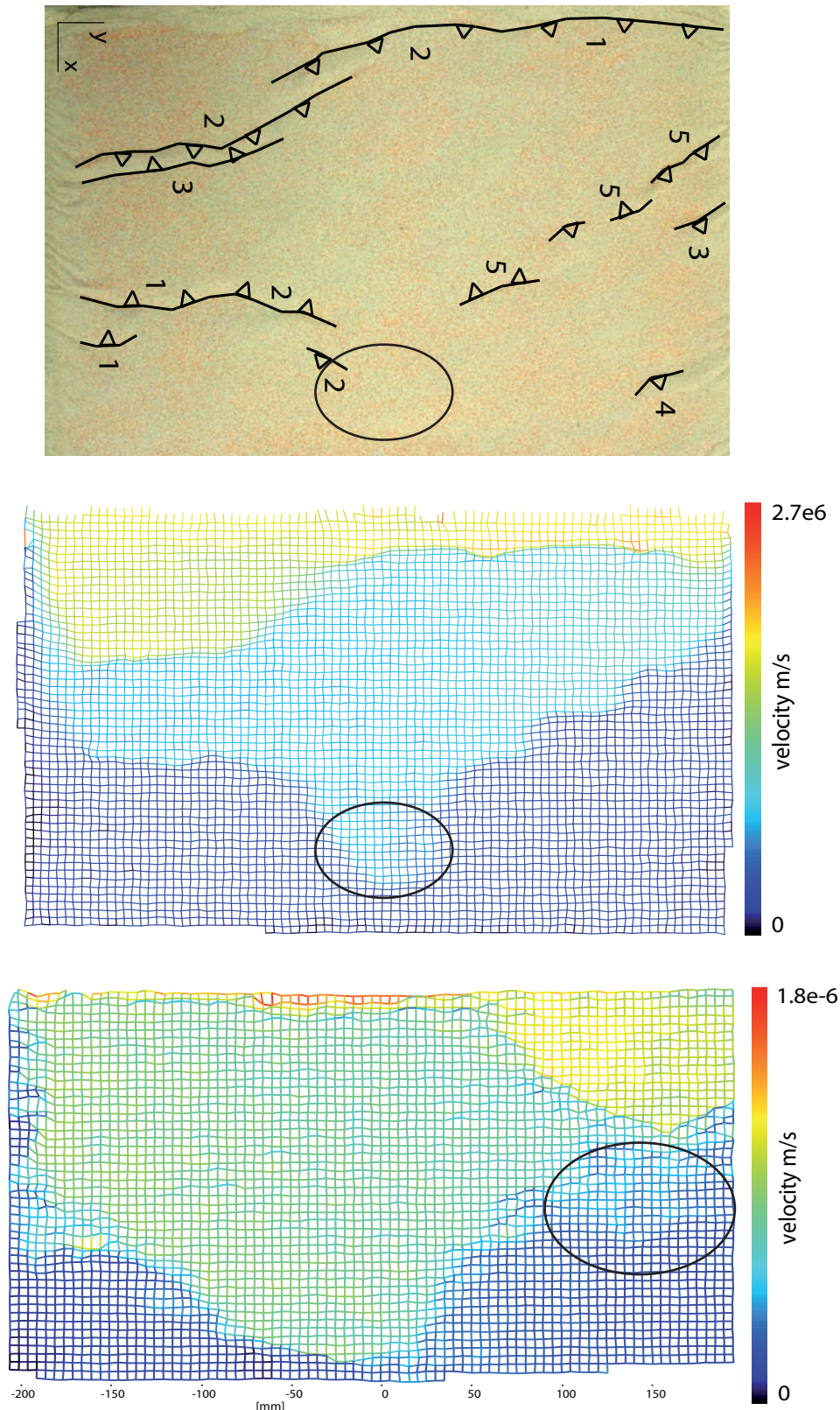


Fig. 8.1a (top), b (center), 8.2 (bottom): a) The experimental surface in top view shows the finite strain pattern after 27.7% of bulk shortening with thrusts numbered in order of appearance. Convergence was in x-direction (from top to bottom). The finite dimensions are 28 cm (x) and 42 cm (y); b) The incremental velocity field of the final stage of Exp. 4 (cf. Chapter 7). The colour contrasts are velocity contrasts, which have sharp boundaries (marked in Fig. 8.1b) and outline the structures where strain localizes (thrusts in Fig. 8.1a, marked). Velocity contrasts indicate the positions of structures before they have actually formed; (cf. Fig. 8.1a); Fig. 8.2: The incremental velocity field of the final stage of Exp. 6 (cf. Chapter 7). Velocity contrasts have diffuse boundaries (marked) unlike Fig. 8.1b. Due to the lack of sharp contacts, the position of future structures cannot be made out beforehand.

8. Additional analogue data

Extensive data sets result from the PIV monitoring of the physical simulations. In the following I point out some interesting data that could be subjects for future studies, as they deal with 1) the variation of deformation modes in time and space (e.g., strain hardening and strain weakening), 2) the aspects of uncertainty due to incomplete data resolution, e.g., for velocity fields, and 3) the interaction and variation of strain accumulation along structures within profiles orogen-normal and orogen-parallel over time.

1) Figure 8.1a shows the real experimental surface, Figure 8.1b the corresponding incremental velocity field of the final stage after 27.7% of bulk shortening (Exp. 4, cf. Chapter 7). Colour contrasts mark locations of velocity changes, where faults localize (i.e., thrusts with oblique components in step-over zones). These velocity contrasts are sharp in Figure 8.1b, and rather diffuse (marked) in the incremental velocity field of Exp. 6 in Figure 8.2 (cf. Chapter 7). Due to this diffuseness the exact position of faults could not be located from the velocity contrasts in the incremental velocity field.

Another obvious feature is the missing coincidence of velocity contrast or gradient development with the actual formation of structures that are visible at the real surface. Instead some time elapse between a diffuse velocity contrast (marked in Fig. 8.1b) and the actual strain localization (marked in Fig. 8.1a) can be noticed. This may be interpreted in terms of initial strain hardening (diffuse strain accumulation) and subsequent strain weakening (localized deformation). A future study should involve an analysis of the time elapsing between stages of different deformation modes.

2) Without proper spatial resolution of the velocity data, velocity contrasts and therefore the structures cannot be precisely located. This problem is also depicted in Figures 8.3 and 8.4 showing that a given dataset can be variously interpreted when the spatial coverage between the data is incomplete. A similar problem can arise for GPS data: without the appropriate GPS station coverage, the data cannot be used for the prediction of deformation events or future structures. However, we have to bear in mind that GPS data also include the elastic component of deformation and record

velocity fields for much shorter time spans that are not sampled by the analogue incremental velocity data. Also, lithospheric deformation in nature is certainly more complex than the strain accumulation in the models.

3) Strain data were extracted along profile 1300 (cf. Fig. 8.5 for location) for all 180 time increments equalling 40 Ma in nature, and compiled into a time series of strain profiles (Fig. 8.6). Time increases from top to bottom, and the piston advances from left to right. This motion over time causes all structures to appear obliquely. Strain accumulation is high for dark colours, and low for light grey colours. Thus, the presence of light colours horizontal within dark structures (“zebra pattern”) shows that strain accumulation is not continuous over time, but that there are phases when no or only little strain is accumulated. We can study this variation over time and how the active structures correlate when plotting the incremental vector displacement for some points along the profile (1300) and other profiles (1240, 1270, 1330, 1360, 1390) in a different plot (Fig. 8.7). Figure 8.8 gives an idea how strain accumulation varies along-strike of the orogen within a given structure.

Such temporal patterns might show scale-dependent stages of deformation, each possibly following a particular deformation mode which could also give more information on the underlying deformation framework. In that respect, strain weakening effects are characteristic for the “continuum-Euclidean” framework, strain hardening effects for the block model, and both effects in balance for the fractal complexity (e.g., Ben-Zion and Sammis, 2003).

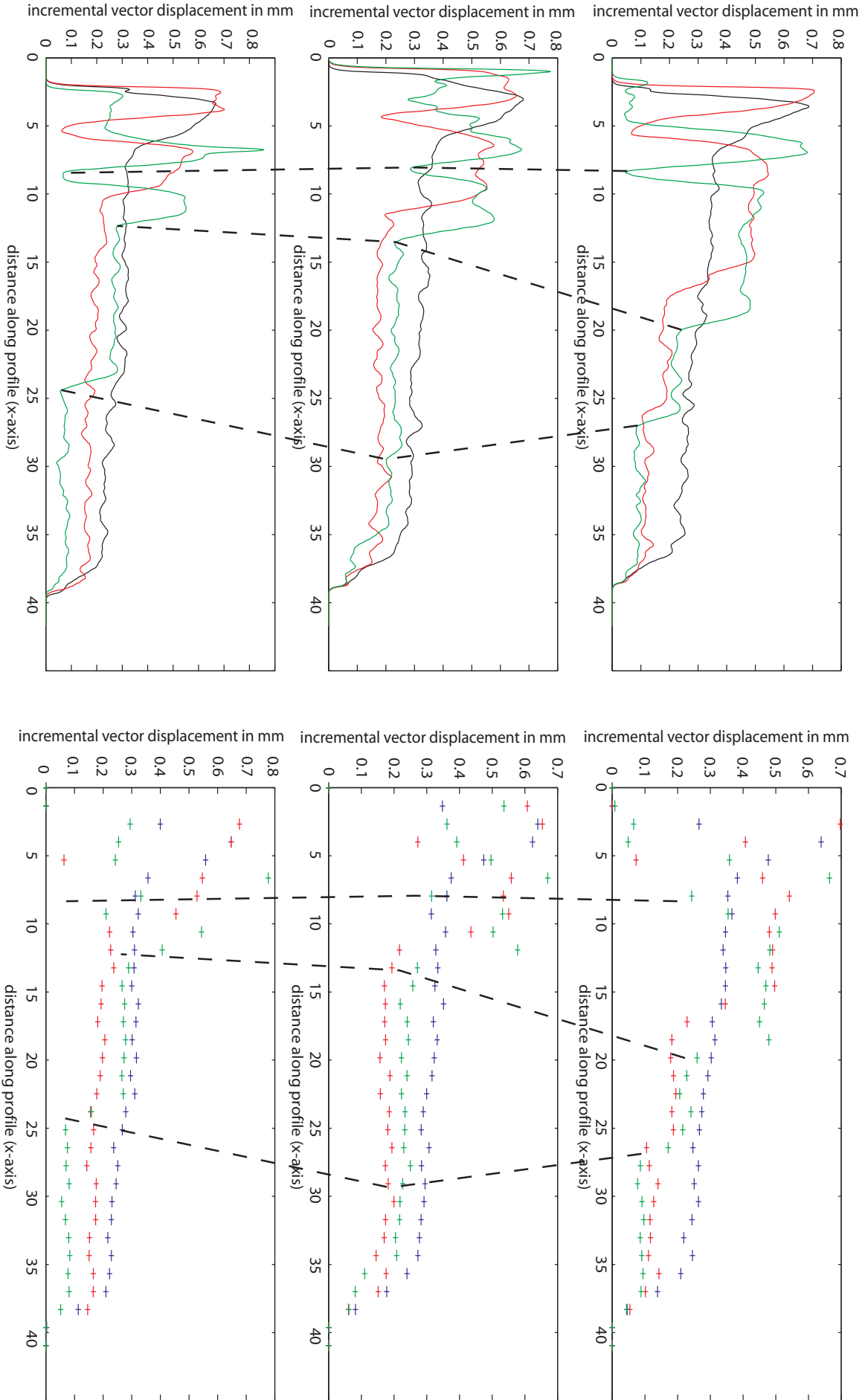


Fig. 8.3: This figure aims to show the difficulties in using velocity gradients to locate active structures in the upper crust and follow them along-strike of the deformation system (black dashed lines), when the data resolution is not good (right: velocity data present for every fifth time increment), compared to the complete coverage (left: velocity data are present for every time increment). Each of the plots gives the information for one profile (Exp. 4, cf. Fig. 7.9a for location of profiles). The colour code for the profiles for within one plot indicates the time step (blue: 60, red: 120, green: 180). The x-axis indicates the position of the velocity displacement in the direction of convergence.

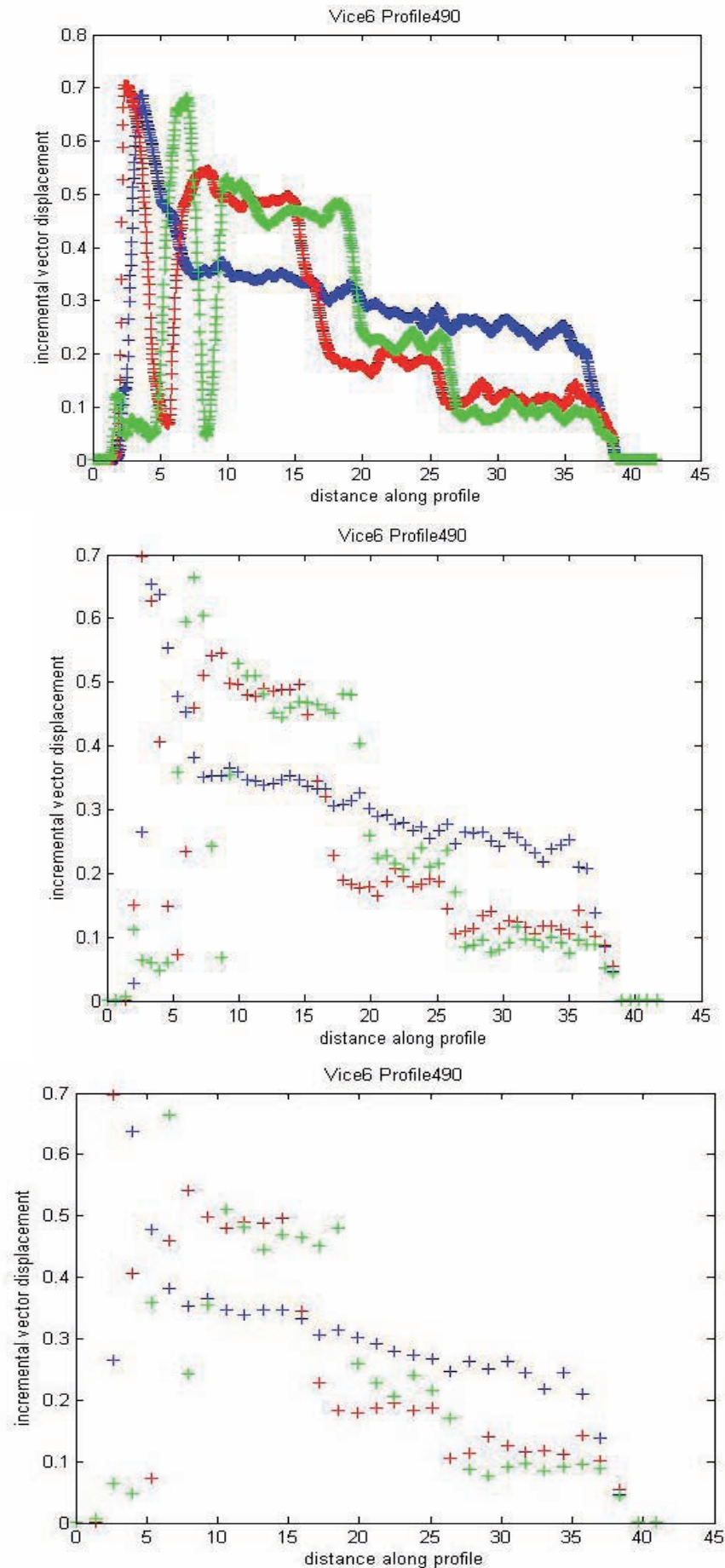


Fig 8.4: These figures again show that extrapolation from few velocity data points (e.g., data from GPS stations) to get a continuous data set is not straightforward and gives more than one option to construct the “real” continuous displacement field. The colour code for the profiles within one plot indicates the time step (blue: 60, red: 120, green: 180). The profile number is given in each plot.

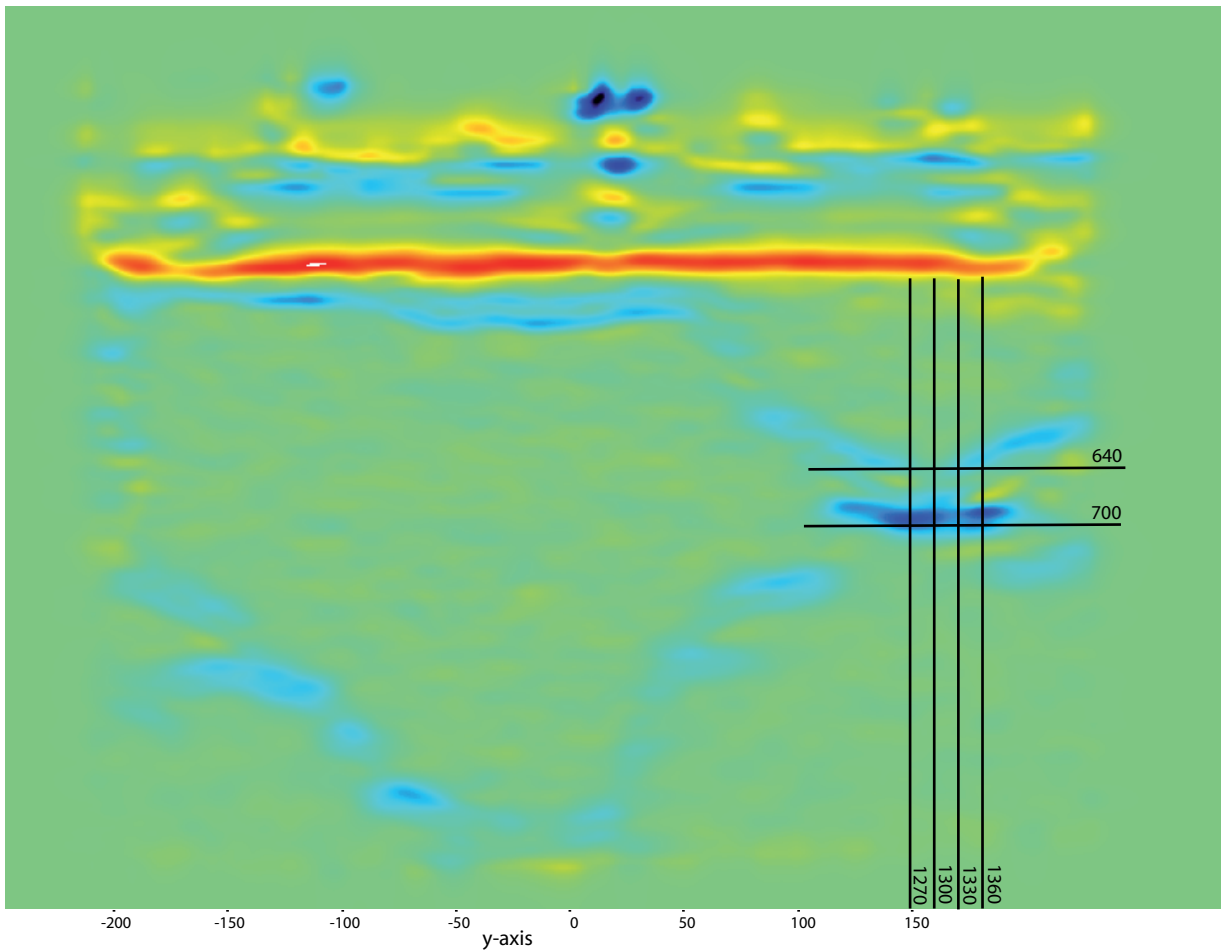
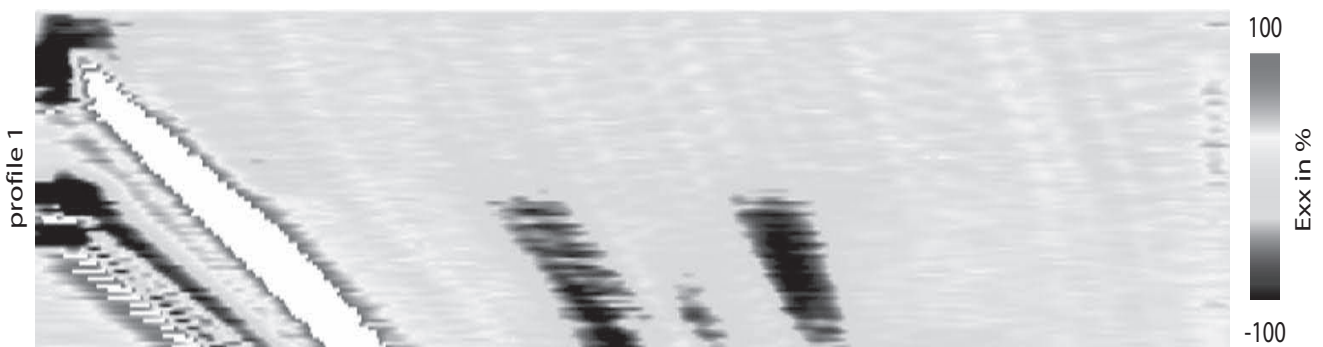


Fig. 8.5 (top): The surface of the experiment is colour coded for strain E_{xx} (at 27.7% bulk shortening). Blue colours indicate locations with high strain accumulation, not coinciding everywhere with the velocity contrasts of Figure 8.2. Black lines show profiles of point locations used in Figures 8.7 and 8.8. Convergence was from top to bottom. Only structures below the piston (red horizontal stripe) are actually part of the experiment.

Fig. 8.6 (bottom): This figure shows strain data extracted across the strain surface (E_{xx}) of Figure 8.5 through the profile position 1300 for each time step. The time increases from top to bottom, and the piston advances from left to right. The oblique white patch marks the steady convergence over time. The black patches indicate locations of high strain accumulation along three structures that are located within the same profile (cf. Fig. 8.5). Within these structures a horizontally striped pattern is defined by several changes from black to grey to black. This shows the successive stages of high and low to no strain accumulation over time.



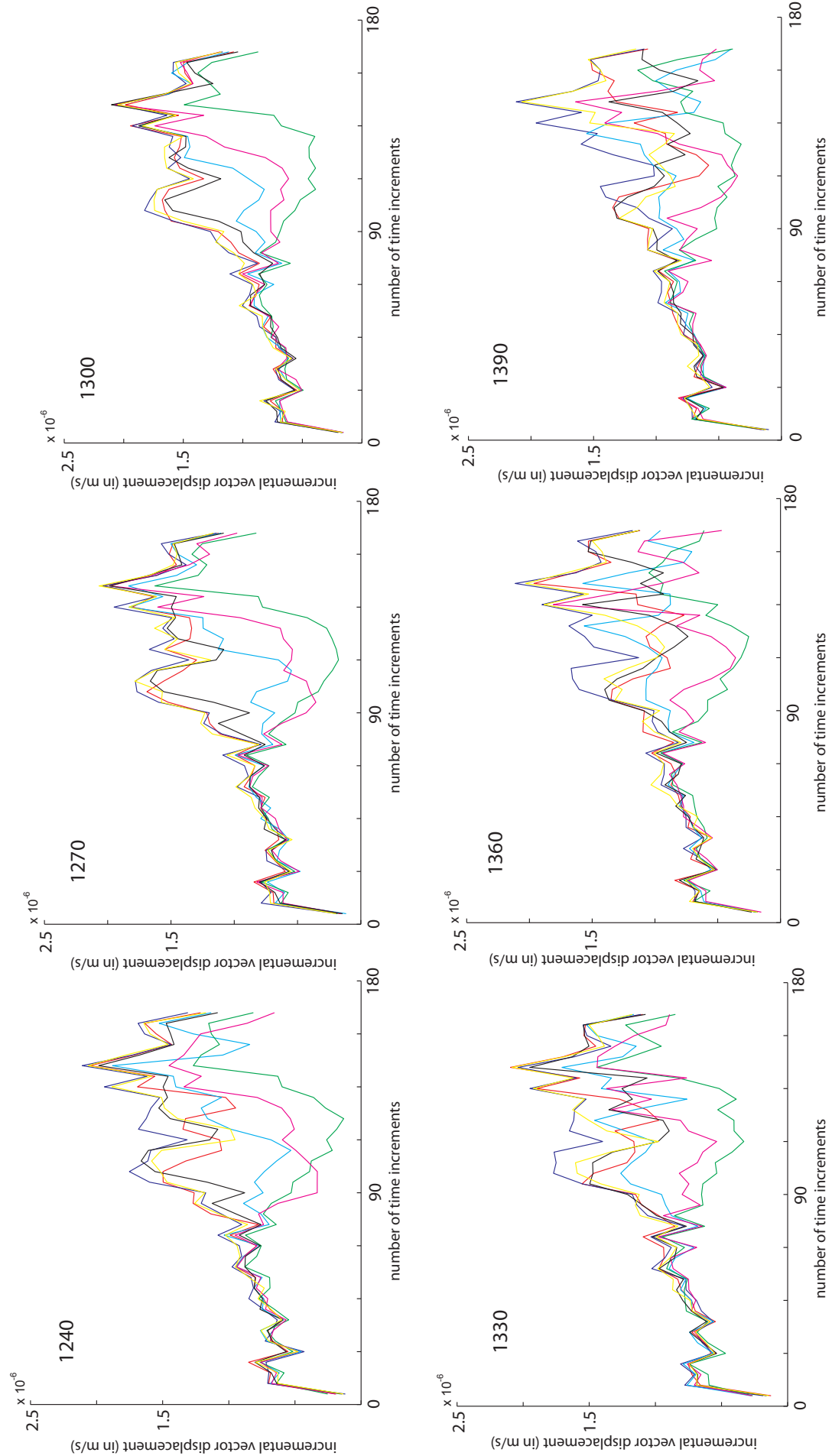


Fig. 8.7: Incremental vector displacement (in m/s) for seven points located in orogen-normal profiles (1240, 1270, 1300, 1330, 1360, 1390, cf. Fig. 8.5 for location of profiles). The x-axis represents the number of time increments equivalent to the observed amount of shortening (180 equals 27.7% of bulk shortening). Colours indicate the position of points along the profile with increasing distance from the piston (blue: 600, yellow: 620, red: 640, black: 660, bright blue: 680, pink: 700, green: 720). Distances between the profile numbers are 30 pixels equalling 9.9 mm; distance between points along profile is 20 pixels (6.6 mm).

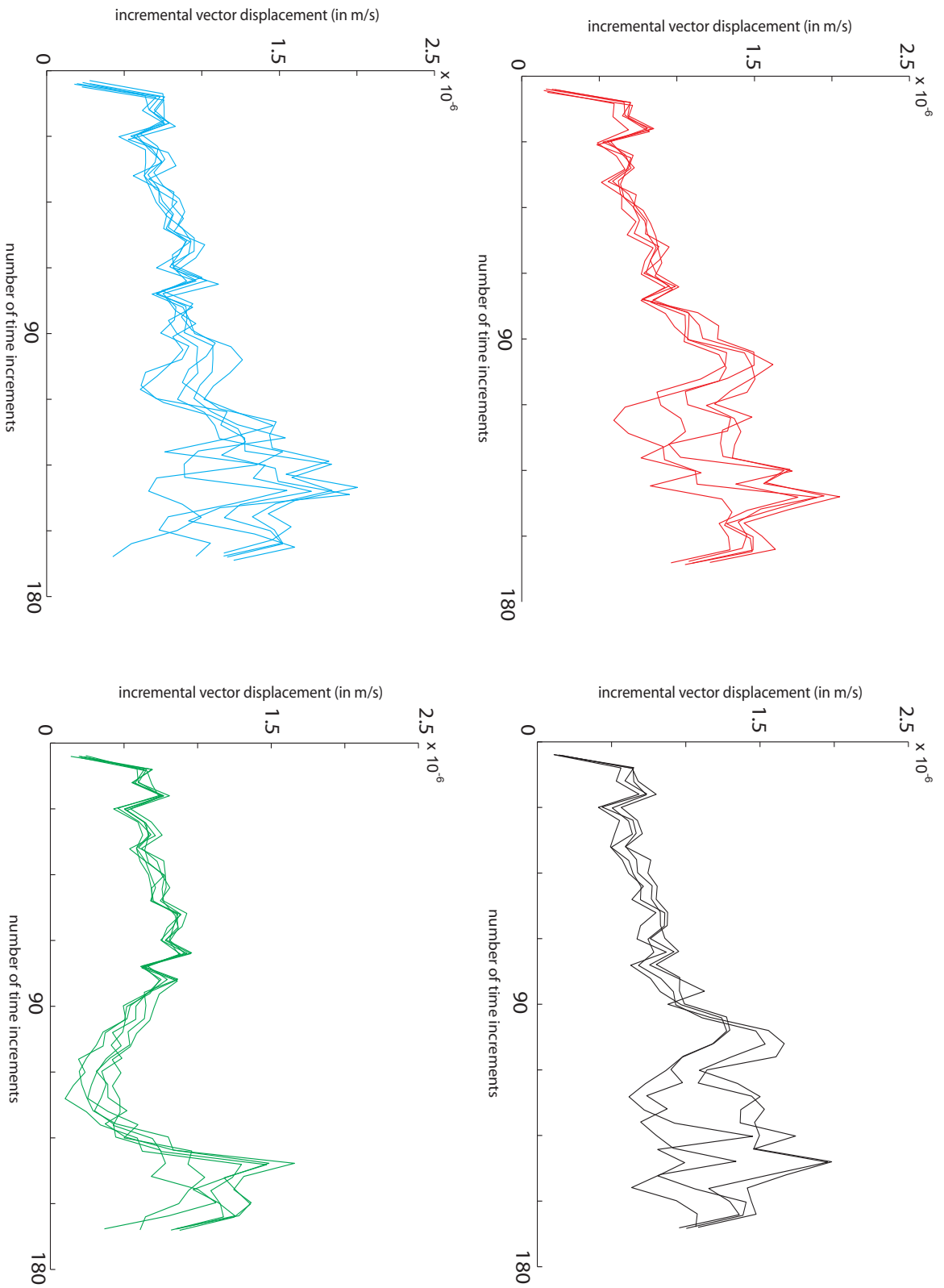


Fig. 8.8: Incremental vector displacement (in m/s) for points located in a profile along-strike (1240, 1270, 1330, 1360, cf. Fig. 8.5 for location of profiles). The x-axis represents the number of time increments equivalent to the observed amount of shortening (180 equals 27.7% of bulk shortening). Colours indicate the position of points along the profile (red: 640, black: 660, bright blue: 680, green: 720). Distances between the profile numbers are 30 pixels equalling 9.9 mm; distance between points along profile is 20 pixels (6.6 mm).

9. Discussion, Conclusions and Outlook

9.1.1. Degree of localization

In Figure 9.1 we plot the number of active points (blue) against the westward drift curve of the South American plate, i.e., the upper plate (from Silver et al., 1998) for the last 46 Ma. This drift has an influence on the deformation mode of the upper plate (Heuret and Lallemand, 2005). For active points plotting below the velocity curve, the deformation distribution is localized, whereas it is rather diffuse when points plot above the curve. At 46 Ma, the velocity of westward drift is about 2 cm/year increasing to 3 cm/year during the evolution of the Central Andean plateau, showing that deformation was localized in the initial stage. Over time, more points became active within the plateau area and the Eastern Cordillera. Thus, two neighbouring structural units are active and deformation is distributed over a wider area, i.e., strain accumulates in a diffuse fashion. When deformation within the plateau becomes inactive after 10 Ma, strain accumulation “shifts” to the Subandean fold-and-thrust belt, where deformation again localizes.

9.1.2. Aspect ratios

Next, we plot aspect ratios of the geometry of the biggest active areas for a given Ma step

in the same diagram (Fig. 9.1, green points). Aspect ratios can be calculated according to the characteristic widths and lengths of active areas. They yield values of 1 when the active areas have the same extent both orogen-parallel and orogen-normal. The value decreases the larger the length is compared to the width.

Again, we can see that strain initially accumulates at small structures of generally low aspect ratios. As soon as more points become active, the aspect ratio is 1, eventually decreasing again. This marks the time of first activity of neighbouring structural units, i.e., the plateau interior (the plateau and the Eastern Cordillera), with subsequent strain accumulation at the plateau margins. Further decrease of the aspect ratio shows increasing strain localization within narrow areas, namely the Subandean fold-and-thrust belt and parts of the Puna margin.

9.1.3. Frequency-size distribution

Figure 9.2 correlates the size of the actively deforming zones with their frequency of occurrence. The size is hereby defined as the number of neighbouring active points in our point grid for one area. Zones were grouped into classes covering five or ten points (e.g., 11 points, 16, 21, 26 points and so on). Zones with 60 points represent areas of e.g., 150 km width and 600 km length.

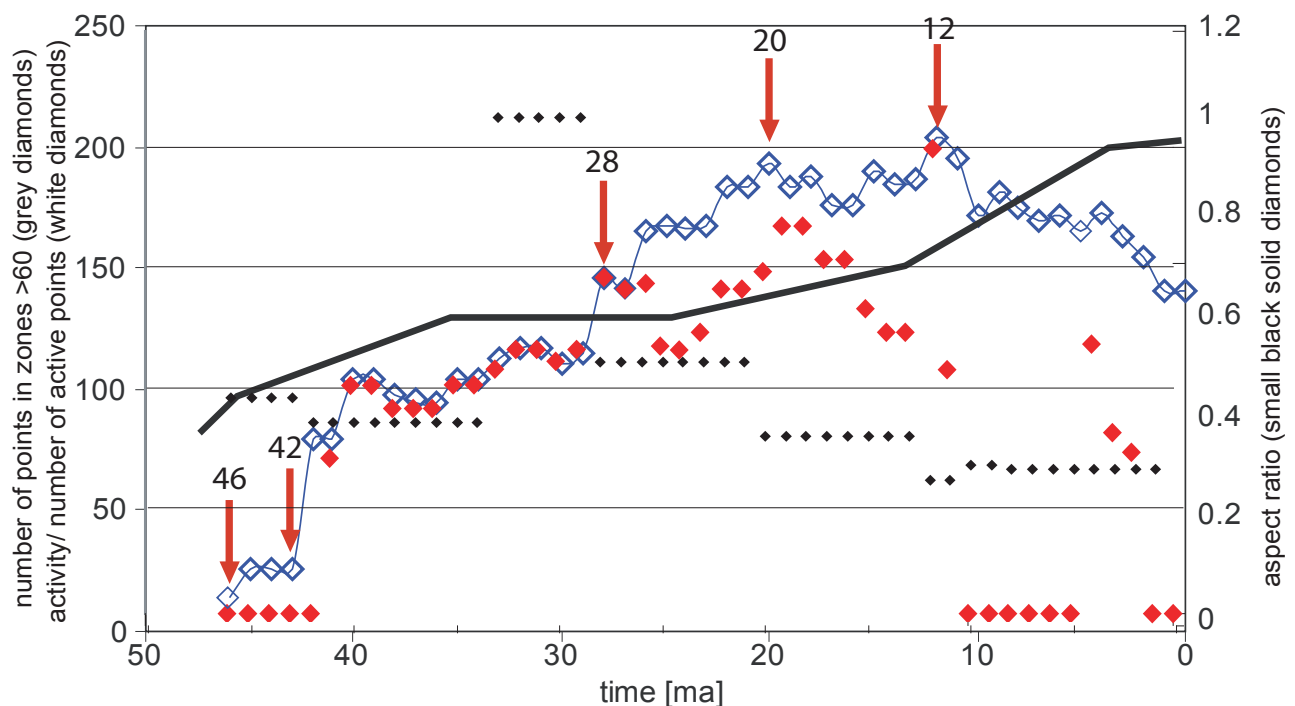


Fig. 9.1: Number of total active points per Ma (outlined diamonds), number of active points in areas with more than 60 neighbouring points (grey diamonds), aspect ratios (small black diamonds) and curve (black) of westward drift of South America (from Silver et al., 1998).

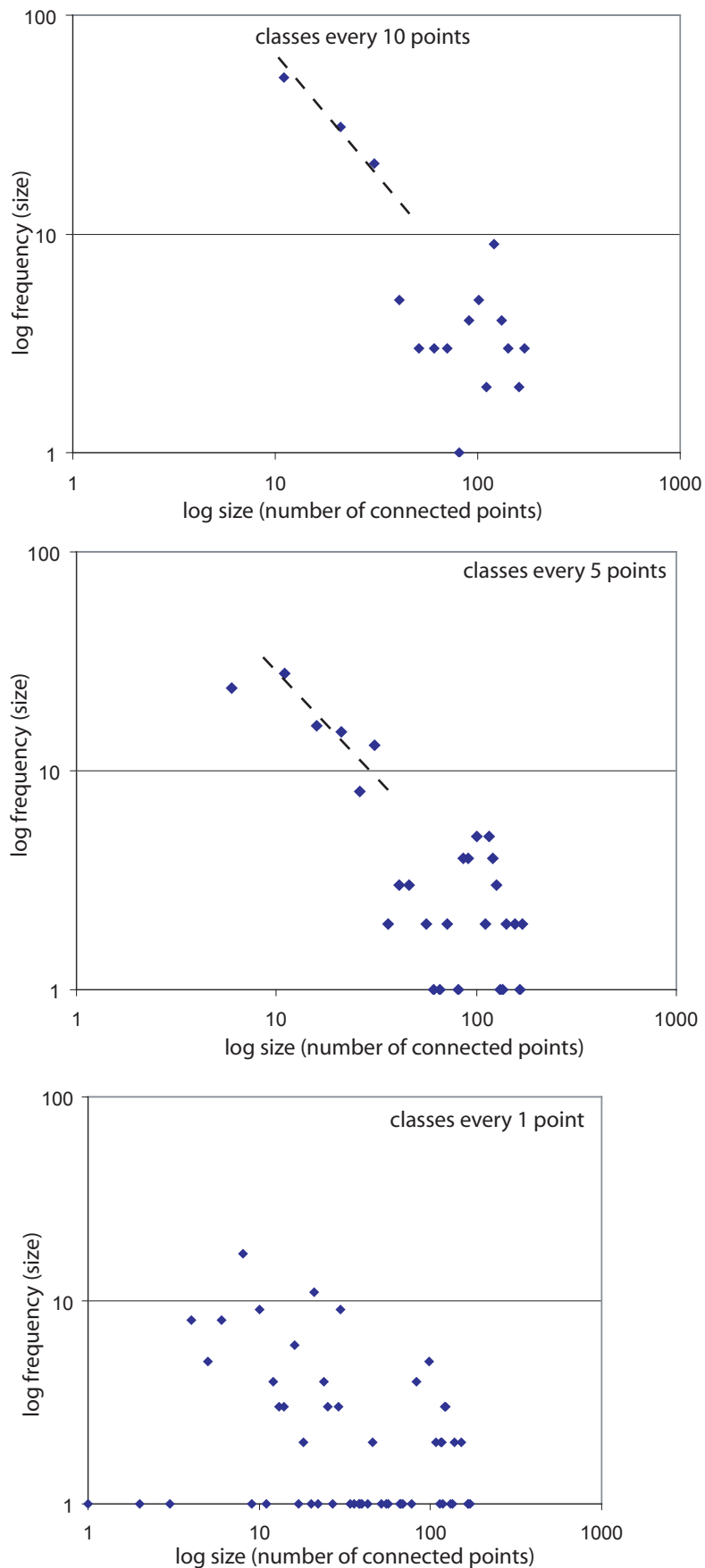


Fig. 9.2: Frequency-size distribution of active structures on the orogen scale in a log-log plot. The size of an active area is defined as the number of active neighbouring points. The three plots have different numbers of classes in which points are grouped. Cut-off values for classes are chosen below 11, 21, 31 points etc. for the figure at the top and every 6, 11, 16, 21 points etc. for the plot in the center. The plot at the bottom shows the original data without redistribution into classes. When classes are present, the points of small sizes could be approximated by a linear function (with a slope of ~ -1.8) up to a point beyond which points tend to cluster.

For areas with less than 60 points, the frequency size distribution indicates a power law over a very limited scale range for temporal sample windows of 1 Ma (dashed line with a slope of ~ -1.8 , Fig. 9.2). Areas with more than 60 points are less frequent, and the power law ceases to be applicable. This cut-off value will shift towards smaller sizes (less points) when smaller time windows are sampled, due to better capability of resolving active structures of smaller extent. The cut-off value would move to the right for larger time windows, as we are summarizing several active structures. In this respect, for the finite pattern of the entire system over the total duration of deformation, every point will have been active at least once, representing an area with all points as active neighbours.

As proposed in Chapter 5, the active structures on the orogen scale are a multiple of the suborogen scale ones. This might be due to a summarizing effect of coevally active neighbours on the smaller scale. This summary is an unintentional integration of data in space to form a larger active area, which, when sampled with higher temporal and spatial resolution, will be divided into several small areas, as inactive areas may occur within originally large areas. So, the small areas in our frequency-size plot are real, whereas the areas with more than 60 points are not “real”, but only due to the summarizing effect arising from the resolution which is still too low.

9.1.4. Percentage of small vs. big areas

Based on the value of power law failure (Fig. 9.2), we calculated the number of active points that are part of areas with more than 60 points. The curve (Fig. 9.1, red points) shows that during the very first stage, when deformation was active only in a few regions in the Western and Eastern Cordillera (46-40 Ma), all points were active in areas with less than 60 points. Up to 27 Ma, almost all points were active in areas with more than 60 points, thus activity was clustered in large areas. From 26 to 11 Ma, the number of points varies, meaning that both large and small areas are active. From 10 Ma to the present, deformation became inactive in the plateau interior and shifted to the Subandean fold-and-thrust belt. Thus, another “initial” stage is represented by rather small areas. However, we have to bear in mind, that large areas are actually small areas: many coevally active and spatially neighbouring small areas.

9.1.5. Power spectra over time

When regarding the spatially distributed deformation values as signals, we can also examine them by means of auto-correlation, determining how well the data are correlated with themselves when shifted, e.g., in time. To analyze the variance of a signal over its frequency we apply a Fast Fourier Transform to generate energy spectra, or, in our case, power spectra. From the resulting power spectra (Fig. 9.3) we are now able to detect any underlying pattern in the variation of the variable for a given frequency (here spatial distance), e.g., patterns that are characteristic of deterministic or stationary stochastic processes (such as fractal patterns).

Figure 9.3 indicates that the power spectra of the shortening dataset in their current form reflect a fractal pattern of the spatial distribution of shortening rates per Ma from 36 Ma to 17 Ma. Generally, peaks in auto-correlation plots indicate characteristic lengths (Fig. 9.3). If these lengths of active deformation on the regional scales and their multiples on the orogen scale described in Chapter 5 were real, we should expect to find two peaks in the lag of the auto-correlation plots (x-axis). As we only observe one peak, the value is not periodical (i.e., not appearing for one length scale and again as a multiple for another length scale). Looking at the power spectra (Fig. 9.3), the only peak present for a lag of ~ -0.5 or 0.5 (e.g., for 40 Ma and 38 Ma) coincides with a bulge in the curve at about 100 km. This value is not equivalent to any value of the characteristic lengths described in Chapter 5. Rather, this alleged break in power law (indicated by the curve's slope) is not a break in the scale-invariant distribution of shortening values, but an artefact of the balanced cross sections giving shortening estimates for one degree of latitude (~ 100 km). Therefore, in a N-S direction values show less variation for distances of ~ 100 km. This does however not preclude the general fractality over the scale range between 40 km (lower resolution cut-off) and 1000 km (upper resolution limit).

These plots will be subject of further examination with respect to their robustness against variation in the initial data set. Presently the shortening data follow the assumption that strain was homogeneously distributed in space and time (cf. 9.1.6. for discussion on properties of the dataset).

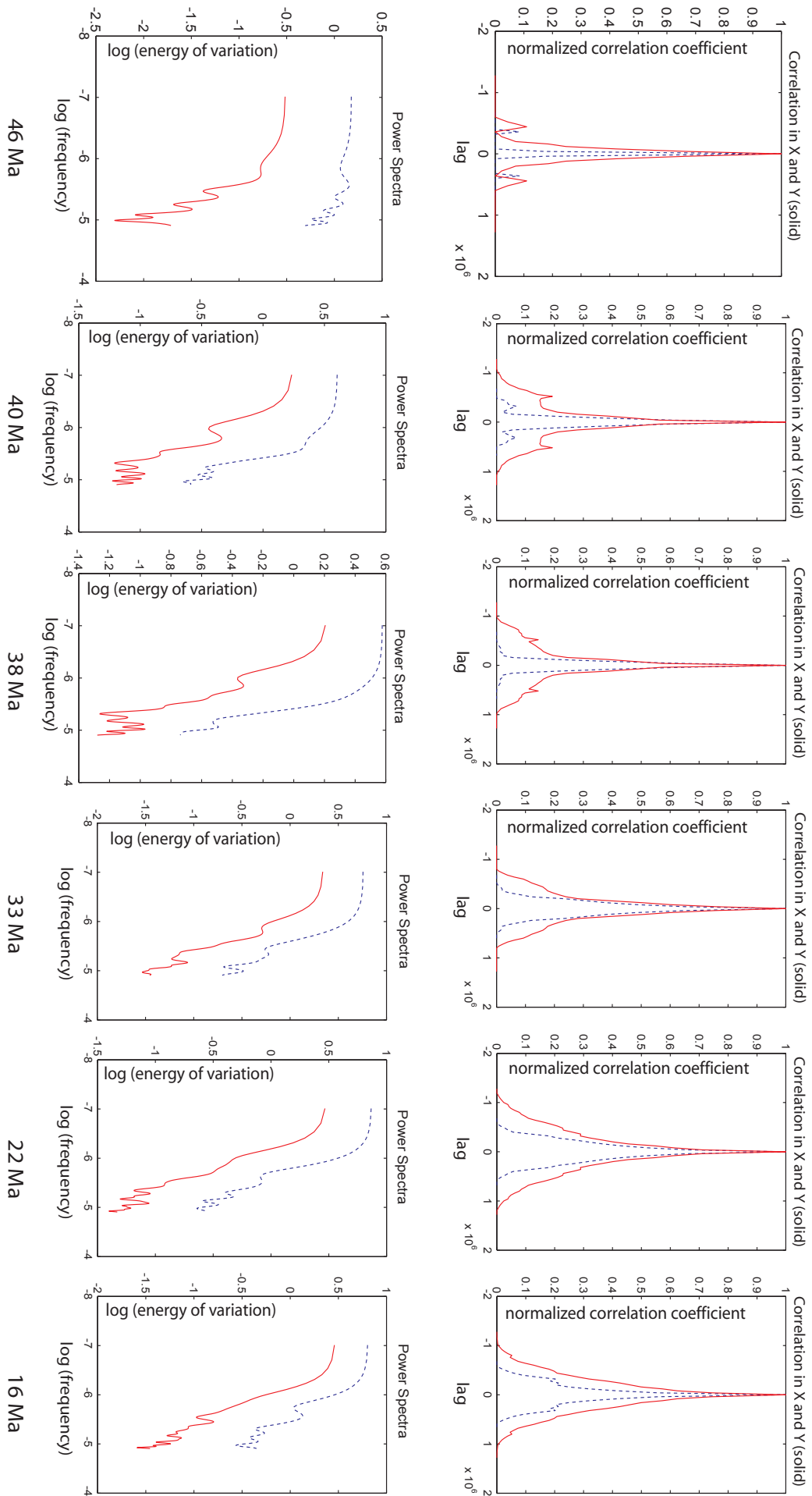


Fig. 9.3: Auto-correlation functions (top) and associated power spectra (bottom) for the spatial distribution of shortening rates per Ma (as given below each plot). The solid red curve depicts data in a N-S direction, and dashed blue data in E-W. More information in-text. Figures produced with Matlab codes by A. Levander.

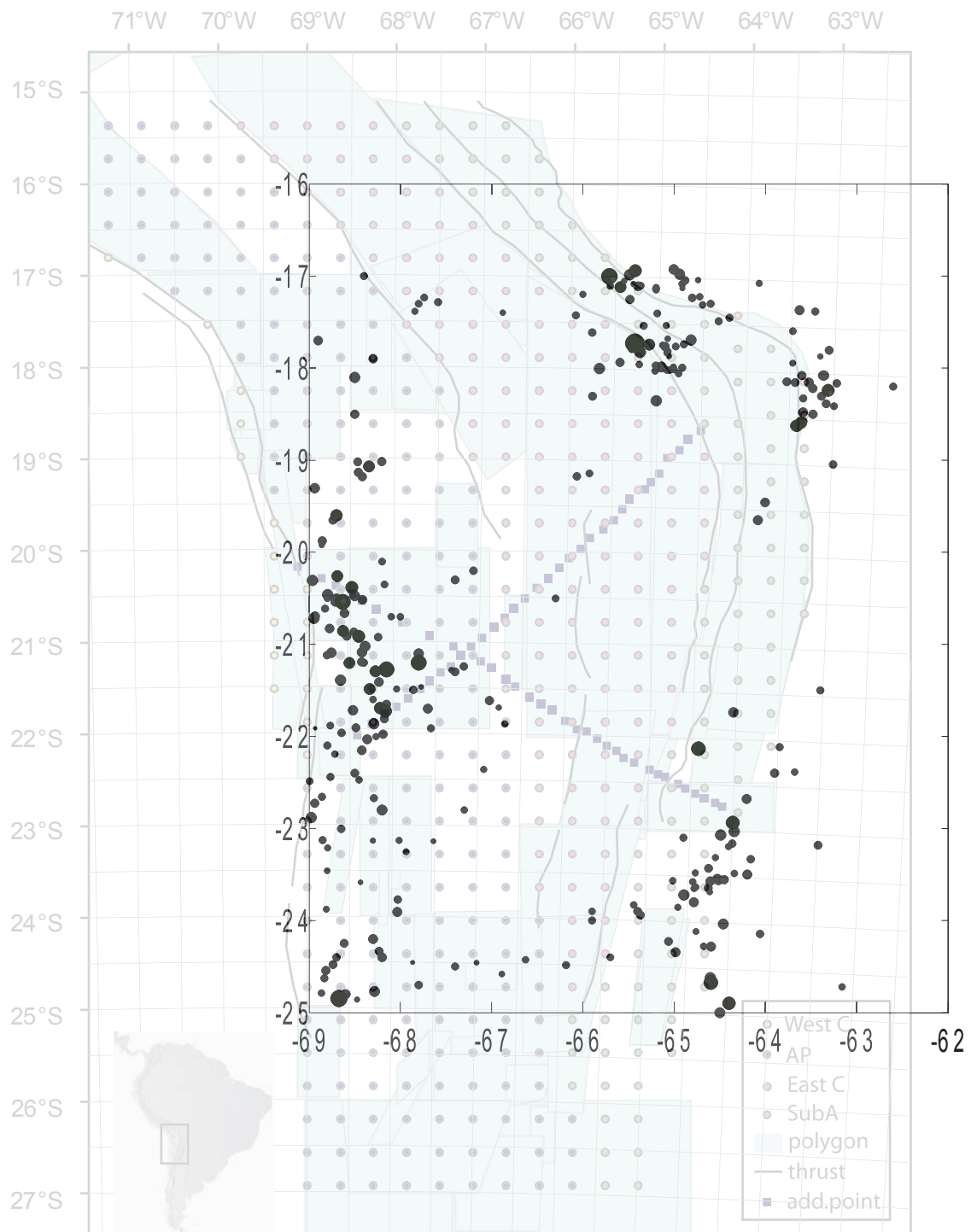


Fig. 9.4a: Distribution of earthquakes in the Central Andes. Earthquake data are from the NEIC catalogue including earthquakes that occurred between 1963-2006 up to a depth of 35 km and with magnitudes >3. The diameter is scaled to the destructed area at the surface (cf. Ritznitchenko, 1976).

9.1.6. Influence of quality of database

When compiling the data base we carefully paid attention to the quality of available deformation data, and included them only when the geographical position of their study areas and sample locations, the sample method for age dating, and the error of their measurements were precisely stated by the authors. Apart from the initial stages of deformation when only a few

areas have been active, deformation data exist from more than one author for any studied area. When independent authors yield similar results, the data can be considered solid.

The study areas in the original data set generally have sizes of 100-200 km in length and width. Cases when authors have inferred a given deformation for a very big region up to ~600 km in length and ~300 km in width, are present only four

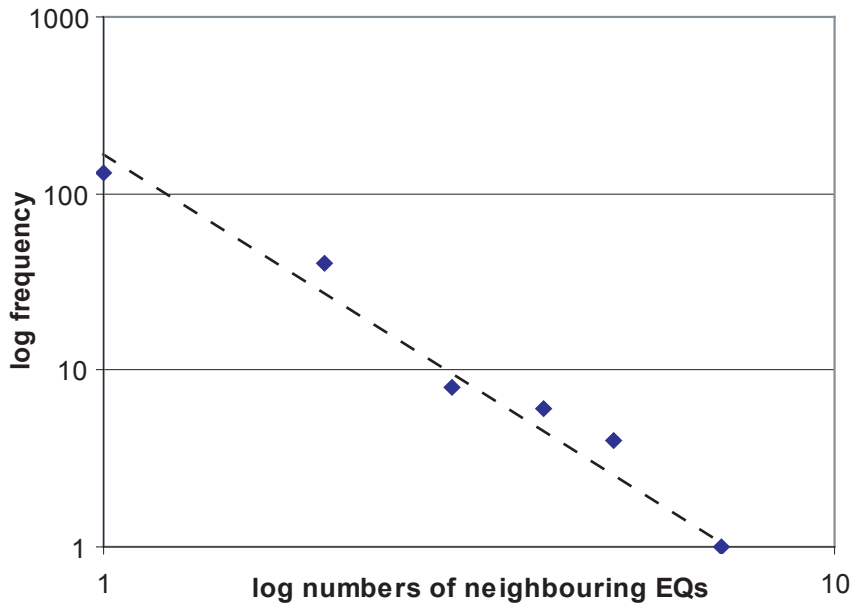
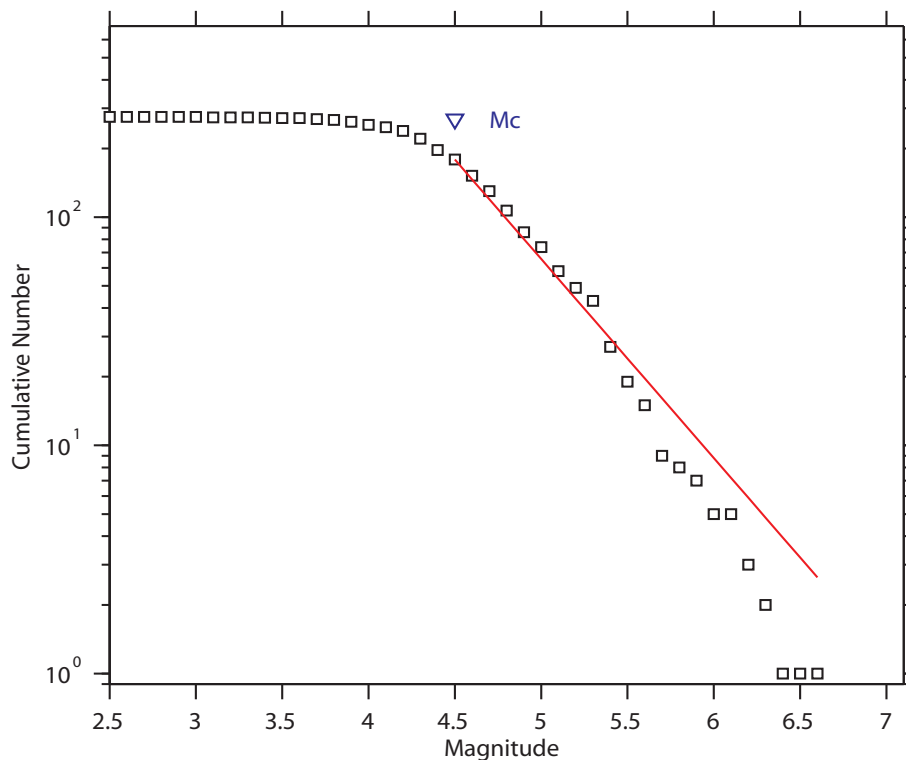


Fig. 9.4b: Frequency-size distribution of neighbouring earthquakes for the Central Andes (details in-text). Earthquakes are defined as neighbouring, when they share parts of their destructed surface area (cf. Fig. 9.4a).

times. As the characteristic length scales (with 150 km in width and 200-300 km in length), quantified in Chapter 5 neither have the same size as the small initial areas nor the large areas, the different study area sizes did not influence our results.

However, as we cannot resolve active structures below ~40-100 km, small areas are

integrated into a large one simulating the above mentioned characteristic length scale. If our spatial resolution was better, we would be able to identify active and inactive parts within our regional areas, which would then break up into smaller areas. Thus, the characteristic length described in Chapter 5 must be seen as an artefact.



Maximum Likelihood Solution
 b-value = 0.872 +/- 0.05, a value = 6.18, a value (annual) = 4.54
 Magnitude of Completeness = 4.5

Fig. 9.4c: Magnitude-frequency distribution of earthquakes for the Central Andes (details in-text). Plotted with ZMap.

In contrast to the deformation activity data, which only have discrete values (0 or 1), the inferred shortening rates are more prone to inherit errors from the initial data set. To obtain a comprehensive data set with continuous rather than discrete values for such a large spatial extent down to a temporal resolution of only one million years, we had to accept the underlying assumption that both the spatial and temporal distribution of deformation was homogeneous. This affects the analysis of variation of values on scales $<10^2$ km for the E-W direction (i.e., we detect less variation $<10^2$ km), due to the fact that 1) the initial width of areas is 100 km or more, and 2) the structural units have extents of up to 300 km with known shortening estimates (e.g., the plateau or the Eastern Cordillera between 18 and 21°S). The N-S direction has a lack of variation for ~ 100 km (cf. 9.1.5.), as shortening estimates are very similar for each degree of latitude.

Some authors have worked with a higher spatial resolution (i.e., in smaller areas), but did not necessarily quantify the displacement for their study areas. In any case, the integration of a few higher resolved values among the majority of values with assumed homogeneity, would not change the correlation functions significantly. Despite being homogeneous, the correlation functions still change over time and for different analyzed directions (cf. Chapter 5 and Fig. 9.3). The next step is to evaluate the robustness of, e.g., correlation functions and power spectra against further changes and variation within the original data from the database. This can be done by comparing our results 1) to models of known underlying patterns, and 2) to a dataset that is less homogeneous than ours and one that is even more homogeneous. Future research should nevertheless attempt to increase the spatial resolution below 10^2 km, for example by consulting seismic sections for the quantification of both displacement and its timing.

9.2. Discussion

Power law relations of size-frequency distributions and spatial distributions of earthquakes and faults are commonly based on the respective finite patterns and therefore do not include the temporal evolution of a deformation system. But is the power law relation valid for all evolutionary stages of spatial distribution of deformation (earthquakes, faults and regional

deformation) or only for the finite pattern?

Earthquakes follow the Gutenberg-Richter relation (e.g., Bak and Chang, 1989; Kagan and Jackson, 1991; Wesnousky, 1994) which correlates earthquake magnitudes with their frequency. This relation can only be established after a critical amount of earthquakes has occurred; in other words, when monitoring a completely undeformed domain from the beginning, it takes some time to accumulate several events before establishing a fractal pattern. Yet, this fractal pattern can only be observed when the sample time window is appropriately chosen: if the time window is too small, we would only sample single events (e.g., for an hour or a day); if it was too big, we would sample spatial clusters of deformation.

This clustering effect is also present when we assume that the spatial extent of earthquake occurrences is limited. In nature, any given spatial extent (i.e., study area of limited size) will be saturated at some time, with subsequent strain accumulation in another location.

We counted adjacent earthquakes (i.e., sharing a common destruction area, cf. Ritznitchenko, 1976) recorded between 1963 and 2006 for the Central Andean plateau (17°-25°S and 69°-63°W) in the upper plate down to 35 km depth with magnitudes >3 (Fig. 9.4a). Their zone size-frequency distribution (Fig. 9.4b) is similar to that of active areas (Fig. 9.2) insofar as they follow a power law distribution (slope ~ -2.4). Their magnitude-frequency relation has a power law with a b-value of ~ 0.87 (Fig. 9.4c).

The evolution of faults and fault systems in space is similar to that of earthquakes. In any completely undeformed domain, one or several faults develop first; more faults will occur with time, as earthquakes and aseismic events either increase the size of an existing fault, or lead to formation of a new fault. At some time, the spatial distribution of faults will establish a fractal pattern (e.g., Allègre et al., 1982; King, 1983; Turcotte, 1986) and their frequency-size distribution will follow a power law. Typical estimates for fractal dimensions are 1.7 (Sornette et al., 1990) or 1.8 (Marrett and Allmendinger, 1990) (cf. Bonnet et al., 2001 for a thorough review).

If we again consider a fixed spatial extent, there will be a time when the area is saturated with faults. Faults have eventually grown to their maximum possible lengths, and faulting will then move out of the area to form elsewhere, where

strain accumulation is more favourable. Thus, a once established fractal pattern will remain fractal in the future, as in the long run, strain accumulation occurs no longer in the first spatial extent (i.e., area in space) but a second rock volume where another fractal pattern will be established. Bonnet et al. (2001) point out that fault patterns are fractal due to the scale invariance of the fracture growth process arising from material heterogeneities in the crust.

The spatial size of such established fractal patterns will have the size of regional areas, e.g., ~150 km in width, 200-300 km in length or smaller (cf. Chapter 5), beyond which scale-invariance becomes invalid for sizes of active structures. As discussed before, this effect is due to the lack of spatial and temporal resolution beyond 40 km and 1 Ma, respectively. Thus, with the current resolution, large areas summarize smaller areas, which could otherwise be distinguished with higher resolution. In contrast, the shortening values are spatially distributed in a fractal way (cf. Section 9.1.5.). As mentioned before (9.1.6.), stability of results against variation in the initial data set has yet to be analyzed. However, in their present form, data reveal evolutionary stages of the spatial distribution and its fractal pattern in the Central Andes. Figure 9.1 shows that, in the beginning, only small areas are active (Western and Eastern Cordillera, 46-38 Ma), analogue to faults reaching a critical number before a fractal pattern can be established. These small regional areas will have established their fractal patterns by the end of this stage. In the next stage (37-16 Ma), the pattern will have evolved to be fractal also on the orogen scale (Fig. 9.3). At the “saturation stage”, the plateau no longer accumulates strain, and the pattern becomes stable. The establishment of the fractal pattern from the regional scale to the entire orogen can be comparably fast with ~8-10 Ma. Fractal fault patterns for a regional area of less than 100 km in the Puna has been similar or faster (Marrett and Allmendinger, 1990; Marrett et al., 1994).

At 10 Ma, the Subandean fold-and-thrust belt starts to deform, blurring the fractal pattern of the preceding stage, as we see now another initiation of strain accumulation in small areas which can already create a fractal pattern inside, as faults generally exhibit fractal patterns (e.g., references in Bonnet et al., 2001). The orogen itself is inactive and its distribution of active shortening is not fractal any more.

This procedure can be summarized: strain accumulation is initially diffuse or localized in “stage 1” (depending on the dominant deformation mode, see below), balancing itself over a critical time period (or equivalent amount of strain) to become fractal for the regional area. By and by, a fractal pattern will also establish for the orogen, namely when several regional areas are active which themselves are fractal within (“stage 2”, fractal orogen). Once a fractal pattern is established for a given spatial extent (i.e., the analyzed area in space), strain accumulates in another “rock body” to repeat the procedure (initial “stage 3” with regional fractals). The first fractal pattern will be kept.

However, we can only observe these patterns, when the time window is well chosen to actually resolve the spatial extent of crucial features. For smaller structures (e.g., earthquakes or faults), the time window must be chosen relatively smaller, not to include structures that are part of another spatial extent or temporal stage. This effect is also relevant on the regional to orogen scale where we can only resolve time down to a million years (minimum). Therefore, active areas suggest a characteristic structural length on the regional scale, which will be a multiple on the orogen scale (cf. Chapter 5). In other words, the big scale merely summarizes the small scale as we might resolve structures of different temporal stages and spatial extents. This is due to the still too low temporal resolution and relatively big spatial sample extents precluding the identification of the underlying fractal pattern. This is also the reason why the power law is not valid beyond a value of 60 points (Fig. 9.2).

Ben-Zion and Sammis (2003) previously suggested that a finite fractal pattern exists, which balances strain hardening and weakening effects during its evolution. Thus, we also need to consider the differences between dominant processes and patterns, as the scaling relations might vary depending on what we analyze (also review by Bonnet et al., 2001). Deformation processes are effective on all spatial scales, and depending on the observed spatial and temporal scales, different deformation frameworks might be dominant (cf. Chapter 2). As we lack the high data resolution both in space and time, we do not know the various coupling relationships of processes and parameter effects within and across the scales (e.g., the influence of erosion on isostatic effects

and together on deformation).

Generally, some faults are dominantly active, losing their roughness with increased slip. This is a characteristic for the continuum-Euclidean deformation framework. Yet, this fault will not have a notable impact in a spatial distribution, and will simply be part of the frequency-size distribution as one of the long faults. This again shows that a fractal pattern does not determine which type of strain accumulation is dominant, e.g., strain hardening or strain weakening. Thus, the frameworks do not exclude each other, but they are coexisting or alternating in time and space (see summary by Ben-Zion and Sammis, 2003).

In general, the indicators for the continuum-Euclidean frameworks might be stronger as Regenauer-Lieb et al. (2006) pointed out. They have proposed a multi-scale approach with various weakening processes, effective on different spatial and temporal scales (i.e., grain size dependent creep processes in the time interval <1000 years; thermal diffusion processes within shear zones for hundred thousand years or more; and water weakening processes on millions of years and more).

Ben-Zion and Sammis (2003) also conclude that long-term evolution of deformation favours the first order influence of the continuum-Euclidean framework, due to its positive feedback mechanism associated with strain weakening. An explanation for this can again be found in the spatial resolution or the area size that is analyzed. As discussed above, we assumed an unlimited spatial extent, in which strain accumulation can eventually establish a fractal pattern. Heterogeneities in the crust produce zones of weakness, where strain

preferably accumulates. This represents a limited spatial extent, as strain accumulation would rather accumulate in a weak zone than move outside, where strain localization is not favourable. Bonnet et al. (2001) state that the fracture growth process is scale-invariant due to material heterogeneities. With time, a weak zone will be saturated with strain, and eventually will not be a weak zone any more, as Townend and Zoback (2000) propose that faulting keeps the crust strong. Thus, at some evolutionary stage, a weak zone does not attract particular strain accumulation any longer, and a fractal pattern can generally be established.

More artificial reasons also suggest the continuum-Euclidean framework to be dominant over time: planar structures have been highly active (i.e., they have lost their initial roughness with increased slip), and their potential of being stored in the exposed rock record is much higher than for small structures that hardly accumulate strain. Also, faults cannot regain their roughness. Thus, a particular fault might be interpreted to be dominant at all times merely due to the lack of roughness, although it might not have had accumulated any strain over certain periods (and thus might have been part of a complex system in which all faults equally accumulate strain, or might have accumulated strain in a diffuse fashion).

The contribution of deformation processes to strain accumulation in space and time, which is in favour of different deformation frameworks, is further complicated by other processes that act on any deformation system. Causes and effects are not easily correlated (e.g., erosion and deformation), as these causes do not only become effective on one scale, but across the scales; and smaller scales “imprint” on the larger scales. This was shown in Chapter 7, where second order parameters have an effect on the regional scale (e.g., additional decoupling horizons), whereas the orogen scale pattern remains the same. In a schematic sketch (Fig. 9.5), it becomes clear that too many unknown variables exist, i.e., relations between causes and effects ($a+I$, $b+I$, $a+b+I$, $a+II$, $b+II...$, e.g., erosion and its effect on topography development and deformation), and between causes themselves ($a+b$, $a+c...$, e.g., climate and erosion) and effects themselves ($I+II$, $II+III...$, e.g., isostasy, topography and deformation). Yet, these relations might change over time. Thus, we might never fully understand highly complex coupled systems.

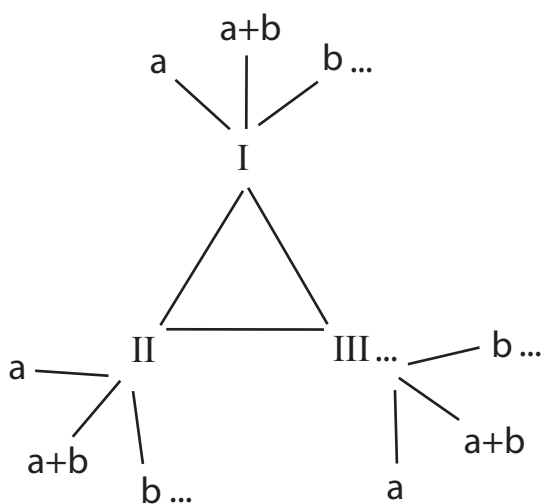


Fig. 9.5: Relation of causes and effects

In Chapter 6, I studied the coupling relation between mechanical heterogeneities, namely basal (20%) and lateral (35%) strength contrasts for which threshold values exist that determine if either a plateau-style or a wedge-like system develops. I also showed that the relation between causes and effects does not produce a unique strain evolution in space and time. Thus, we cannot use the finite pattern for the relation of causes and effects, as it can be explained by more than one parameter combination.

The model results yield a similar spatiotemporal evolution to the one for the Central Andean plateau, yet with a very different parameter combination (for the latter coupling mechanical heterogeneities vs. differential trench-upper plate velocity evolution, high plate interface coupling from low trench infill, and the weak zones in the upper plate, cf. Oncken et al., 2006). In both experimental series, I was also able to show that there is a hierarchy among parameters affecting the system. Thus, some parameters (single or in combination) have first order influence actively changing the type of pattern (e.g., plate geometry, cf. Chapter 7). Second order effects can merely affect a pattern by varying the strain accumulation in space and time on a scale smaller than the entire system (e.g., additional decoupling horizons, cf. Chapter 7).

9.3. Conclusions

What did this study show?

- 1) Spatial distributions of deformation structures of all sizes (e.g., earthquakes, faults, and regionally active structures) have a fractal pattern and a power law relating size and frequency. However, depending on the available temporal and spatial resolution, the underlying patterns cannot always be identified, as 1. the resolution might not be appropriate for the analyzed structures (i.e., small structures need higher resolution to be detected), 2. too many structures might overlie each other for a given temporal sample length (i.e., if the time window is chosen too large, deformation events and structures might cluster), and 3. we unintentionally summarize structures on larger scales that belong to smaller ones, blurring the real pattern for the larger scale (cf. Chapter 5 and 9.1.6.).
- 2) Deformation systems undergo stages. The “initial” strain accumulation on the upper end of spatial scales (namely the orogen scale and the next smaller regional scale) is limited to a few active regional areas with a fractal fault pattern (cf., e.g., Bonnet et al., 2001). On these lines, the initial strain accumulation in the Western and Eastern Cordillera from 46 Ma to ~38 Ma commonly occurs in such structures that are 150 km in width (E-W) and 200-300 km in length (N-S) for the used spatial and temporal resolution, and have established a fractal pattern at the end of this stage.
- 3) Over time, more regional areas with a fractal pattern become active throughout the entire orogen. Therefore, the spatial distribution of shortening follows a power law for the entire orogen during a second stage of Central Andean plateau formation, i.e., from ~37 Ma to ~16 Ma.
- 4) Once a spatial extent or “rock volume” is saturated with strain, strain will accumulate elsewhere. The above mentioned stages can therefore repeat themselves in another area. This occurs after 15 Ma, when the plateau interior becomes stable and strain accumulation will occur in the Interandean and eventually in the Subandean (after 10 Ma). The fractal pattern of the first established stage is preserved.
- 5) A fractal pattern can result irrespectively of the various deformation processes that coexist or alternate during strain evolution (e.g., strain hardening and weakening). However, effects of the different deformation processes as well as other factors influencing a deformation system, can blur the underlying patterns and preclude their identification.
- 6) Various controlling factors have either a first order impact on a deformation system, thereby actively changing the orogen scale pattern (e.g., plate geometry, cf. Chapter 7), or a second order influence, thus affecting only the suborogen scales (e.g., additional decoupling horizons).
- 7) Parameters themselves are likely to be coupled and therefore have a different influence on a deformation system than if they acted alone. Threshold values exist that determine either one or another type of

e.g., deformation mode or the resulting type of deformation system. This was shown in Chapter 6, where threshold values for basal (20%) and lateral strength contrasts (35%) coupled together, determine the result to be wedge-like or plateau-style. There are no gradual transitions in between these two types.

- 8) The spatiotemporal evolution of the Central Andean plateau was reproduced on the orogen scale and below in analogue models that followed a parameter combination of mechanical heterogeneities. In contrast, the parameter combination in nature is supposed to be more complex. This shows that a strain pattern can be caused by more than one parameter combination and is therefore not unique. Thus, we cannot conclude the controlling parameters from the observed strain patterns.

9.4. Future research

First of all we should always bear in mind that scaling up and down of processes or patterns is only valid, when they follow a similar mathematical relation. However, even if the pattern or process is generally scale-invariant, it might look different on some scales thereby suggesting scale-dependent behaviour, depending on the temporal and spatial resolution, the current deformation mode within a structure of a deformation system, and the evolutionary stage of the system.

Therefore, we should aim for an even more comprehensive database including deformation data with a higher spatial resolution, allowing areas and variation of strain accumulation to be resolved below 40 km. This can probably be done with the help of seismic sections covering a 3D volume, where information on the displacement of faults and their timing is gained from the stratigraphy. This would certainly require a lot of seismic sections. Possibly, for the later stages of deformation, paleoseismological data could be integrated when available in order to also increase the temporal resolution. Again, the robustness of data results against uncertainty in the initial data set has to be examined.

Also, we need to mathematically quantify geological observations and changes over time on different spatial scales. Unfortunately, outcrops where a given spatial pattern can be studied over various time scales are very rare. And it is almost

impossible to relate processes and patterns over time from outcrop data.

Certainly, our best resolved data are still those from modelling studies. They should try to quantify existing threshold values, and the robustness of studied parameters, e.g., by coupling them to other parameters (Is it still the same effect or not? Does the parameter have a first or second order influence?). The knowledge of threshold values simplifies the understanding of a particular parameter influence.

If modelling studies directly address a certain natural example (rather than staying general to be applicable to several similar natural examples), we can better relate the modelling study to natural data on smaller scales as well. Generally, models reproduce the big scale strain patterns for different orogens, which might look alike. However, as was shown in the viscous-brittle series (Chapter 7), even though a strain pattern on the orogen-scale looks similar, the variation on the subscales might be significantly different. Further modelling on the smaller scales should involve detailed analysis of small scale processes such as, e.g., fluid flow and fluid reactions.

10. References

- Adam, J., Urai, J.L., Wieneke, B., Oncken, O., Pfeiffer, K., Kukowski, N., Lohrmann, J., Hoth, S., van der Zee, W., Schmatz, J., 2004. Shear localisation and strain distribution during tectonic faulting - new insights from granular-flow experiments and high-resolution optical image correlation techniques. *Journal of Structural Geology* 27, 283-301.
- Allègre, C. J., Lemouel, J.L., Provost, A., 1982. Scaling rules in rock fracture and possible implications for earthquake prediction. *Nature*, 297, 47-49.
- Allmendinger, R.W., Gubbels, T., 1996. Pure and simple shear plateau uplift, Altiplano-Puna, Argentina and Bolivia. *Tectonophysics* 259, 1-13.
- Allmendinger, R.W., Jordan, T.E., Mahlburg Kay, S., Isacks, B.L., 1997. The evolution of the Altiplano-Puna Plateau of the Central Andes. *Annual Reviews of Earth and Planetary Science* 25, 139-174.
- ANCORP-Working Group, 2003. Seismic imaging of an active continental margin – the Central Andes (ANCORP'96). *Journal of Geophysical Research* 108, doi: 10.1029/2002JB001771.
- Babeyko, A.Y., Sobolev, S.V., Trumbull, R.B., Oncken, O., Lavier, L.L., 2002. Numerical models of crustal scale convection and partial melting beneath the Altiplano-Puna plateau. *Earth and Planetary Science Letters* 199, 373-388.
- Babeyko, A.Y., Sobolev, S.V., 2005. Quantifying different modes of the late Cenozoic shortening in the central Andes. *Geology* 33, 621-624.
- Babeyko, A.Y., Sobolev, S.V., Vietor, T., Oncken, O., Trumbull, R.B., 2006. Numerical study of weakening processes in the Central Andean back-arc. In: Oncken, O., Chong, G., Franz, G., Giese, P., Götze, H.-J., Ramos, V.A., Strecker, M.R., Wigger, P. (Eds.), *The Andes – active Subduction Orogeny*, *Frontiers in Earth Science Series*, vol. 1, Springer Verlag, Berlin Heidelberg, New York, 495-512.
- Bak, P. 1996. *How nature works: the science of self-organized criticality*, Springer, New York, 212 pp.
- Bak, P., Chang, C., 1989. Earthquakes as a self-organized critical phenomenon. *Journal of Geophysical Research* 94, 15635-15637.
- Beck, S., Zandt, G., 2002. The nature of orogenic crust in the Andes. *Journal of Geophysical Research* 107, 2230, doi: 10.1029/2000JB000124.
- Behn, M.J., Lin, J., Zuber, M.T., 2002. A continuum mechanics model for normal faulting using a strain-rate softening rheology: implications for thermal and rheological controls on continental and oceanic rifting. *Earth and Planetary Science Letters* 202, 725-740.
- Bellahsen, N., Daniel, J.-M., Bollinger, L., Burov, E., 2003. Influence of viscous layers on the growth of normal faults: insights from experimental and numerical models, *Journal of Structural Geology* 25, 1471-1485.
- Ben-Zion, Y., Sammis, C.G., 2003. Characterization of Fault Zones. *Pure and Applied Geophysics* 160, 677-715.
- Billi, A., Storti, F., 2004. Fractal distribution of particle size in carbonate cataclastic rocks from the core of a regional strike-slip fault zone. *Tectonophysics* 384, 115-128.
- Biot, M., 1961. Theory of folding of stratified viscoelastic media and its implications in tectonics and orogenesis. *Geological Society of America Bulletin* 72, 1595-1620.
- Bonnet, E., Bour, O., Odling, N.E., Davy, P., Main, I., Cowie, P., Berkowitz, B., 2001. Scaling of fracture systems in geological media. *Reviews of Geophysics* 39, 347-383.
- Burg, J.P., Podladchikov, Y., 1999. Lithospheric scale folding: numerical modeling and application to the Himalayan syntaxes. *International Journal of Earth Sciences* 88, 190-200.
- Butler, R.F., Richards, D.R., Sempere, T., Marshall, L.G., 1995. Paleomagnetic determinations of vertical-axis tectonic rotations from Late Cretaceous and Paleocene strata of Bolivia. *Geology* 23, 799-802.
- Byerlee, J., 1978. Friction of rocks. *Pure and Applied Geophysics* 116, 615-626.
- Cagnard, F., Brun, J.-P., Gapais, D., 2006. Modes

- of thickening in analogue weak lithospheres. *Tectonophysics* 421, 145-160.
- Cartwright, J.A., Trudgill, B.D., Mansfield, C.S., 1995. Fault growth by segment linkage; an explanation for scatter in maximum displacement and trace length data from the Canyonlands Grabens of SE Utah. *Journal of Structural Geology* 17, 1319-1326.
- Chapple, W.M., Tullis, T.E., 1977. Evaluation of the forces that drive the plates. *Journal of Geophysical Research* 82, 1967-1984.
- Cladouhos, T.T., Marrett, R., 1996. Are fault growth and linkage models consistent with power-law distributions of fault lengths? *Journal of Structural Geology* 18, 281-293.
- Coney, P.J., Evenchick, C.A., 1994. Consolidation of the American cordilleras. *Journal of South American Earth Sciences* 7, 241-262.
- Corti, G., Bonini, M., Conticelli, S., Innocent, F., Manetti, P., Sokoutis, D., 2003. Analogue modelling of continental extension: a review focused on the relations between the patterns of deformation and the presence of magma. *Earth Science Reviews* 63, 169-247.
- Cowie, P.A., Scholz, C.H., 1992. Displacement-length scaling relationship for faults; data synthesis and discussion. *Journal of Structural Geology* 14, 1149-1156.
- Cruden, A.R., Nasser, M.H., Pysklywec, R., 2006. Surface topography and internal strain variation in wide hot orogens from three-dimensional analogue and two-dimensional numerical visco models. In: Buitter, S.J.H., Schreurs, G. (Eds.), *Analogue and Numerical Modelling of Crustal-Scale Processes*, Geological Society of London Special Publication 253, 79-104.
- Davy, P., Sornette, A., Sornette, D., 1992. Experimental discovery of scaling laws relating fractal dimensions and the length distribution exponent of fault systems. *Geophysical Research Letters* 19, 361-363.
- Dawers, N.H., Anders, M.A., Scholz, C.H., 1993. Fault length and displacement: scaling laws. *Geology* 21, 1107-1110.
- Dawers, N.H., Anders, M.A., 1995. Displacement-length scaling and fault linkage. *Journal of Structural Geology* 17, 607-514.
- Deutsch, C.V., Journel, A.G., 1992. *GSLIB Geostatistical Software Library and User's Guide*, Oxford University Press, 340 pp.
- Dewey, J.F., 1980. Episodicity, sequence and style at convergent plate boundaries. *Geological Association of Canada Special Paper* 20, 553-573.
- Echavarría, L., Hernández, R., Allmendinger, R., Reynolds, J., 2003. Subandean thrust and fold belt of northwestern Argentina: Geometry and timing of the Andean evolution. *American Association of Petroleum Geologists Bulletin* 87, 965-985.
- Ege, H., Sobel, E.R., Scheuber, E., Jacobshagen, V., 2007. Exhumation history of the southern Altiplano plateau (southern Bolivia) constrained by apatite fission track thermochronology. *Tectonics* 26, doi: 10.1029/2005TC001869.
- Eiler, J., Garzione, C., Ghosh, P., 2006. Response to Comment on „Rapid uplift of the Altiplano revealed through ¹³C-¹⁸O bonds in paleosol carbonates”. *Science* 314, 760 doi: 10.1126/science.1133131.
- Eisbacher, G.H., 1996. *Einführung in die Tektonik*, Enke Verlag, Stuttgart, 374 pp.
- Elger, K., 2003. *Analysis of deformation and tectonic history of the Southern Altiplano Plateau (Bolivia) and their importance for plateau formation*, Scientific Technological Report STR03/05, Potsdam, 152 pp.
- Elger, K., Oncken, O., Glodny, J., 2005. Plateau-style accumulation of deformation – the Southern Altiplano. *Tectonics* 24, doi: 10.1029/2004TC001675.
- Ellis, S., Beaumont, C., Jamieson, R.A., Quinlan, G., 1998. Continental collision including a weak zone: The visco model and its application to the Newfoundland Appalachians. *Canadian Journal of Earth Sciences* 35, 1323-1346.
- England, P., McKenzie, D., 1982. A thin viscous sheet model for continental deformation. *Geophysical Journal of the Royal Society of Astronomy* 70, 295-321.
- Fariás, M., Charrier, R., Comte, D., Martinod, J., Hérial, G., 2005. Late Cenozoic deformation and uplift of the western flank of the Altiplano: *Journal of Structural Geology* 17, 607-514.

- Evidence from the depositional, tectonic, and geomorphologic evolution and shallow seismic activity (northern Chile at 19°30'S). *Tectonics* 24, TC4001, doi: 10.1029/2004TC001667.
- Fletcher, R.C., 1974. Wavelength selection in the folding of a single layer with power law rheology. *American Journal of Science* 284, 1029-1043.
- Forsyth, D.W., Uyeda, S., 1975. On the relative importance of driving forces of plate motions. *Geophysical Journal of the Royal Astronomical Society* 43, 163-200.
- Fossen, H., Hesthammer, J., 1997. Geometric analysis and scaling relations of deformation bands in porous sandstone. *Journal of Structural Geology* 19, 1479-1493.
- Friedrich A.M., Wernicke, B.P., Niemi, N.A., Bennett, R.A., Davis, J.L., 2003. Comparison of geodetic and geologic data from the Wasatch region, Utah, and implications for the spectral character of Earth deformation at periods of 10 to 10 million years. *Journal of Geophysical Research* 108, 2199, doi: 10.1029/2001JB000682.
- Friedrich, A.M., Lee, J., Wernicke, B.P., Sieh, K., 2004. Geologic context of geodetic data across a Basin and Range normal fault, Crescent Valley, Nevada. *Tectonics* 23, TC2015, doi: 10.1029/2003TC001528.
- Gallagher, J.J., Jr., 1981. *Tectonics of China: Continental Style Cataclastic Flow. Mechanical Behavior of Crustal Rocks. The Handin Volume*, Washington, D.C., American Geophysical Union, *Geophysical Monograph* 24, 259-273.
- Garzzone, C.N., Molnar, P., Libarkin, J.C., MacFadden, B.J., 2006. Rapid late Miocene rise of the Bolivian Altiplano: Evidence for removal of mantle lithosphere. *Earth and Planetary Science Letters* 241, 543-556.
- Gephart, J.W., 1994. Topography and subduction geometry in the Central Andes: clues to the mechanics of a noncollisional orogen. *Journal of Geophysical Research* 99, 12279-12288.
- Gerbault, M., Willingshofer, E., 2005. Lower crust indentation or horizontal ductile flow during continental collision? *Tectonophysics* 387, 169-187.
- Ghosh, P., Garzzone, C.N., Eiler, J.M., 2006. Rapid uplift of the Altiplano revealed through ¹³C-¹⁸O bonds in paleosol carbonates. *Science* 311, 511-514.
- Giese, P., Scheuber, E., Schilling, F., Schmitz, M., Wigger, P., 1999. Crustal thickening processes in the Central Andes and the different natures of the Moho-discontinuity. *Journal of South American Earth Sciences* 12, 201-220.
- Gregory-Wodzicki, K.M., 2000. Uplift history of the Central and Northern Andes: a review. *Geological Society of America Bulletin* 112, 1091-1105.
- Gross, M.R., Gutiérrez-Alonso, G., Bai, T., Wacker, M.A., Collinsworth, K.B., 1997. Influence of mechanical stratigraphy and kinematics on fault scaling relations. *Journal of Structural Geology* 19, 171-183.
- Gubbels, T.L., Isacks, B.L., Farrar, E., 1993. High-level surfaces, plateau uplift, and foreland development, Bolivian Central Andes. *Geology* 21, 695-698.
- Gutscher, M.A., Maury, R., Eissen, J.P., Bourdon, E., 2000a. Can slab melting be caused by flat subduction? *Geology* 28, 535-538.
- Gutscher, M.A., Spakman, W., Bijwaard, H., Engdahl, E.R., 2000b. Geodynamics of flat subduction; seismicity and tomographic constraints from the Andean margin. *Tectonics* 19, 814-833.
- Hampel, A., Kukowski, N., Adam, J., 2004. Response of the tectonically erosive south Peruvian forearc to subduction of the Nazca Ridge: Analysis of three-dimensional analogue experiments. *Tectonics* 23, TC5003, doi: 10.1029/2003TC001585.
- Haschke, M., Günther, A., 2003. Balancing crustal thickening in arcs by tectonic vs. magmatic means. *Geology* 31, 933-936.
- Heuret, A., Lallemand, S., 2005. Plate motions, slab dynamics and back-arc deformation. *Physics of the Earth and Planetary Interiors* 149, 31-51.
- Hindle, D., Kley, J., 2002. Displacements, strains and rotations in the Central Andean plate boundary zone. In: Stein, S., Freymuller, J., (Eds.), *Plate Boundary Zones*, AGU Geodynamics Series 30, 135-144.
- Horton, B.K., 1999. Erosional control on the geometry and kinematics of thrust belt development

- in the Central Andes. *Tectonics* 18, 1292-1304.
- Hoth, S., Adam, J., Kukowski, N. Oncken, O., 2004. Influence of erosion on the kinematics of bivergent orogens: Results from scaled sandbox-simulations. In: Willett, S.D., Hovius, N., Brandon, M.T., Fisher, D.M. (Eds.), *Tectonics, Climate and Landscape Evolution*, Geological Society of America Special Paper 398, 201-226.
- Hoth, S., 2005. Deformation, erosion and natural resources in continental collision zones: insights from scaled sandbox simulations, PhD thesis, Freie Universität Berlin, <http://www.diss.fuberlin.de/2004/125/index.html>
- Hubbert, M.K., 1937. Theory of scale models as applied to the study of geological structures. *Geological Society of America Bulletin* 48, 1459-1520.
- Husson, L., Sempere, T., 2003. Thickening the Altiplano crust by gravity-driven crustal channel-flow. *Geophysical Research Letters* 30, doi: 10.1029/2002GL016877.
- Husson, L., Ricard, Y., 2004. Stress balance above subduction zones - application to the Andes. *Earth and Planetary Science Letters* 222, 1037-1050.
- Isacks, B.L., 1988. Uplift of the Central Andean Plateau and bending of the Bolivian Orocline. *Journal of Geophysical Research* 93, 3211-3231.
- Jackson, J., 2002. Faulting, flow, and the strength of the continental lithosphere. *International Geology Review* 44, 39-61.
- Journel, A.G., 1977. *Géostatistique minière: I. et II.* Centre de Géostatistique, Fontainebleau, 720 pp.
- Kagan, Y.Y., Jackson, D.D., 1991. Long-term earthquake clustering. *Geophysical Journal International* 104, 117-133.
- Kay, R.W., Mahlburg Kay, S., 1993. Delamination and delamination magmatism. *Tectonophysics* 219, 177-189.
- King, G.C.P., 1983. The accomodation of large strain in the upper lithosphere of the earth and other solids by self-similar fault systems: the geometrical origin of b-values. *Pure and Applied Geophysics* 121, 761-814.
- King, G., Oppenheimer, D., Amelung, F., 1994. Block versus continuum deformation in the western United States. *Earth and Planetary Science Letters* 128, 55-64.
- Klepeis, K.A., Clarke, G.L., Gehrels, G., Vervoort, J., 2004. Processes controlling vertical coupling and decoupling between the upper and lower crust of orogens: results from Fiordland, New Zealand. *Journal of Structural Geology* 26, 765-791.
- Kley, J., 1996. Transition from basement-involved to thin-skinned thrusting in the Cordillera Oriental of southern Bolivia. *Tectonics* 15, 763-775.
- Kley, J., Gangui, A.H., Krüger, D., 1996. Basement-involved blind thrusting in the eastern Cordillera Oriental, southern Bolivia: evidence from cross-sectional balancing, gravimetric and magnetotelluric data. *Tectonophysics* 259, 171-184.
- Kley, J., 1999. Geologic and geometric constraints on a kinematic model of the Bolivian orocline. *Journal of South American Earth Sciences* 12, 221-235.
- Klosko, E.R., Stein, S., Hindle, D., Kley, J., Norabuena, E., Dixon, T., Liu, M., 2002. Comparison of GPS, seismological, and geological observations of Andean mountain building. In: Stein, S., Freymuller, J., (Eds.), *Plate Boundary Zones*, AGU Geodynamics Series 30, 123-132.
- Koyi, H., 1995. Mode of internal deformation in sand wedges. *Journal of Structural Geology* 17, 293-300.
- Koyi, H.A., 1997. Analogue modeling: From a qualitative to a quantitative technique: A historical outline. *Journal of Petroleum Geology* 20, 223-283.
- Krantz, R.W., 1991. Measurement of friction coefficients and cohesion for faulting and fault reactivation in laboratory models using sand and sand mixtures. *Tectonophysics* 188, 203-207.
- Lamb, S.H., Hoke, L., Kennan, L., Dewey, J., 1997. Cenozoic evolution of the Central Andes in Bolivia and northern Chile. In: Burg, J.P., Ford, M. (Eds.), *Orogeny through time*, Geological Society of London Special Publication 121, 237-264.
- Lamb, S., Davis, P., 2003. Cenozoic climate change as a possible cause for the rise of the Andes. *Nature* 425, 792-797.

- Leffler, L., Stein, S., Mao, A., Dixon, T., Ellis, M.A., Ocola, L., Sacks, I.S., 1997. Constraints in present-day shortening rate across the central eastern Andes from GPS data. *Geophysical Research Letters* 24, 1031-1034.
- Liu, M., Yang, Y., Stein, S., Zhu, Y., Engeln, J., 2000. Crustal shortening in the Andes: Why do GPS rates differ from geological rates? *Geophysical Research Letters* 27, 3005-3008.
- Lohrmann, J., 2002. Identification of parameters controlling the accretive and tectonically erosive mass-transfer mode at the South-Central and North Chilean forearc using scaled 2D sandbox experiments, Scientific Technical Report 02/10, Potsdam, 231 pp.
- Lohrmann, J., Kukowski, N., Adam, J., Oncken, O., 2003. The impact of analogue material properties on the geometry, kinematics, and dynamics of convergent sand wedges. *Journal of Structural Geology* 25, 1691-1711.
- Macedo-Sánchez, O., Surmont, J., Kissel, C., Laj, C., 1992. New temporal constraints on the rotation of the Peruvian Central Andes obtained from paleomagnetism. *Geophysical Research Letters* 19, 1875-1878.
- Mandl, G., 1988. *Mechanics of tectonic faulting: models and basic concepts*, Elsevier, New York, 407 pp.
- Marone, C., 1998. Laboratory-derived friction laws and their application to seismic faulting. *Annual Reviews Earth Planetary Science Letters* 26, 643-696.
- Marques, F.O., Cobbold, P.R., 2002. Topography as a major factor in the development of arcuate thrust belts: insights from sandbox experiments. *Tectonophysics* 348, 247-268
- Marrett, R. A., Allmendinger, R. W., 1990. Kinematic analysis of faultslip data. *Journal of Structural Geology* 12, 973-986.
- Marrett, R.A., Allmendinger, R.W., Alonso, R.N., Drake, R.E., 1994. Late Cenozoic tectonic evolution of the Puna Plateau and adjacent foreland, northwestern Argentine Andes. *Journal of South American Earth Sciences* 7, 179-207.
- Martinod, J., Davy, P., 1994. Periodic instabilities during compression of the lithosphere, 2. Analogue Experiments. *Journal of Geophysical Research* 99, 12057-12069.
- Masek, J.G., Isacks, B.L., Gubbels, T.L., Fielding, E.J., 1994. Erosion and tectonics at the margins of continental plateaus. *Journal of Geophysical Research* 99, 13941-13956.
- Matheron, G., 1962. *Traité de Géostatistique Appliqué*, Vol. 1., Memoir BRGM 14, Paris, 334 pp.
- Matheron, G., 1970. *La théorie des variables régionalisées et ses applications*. Les Cahiers du Centre de Morphologie Mathématique de Fontainebleau, 212 pp.
- McKenzie, D.P., 1969. Speculations on the consequences and causes of plate motions. *Geophysical Journal of the Royal Astronomical Society* 18, 1-32.
- Meyer, B., Tapponnier, P., Bourjot, L., Métivier, F., Gaudemer, Y., Peltzer, G., Guo Shunmin, Chen Zhitai, 1998. Crustal thickening in Gansu-Qinghai, lithospheric mantle subduction, and oblique, strike-slip controlled growth of the Tibetan plateau. *Geophysical Journal International* 135, 1-47.
- Montgomery, D.R., Balco, G., Willett, S.D., 2001. Climate, tectonics, and the morphology of the Andes. *Geology* 29, 579-582.
- Morellato, C., Redini, F., Doglioni, C., 2003. On the number and spacing of faults. *Terra Nova* 15, 315-321.
- Mortimer, E., Carrapa, B., Coutand, I., Schoehnbohm, L., Sobel, E.R., Gomez, J.S., Strecker, M.R., 2007. Fragmentation of a foreland basin in response to out-of-sequence basement uplifts and structural reactivation: El Cajón–Campo del Arenal basin, NW Argentina. *Geological Society of America Bulletin* 119, 637-653.
- Müller, J.P., Kley, J., Jacobshagen, V., 2002. Structure and Cenozoic kinematics of the Eastern Cordillera, southern Bolivia (21°S). *Tectonics* 21, 1037 doi: 10.1029/2001TC001340.
- Mulugeta, G., Koyi, H., 1992. Episodic accretion and strain partitioning in a model sand wedge. *Tectonophysics* 202, 319-333.
- Nicol, A., Walsh, J.J., Watterson, J., Gillespie, Scientific Technical Report STR 07/09 DOI:10.2312/GFZ.b103-07094 GeoForschungsZentrum Potsdam

- P.A., 1996. Fault size distributions are they really power-law? *Journal of Structural Geology* 18, 191-197.
- Nur, A., Ron, H., Scotti, O., 1989. Kinematics and mechanics of tectonic block rotations. *Geophysical Monographs* 49, 31-46.
- Okubo, P.G., Aki, K. 1987. Fractal geometry in the San Andreas fault system. *Journal of Geophysical Research* 92, 345-355.
- Oncken, O., Hindle, D., Kley, J., Elger, K., Victor, P., Schemmann, K., 2006. Deformation of the Central Andean upper plate system – facts, fiction, and constraints for plateau models. In: Oncken, O., Chong, G., Franz, G., Giese, P., Götze, H.-J., Ramos, V.A., Strecker, M.R., Wigger, P. (Eds.), *The Andes – active Subduction Orogeny*, *Frontiers in Earth Science Series 1*, Springer Verlag, Berlin Heidelberg, New York, 2006, 3-27.
- Oncken, O., Chong, G., Franz, G., Giese, P., Götze, H.-J., Ramos, V.A., Strecker, M.R., Wigger, P. (Eds.), *The Andes – active Subduction Orogeny*. *Frontiers in Earth Science Series*, vol. 1, Springer Verlag, Berlin, Heidelberg, New York, 2006, 568 pp.
- Pardo-Casas, F., Molnar, P., 1987. Relative motion of the Nazca (Farallon) and South American plates since late Cretaceous time. *Tectonics* 6, 233-248.
- Pysklywec, R.N., Beaumont, C., Fullsack, P., 2002. Lithospheric deformation during the early stages of continental collision: Numerical experiments and comparison with South Island, New Zealand. *Journal of Geophysical Research* 107, 2133, doi: 10.1029/2001JB000252.
- Ranalli, G., 1987. *Rheology of the earth*. Allen and Unwin, Winchester, U.S.A., 348 pp.
- Rech, J.A., Currie, B.S., Michalski, G., Cowan, A.M., 2006. Neogene climate change and uplift in the Atacama desert, Chile. *Geology* 34, 761-764.
- Regenauer-Lieb, K., Hobbs, B., Yuen, D.A., Ord, A., Zhang, Y., Mulhaus, H.B., Morra, G., 2006. From point defects to plate tectonic faults. *Philosophical Magazine, Instabilities Across the Scales*, Special Issue 86, 3373-3392.
- Richardson, R.M., Solomon, S.C., Sleep, N.H., 1979. Tectonic stress in the plates. *Review of Geophysics* 17, 981-1019.
- Ritznitchenko, Yu.V., 1976. *Studies of Physics of the Earth*, Nauka, Moscow, 9-27.
- Roperch, P., Hérial, G., Fornari, M., 1999. Magnetostratigraphy of the Miocene Corque basin, Bolivia: Implications for the geodynamic evolution of the Altiplano during the late Tertiary. *Journal of Geophysical Research* 104, 20415-20429.
- Roperch, P., Fornari, M., Hérial, G., Parraguez, G.V., 2000. Tectonic rotations within the Bolivian Altiplano: Implications for the geodynamic evolution of the central Andes during the late Tertiary. *Journal of Geophysical Research* 105, 795-820.
- Rosenau, M., Oncken, O., Anderssohn, J., Kaufmann, H., Lohrmann, J., 2006. Shocks in a box - Analogue simulations of the seismic cycle in subduction settings. *Geophysical Research Abstracts* 8, 1-2.
- Rousse, S., Gilder, S., Fornari, M., Sempere, T., 2005. Insight into the Neogene tectonic history of the northern Bolivian Orocline from new paleomagnetic and geochronologic data. *Tectonics* 24, doi: 10.1029/2004TC001760.
- Royden, L.H., 1996. Coupling and decoupling of crust and mantle in convergent orogens: implications for strain partitioning in the crust. *Journal of Geophysical Research* 101, 17679-17705.
- Schellart, W.P., 2000. Shear test results for cohesion and friction coefficients for different granular materials; scaling implications for their usage in analogue modelling. *Tectonophysics* 324, 1-16.
- Scheuber, E., Bogdanic, T., Jensen, A., Reutter, K.-J., 1994. Tectonic development of the north Chilean Andes in relation to plate convergence and magmatism since the Jurassic. In: Reutter, K.-J., Scheuber, E., Wigger, P.J. (Eds.), *Tectonics of the southern Central Andes, structure and evolution of an active continental margin*, Springer, Berlin, 121-139.
- Schlunegger, F., Willett, S., 1999. Spatial and temporal variations in exhumation of the central Swiss Alps and implications for exhumation mechanisms. *Geological Society of America Special Publication* 154, 157-179.

- Scholz, C. H., Dawers, N. H., Yu, J.-Z., Anders, M. H., Cowie, P.A. 1993. Fault growth and fault scaling laws: preliminary results. *Journal of Geophysical Research* 98, 21951-21962.
- Schreurs, G., Buiter, S.J.H., Boutelier, D., Corti, G., Costa, E., Cruden, A.R., Daniel, J.-M., Hoth, S., Koyi, H.A., Kukowski, N., Lohrmann, J., Ravaglia, A., Schlische, R.W., Oliver, M., Withjack, M., Yamada, Y., Cavozi, C., Delventisette, C., Elder Brady, J.A., Hoffmann-Rothe, A., Mengus, J.-M., Montanari, D., Nilforoushan, F., 2006. Analogue benchmarks of shortening and extension experiments. In: Buiter, S.J.H., Schreurs, G. (Eds.), *Analogue and Numerical Modelling of Crustal-Scale Processes*, Geological Society of London Special Publication 253, 1-27.
- Sempere, T., Carlier, G., Soler, P., Fornari, M., Carlotto, V., Jacay, J., Arispe, O., Neraudeau, D., Cardenas, J., 2002. Late Permian–Middle Jurassic lithospheric thinning in Peru and Bolivia, and its bearing on Andean-age tectonics. *Tectonophysics* 345, 153-181.
- Sempere, T., Hartley, A., Roperch, P., 2006. Comment on “Rapid uplift of the Altiplano revealed through ^{13}C - ^{18}O bonds in paleosol carbonates”. *Science* 314, 760 doi: 10.1126/science.1132837.
- Sengör, A.M. Celâl, 1990. Plate tectonics and orogenic research after 25 years: A Tethyan Perspective. *Earth Science Reviews* 27, 1-201.
- Silva-González, P., 2004. Der südliche Altiplano im Tertiär: Sedimentäre Entwicklung und tektonische Implikationen, PhD thesis, Freie Universität Berlin, <http://www.diss.fuberlin.de/2004/125/index.html>
- Silver, P.G., Russo, R.M., Lithgow-Bertelloni, B.C., 1998. Coupling of South American and African Plate motion and plate deformation. *Science* 279, 60-63.
- Smith, R. B., 1975. A unified theory of the onset of folding, boudinage, and mullion structure. *Geological Society of America Bulletin* 86, 1601-1609.
- Sobel, E.R., Strecker, M.R., 2003. Uplift, exhumation, and precipitation: tectonic and climatic control of Late Cenozoic landscape evolution in the northern Sierras Pampeanas, Argentina. *Basin Research* 15, 431-451.
- Sobel, E.R., Hilley, G.E., Strecker, M.R., 2003. Scientific Technical Report STR 07/09 DOI:10.2312/GFZ.b103-07094
- Formation of internally drained contractional basins by aridity-limited bedrock incision. *Journal of Geophysical Research* 108, 2344, doi: 10.1029/2002B001883.
- Sobolev, S.V., Babeyko, A.Y., 2005. What drives orogeny in the Andes? *Geology* 33, 617-620.
- Somoza, R., 1998. Updated Nazca (Farallon)-South America relative motions during the last 40 My: Implications for mountain building in the central Andean region. *Journal of South American Earth Sciences* 11, 211-215.
- Somoza, R., Singer, S., Tomlinson, A., 1999. Paleomagnetic study of upper Miocene rocks from northern Chile: Implications for the origin of late Miocene-Recent tectonic rotations in the southern Central Andes. *Journal of Geophysical Research* 104, 22923-22936.
- Sornette, A., Davy, P., Sornette, D., 1990. Growth of fault patterns. *Physical Review Letters* 65, 2266-2269.
- Sornette, D., Davy P., 1991. Fault growth model and universal fault length distribution. *Geophysical Research Letters* 18, 17353-17361.
- Tassara, A., 2005. Interaction between the Nazca and South American plates and formation of the Altiplano–Puna plateau: Review of a flexural analysis along the Andean margin (15°–34°S). *Tectonophysics* 399, 39-57.
- Tchalenko, J.S., 1970. Similarities between shear zones of different magnitudes. *Bulletin of the Geological Society of America* 81, 1625-1640.
- Thatcher, W., 1995. Microplate versus continuum descriptions of active tectonic deformation. *Journal of Geophysical Research* 100, 3885-3894.
- Townend, J., Zoback, M.D., 2000. How faulting keeps the crust strong. *Geology* 28, 399-402.
- Townend, D.A., Sonder, L.J., 2001. Rheologic control of buoyancy-driven extension of the Rio Grande rift. *Journal of Geophysical Research* 106, 16515-16523.
- Trumbull, R.B., Riller, U., Oncken, O., Scheuber, E., Hongn, F., 2006. The time-space distribution of Cenozoic arc volcanism in the Central Andes: a new data compilation and its tectonic implications. In: Oncken, O., Chong, G., Franz, G., Giese, P., GeoForschungsZentrum Potsdam

- Götze, H.-J., Ramos, V.A., Strecker, M.R., Wigger, P. (Eds.), *The Andes – active Subduction Orogeny*, *Frontiers in Earth Science Series 1*, Springer Verlag, Berlin Heidelberg, New York, 2006, 29-44.
- Turcotte, D.L., 1986. A fractal model for crustal deformation, *Tectonophysics* 132, 261-269.
- Turcotte, D.L., 1992. *Fractals and chaos in geology and geophysics*. New York, Cambridge University Press, 422 pp.
- Turcotte, D.L., Glasscoe, M.T., 2004. A damage model for the continuum rheology of the upper continental crust. *Tectonophysics* 383, 71-80.
- Vanderhaeghe, O., Teyssier, C., 2001. Partial melting and flow of orogens. *Tectonophysics* 342, 451-472
- Victor, P., Oncken, O., Glodny, J., 2004. Uplift of the western Altiplano Plateau: Evidence from the Precordillera between 20°S and 21°S (northern Chile). *Tectonics* 23, doi: 10.1029/2003TC001519.
- Vietor, T., Oncken, O., 2005. Controls on the shape and kinematics of the Central Andean plateau flanks: Insights from numerical modelling. *Earth and Planetary Science Letters* 236, 814-827.
- Vietor, T., 2007, pers.comm.
- Walsh, J.J., Watterson, J., 1988. Analysis of the relationship between displacements and dimensions of faults. *Journal of Structural Geology* 10, 239-247.
- Watterson, J., 1986. Fault dimension, displacements and growth. *Pure and Applied Geophysics* 124, 365-373.
- Wdowinski, S., Bock, Y., 1994a. The evolution of deformation and topography of high elevated plateaus 1. Model, numerical analysis, and general results. *Journal of Geophysical Research* 99, 7103-7119.
- Wdowinski, S., Bock, Y., 1994b. The evolution of deformation and topography of high elevated plateaus 2. Application to the central Andes. *Journal of Geophysical Research* 99, 7121-7130.
- Wesnousky, S., 1994. The Gutenberg-Richter or Characteristic Earthquake Distribution, which is it? *Bulletin of the Seismological Society of America* 84, 1940-1959.
- Willett, S., Beaumont, C., Fullsack, P., 1993. Mechanical model for the tectonics of doubly vergent compressional orogens. *Geology* 21, 371-374.
- Willingshofer, E., Sokoutis, D., Burg, J.-P., 2005. Lithospheric-scale analogue modelling of collision zones with a pre-existing weak zone. In: Gapais, D., Brun, J.-P., Cobbold, P.R. (Eds.), *Deformation Mechanisms, Rheology and Tectonics: from Minerals to the Lithosphere*, Geological Society of London Special Publication 243, 277-294.
- Wojtal, S. F. 1994. Fault scaling laws and the temporal evolution of fault systems. *Journal of Structural Geology* 16, 603-612.
- Wojtal, S. F., 1996. Changes in fault displacement populations correlated to linkage between faults. *Journal of Structural Geology* 18, 265-279.
- Yañez, G.A., Ranero, C.R., von Huene, R., Diaz, J., 2001. Magnetic anomaly interpretation across the southern Central Andes (32°-34°S); the role of the Juan Fernandez Ridge in the late Tertiary evolution of the margin. *Journal of Geophysical Research* 106, 6325-6345.
- Yuan, X., Sobolev, S.V., Kind, R., Oncken, O., Bock, G., Asch, G., Schurr, B., Graeber, F., Rudloff, A., Hanka, W., Wylegalla, K., Tibi, R., Haberland, C., Rietbrock, A., Giese, P., Wigger, P., Roewer, P., Zandt, G., Beck, S., Wallace, T., Pardo, M., Comte, D., 2000. Subduction and collision processes in the Central Andes constrained by converted seismic phases. *Nature* 408, 958-96.
- Zeitler, P.K., Koons, P.O., Bishop, M.P., Chamberlain, C.P., Craw, D., Edwards, M.A., Hamidullah, S., Jan, M.Q., Khan, M.A., Khattak, M. U.K., Kidd, W.S.F., Mackie, R.L., Meltzer, A.S., Park, S.K., Pecher, A., Poage, M.A., Sarker, G., Schneider, D.A., Seeber, L., Shroder, J.F., 2001. Crustal reworking at Nanga Parbat, Pakistan: Metamorphic consequences of thermal-mechanical coupling facilitated by erosion. *Tectonics* 20, 712-728.
- Zoback, M.D., Townend, J., 2001. Implications of hydrostatic pore pressures and high crustal strength for the deformation of intraplate lithosphere. *Tectonophysics* 336, 19-30.
- Zoback, M.D., Townend, J., Grollimund, B., 2002. Steady-state failure equilibrium and deformation

of intraplate lithosphere. *International Geology Review* 44, 383-401.

Appendix A-1

Deformation Database

DEFORMATION DATA BANK

ALTIPLANO PLATEAU

Oncken, O., Hindle, D., Kley, J., Elger, K., Victor, P. and Schemmann, K.

Deformation of the Central Andean upper plate system –

Facts, fiction, and constraints for plateau models

Locality	latitude °S (N border)	latitude °S (S border)	center point (latitude °S)	longitude °W (W border)	longitude °W (E border)	center point (longitude °W)	beginning (Ma)	end (Ma)	kinematics	reference
Western Cordillera, Chuca-Lauca basin	18	19	18,5	68,6	69,5	69,05	22	7,5	c	[9]
Western Cordillera, Chuca-Lauca basin	18	19	18,5	68,6	69,5	69,05	12	0,5	c	[9]
Precordillera, Western Cordillera	18,2	19	18,6	69,1	69,4	69,25	8	0	c, ss	[18], [21], [69]
Precordillera	20	22,5	21,25	68,6	69,8	69,2	46	38	c	[24], [39]
Precordillera	22	22,5	22,25	68,7	69,1	68,9	10	0	ss	[67]
Altiplano, W-flank, Western Cordillera	13	15	14	75	77	76	44	38	c	[53]
Altiplano, W-flank, Western Cordillera	13	15	14	75	77	76	25	8	c	[53]
Altiplano, W-flank	15	16	15,5	72	75	73,5	2,5	1	c	[47]
Altiplano, W-flank	15	16	15,5	72	75	73,5	1	0	e	[47]
Altiplano, W-flank	17	18	17,5	69,5	70,5	70	22	6	c	[63]
Altiplano, W-flank	18	18,9	18,45	69,2	69,8	69,5	22	6	c	[21], [51], [70]
Altiplano, W-flank	18,3	18,7	18,5	69,4	69,9	69,65	9	7,7	c	[20]
Altiplano, W-flank	18,8	19,2	19	69,7	70	69,85	>27	22	c	[21]
Altiplano, W-flank	19	19,7	19,35	69	69,8	69,4	22	6	c	[18], [21], [55]
Altiplano, W-flank	19	22	20,5	68,7	69,3	69	7	0	tt	[18], [69]
Altiplano, W-flank	20	21	20,5	68,5	69,5	69	29	23	c	[69]
Altiplano, W-flank	20	21	20,5	68,5	69,5	69	20	7	c	[69]
Altiplano, W-flank	21,5	22,5	22	68,5	69	68,75	12	6	c	[7], [24]
Altiplano Peru	13	15	14	71	73	72	7	2,5	e	[47]
Altiplano Peru	13	15	14	71	73	72	2,5	1	c	[47]

Locality	latitude °S (N border)	latitude °S (S border)	center point (latitude °S)	longitude °W (W border)	longitude °W (E border)	center point (longitude °W)	beginning (Ma)	end (Ma)	kinematics	reference
Altiplano Peru	13	15	14	71	73	72	1	0	e	[47]
Altiplano Peru	13	15	14	71	73	72	27	8	c	[53]
Altiplano Peru	15	17	16	69	72	70,5	45	30	c	[8], [44]
Altiplano Peru	15	17	16	69	72	70,5	20	15	c	[44]
Altiplano Peru	15	17	16	69	72	70,5	12	5	c	[44]
Altiplano, Tambo-Tambillo	19,3	20,2	19,75	67	67,5	67,25	>30	25	c	[38]
Altiplano, Tambo-Tambillo	19,3	20,2	19,75	67	67,5	67,25	17	13-10	c	[33], [38]
Altiplano, S	20	21	22	66,8	68,5	67,65	33	28	c	[16], [17]
Altiplano, S	20	21	22	66,8	68,5	67,65	28	19	c	[5], [17]
Altiplano, S	20	21	22	66,8	68,5	67,65	19	8	c	[16], [17], [31]
Corque Syncline	16,5	18,5	17,5	67,5	68,5	68	10	5,4	c	[26], [33], [38], [59]
Corque Syncline	16,5	18,5	17,5	68	68,5	68,25	5	0	c	[38]
Corque Syncline	17	18	17,5	68,3	69,5	68,9	28	14	c	[5], [45]
Corque Syncline	17,5	18,5	18	67	68	67,5	14	10	tt	[26], [59]
Calama Basin	22	22,5	22,25	68,3	69	68,65	25	7	ss	[43], [67]
Calama Basin	22	22,5	22,25	68,3	69	68,65	5	0	tp	[43], [67]
Atacama Basin	22,5	23,5	23	68	68,4	68,2	7	0	c	[19], [30], [31], [52]
Atacama Basin, Pacciencia fault			23,05			68,5	33,70	16,40	e	[54]
Atacama Basin, Cordillera de la Sal			23,2			68,4	16,4-11,2		e	[54]
Atacama Basin	22,5	24	23,25	67,8	68,4	68,1	18-17	12-10	c	[30], [31], [37], [50], [52], [57], [58]

Locality	latitude °S (N border)	latitude °S (S border)	center point (latitude °S)	longitude °W (W border)	longitude °W (E border)	center point (longitude °W)	beginning (Ma)	end (Ma)	kinematics	reference
Atacama, Cordillera Domeyko	22,5	24	23,25	68,3	68,8	68,55	60	38	c	[30], [37], [52], [57]
Atacama, Cordillera Domeyko	22,5	24	23,25	68,3	68,8	68,55	12	0	c	[52]
Salar Fault System			23,6			68,3	5	0	c	[54]
Atacama Basin	23,5	23,7	23,6	67,9	68,05	67,975	2,4-3,8	<2,4- 2,8	tp	[37]
Atacama Basin	23,5	24,1	23,8	68,05	68,15	68,1	3,2±0,3	<1	c	[37]
Puna, W-flank	22,5	24	23,25	67,5	68	67,75	12	0	c	[37], [49], [52]
Puna, W-flank	25	25,5	25,25	69	69,5	69,25	46	40	c	[39]
Puna, W-flank	25	26	25,5	69	69,5	69,25	12	0	c	[4], [10]
Salar de Antofalla	25,1	26,6	25,85	67	68	67,5	28	25	c	[36]
Salar de Antofalla	25,1	26,6	25,85	67	68	67,5	20	17	c	[36]
Salar de Antofalla	25,3	25,6	25,45	67,1	67,7	67,4	<5,3±0,3	<1,7	ss	[36]
Salar de Antofalla	25,7	26,6	26,15	67,5	68	67,75	12	10	c	[36]
Salar de Antofalla	25,7	26,6	26,15	67,5	68	67,75	4	0	c	[36]
Puna	21,7	23	22,35	65	66,2	65,6	14	12,5- 8,8	c	[11]
Puna	21,7	23	22,35	65	66,2	65,6	9	<9	tt	[11]
Puna	23	26	24,5	65,5	67,7	66,6	15-13	1	c	[40], [46], [68]
Puna	23	26	24,5	65,5	67,7	66,6	1,5-0,2	0	tp, ss	[40], [49]
Puna	24	25	24,5	67,3	68,2	67,75	>24	11-10	c	[13], [40]
Puna	24	26	25	66	67,7	66,85	28-24	15	c	[40], [68]
Puna	24,5	24,8	24,65	66,5	67,1	66,8	<5	0	c	[40]

Locality	latitude °S (N border)	latitude °S (S border)	center point (latitude °S)	longitude °W (W border)	longitude °W (E border)	center point (longitude °W)	beginning (Ma)	end (Ma)	kinematics	reference
Puna	25,3	25,5	25,4	66,8	67,3	67,05	5,86±0,14	0,5-1	c	[40]
Puna	25,3	26,1	25,7	65,6	66,1	65,85	13,4±0,4	3	c	[40]
Puna	26	26,5	26,25	65,7	66,3	66	>9,5±0,3	4,8±0,3	c	[40]
Puna	26	27	26,5	66,5	68,5	67,5	4-2	2	c	[70]
Puna	26	27	26,5	66,5	68,5	67,5	2	0	e	[31]
Puna	26,4	27,4	26,9	66,1	67,2	66,65	6,7 ±0,05	2,35	c	[1], [40]
Puna	26,5	26,9	26,7	67,1	67,5	67,3	10,4 ±0,05	1,3±0,6	c	[40]
Puna	26,5	26,9	26,7	67,1	67,5	67,3	1,3±0,6	<1,3 ±0,6	c	[40]
Puna	26,5	27,5	27	66,2	67,2	66,7	2	0	c, (e)	[1]
Puna	26,6	27,2	26,9	66	66,3	66,15	10,7±1,7	2,51 ±0,6	c	[40]
Eastern Cordillera, W-margin	17	18,5	17,75	65,5	67	66,25	42	30	c	[38]
Eastern Cordillera, W-margin	17	19	18	66	68	67	30-25	20-16	c	[5], [26], [28], [38], [59]
Eastern Cordillera, W-margin	20,5	21,5	21	65,5	66,5	66	30	17	c	[16], [48]
Eastern Cordillera, W-margin	20,5	21,5	21	65,5	66,5	66	19	8	c	[17], [48]
Eastern Cordillera, W-margin	20,5	21,5	21	66,3	66,7	66,5	33	27	c	[16], [17]
Eastern Cordillera, N	14,5	17,5	16	66	68,5	67,25	28-27	19	c	[5], [65]
Eastern Cordillera, N	16,5	17,5	17	66,5	67,5	67	45	35	c	[6], [38]
Cochabamba Shear zone	17,5	18,5	18	64,5	67,5	66	7	0	tp	[33], [38]
Eastern Cordillera, C	15,5	16,5	16	67,2	68,2	67,7	15	10	c	[6], [38], [42]
Eastern Cordillera, C	17	21,5	19,25	65	66,5	65,75	25-21	8-10	c, tp	[23], [25], [29], [33], [48]

Locality	latitude °S (N border)	latitude °S (S border)	center point (latitude °S)	longitude °W (W border)	longitude °W (E border)	center point (longitude °W)	beginning (Ma)	end (Ma)	kinematics	reference
Eastern Cordillera, C	17	22	19,5	65	66,5	65,75	42-40	21-25	c	[16], [27], [29], [48]
Eastern Cordillera, C	19	19,1	19,05	65,15	65,2	65,175	4	3	ss	[33]
Eastern Cordillera, C	21	23	22	64,5	66,5	65,5	23-19	>9-10	c	[2], [5], [60]
Eastern Cordillera, E	17	21	19	64,5	65,5	65	35	10	c	[16], [29]
Eastern Cordillera, S	22	23	22,5	64,6	66	65,3	40	30	c	[60]
Eastern Cordillera, S	22	24	23	64,6	66,5	65,55	<7	<2	c	[2], [40], [60], [61]
Eastern Cordillera, S	22,7	23,15	22,925	65	65,5	65,25	40-35	10-3	c	[12]
Eastern Cordillera, S	23	26	24,5	64,5	66,5	65,5	40	33	c	[61]
Eastern Cordillera, S	24	25	24,5	64,8	66,2	65,5	17-12	7	c	[41]
Eastern Cordillera, S	24	25	24,5	64,8	66,2	65,5	7	0	c	[41]
Eastern Cordillera, S	25,5	26,5	26	65	66,2	65,6	20	2	c	[3], [22]
Interandean	21	22	21,5	64,3	65,3	64,8	30	6-9	c	[5], [16], [34], [62]
Subandean	19	22	20,5	63	64,5	63,75	10	0	c	[14]
Subandean	20	23	21,5	63	64	63,5	10	0	c	[3], [5], [31]
Subandean	20,5	21,5	21	63,3	64,3	63,8	11	2	c	[3], [5], [16], [31], [48]
Subandean	20,5	21,5	21	62,6	63,5	63,05	8	0	c	[3], [5], [16], [31], [48]
Subandean	22,5	23	22,75	64,8	65	64,9	8,5-9	7,5	c	[15]
Subandean	22,5	23	22,75	64	64,2	64,1	4-4,5	<3,2	c	[15]
Subandean	22,5	23	22,75	63,7	63,9	63,8	2,5-3	1,2	c	[15]
Subandean	22,5	23	22,75	63,5	65	64,25	9	7	c	[15]

Locality	latitude °S (N border)	latitude °S (S border)	center point (latitude °S)	longitude °W (W border)	longitude °W (E border)	center point (longitude °W)	beginning (Ma)	end (Ma)	kinematics	reference
Subandean	22,5	23	22,75	64,6	64,8	64,7	8,5	7	c	[15]
Subandean	22,5	23	22,75	64,5	64,6	64,55	7,6	4,5-5	c	[15]
Subandean	22,5	23	22,75	63,5	65	64,25	7	2	c	[15]
Subandean	22,5	23	22,75	64,4	64,5	64,45	6,9	<4,7	c	[15]
Subandean	22,5	23	22,75	63,5	65	64,25	4,5	0	c	[15]
Santa Barbara belt	24	25,5	24,75	64,5	65	64,75	<30	>9-10	c, (e)	[3]
Santa Barbara belt	24	25,5	24,75	64	65	64,5	2-5	1-0	c, (e)	[3], [35], [40]
Santa Barbara belt	24	25,5	24,75	64,5	65	64,75	1	0	tt	[3], [40]
Sierras Pampeanas	26	33	29,5	64	69	66,5	11-8	2-4	c	[2], [32], [56], [66]
Sierras Pampeanas	26	33	29,5	64	69	66,5	4-3	0	c	[32], [66]

Each of the data sets consist of the following:

- name of the region in the study areas of given references are located,
- coordinates of boundaries defining polygons and its center points in which the study areas are located,
- beginning and end of deformation activity in millions of years (Ma),
- kinematics inferred from field studies (c – compressive, e – extensive, tt – transtensional, tp – transpressional, ss – strike-slip)
- references which contribute any of the given information.

We scanned each of the references for the mentioned details, which we weighted, and in certain cases reinterpreted, according to the following criteria:

- number and quality of the methods used for age constraints (e.g. isotopic age dating, sedimentary or structural cross-cutting relationships, seismic data, apatite-fission-track data),
- clear and detailed documentation of : a) used method, b) sample collection, c) sample processing, d) location of both study area and samples,
- number of available references for one location (e.g. spatial or temporal overlap of data),
- accuracy of spatial and temporal coverage,
- age of publication.

[1]

Allmendinger, R.W., 1986. Tectonic development, southeastern border of the Puna Plateau, northwestern Argentine Andes. *Geological Society of America Bulletin*, 97: 1070-1082.

[2]

Allmendinger, R.W., Gubbels, T., Isacks, B. and Cladouhos, T.T., 1993. Lateral variations in Late Cenozoic deformation, Central Andes, 20-28°S, Second International Symposium on Andean Geodynamics, Oxford, pp. 155-158.

[3]

Allmendinger, R.W. and Gubbels, T., 1996. Pure and simple shear plateau uplift, Altiplano-Puna, Argentina and Bolivia. *Tectonophysics*, 259(1-3): 1-13.

[4]

Audin, L., Hérail, G., Riquelme, R., Darrozes, J., Martinod, J. and Font, E., 2003. Geomorphological markers of faulting and neotectonic activity along the western Andean margin, northern Chile. *Journal of Quaternary Science*, 18(8): 681-694.

[5]

Baby, P., Rochat, P., Mascle, G. and Hérail, G., 1997. Neogene shortening contribution to crustal thickening in the back arc of the Central Andes. *Geology*, 25(10): 883-886.

[6]

Benjamin, M.T., Johnson, N.M. and Naeser, C.W., 1987. Recent rapid uplift in the Bolivian Andes: evidence from fission-track dating. *Geology*, 15(7): 680-683.

[7]

Buddin, T.S., Stimpson, I.G. and Williams, G.D., 1993. North Chilean forearc tectonics and Cenozoic plate kinematics. *Tectonophysics*, 220(1-4): 193-203.

[8]

Carlotto, V., Carlier, G., Jaillard, E., Sempere, T. and Mascle, G., 1999. Sedimentary and structural evolution of the Eocene-Oligocene Capas Rojas basin: evidence for a late Eocene lithospheric delamination event in the southern Peruvian Altiplano, Fourth International Symposium on Andean Geodynamics, Göttingen, pp. 141-145.

[9]

Charrier, R., Hérail, G., Flynn, J.J., Riquelme, R., García, M., Croft, D. and Wyss, A.R., 2002. El Cordón Chapiquiña en el borde occidental del Altiplano chileno: significado paleogeográfico y contexto tectónico regional. *Proceedings ninth Congreso Geológico Chileno, Puerto Varas*, pp. 763-767.

[10]

Chong, G., 2003, personal communication

[11]

Cladouhos, T.T., Allmendinger, R.W., Coira, B. and Farrar, E., 1994. Late Cenozoic deformation in the Central Andes: fault kinematics from the northern Puna, northwestern Argentina and southwestern Bolivia. *Journal of South American Earth Sciences*, 7(2): 209-228.

[12]

Coutand, I., Cobbold, P., Chauvin, A., Rossello, E. and Lopez-Gamundi, O., 1999. Cenozoic deformation and tectonic style of the Puna plateau (northwestern Argentina, Central Andes), Fourth International Symposium on Andean Geodynamics, Göttingen, pp. 192-196.

[13]

Coutand, I., Gautier, P., Cobbold, P., de Urreiztieta, M., Chauvin, A., Gapais, D., Rossello, E. and Lopez-Gammundi, O., 2001. Style and history of Andean deformation, Puna Plateau, northwestern Argentina. *Tectonics*, 20: 210-234.

[14]

Dunn, J.F., Hartshorn, K.G. and Hartshorn, P.W., 1995. Structural styles and hydrocarbon potential of the Subandean thrust belt of southern Bolivia. In: A.J. Tankard, R.S., Soruco and H.J. Welsink (Editors), *Petroleum basins of South America*. AAPG Memoir 62: 523-543.

[15]

Echavarria, L., Hernandez, R., Allmendinger, R. and Reynolds, J., 2003. Subandean thrust and fold belt of northwestern Argentina; geometry and timing of the Andean evolution. *AAPG Bulletin*, 87(6): 965-985.

[16]

Ege, H., 2004. Exhumations- und Hebungsgeschichte der zentralen Anden in Südbolivien (21°S) durch Spaltspur-Thermochronologie an Apatit. PhD Thesis, Freie Universität, <http://www.diss.fu-berlin.de/2004/64/index.html>, Berlin, Germany, 161 pp.

[17]

Elger, K., Oncken, O. and Glodny, J., 2005. Plateau-style accumulation of deformation: Southern Altiplano. *Tectonics*, 24: TC4020, doi: 10.1029/2004TC001675.

[18]

Farias, M., Charrier, R., Comte, D., Martinod, J. and Hérail, G., 2005. Late Cenozoic uplift of the western flank of the Altiplano: evidence from the depositional, tectonic, and geomorphologic evolution and shallow seismic activity (northern Chile at 19°30'S). *Tectonics*, 24: TC4001, doi: 10.1029/2004TC001667.

[19]

Flint, S., Turner, P., Jolley, E.J. and Hartley, A.J., 1993. Extensional tectonics in convergent margin basins; an example from the Salar de Atacama, Chilean Andes. *Geological Society of America Bulletin*, 105(5): 603-617.

[20]

Garcia, M., Hérail, G. and Charrier, R., 1999. Age and structure of the Oxaya anticline: a major feature of the Miocene compressive structures of northernmost Chile, Fourth International Symposium on Andean Geodynamics, Göttingen, pp. 249-252.

[21]

García, M., Hérail, G., Charrier, R., Mascle, G., Fornani, M. and de Arce, C.P., 2002. Oligocene-Neogene tectonic evolution of the Altiplano of Northern Chile (18-19°S), Fifth International Symposium on Andean Geodynamics, Toulouse, pp. 235-238.

[22]

Grier, M.E., Salfity, J.A. and Allmendinger, R.W., 1991. Andean reactivation of the Cretaceous Salta rift, northwestern Argentina. *Journal of South American Earth Sciences*, 4(4): 351-372.

[23]

Gubbels, T.L., Isacks, B.L. and Farrar, E., 1993. High-level surfaces, plateau uplift, and foreland development, Bolivian Central Andes. *Geology*, 21: 695-698.

[24]

Haschke, M. and Guenther, A., 2003. Balancing crustal thickening in arcs by tectonic vs. magmatic means. *Geology*, 31(11): 933-936.

[25]

Hérail, G., Oller, J., Baby, P., Bonhomme, M. and Soler, P., 1996. Strike-slip faulting, thrusting and related basins in the Cenozoic evolution of the southern branch of the Bolivian Orocline: *Tectonophysics*, 259: 201-212.

[26]

Hérail, G., Rochat, P., Baby, P., Aranibar, O., Lavenu, A. and Mascle, G., 1997. El Altiplano norte de Bolivia: Evolucion Geológica Terciaria. In: R. Charrier (Editor), *El Altiplano - Ciencia y conciencia en los Andes*. Universidad de Chile - Vicerrectoria Academica y Estudiantil – Departamento de Postgrado y Postitulo, Santiago de Chile.

[27]

Horton, B.K., 1998. Sediment accumulation on top of the andean orogenic wedge: Oligocene to late Miocene basins of the Eastern Cordillera, southern Bolivia. *Geological Society of America Bulletin*, 110(9): 1174-1192.

[28]

Horton, B.K., Hampton, B.A., Lareau, B.N. and Baldellon, E., 2002. Tertiary provenance history of the northern and central Altiplano (Central Andes, Bolivia); a detrital record of plateau-margin tectonics. *Journal of Sedimentary Research*, 72(5): 711-726.

[29]

Horton B.K., 2005. Revised deformation history of the central Andes: Inferences from Cenozoic foredeep and intermontane basins of the Eastern Cordillera, Bolivia. *Tectonics*, 24: TC3011, doi: 10.1029/2003TC001619.

[30]

Jolley, E.J., Turner, P., Williams, G.D., Hartley, A.J. and Flint, S., 1990. Sedimentological response of an alluvial system to Neogene thrust tectonics, Atacama Desert, northern Chile. *Journal of the Geological Society of London*, 147(5): 769-784.

[31]

Jordan, T.E. and Alonso, R.N., 1987. Cenozoic Stratigraphy and Basin Tectonics of the Andes Mountains, 20°-28° South Latitude. *American Association of Petroleum Geologists Bulletin*, 71(1): 49-64.

[32]

Jordan, T.E., 2000. Deformation and topography in the Sierras Pampeanas, Argentina; responses to flat-subduction, *Geological Society of America, Abstracts with Programs*, 32(7): 505.

[33]

Kennan, L., Lamb, S. and Rundle, C., 1995. K-Ar dates from the Altiplano and Cordillera Oriental of Bolivia; implications for Cenozoic stratigraphy and tectonics. *Journal of South American Earth Sciences*, 8(2): 163-186.

[34]

Kley, J., 1996. Transition from basement-involved to thin-skinned thrusting in the Cordillera Oriental of southern Bolivia. *Tectonics*, 15(4): 763-775.

[35]

Kley, J. and Monaldi, C.R., 2002. Tectonic inversion in the Santa Barbara System of the central Andean foreland thrust belt, northwestern Argentina. *Tectonics*, 21(6): 11-1 - 11-18.

[36]

Kraemer, B., Adelman, D., Alten, M., Schnurr, W., Erpenstein, K., Kiefer, E., van den Boogard, P. and Görler, K., 1999. Incorporation of the Paleogene foreland into the Neogene Puna Plateau: The Salar de Antofalla area, NW Argentina. *Journal of South American Earth Sciences*, 12: 157-182.

[37]

Kuhn, D., 2002. Fold-and-thrust belt structures and strike-slip faulting at the SE margin of the Salar de Atacama Basin, Chilean Andes. *Tectonics*, 21(4): 10.1029/2001TC901042.

[38]

Lamb, S. and Hoke, L., 1997. Origin of the high plateau in the Central Andes, Bolivia, South America. *Tectonics*, 16(4): 623-649.

[39]

Maksaev, V. and Zentilli, M., 1999. Fission track thermochronology of the Domeyko Cordillera, northern Chile; implications for Andean tectonics and porphyry copper metallogenesis, Latin American mineral deposits. *Canadian Institute of Mining Metallurgy and Petroleum, Montreal, PQ, Canada*, pp. 65-89.

[40]

Marrett, R.A., Allmendinger, R.W., Alonso, R.N. and Drake, R.E., 1994. Late Cenozoic tectonic evolution of the Puna Plateau and adjacent foreland, northwestern Argentine Andes. *Journal of South American Earth Sciences*, 7(2): 179-207.

[41]

Marrett, R. and Strecker, M.R., 2000. Response of intracontinental deformation in the Central Andes to late Cenozoic reorganization of South American Plate motions. *Tectonics*, 19(3): 452-467.

[42]

Masek, J.G., Isacks, B.L., Gubbels, T.L. and Fielding, E.J., 1994. Erosion and tectonics at the margins of continental plateaus. *Journal of Geophysical Research*, 99(B7): 13941-13956.

[43]

May, G., Hartley, A.J. and Stuart, F.M., 1996. Oligocene-recent sedimentary and tectonic evolution of the Calama basin, N. Chilean forearc, Third International Symposium on Andean Geodynamics, St. Malo (France), pp. 435-437.

[44]

McKee, E.H. and Noble, D.C., 1989. Cenozoic tectonic events, magmatic pulses, and base- and precious-metal mineralization in the Central Andes. In: G.E. Ericksen, M.T.C. Pinochet and J.A. Reinemund (Editors), *Geology of the Andes and its relation to hydrocarbon and mineral resources*. Circum-Pacific Council for Energy and Mineral Resources, Earth Science Series. Circum-Pacific Council for Energy and Mineral Resources, Houston, TX, United States, pp. 189-194.

[45]

McQuarrie, N. and DeCelles, P., 2001. Geometry and structural evolution of the Central Andean backthrust belt, Bolivia. *Tectonics*, 20(5): 669-692.

[46]

McQuarrie, N., 2002. Initial plate geometry, shortening variations, and evolution of the Bolivian Orocline. *Geology*, 30(10): 867-870.

[47]

Mercier, J.L., Sebrier, M., Lavenu, A., Cabrera, J., Bellier, O., Dumont, J.-F. and Machare, J., 1992. Changes in the tectonic regime above a subduction zone of Andean type: the Andes of Peru and Bolivia during the Pliocene-Pleistocene. *Journal of Geophysical Research*, 97(8): 11,945-11,982.

[48]

Müller, J.P., Kley, J. and Jacobshagen, V., 2002. Structure and Cenozoic kinematics of the Eastern Cordillera, southern Bolivia (21°S). *Tectonics*, 21(5): 1037, doi: 10.1029/2001TC001340.

[49]

Mon, R., Mena, R. and Amengual, R., 1996. Plegamiento cenozoico del basamento proterozoico de la cordillera oriental del norte argentino. *Revista de la Asociación Geológica Argentina*, 51(3): 213-223.

[50]

Mpodosis, C., Arriagada, C. and Roperch, P., 1999. Cretaceous to Paleogene geology of the Salar de Atacama basin, northern Chile: a reappraisal of the Purilactis group stratigraphy, Fourth International Symposium on Andean Geodynamics, Göttingen, pp. 523-526.

[51]

Muñoz, N. and Charrier, R., 1996. Uplift of the western border of the Altiplano on a westvergent thrust system, northern Chile. *Journal of South American Earth Sciences*, 9(3-4): 171-181.

[52]

Muñoz, N., Charrier, R. and Jordan, T., 2002. Interactions between basement and cover during the evolution of the Salar de Atacama, northern Chile. *Revista Geológica de Chile*, 29(1): 55-80.

[53]

Noblet, C., Lavenue, A. and Marocco, R., 1996. Concept of continuum as opposed to periodic tectonism in the Andes. *Tectonophysics*, 255(1-2): 65-78.

[54]

Pananont, P., Mpodozis, C., Blanco, N., Jordan, T.E. and Brown, L.D., 2004. Cenozoic evolution of the northwestern Salar de Atacama. *Tectonics*, 23: TC6007, doi: 10.1029/2003TC001595.

[55]

Pinto, L., Hérail, G. and Charrier, R., 1999. Sedimentary register of the Cenozoic deformation of the western border of the Altiplano in northern Chile (region of Tarapacá, 19°00' - 19°30'), Fourth International Symposium on Andean Geodynamics, Göttingen, pp. 593-596.

[56]

Ramos, V.A., Cristallini, E.O. and Perez, D.J., 2002. The Pampean flat-slab of the Central Andes. *Journal of South American Earth Sciences*, 15(1): 59-78.

[57]

Reutter, K.-J., Charrier, R., Götze, H.-J., Schurr, B., Wigger, P., Scheuber, E., Giese, P., Reuther, C.-D., Schmidt, S., Rietbrock, A., Chong, G. and Belmonte-Pool, A., this volume. The Salar de Atacama basin: a subsiding block within the western edge of the Altiplano-Puna Plateau.

[58]

Riquelme, R., Martinod, J., Hérail, G., Darrozes, J. and Charrier, R., 2003. A geomorphological approach to determining the Neogene to recent tectonic deformation in the Coastal Cordillera of Northern Chile (Atacama). *Tectonophysics*, 361: 255-275.

[59]

Rochat, P., Hérail, G., Baby, P., Mascle, G. and Aranibar, O., 1998. Analyse géométrique et modèle tectonosédimentaire de l'Altiplano Nord-Bolivien. *Comptes Rendus de l'Académie des Sciences, Serie II, Sciences de la Terre et des Planètes*, 327: 769-775.

[60]

Rubiolo, D., Seggiaro, R., Rodriguez, R., Disalvo, A. and Repol, D., 1999. Tectonic and sedimentary evolution of Cenozoic basins in the Eastern Cordillera, NW-Argentina (22°- 23°), Fourth International Symposium on Andean Geodynamics, Göttingen, pp. 630-633.

[61]

Salfity, J.A. and Marquillas, R.A., 1994. Tectonic and sedimentary evolution of the Cretaceous-Eocene Salta Group basin, Argentina. In: A. Salfity (Editor), Cretaceous tectonics of the Andes. Vieweg, Braunschweig, pp. 266-315.

[62]

Schmitz, M. and Kley, J., 1997. The geometry of the central Andean backarc crust: joint interpretation of cross-section balancing and seismic refraction data. *Journal of South American Earth Sciences*, 10(1): 99-110.

[63]

Sebrier, M., Mercier, J.L., Megard, F., Laubacher, G. and Carey, G.E., 1985. Quaternary normal and reverse faulting and the state of stress in the Central Andes of South Peru. *Tectonics*, 4(7): 739-780.

[64]

Sempere, T., Butler, R.F., Richards, D.R., Marshall, L.G., Sharp, W. and Swisher, C.C. III, 1997. Stratigraphy and chronology of upper Cretaceous - lower Paleogene strata in Bolivia and northwest Argentina. *Geological Society of America Bulletin*, 109(6): 709- 727.

[65]

Sempere, T., Hérail, G., Oller, J. and Bonhomme, M.G., 1990. Late Oligocene-Early Miocene major tectonic crisis and related basins in Bolivia. *Geology*, 18(10): 946-949.

[66]

Strecker, M.R., Cerveny, P., Bloom, A.L. and Malizia, D., 1989. Late Cenozoic tectonism and landscape development in the foreland of the Andes: Northern Sierras Pampeanas (26°-28°S), Argentina. *Tectonics*, 8: 517-534.

[67]

Tomlinson, A. and Blanco, N., 1997. Structural evolution and displacement history of the West Fault System, Precordillera, Chile: Part 1, synmineral history. *Actas VIII Congreso Geológico de Chile*, 3: 1873-1877.

[68]

Vandervoort, D.S., Jordan, T.E., Zeitler, P.K. and Alonso, R.N., 1995. Chronology of internal drainage development and uplift, southern Puna plateau, Argentine central Andes. *Geology*, 23(2): 145-148.

[69]

Victor P., Oncken, O. and Glodny, J., 2004. Uplift of the western Altiplano plateau: Evidence from the Precordillera between 20° and 21°S (northern Chile). *Tectonics*, 23: TC4004, doi:10.1029/2003TC001519.

[70]

Wörner, G., Hammerschmidt, K., Henjes-Kunst, F., Lezaun, J. and Wilke, H., 2000. Geochronology (⁴⁰Ar/³⁹Ar, K-Ar and He-exposure ages) of Cenozoic magmatic rocks from northern Chile (18-22°S): implications for magmatism and tectonic evolution of the Central Andes. *Revista Geológica de Chile*, 27(2): 205-240.

[\[71\]](#)

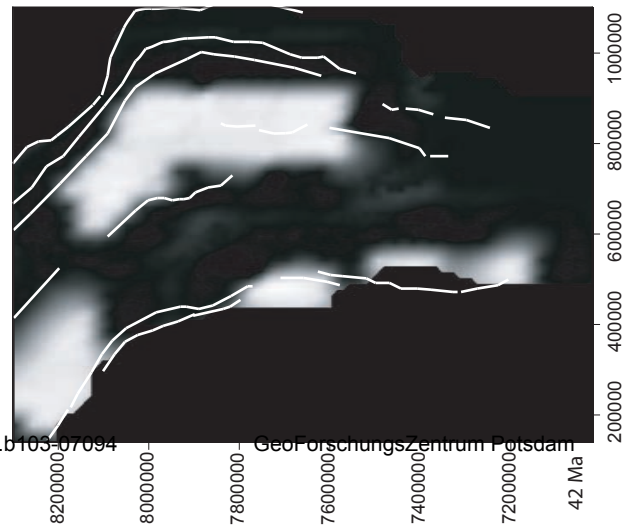
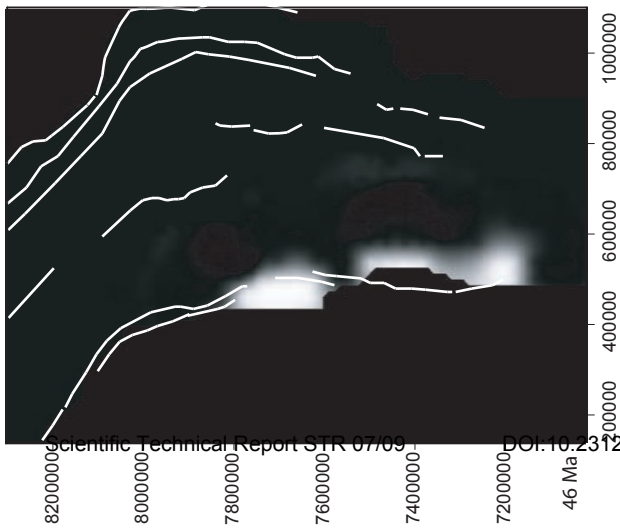
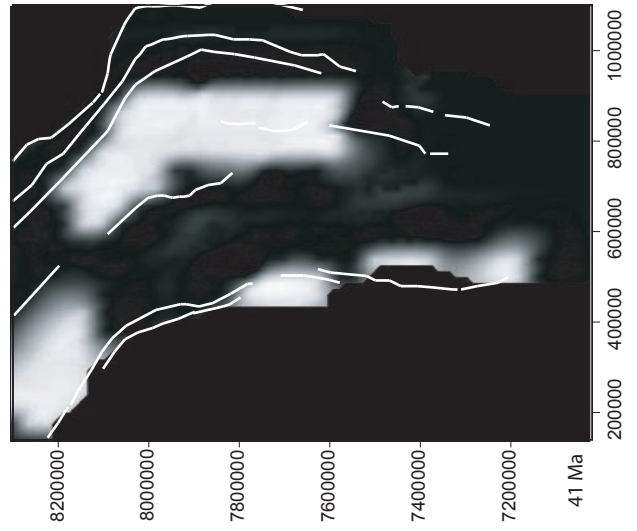
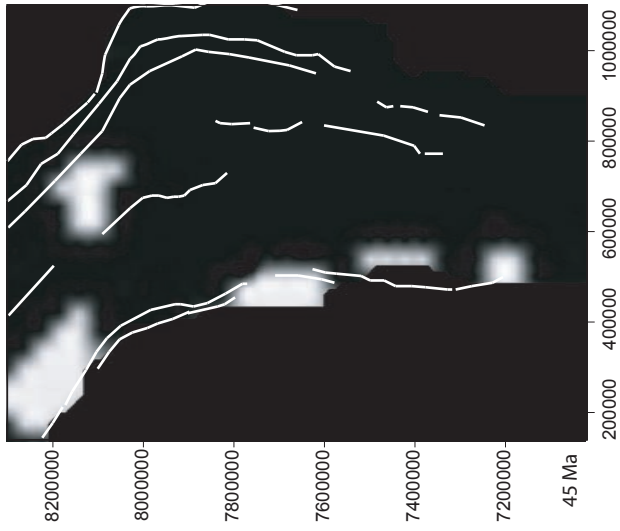
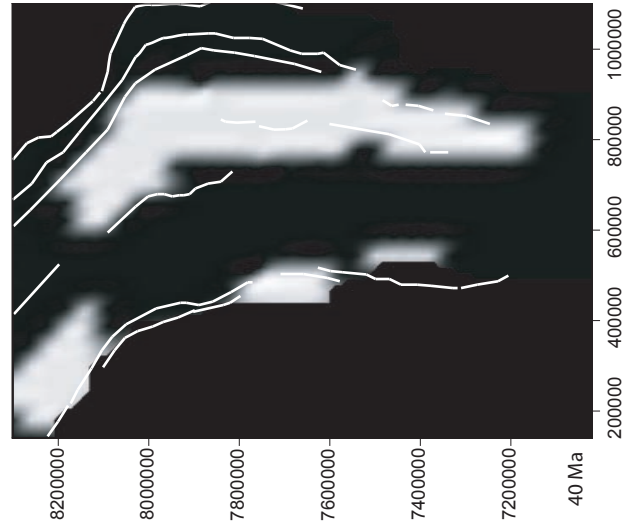
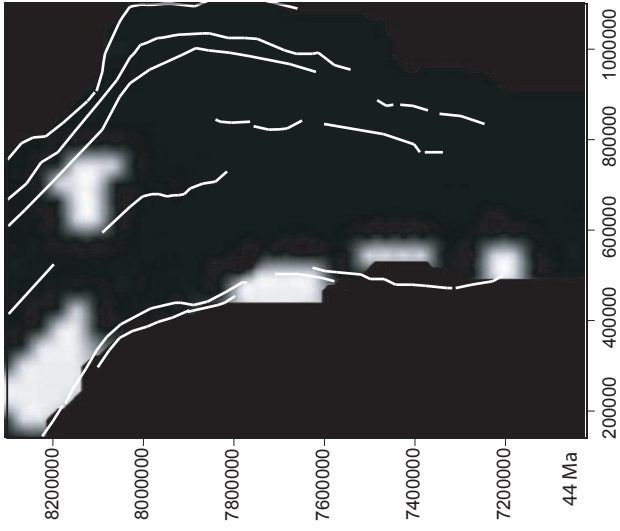
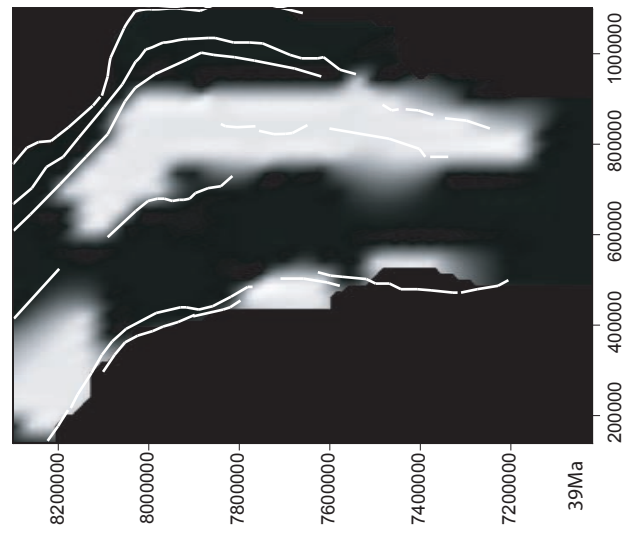
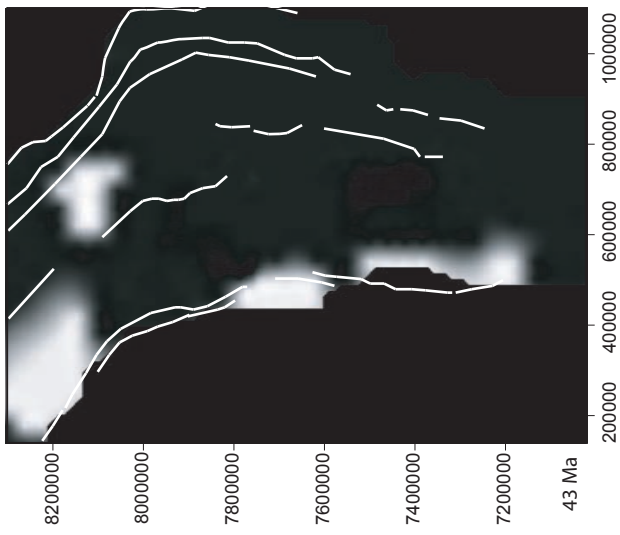
Wörner, G., Uhlig, D., Kohler, I. and Seyfried, H., 2002. Evolution of the West Andean Escarpment at 18 degrees S (N. Chile) during the last 25 Ma; uplift, erosion and collapse through time. *Tectonophysics*, 345: 183–198.

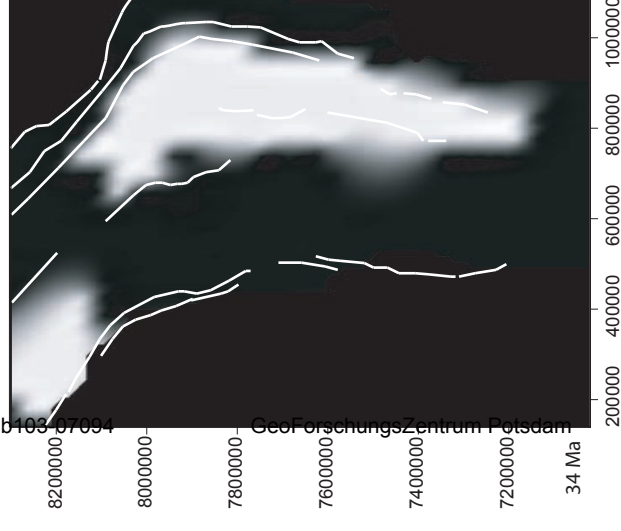
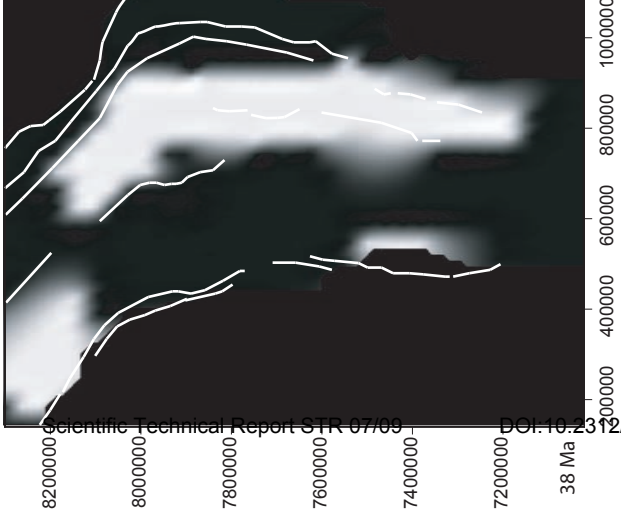
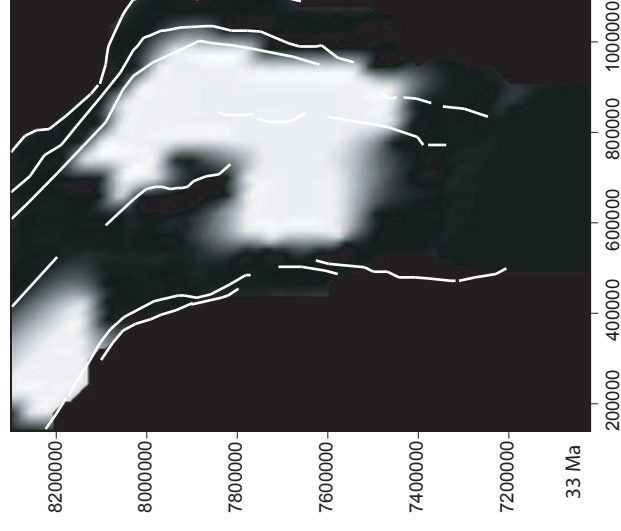
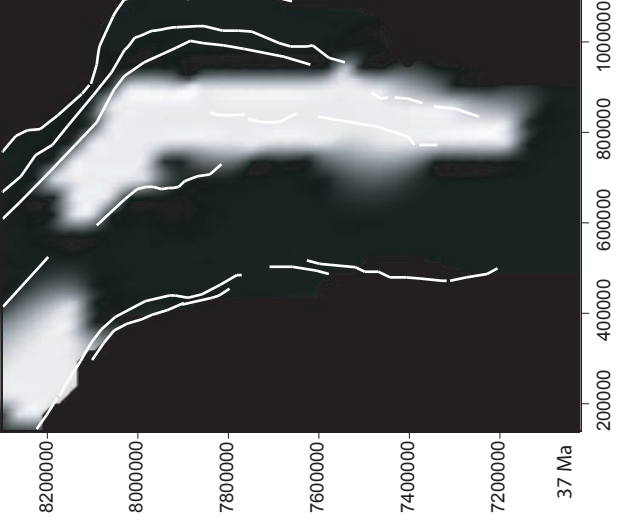
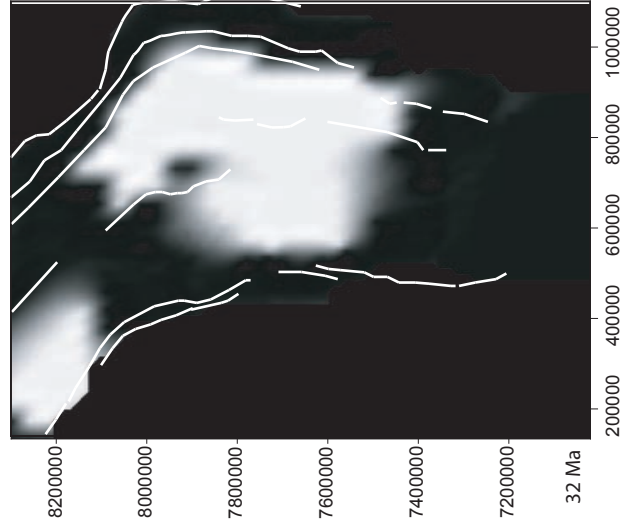
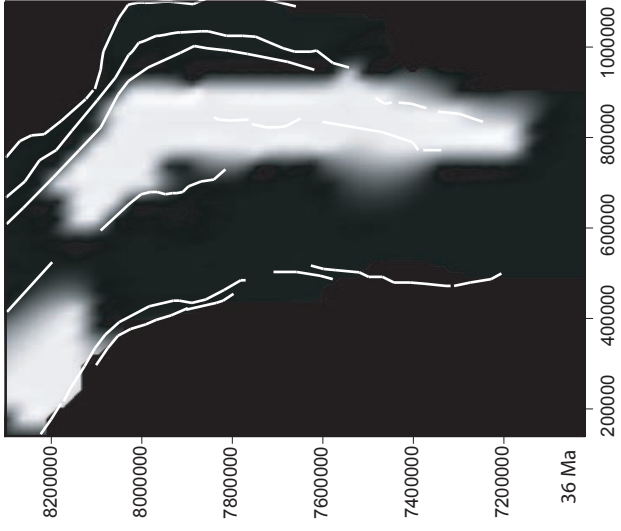
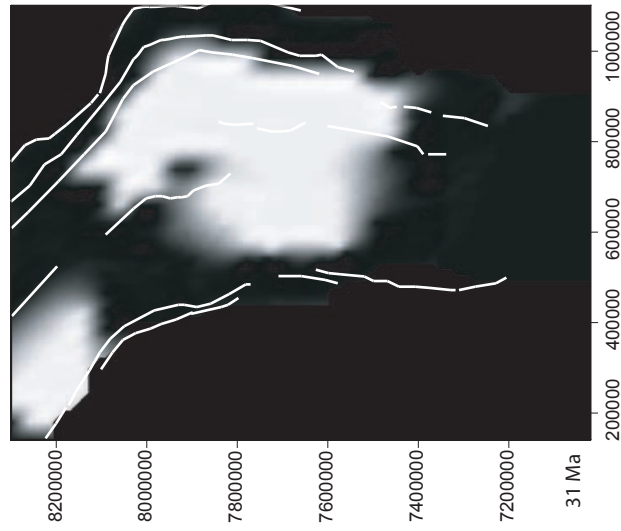
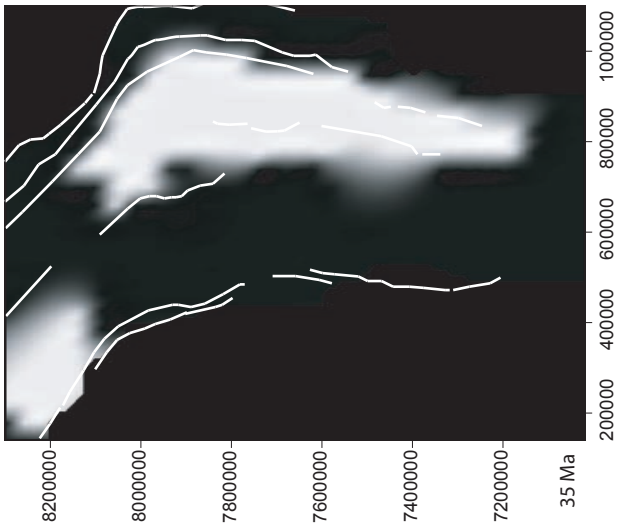
[\[72\]](#)

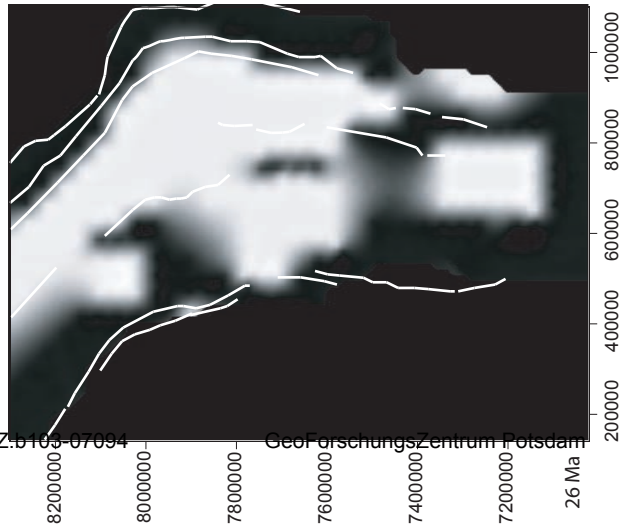
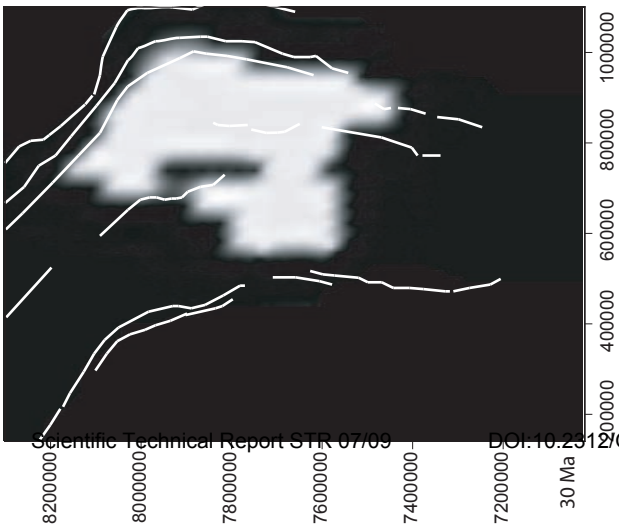
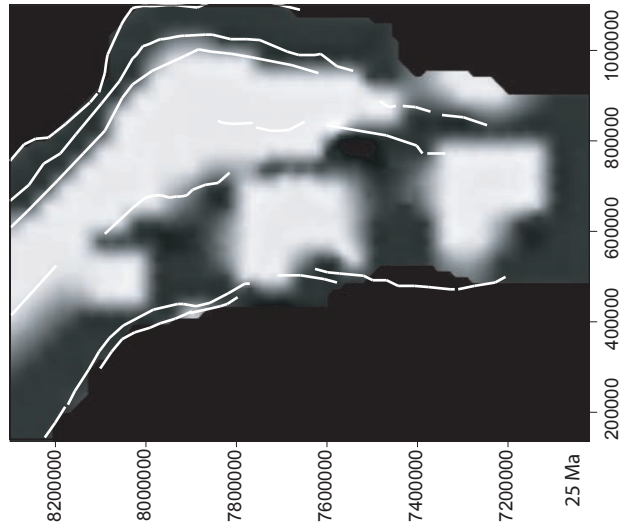
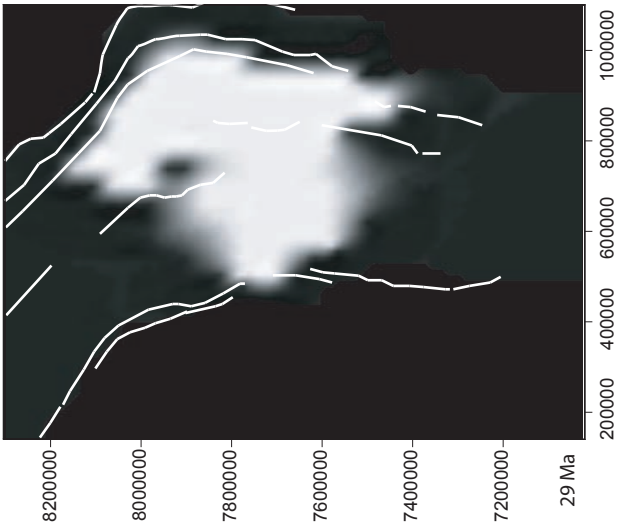
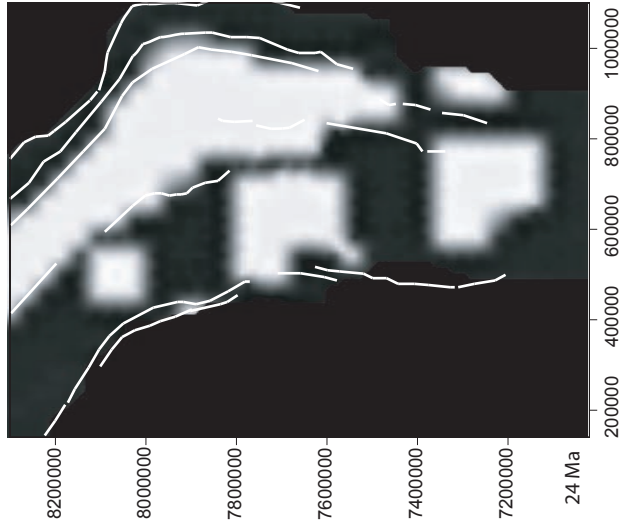
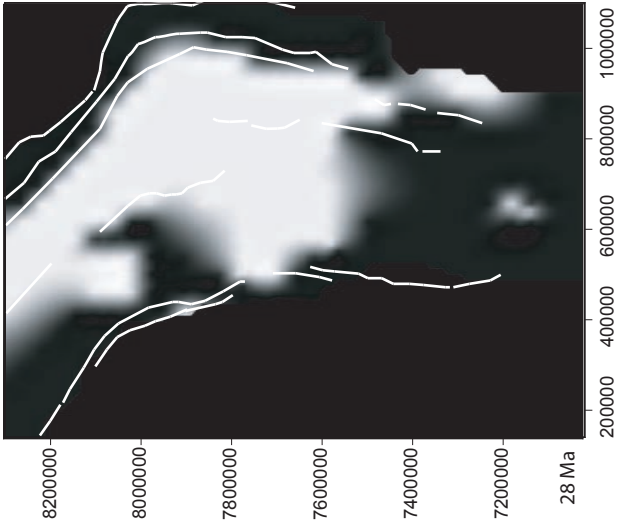
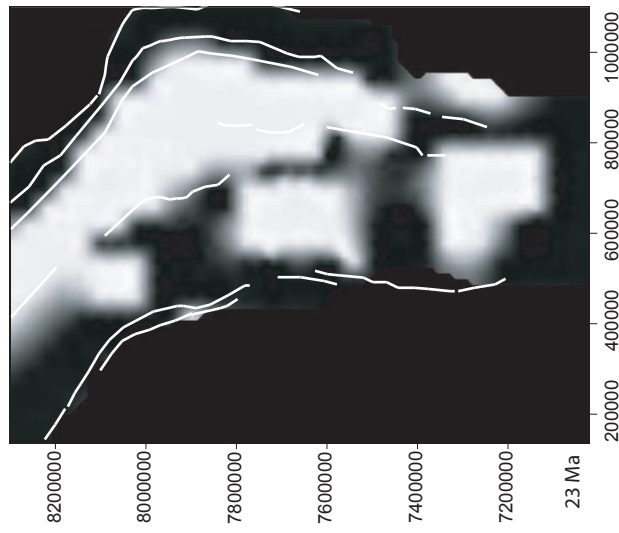
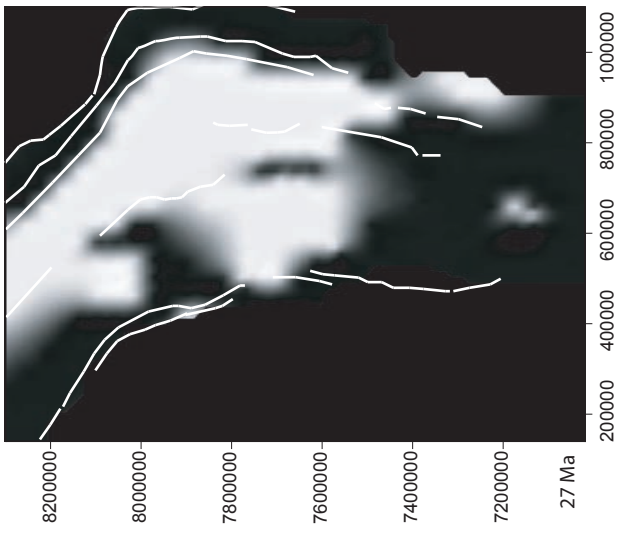
Zapata, T.R. and Allmendinger, R.W., 1996. Growth stratal records of instantaneous and progressive limb rotation in the Precordillera thrust belt and Bermejo Basin, Argentina. *Tectonics*, 15(5): 1065-1083.

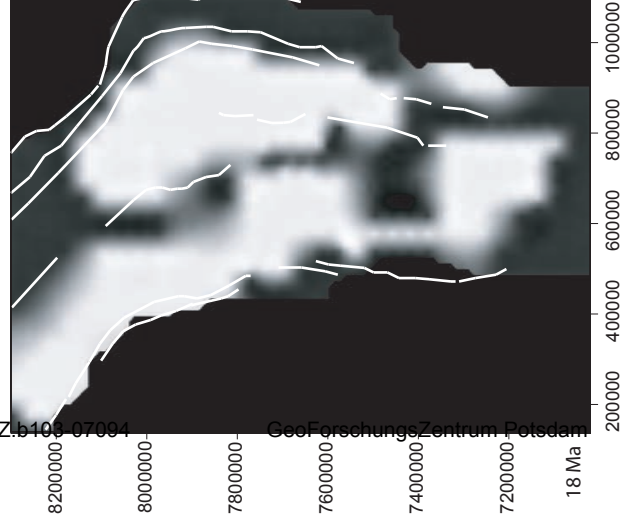
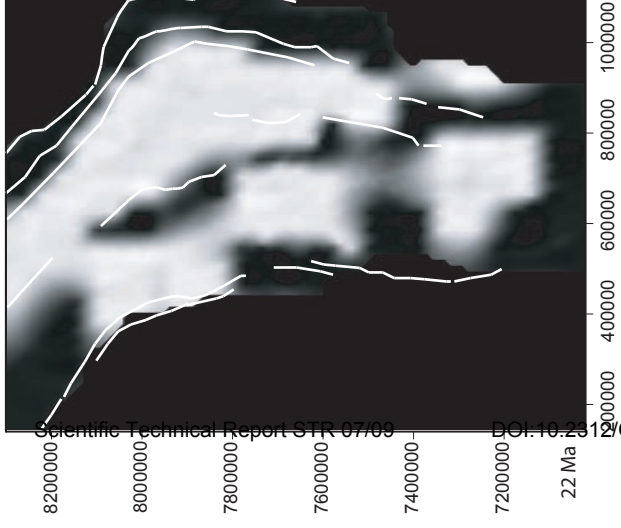
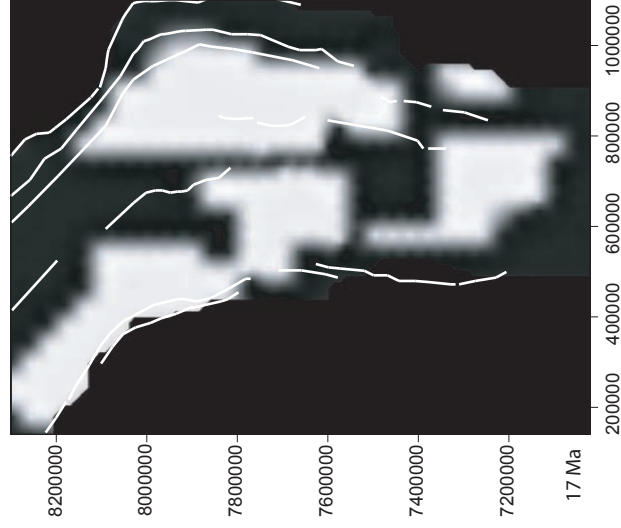
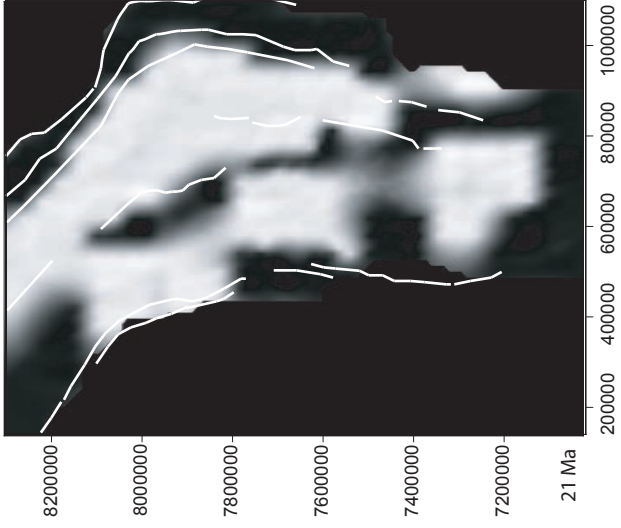
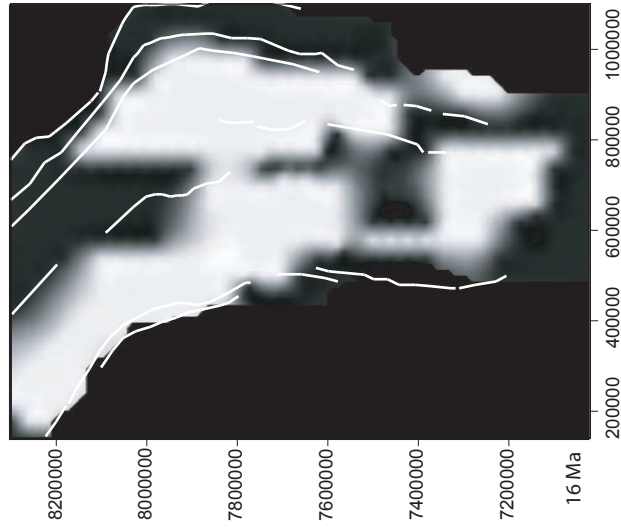
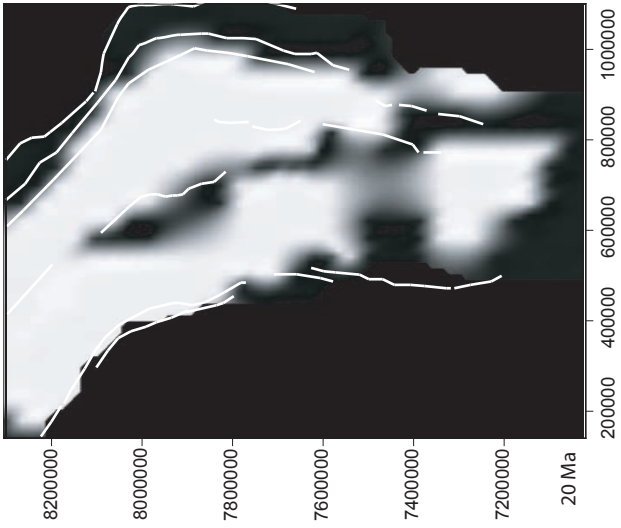
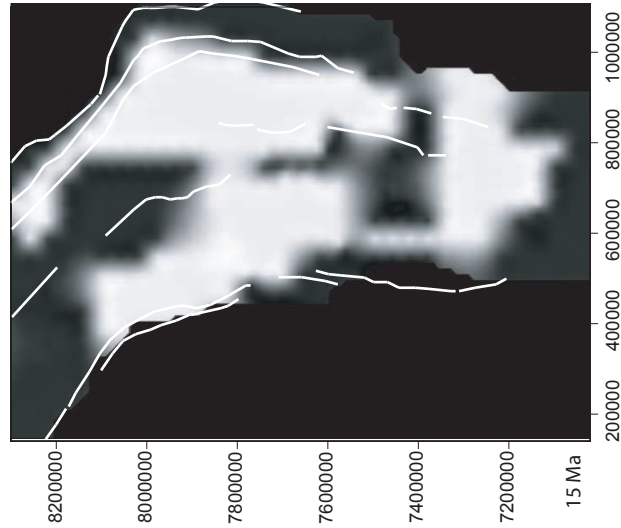
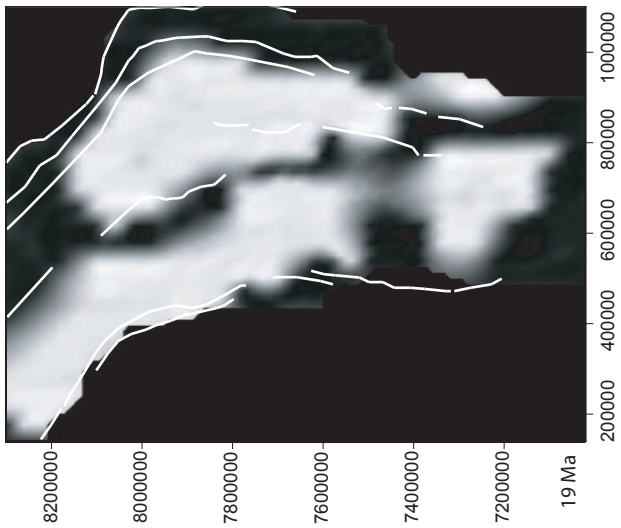
Appendix A-2

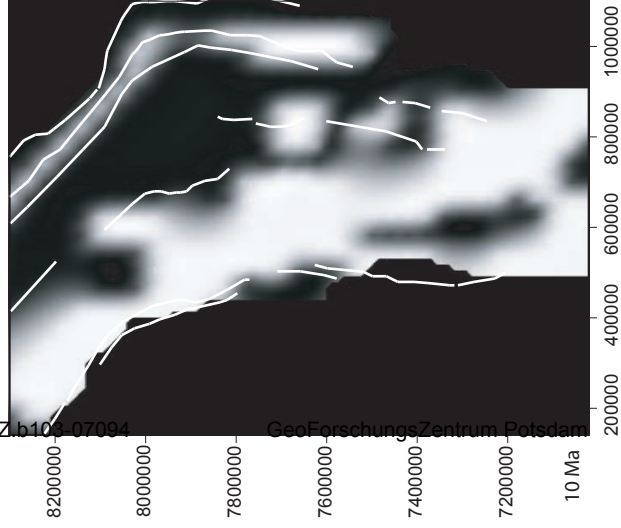
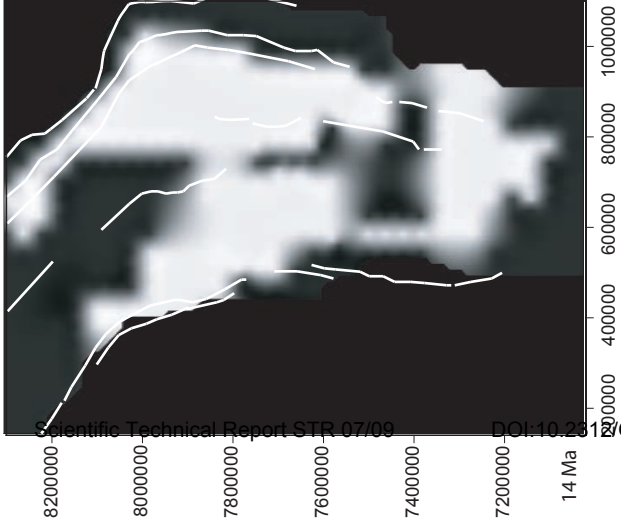
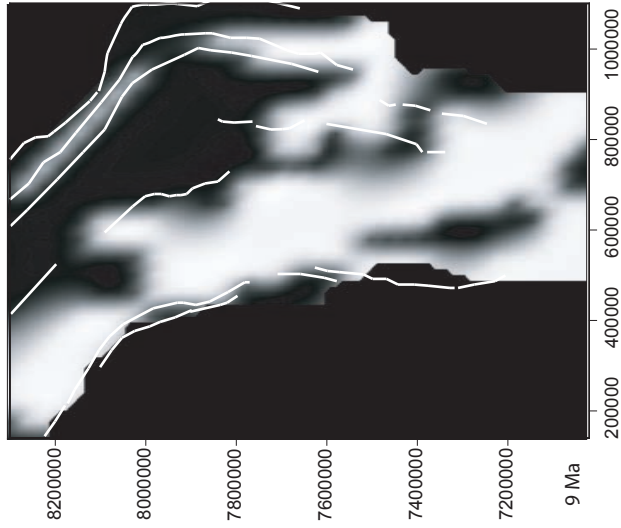
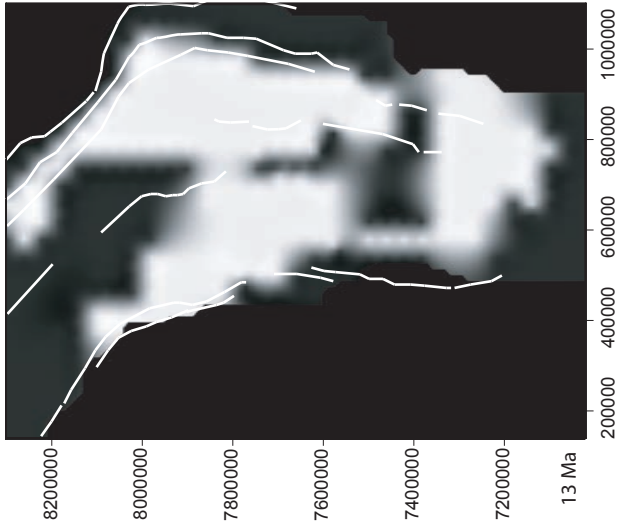
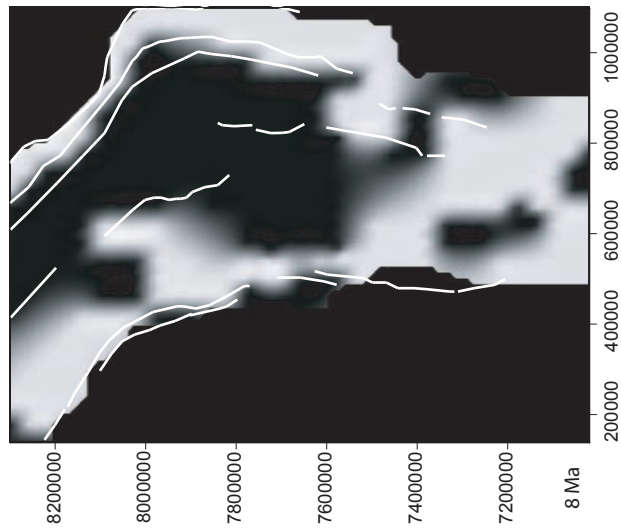
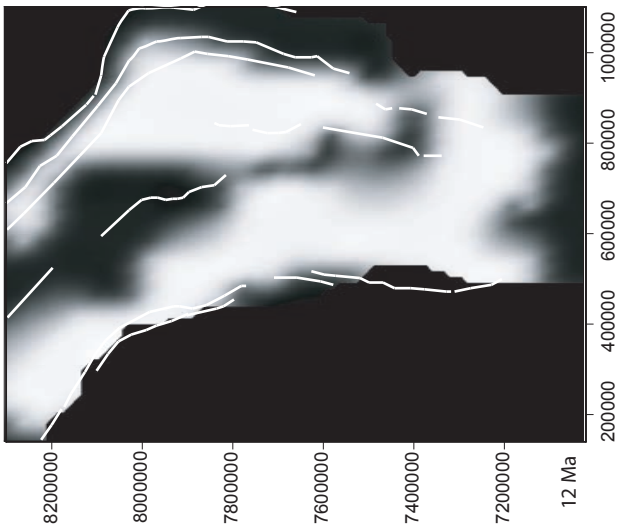
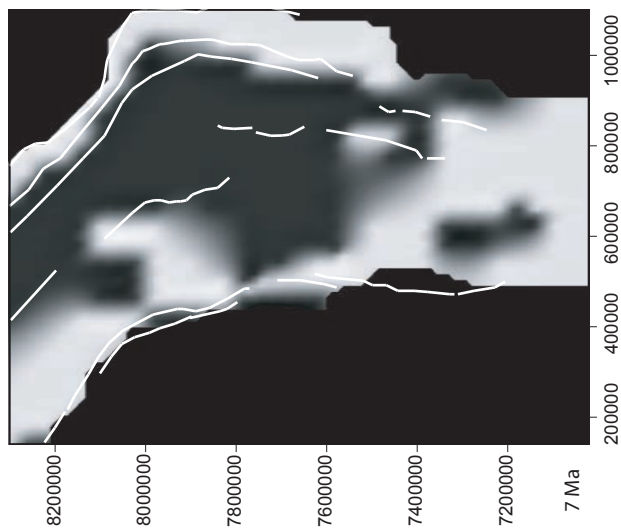
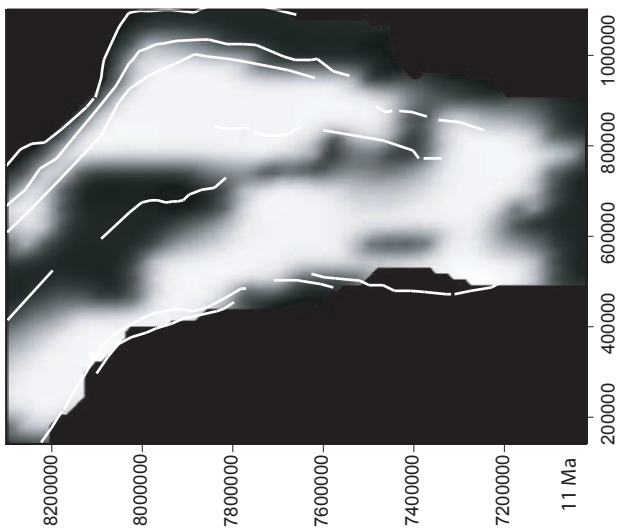
Deformation distribution in 1 Ma steps

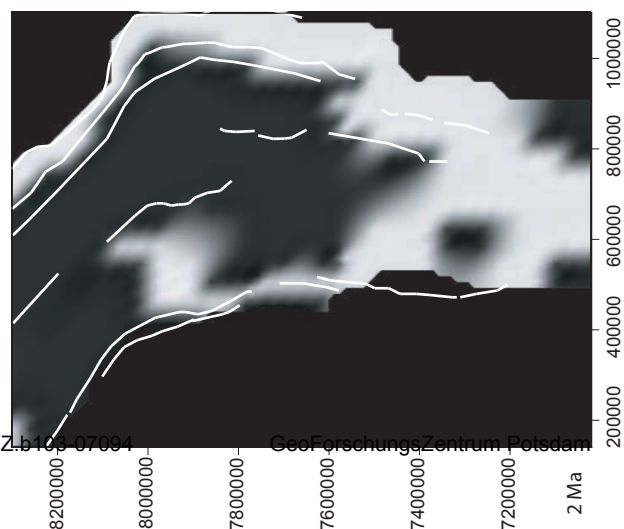
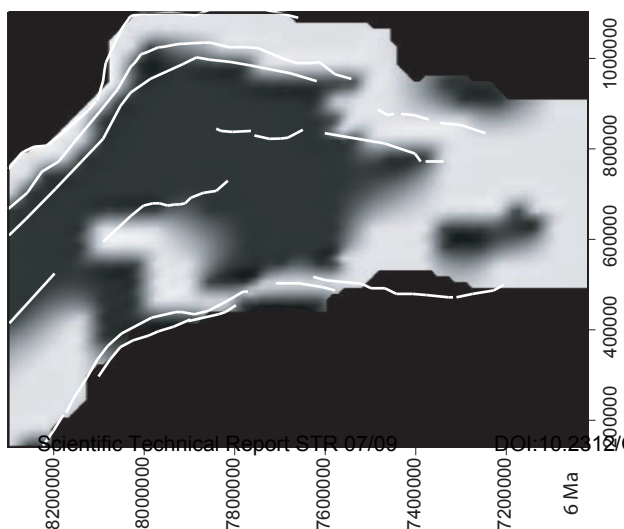
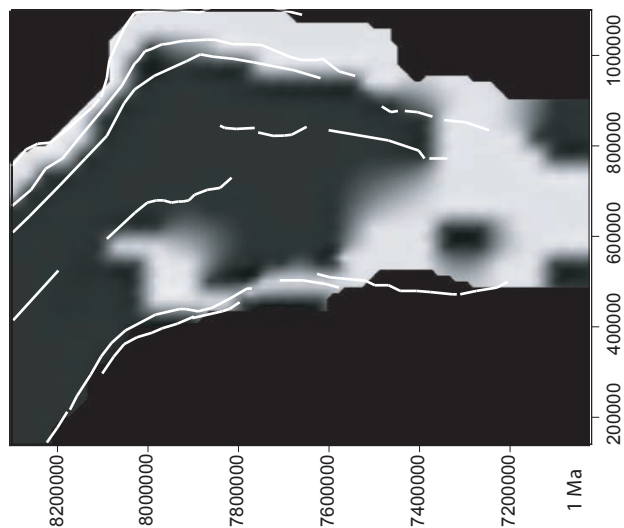
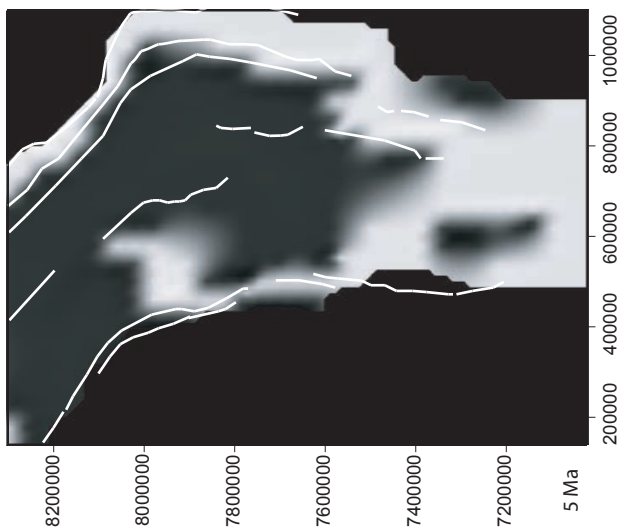
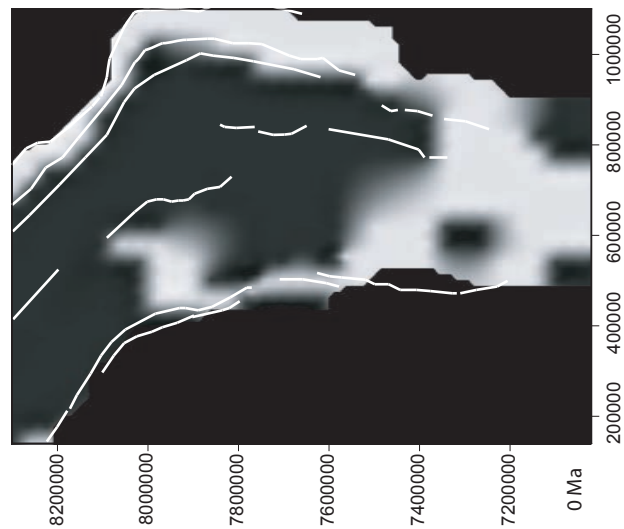
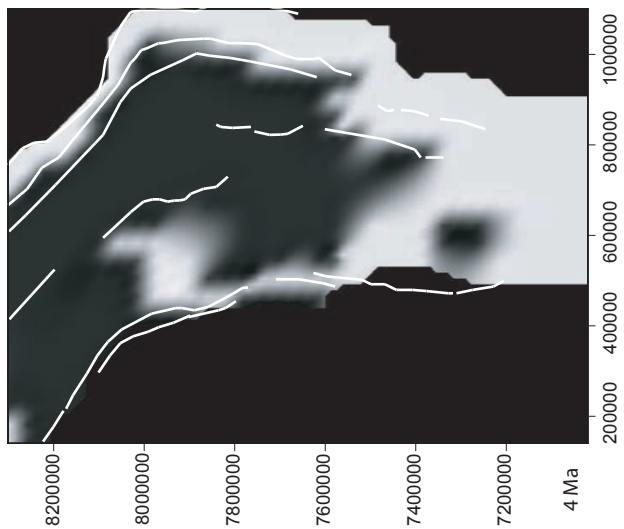
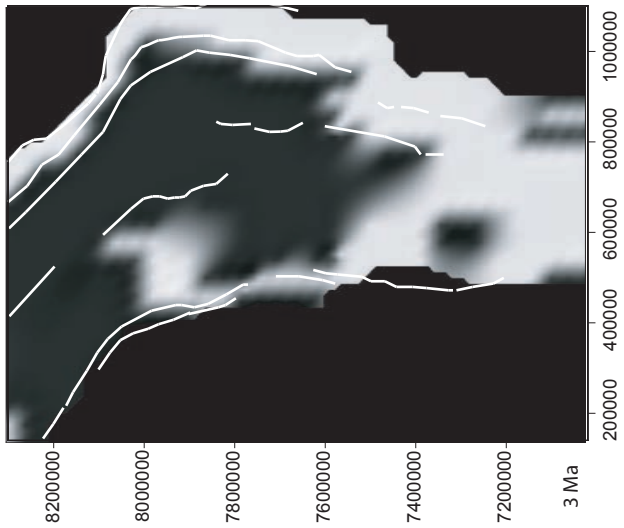












Appendix A-3

Variogram Surfaces Deformation Activity in 1 Ma steps

42 Ma

38 Ma

43 Ma

39 Ma

44 Ma

40 Ma

45 Ma

41 Ma

34 Ma

35 Ma

36 Ma

37 Ma

30 Ma

31 Ma

32 Ma

33 Ma

26 Ma

27 Ma

28 Ma

29 Ma

22 Ma

23 Ma

24 Ma

25 Ma

18 Ma

19 Ma

20 Ma

21 Ma

14 Ma

15 Ma

16 Ma

17 Ma

10 Ma

6 Ma

11 Ma

7 Ma

12 Ma

8 Ma

13 Ma

9 Ma

2 Ma

3 Ma

4 Ma

5 Ma

0 Ma

1 Ma

Appendix A-4

Database Sensitivity Analysis

number of active stages of t1ma areas	number of active areas	ID	no	location	begin	stop	number of points in unit	intersecting points	points total	change of active points plus or minus	changing points	effectively changed points	latitude for shortening estimates	unit
43-42	2	14	1	Eastern Cordillera, central	42	25	52		58	plus 52	58	58	17-22.5	Eastern Cordillera
		45	1	Eastern Cordillera W-margin	42	32	6			plus 6			17.5-18.5	Eastern Cordillera
41-40	4	29	1	Puna-W margin	46	40	1	4	26	minus 1	27	25	25	Altiplano
		85	1	Eastern Cordillera S	40	30	8	10		plus 8			22.5-23.0	Eastern Cordillera
		113	1	Eastern Cordillera S	40	8	2			plus 2			23	Eastern Cordillera
		88	1	Eastern Cordillera S	40	33	16	17		plus 16			23-25	EastC+AP+FTB
38-37	2	23	1	Atacama, Cordillera Domeyko	60	38	3	4	11	minus 3	9	-9	22.5-24.0	Altiplano
		28	1	Precordillera	46	38	7	9		minus 7			20-21	Western Cordillera
34-33	4 (5)	16	1	Eastern Cordillera W-margin	33	27	2	4	51 (60)	plus 2 (4)	51 (57)	13 (7)	21	Eastern Cordillera
		18	1	Altiplano S	33	28	24			plus 24			20-22.5	Altiplano
		43	1	Altiplano, Tambo-Tambillo	32	25	6			plus 4			19-20	Altiplano
		88	1	Eastern Cordillera S	40	33	16	19		minus 16 (19)			23-25.5	Eastern Cordillera+AP
		216	1	(Eastern Cordillera N)	45	35	9			minus 6			17	Eastern Cordillera
29-28	10	16	1	Eastern Cordillera W-margin	33	27	2	4	84	minus 2 (4)	59	51	20-21	Eastern Cordillera
		18	1	Altiplano S	33	28	24			0			20-22.5	Altiplano
		18	2	Altiplano S	28	19	24			0			20-22.5	Altiplano
		21	1	AP-W margin	29	23	5	6		plus 5 (6)			20-21	West C+Altiplano
		66	1	Santa Barbara belt (zone 20)	28	11	4	6		plus 4 (6)			24-25	fold-and-thrust belt
		91	1	Eastern Cordillera N	28	19	20	22		plus 20 (22)			15-17	Eastern Cordillera
		103	1	Corque Syncline	28	14	9			plus 9			17-18	Altiplano
		120	1	AP-W margin/ Western Cordillera	28	22	1			plus 1			19	Western Cordillera
		210	1	Salar de Antofalla	28	25	2			plus 1			25,5	Altiplano
24-23	8	1	1	Eastern Cordillera W-margin	28	17	16	17	80	plus 9 (10)	30	18	17-19	East C+Altiplano
		21	1	AP-W margin	29	23	5	6		minus 5 (6)			20-21	West C+Altiplano
		31	1	AP-W margin	22	6	5			plus 5			17-18	Altiplano
		32	1	AP-W margin	22	6	4			plus 4			18-18.5	West C+Altiplano
		33	1	AP-W margin	22	6	1	3		plus 1 (3)			19-20	West C+Altiplano
		36	1	Western Cordillera, Chuca-Lauca basin	22	7,5	6	9		plus 6 (9)			18.5-19.0	Altiplano
		64	1	Eastern Cordillera, central	23	10	16	18		plus 2 (3)			21-23	Eastern Cordillera
		120	1	AP-W margin/ Western Cordillera	28	22	1			0			19	Western Cordillera
20	6	6	1	Eastern Cordillera, central	23	10	48		54	0	30	-18	17-21	Western Cordillera
		18	2	Altiplano S	28	19	24			0			20-22.5	Altiplano
		18	3	Altiplano S	19	8	24			0			20-22.6	Altiplano
		21	2	AP-W margin	20	7	5	6		plus 5			20-21	West C+Altiplano
		35	1	Eastern Cordillera S	20	2	2			plus 1			25,5	Altiplano
		91	1	Eastern Cordillera N	28	19	21	25		minus 20 (24)			15-17	Eastern Cordillera
		210	2	Salar de Antofalla	20	17	2			0			26,5	Altiplano
18-17	7	25	1	Atacama basin	18	11	4		38	plus 4	24	-12	22.5-24.0	Altiplano
		43	2	Altiplano, Tambo-Tambillo	17	12	6			plus 4			19-20	Altiplano
		73	1	Calama basin	25	17	1			minus 1			22,5	Altiplano
		1	1	Eastern Cordillera W-margin	28	17	16	18		minus 14 (15)			17-19	East C+Altiplano
		12	1	Eastern Cordillera W-margin	30	17	9			0			21	Eastern Cordillera
		12	2	Eastern Cordillera W-margin	17	8	9			0			21	Eastern Cordillera
		210	2	Salar de Antofalla	20	17	2		60	0	25	5	25,5	Altiplano
16-15	7	2	1	Corque syncline	14	10	9			0			17.5-18.8	East C+Altiplano

72	1 Eastern Cordillera N	15	10	5	30	plus 3	16-16.5	Eastern Cordillera
94	1 Puna	14	1	28	30	plus 4 (6)	24-25.5	East C+Altiplano
95	1 Puna	26	15	24		minus 1	24-25.5	Altiplano
103	1 Corque syncline	28	14	9		minus 9	17-18	Altiplano
111	1 Eastern Cordillera S - Puna	14	10	9	11	0	22.5-23.0	Eastern Cordillera
162	1 Eastern Cordillera S	15	7	3	6	plus 4 (6)	24-25	Eastern Cordillera
25	1 Atacama basin	18	11	4		minus 4	22.5-24.0	Altiplano
27	1 Puna-W margin	12	0	4	38	plus 4	22.5-24.0	Altiplano
30	1 Puna-W margin	12	0	3	6	plus 3 (6)	25-25.5	Altiplano
34	1 AP-W margin	12	6	3		plus 3	21-22.5	Altiplano
43	2 Altiplano, Tambo-Tambillo	17	12	6		minus 4	19-20	Altiplano
48	1 Subandean E (zone 20)	11 (10)	2	6		(plus 3)	21	Eastern Cordillera
66	1 Santa Barbara belt (zone 20)	28	11	4	6	minus 4 (6)	24-25	FTB
202	1 Puna	11	2.5	2		plus 2	25.5-27.0	Altiplano
201	1 Puna	13,4	3	2		plus 1	25,5	FTB
212	1 Salar de Antofalla	12	10	1	2	0	25,5	FTB
24	1 Atacama, Cordillera Domeyko	12	0	3	4	plus 3 (4)	22.5-24.0	Altiplano
2	1 Corque syncline	14	10	9		plus 3	17.5-18.5	East C+Altiplano
25	1 Atacama basin	18	11	4	172	minus 4	22.5-24.0	Altiplano
39	1 Puna	25	10	6	9	minus 3 (6)	24-25	Altiplano
41	1 Corque syncline	10	5,4	10		plus 7	16.5-18.5	East C+Altiplano
48	1 Subandean E (zone 20)	11	2	6		plus 3	21	FTB
64	1 Eastern Cordillera, central	23	10	16	17	minus 9 (10)	21-23	Eastern Cordillera
66	1 Santa Barbara belt (zone 20)	28	11	4	6	minus 4 (6)	24-25	FTB
69	1 Subandean	10	0	17		plus 10	20-23	FTB
70	1 Sierras Pampeanas	10	3	33		plus 27	25.5-27.0	Altiplano+FTB
72	1 Eastern Cordillera N	15	10	5		minus 3	16-16.5	Eastern Cordillera
111	1 Eastern Cordillera S - Puna	14	10	9	11	minus 6 (7)	22.5-23.0	Eastern Cordillera
114	1 Subandean (partly zone 20)	10	0	23	25	plus 12	19-21	FTB
198	1 Puna	10	4,5	1	2	0	25,5	Altiplano
199	1 Puna	10	1,3	1	2	plus 1 (2)	27	Altiplano
202	1 Puna	11	2,5	2		plus 1	25.5-27.0	Altiplano
212	1 Salar de Antofalla	12	10	1	2	0	25,5	Altiplano
215	1 Precordillera, Faila Oeste (ss)	10	0	1		plus 1	22,5	Western Cordillera
4	1 Eastern Cordillera E	35	10	23		minus 22	18-21	Eastern Cordillera+FTB
6	1 Eastern Cordillera, central	23	10	40		minus 31	17-21	Eastern Cordillera
18	3 Altiplano S	19	8	24		plus 24	20-22.5	Altiplano
21	2 AP-W margin	20	7	5	6	minus 4	20-21	West C+Altiplano
25	2 Atacama basin	7	0	4		plus 4	22.5-24.0	Altiplano
36	1 Western Cordillera, Chuca-Lauca basin	22	7,5	6	9	0	18.5-19.0	Altiplano
36	2 Western Cordillera, Chuca-Lauca basin	7,5	0,5	6	9	0	18.5-19.0	Altiplano
49	1 Subandean W (zone 20)	8	0	2	4	plus 2 (4)	21	FTB
50	1 Cochabamba shear zone (tp)	7	0	5		0	17,5	Eastern Cordillera
55	1 Precordillera, Westcordillera	8	0	2		minus 2	18,5	Western Cordillera
81	1 AP-W margin (tt)	7	0	7		plus 3	19-22.5	West C+Altiplano
113	1 Eastern Cordillera S	40	8	2		minus 2	23	Eastern Cordillera
116	1 AP-W margin	9	7,7	4		minus 2	18-18.5	West C+Altiplano
140	1 Interandean	30	7	3		0	21-22.5	Eastern Cordillera+FTB
162	1 Eastern Cordillera S	15	7	3	6	0	24-25	Eastern Cordillera
166	1 Subandean	9	7,5	0		0	22.5-23.0	Eastern Cordillera+FTB

167	1	Subandean	8,5	7	2	plus 2	22.5-23.0	Eastern Cordillera+FTB
168	1	Subandean	7,6	4,5	0	0	22.5-23.0	Eastern Cordillera+FTB
169	1	Subandean	6,9	4	0	0	22.5-23.0	Eastern Cordillera+FTB
172	1	Subandean	9	7	5	plus 4	22.5-23.0	Eastern Cordillera+FTB
172	2	Subandean	7	2	5	plus 4	22.5-23.0	Eastern Cordillera+FTB
204	1	Puna	6,7	2,35	6	plus 5	27	Altiplano
12	2	Eastern Cordillera W-margin	17	8	9	minus 9	21	Eastern Cordillera
111	2	Eastern Cordillera S - Puna	9	7	9	plus 6 (7)	22.5-23.0	Eastern Cordillera
162	2	Eastern Cordillera S	7	0	3	0	24-25	Eastern Cordillera
31	1	AP-W margin	22	6	5	minus 5	17-18	Altiplano
32	1	AP-W margin	22	6	4	0	18-18.5	West C+Altiplano
33	1	AP-W margin	22	6	1	minus 0 (2)	19-20	West C+Altiplano
34	1	AP-W margin	12	6	3	minus 2	21-22.5	Altiplano
41	1	Corque Syncline	10	5,4	10	minus 5	16.5-18.5	East C+Altiplano
42	1	Corque Syncline	5	0	5	minus 1	16.5-18.5	East C+Altiplano
51	1	Sierras Pampeanas	3,5	0	12	0	25.5-27.0	Altiplano
58	1	Eastern Cordillera, central (zone 20, ss)	4	3	0	0	19	Eastern cordillera
67	1	Santa Barbara belt (zone 20)	4	0,5	6	plus 6	24-25.5	FTB
87	1	Eastern Cordillera S	6	1	11	plus 9 (10)	22-24	East C+AP+West C
168	1	Subandean	7,6	4,5	0	0	22.5-23.0	Eastern Cordillera+FTB
169	1	Subandean	6,9	4	0	0	22.5-23.0	Eastern Cordillera+FTB
170	1	Subandean	4	3	0	0	22.5-23.0	Eastern Cordillera+FTB
184	1	Puna	4	0	2	0	24	Altiplano
191	1	Puna	6	0,5	0	0	25,5	Altiplano
198	1	Puna	10	4,5	1	0	25,5	Altiplano
214	1	Salar de Antofalla (ss)	5	1,5	1	plus 1	25,5	Altiplano
73	2	Calama basin	5	0	1	0	22,5	Altiplano
212	2	Salar de Antofalla	4	0	1	plus 1 (2)	25,5	Altiplano

Sensitivity analysis

Dependence of stage boundaries on respective units:

boundary	unit
43-42	Eastern Cordillera
41-40	Eastern Cordillera + fold-and-thrust belt
38-37	Altiplano
34-33	Eastern Cordillera + fold-and-thrust belt + Altiplano
29-28	Eastern Cordillera + fold-and-thrust belt + Western Cordillera
24-23	fold-and-thrust belt + Western Cordillera
21-20	Western Cordillera
20-19	Eastern Cordillera
18-17	Eastern Cordillera
16-15	fold-and-thrust belt
13-12	Altiplano
11-10	Eastern Cordillera
9-8	fold-and-thrust belt
6-5	fold-and-thrust belt

boundary	total active points	points changed	number of areas	result	significant?
43-42	58	58	2	1	x
41-40	26	26	4	1,25	x
38-37	11	9	2	0,818181818	
34-33	51	51	4	1,25	x
29-28	84	59	10	3,511904762	x
24-23	80	30	8	0,9375	
20-19	54	30	6	0,925925926	
18-17	38	24	7	1,263157895	x
16-15	60	25	7	0,833333333	
13-12	38	34	11	8,947368421	x
11-10	172	155	19	2,574750831	x
9-8	90	76	23	5,62962963	x
6-5	57	34	19	1,704260652	x

significant when

$[(\text{number of points changed} * 10) / \text{total number of points}] / 12 - \text{number of active areas} > 1$

Appendix B-1

Description of Granular Experiments

Appendix B. Details on initial experimental set-ups (dimensions and materials used), the evolution of each experimental run, and the final deformation pattern

No	Initial Conditions	Material of base	Experiment evolution, structural development (unit 1-3)	Activity unit 4	Final setting
2	GB (5.6), baryte (8), GB (<200mm) (7.2), sand (>5.6)	GB on table	1-2: glass beads of unit 1 are compressed and squeezed out, 3: a thrust in unit 2 forms, 4+: unit 2 shears off unit 3 on to unit 4	no thrusting	c
3	GB (5.6), baryte (8), GB (7.2), sand (>5.6)	GB on table	1-2: glass beads of unit 1 are compressed and squeezed out, 3: glass beads of unit 3 are squeezed out, 4+: unit 2 shears off unit 3 on to unit 4	no thrusting	c
4	GB (5.6), baryte (8), GB (7.2), sand (>5.6)	GB up to 20.8, then sandpaper (<0.4 mm) at 6°	1-2: glass beads of unit 1 are compressed, 3: glass beads of unit 3 are squeezed out, 4+: unit 2 shears off unit 3 on to unit 4	no thrusting	c
5	GB (5.6), baryte (8), GB (1.2), sand (6), sand (>5.6)	GB up to 20.8, then sandpaper (<0.4 mm) at 6°	1-2: glass beads of unit 1 are compressed, 4: thrust, but no uplift in unit 3, 5-12: backthrusts in unit 2 and uplift	one thrust: 13	c
6	GB (5.6), baryte (8), sand (3), GB (1.2), sand (>5.6)	GB up to 20.8, then sandpaper (<0.4 mm) at 6°	1-2: glass beads of unit 1 are compressed, 3: thrusts in unit 3, 6-14: compression and backthrusts in unit 2	one thrust: 15	c
7	sand (3.4), GB (3.4), baryte (6.8), GB (3), sand (3.2), sand (>5.6)	GB up to 20.8, then sandpaper (<0.4 mm) at 6°	1-7: uplift in unit 1, 4-11: uplift in unit 3, 5-10: compression in unit 2, 11+: uplift of unit 2	two thrusts: 16, 17	d
8	sand (3.6), GB (2), baryte (8), GB (1.5), sand (5.7), sand (>5.6)	GB up to 20.8, then sandpaper (<0.4 mm) at 6°	1-7: uplift in unit 1, 4-11: uplift in unit 3, 5-10: compression in unit 2, 11+: uplift of unit 2	one thrust: 16	d
9	sand (2.8), GB (2.8), baryte (8), GB (2.8), sand (4.4), sand (>5.6)	GB up to 20.8, then sandpaper (<0.4 mm) at 6°	1+: uplift unit 1, 3: compression in unit 2, 4: uplift unit 3, 6-14: uplift unit 2	one thrust: 20	d
10	sand (2.8), GB (2.8), baryte (8), GB (2.8), sand (4.4), sand (>5.6)	GB up to 20.8, then sandpaper (<0.4 mm) at 6°	1-8: uplift unit 1, 3-11: uplift unit 3, 5-13: compression and uplift unit 2	one thrust: 17	d
11	sand (4.1), GB (1.5), baryte (8), GB	GB up to 20.8, then	1-5: uplift unit 1, 3-8: uplift unit 3, 7-12: compression and	two thrusts: 13, 15	d

	(1.5), sand (5.7), sand (>5.6)	sandpaper (<0.4 mm) at 6°	uplift unit 2		
12	sand (4.1), GB (1.5), baryte (8), GB (1.5), sand (5.7), sand (>5.6)	teflar foil	1-5: uplift unit 1, 4-11: uplift unit 3, 7-12: compression and uplift unit 2	three thrusts: 17, 19, 20	e
13	sand (4.6), GB (1), baryte (9), GB (1), sand (6.2), sand (>5.6)	teflar foil, sand (<0.4 mm) on top	1-4: uplift unit 1, 3-12: compression in unit 2, but no uplift, 5-7: compression in unit 3	four thrusts: 16, 19, 22, 23	a
14	sand (4.1), GB (1.5), baryte (8), GB (1.5), sand (5.7), sand (>5.6)	teflar foil, sand (<0.4 mm) on top	1-5: uplift unit 1, 4-12: compression in unit 2, 7: compression in unit 3, 9-19: overridding of unit 2 over unit 3	three thrusts: 20, 24, 25	c
15	sand (4.1), GB (1.5), baryte (8), GB (1.5), sand (5.7), sand (>5.6)	teflar foil, on top: viscous gel up to 20.8, then sand	1-4: uplift unit 1, 4-8: compression in unit 2, 4-11: uplift in unit 3	no thrusting	e
16	sand (4.1), GB (1.5), baryte (8), GB (1.5), sand (5.7), sand (>5.6)	teflar foil, sand (<0.4 mm) on top	1-3: compression in unit 1, 4: uplift in unit 3, 4-12: unit 2 thrusts over unit 3, subsequent thrusting	three thrusts: 13, 15, 16	a
18	sand (4.1), salt (1.5), baryte (8), salt (1.5), sand (5.7), sand (>5.6)	teflar foil, salt on top	1-2: compression unit 1, 3-4: compression in unit 2, 5-11: unit 2 thrusts over unit 3, subsequent thrusting	two thrusts: 12, 17	c
19	sand (4.1), salt (1.5), rice pudding (8), salt (1.5), sand (5.7), sand (>5.6)	teflar foil, salt on top	1: compression unit 1, 2-7: compression and uplift unit 2, 8-11: unit 2 thrusts over unit 3, subsequent thrusting	three thrusts: 12, 15, 17	b
20	sand (2.1), GB (1.4), sand (2.1), baryte (8), sand (2.9), GB (1.4), sand (2.9), sand (>5.6)	teflar foil	1-4: uplift in unit 1, 4-10: compression and uplift unit 2, 7-12: uplift in unit 3	two thrusts: 14, 16	e
21	sand (2.1), GB (1.4), sand (2.1), baryte (8), sand (2.9), GB (1.4), sand (2.9), sand (>5.6)	teflar foil, sand (<0.4 mm) beneath unit 2	1-3: uplift unit 1, 4-7: unit 2 is compressed, 4-8: compression in unit 3, 8-13: unit 2 thrusts over unit 3	three thrusts: 17, 20, 21	c
22	sand (3.6), fine sand (2), baryte (8), fine sand (2), sand (5.2), sand (>5.6)	teflar foil, sand (<0.224 mm) on top	1-5: uplift unit 1, 4-9: compression and uplift unit 2, 4-10: uplift unit 3	three thrusts: 12, 15, 18	d

23	sand (4.1), GB (1.5), corn meal (8), GB (1.5), sand (5.7), sand (>5.6)	teflar foil	1-3: uplift unit 1, 3-9: uplift unit 2, 10-12: unit 2 thrusts over unit 3, subsequent thrusting	three thrusts: 14, 18, 22	b
25	sand (4.1), GB (1.5), starch (8), GB (1.5), sand (5.7), sand (>5.6)	teflar foil	1-3: uplift unit 1, 3-10: uplift unit 2, 11+: subsequent thrusting	four thrusts: 11, 14, 17, 21	b
26	sand (4.1), GB (1.5), corn meal (8), GB (1.5), sand (5.7), sand (>5.6)	teflar foil, GB on top	1-3: uplift unit 1, 3-9: uplift unit 2, 7: thrust in unit 3, 10+: unit 2 thrusts over unit 3, subsequent thrusting	four thrusts: 13, 16, 19, 21	b
27	sand (4.1), GB (1.5), starch (8), GB (1.5), sand (5.7), sand (>5.6)	teflar foil, GB on top	1-3: uplift unit 1, 3-8: uplift unit 2, 7-9: uplift in unit 3, 11-12: unit 2 thrusts over unit 3, subsequent thrusting	three thrusts: 13, 17, 19	b
29	sand (2.1), GB (1.4), sand (2.1), baryte (8), sand (2.9), GB (1.4), sand (2.9), sand (>5.6)	teflar foil, GB on top	1-5: uplift unit 1, 3-10: uplift of unit 3, 5-9: compression and uplift unit 2	one thrust: 17	d
30	sand (2.1), GB (1.4), sand (2.1), baryte (8), sand (2.9), GB (1.4), sand (2.9), sand (>5.6)	no foil, surface of table	1-5: uplift unit 1, 5-10: uplift of unit 3, 6+: compression and uplift unit 2, subsequent thrusting	four thrusts: 16, 18, 19, 22	e
31	sand (2.1), GB (1.4), sand (2.1), baryte (8), sand (2.9), GB (1.4), sand (2.9), sand (>5.6)	alcor foil	1-5: uplift unit 1, 5-10: uplift of unit 3, 6+: compression and uplift unit 2, subsequent thrusting	five thrusts: 11, 13, 16, 17, 19	e
32	sand (2.1), GB (1.4), sand (2.1), baryte (8), sand (2.9), GB (1.4), sand (2.9), sand (>5.6)	sandpaper (<0.4 mm)	1-5: thrusting in unit 1, 5-10: compression in unit 2, 6-11: thrusts in unit 3, subsequent thrusting	two thrusts: 18, 24	a
33	sand (2.1), GB (1.4), sand (2.1), baryte (8), sand (2.9), GB (1.4), sand (2.9), sand (>5.6)	glass beads (<400 mm) paper	1-3: compression unit 1, 4-7: compression unit 2, 8+: compression in unit 3, 14+: whole system is moving	no thrusting	a
34	sand (2.1), GB (1.4), sand (2.1), baryte (8), sand (2.9), GB (1.4), sand (2.9), sand (>5.6)	glass beads (<200 mm) paper	1-7: compression unit 1, 8-12: uplift in unit 3, 13-19: overriding of units 1 and 2 over 3, 19+: whole system is moving	no thrusting	a

35	sand (2.1), GB (1.4), sand (2.1), baryte (8), sand (2.9), GB (1.4), sand (2.9), sand (>5.6)	alcor foil up to 20.8, then sandpaper (<0.4 mm)	1-5: uplift unit 1, 6-12: uplift unit 3, 7-12: compression in unit 2, 13-21: system at same position but further compression, 22+ system has one taper angle and is moving as a whole	no thrusting	first e, then a
36	sand (2.1), GB (1.4), sand (2.1), baryte (8), sand (2.9), GB (1.4), sand (2.9), sand (>5.6) → erosion	alcor foil	1-7: uplift unit 1, 4-10: uplift unit 3, 5-11: compression unit 2, subsequent thrusting	four thrusts: 12, 13, 16, 19	e
37	sand (2.1), GB (1.4), sand (2.1), baryte (8), sand (2.9), GB (1.4), sand (2.9), sand (>5.6) → detachment in unit 4	alcor foil	1-3: uplift unit 1, 3-12: compression and uplift unit 2, 6-12: uplift unit 3	three thrusts: 10, 14, 18	e
38	sand (2), GB (1), sand (2), baryte (9), sand (4), GB (1.5), sand (4), sand (10+) → detachment in unit 4	alcor foil	1-5: uplift unit 1, 5-10: compression and uplift unit 2, 6-11: uplift unit 3, subsequent thrusts	eight thrusts: 12, 16, 18, 23, 25, 26, 28, 29	e
39	sand (3.5), GB (1), sand (3.5), baryte (6), sand (5.5), GB (1), sand (5.5), sand (10+)	alcor foil	1-5: uplift unit 1, 5+: compression and uplift unit 2, 6-13: uplift unit 3	two thrusts: 15, 17	e
40	sand (3.5), GB (1), sand (3.5), baryte (6), sand (5.5), GB (1), sand (5.5), sand (10+) → height 1.7	alcor foil	1-3: uplift unit 1, 3-7: compression and uplift unit 2, 5-12: uplift unit 3	eight thrusts: 14, 16, 21, 24, 26, 27, 28, 31	e
41	sand (2), GB (1), sand (2), baryte (9), sand (4), GB (1.5), sand (4), sand (10+)	alcor foil, unit 4 at 10°	1-4: uplift unit 1, 5-12: compression and uplift unit 2, 6-16: uplift unit 3	five thrusts: 18, 21, 23, 24, 25	e
42	sand (2), GB (1), sand (2), baryte (9), sand (4), GB (1.5), sand (4), sand (10+) → erosion	alcor foil	1-4: uplift unit 1, 3-13: compression and uplift unit 2, 6-12: uplift unit 3, subsequent thrusting	seven thrusts: 13, 17, 20, 23, 26, 27, 28	e
43	sand (2), GB (1), sand (2), baryte (9), sand (4), GB (1.5), sand (4), sand (10+)	alcor foil up to 47 cm, sandpaper 47+	1-4: uplift unit 1, 5-15: compression and uplift unit 2, 5-17: uplift unit 3 and compression, 17+: system develops one high taper angle and moves as a whole	no thrusting	first e, then a
44	sand (4), GB (2), sand (4), baryte (18), sand (8.5), GB (2), sand (8.5), sand (20+)	alcor foil	1-5: uplift unit 1, 4-11: compression and uplift unit 2, 5-18: compression and uplift unit 3, subsequent thrusting	four thrusts: 19, 24, 27, 30	e

47	sand (5), baryte (8), sand (5), sand (5+)	alcor foil	subsequent thrusting in units 1-4	no differentiation between unit 3 and 4	a
48	GB (5), sand (8), GB (5), GB (5+)	alcor foil	subsequent thrusting in units 1-4	no differentiation between unit 3 and 4	a
49	GB (5), sugar (8), GB (5), GB (5+)	alcor foil	unit 2 is compressed and uplifted, no thrusts	no differentiation between unit 3 and 4	b
50	GB (40-70 μ m) (5), GB (8), GB (40-70 μ m) (5), GB (5+)	teflar foil	1: thrust in unit 1, 2-5: thrusts in unit 2, 6+: more thrusts in unit 3 and 4	no differentiation between unit 3 and 4	a
51	GB (5), Z-lights (8), GB (5), GB (5+)	teflar foil	1: uplift in unit 1, 2-7: uplift unit 2, no subsequent thrusts visible as they are immediately covered by slope sediments from unit 2	-	b
52	GB (5), sand (8), GB (5), GB (5+)	teflar foil	1-4: uplift unit 1, 5-7: compression unit 2, 5-13: uplift unit 3	two thrusts: 15, 19	d
53	sand	teflar foil	No differentiation in units: thrusts at: 4, 8, 10, 16, 21, 25	-	a
54	GB	teflar foil	No differentiation in units: taper angle constantly increases, no thrusts visible as they are immediately covered by slope sediments	-	a
55	sand (5), sugar (8), sand (5), sand (5+)	teflar foil	1-2: uplift unit 1, 4-9: uplift in unit 2, 5-14: uplift in unit 3	one thrust: 16	b

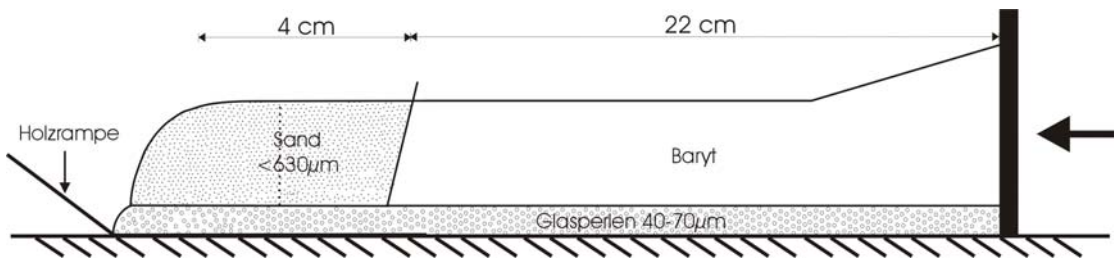
Annotations:

- 1) GB stands for glass beads;
- 2) Numbers in brackets in the column "initial conditions" specify the width of units in centimetres;
- 3) Numbers under "structural evolution development" and "activity in unit 4" indicate the centimetre of convergence at which a certain development has taken place.

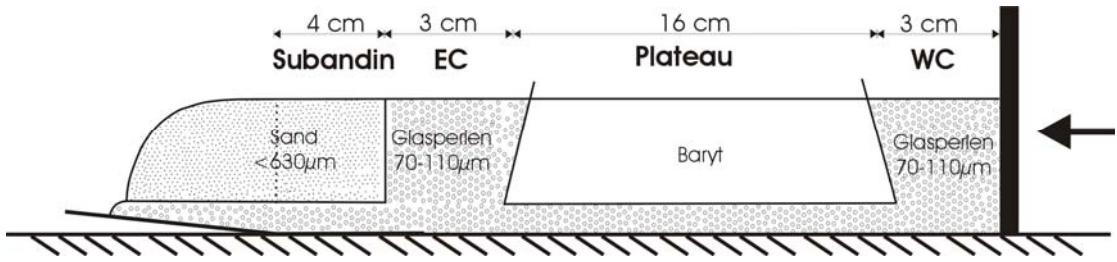
Appendix B-2

Set-up Sketches (Granular Experiments)

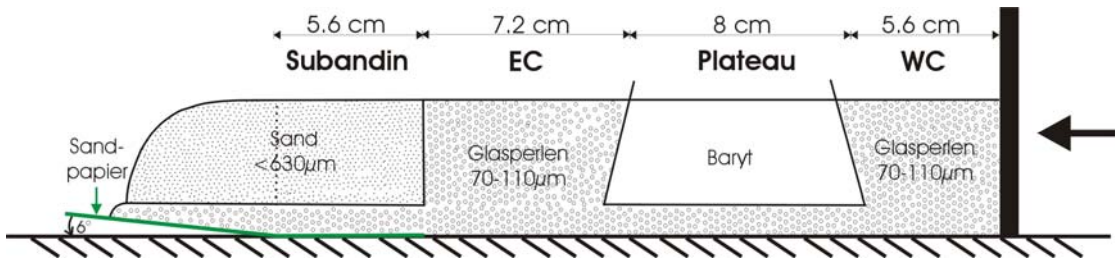
1



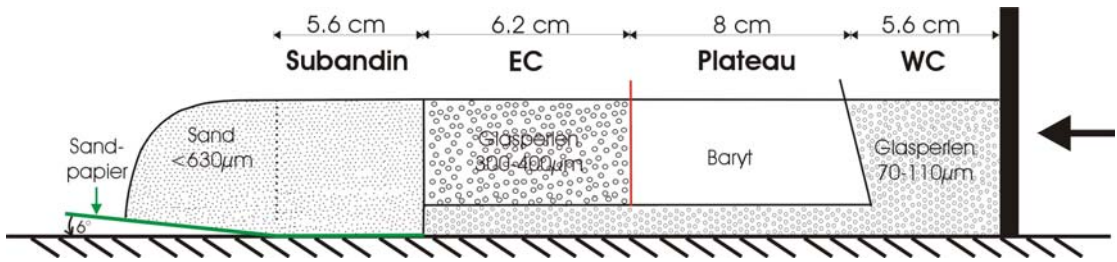
2



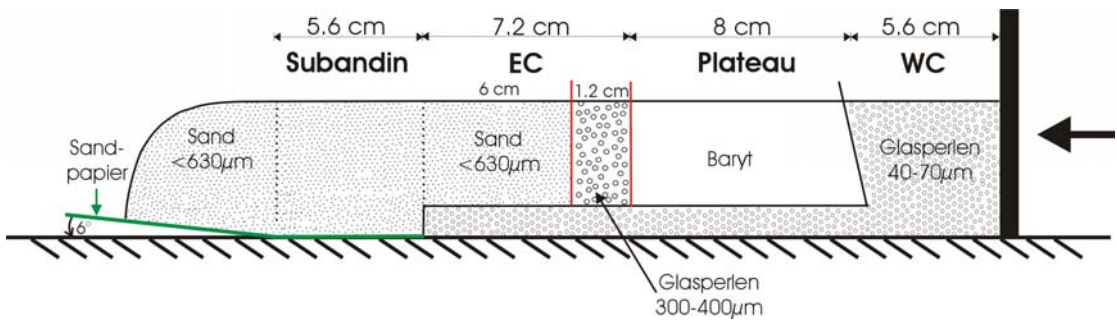
3



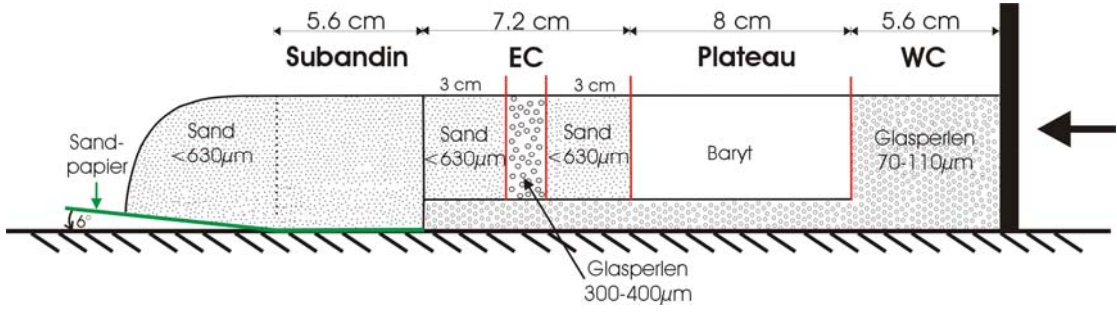
4



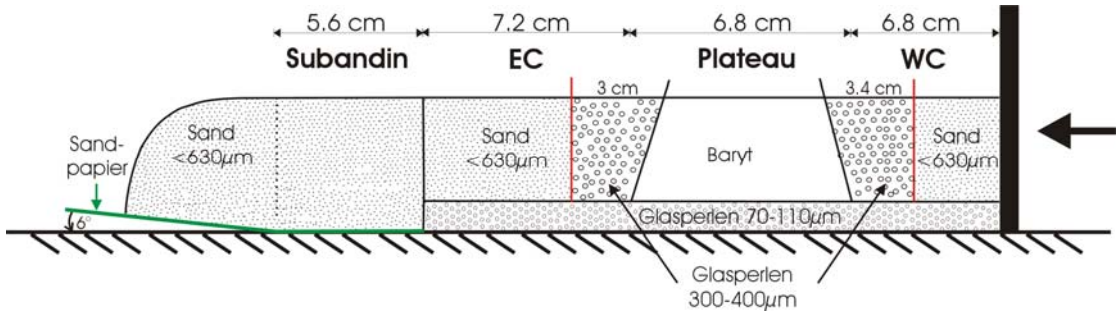
5



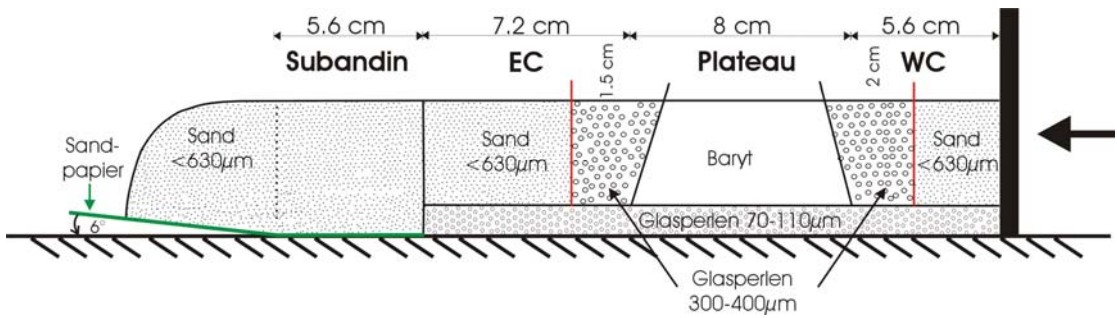
6



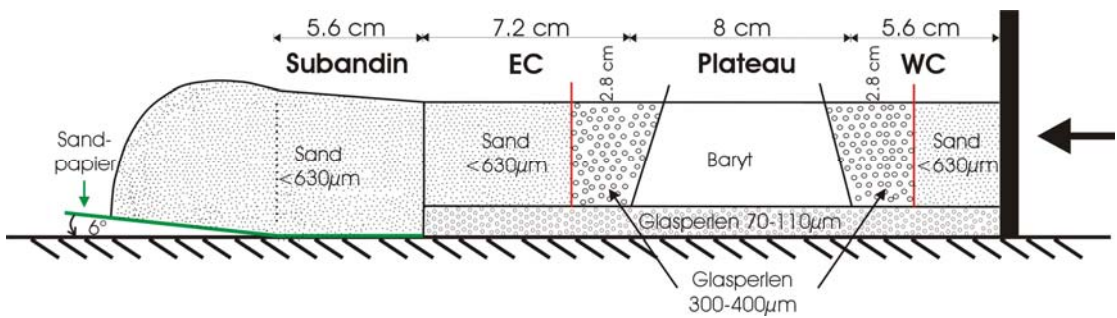
7



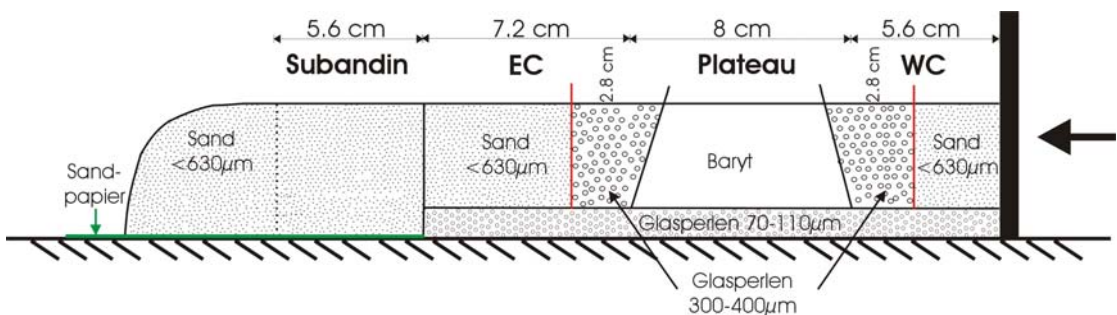
8



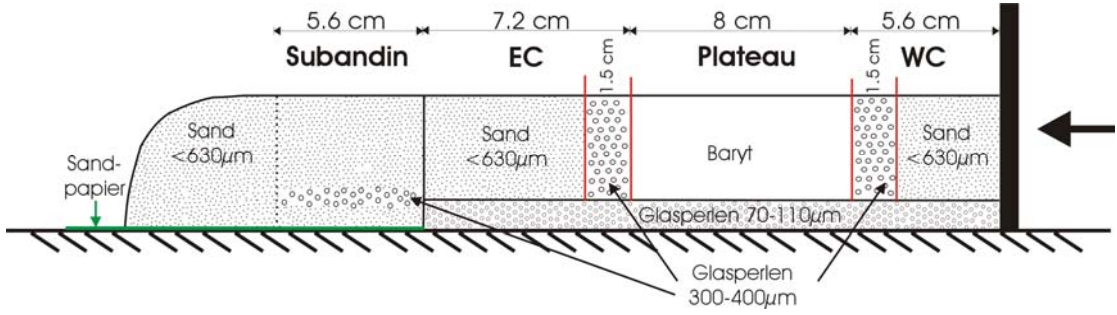
9



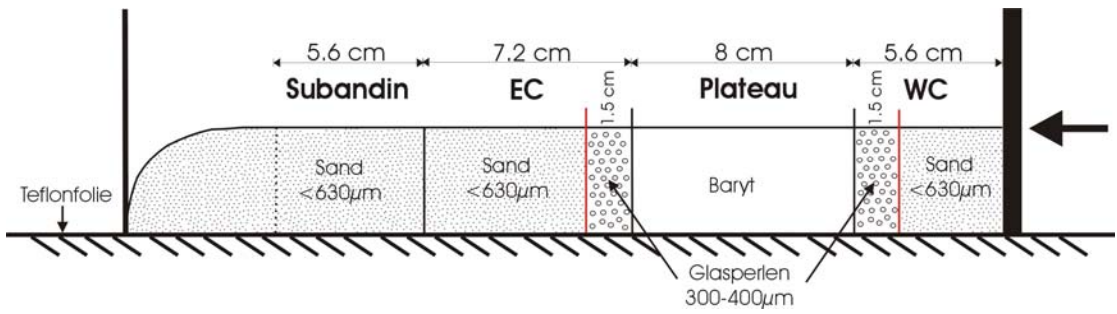
10



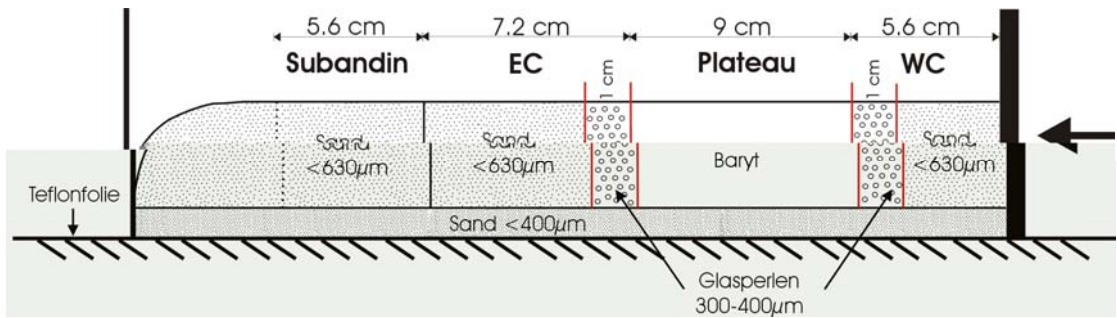
11



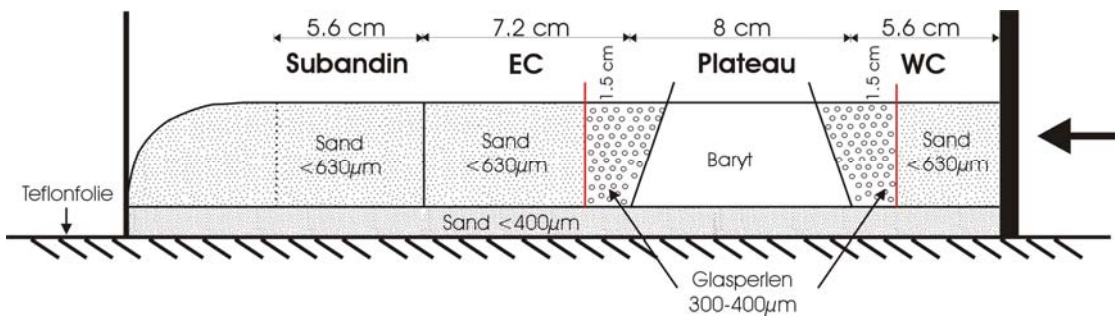
12



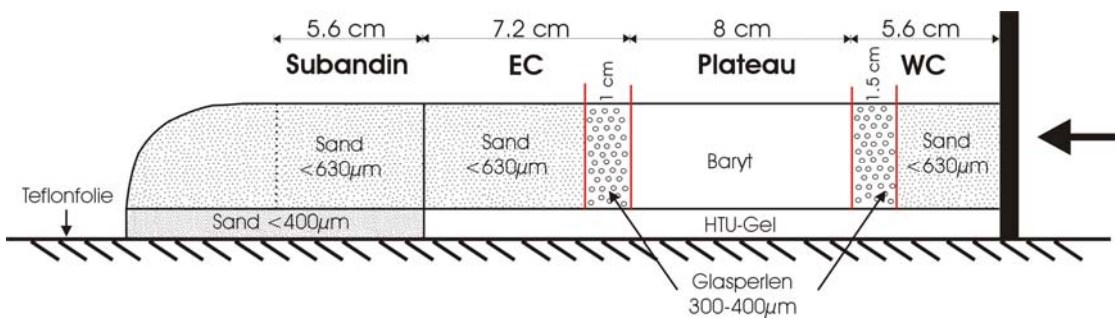
13



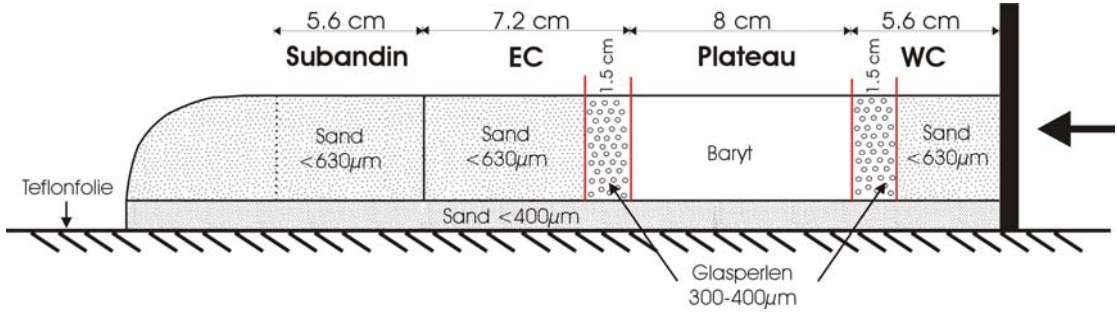
14



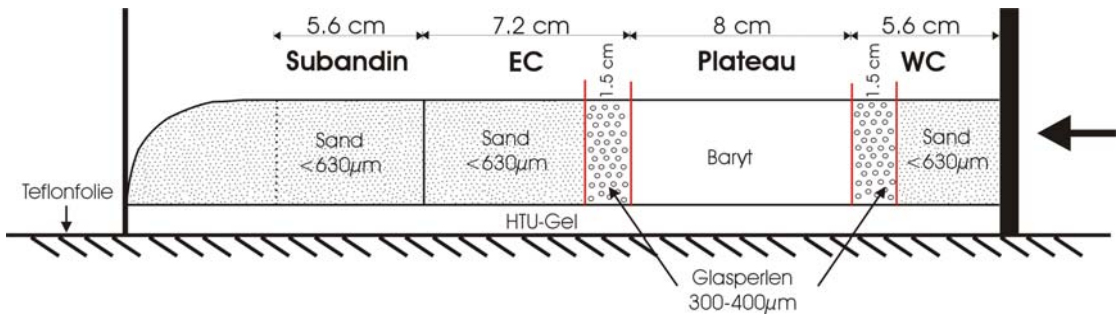
15



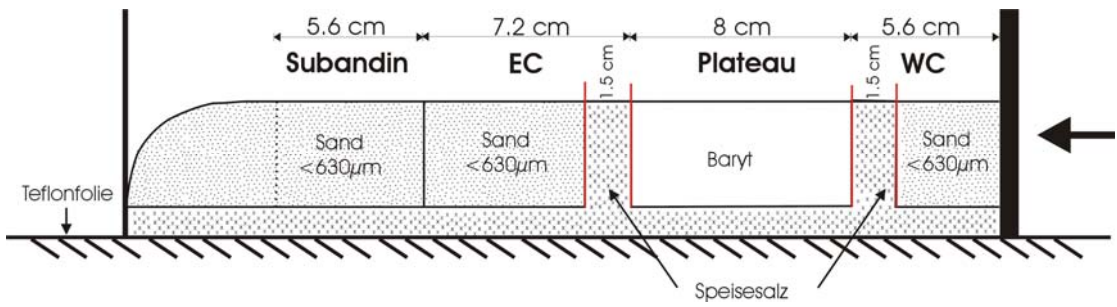
16



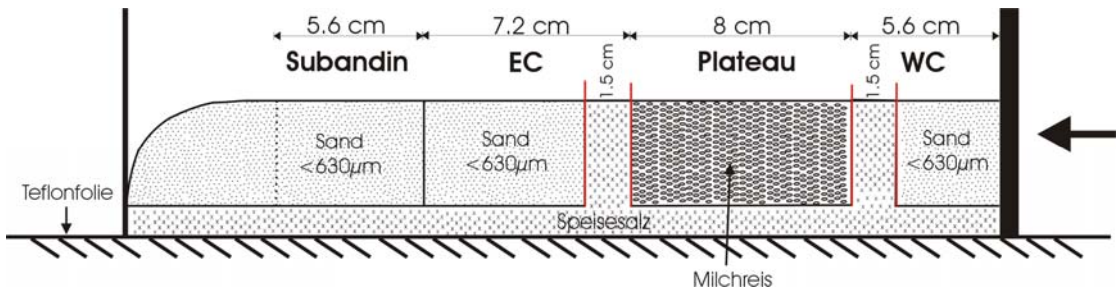
17



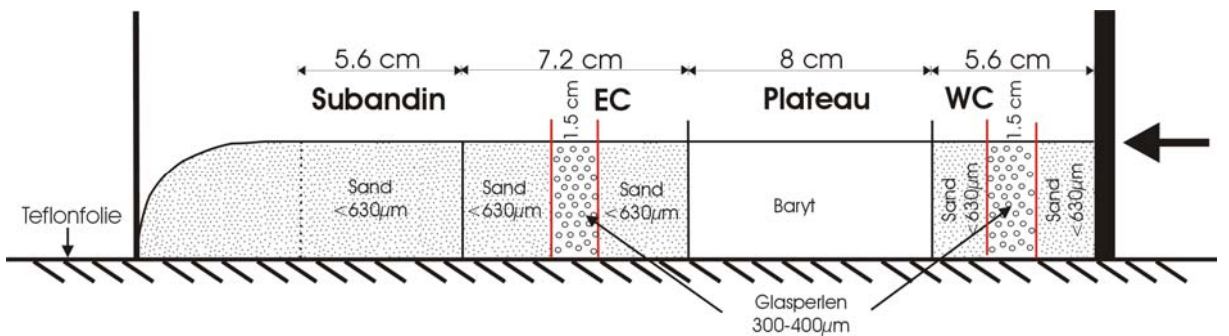
18



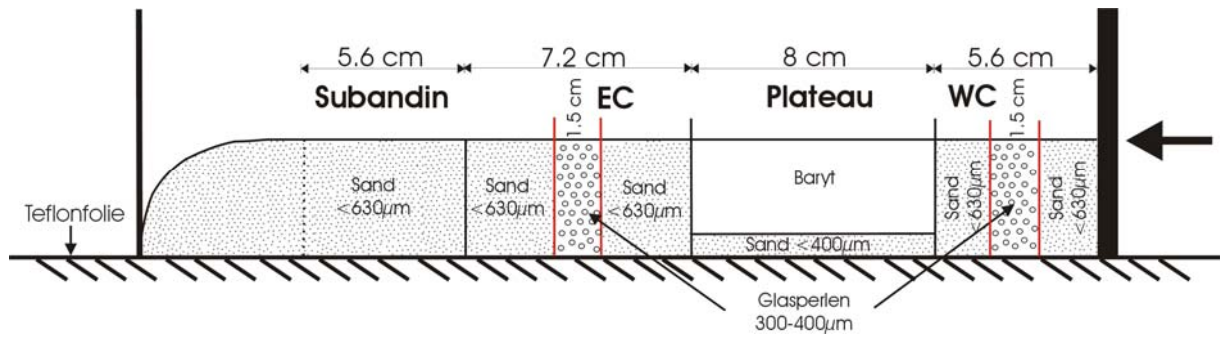
19



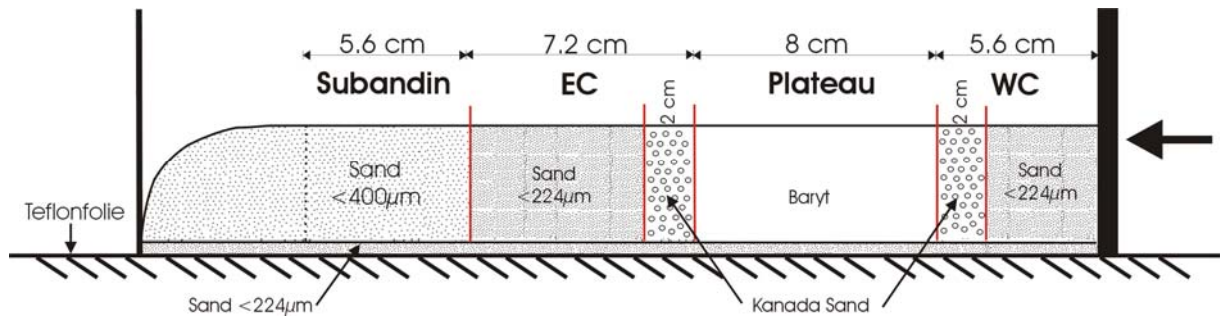
20



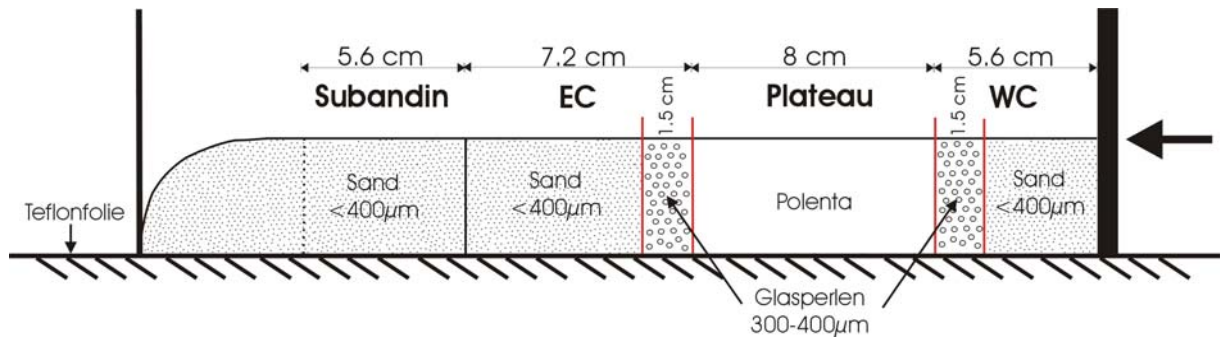
21



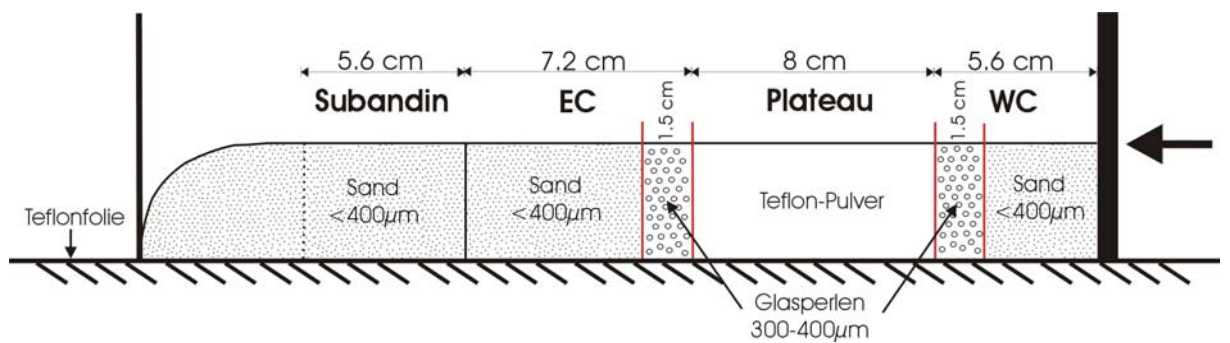
22



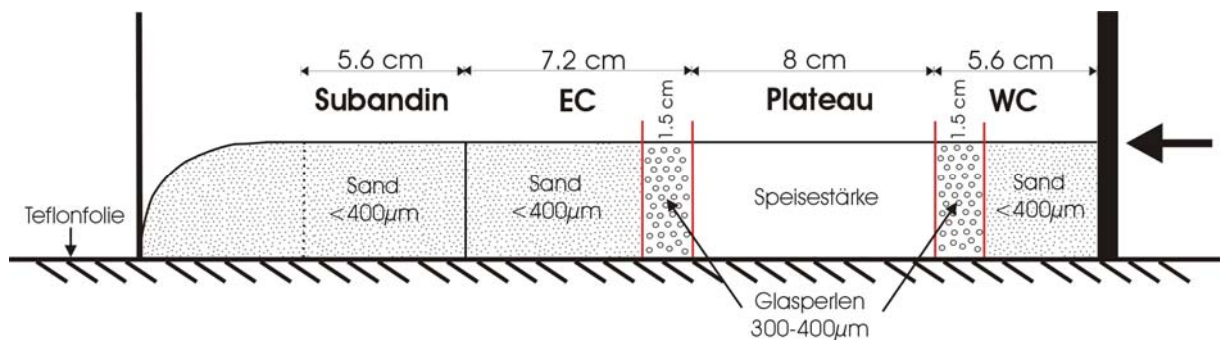
23

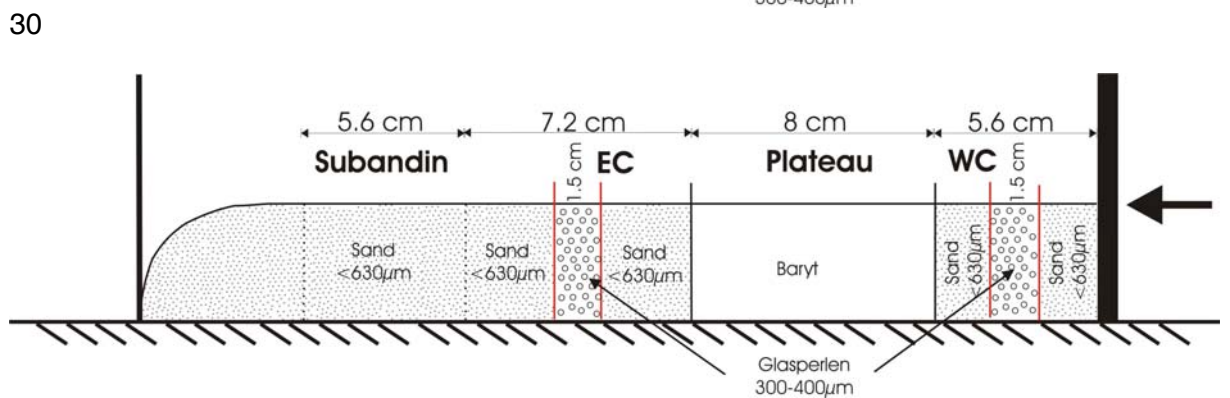
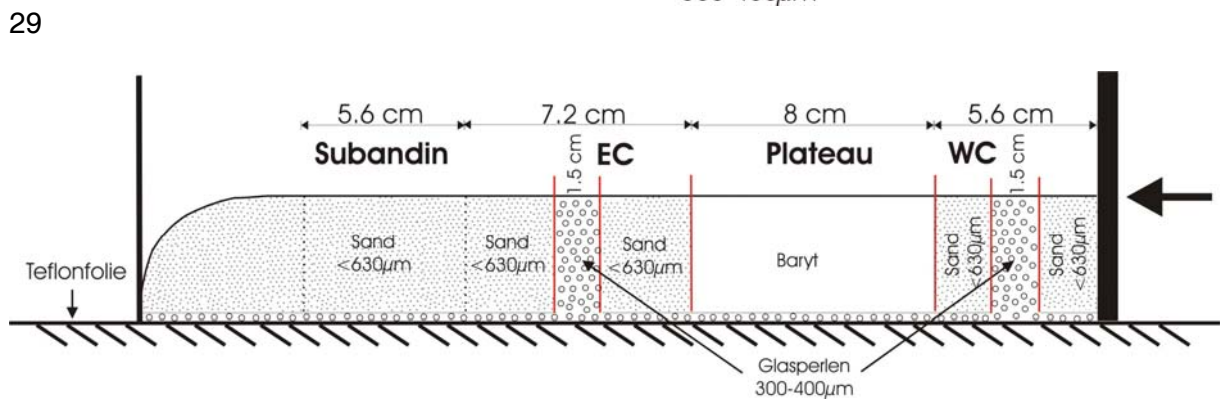
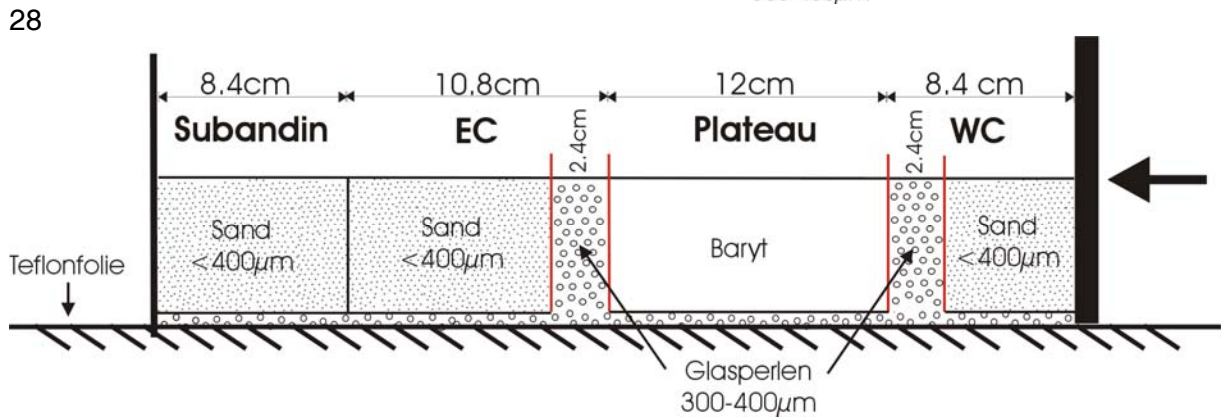
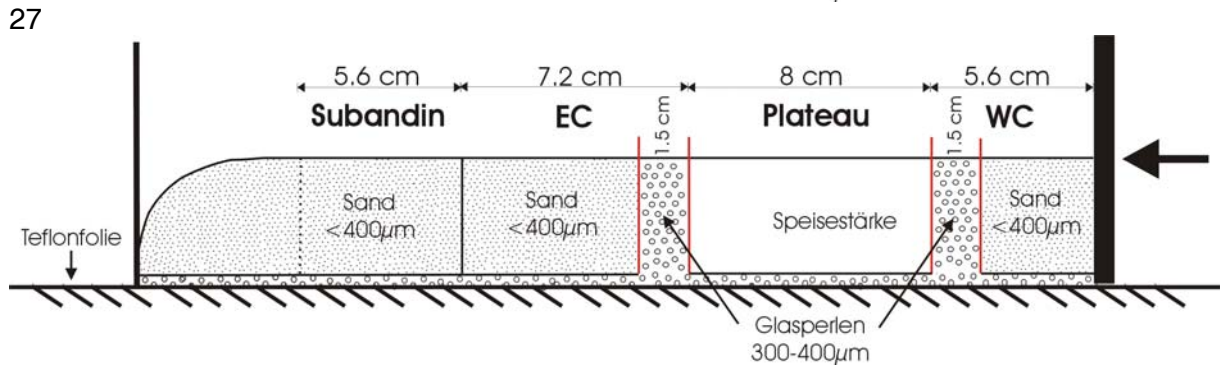
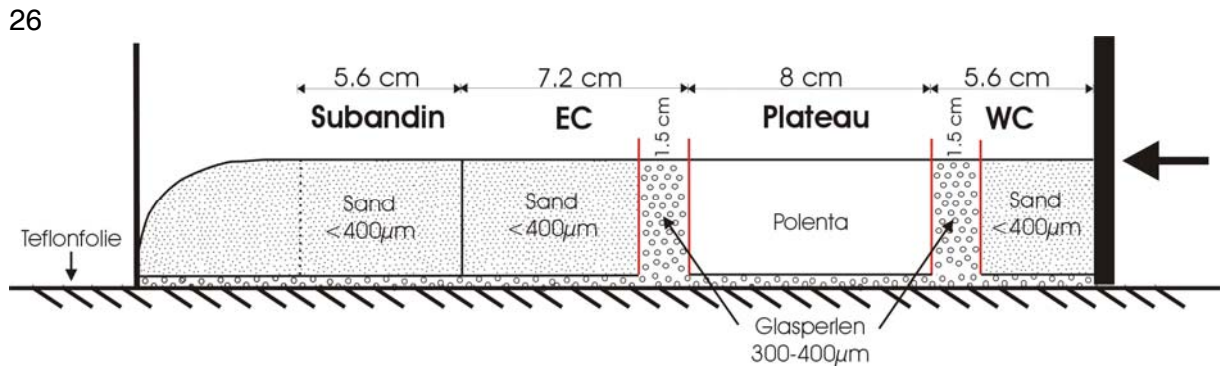


24

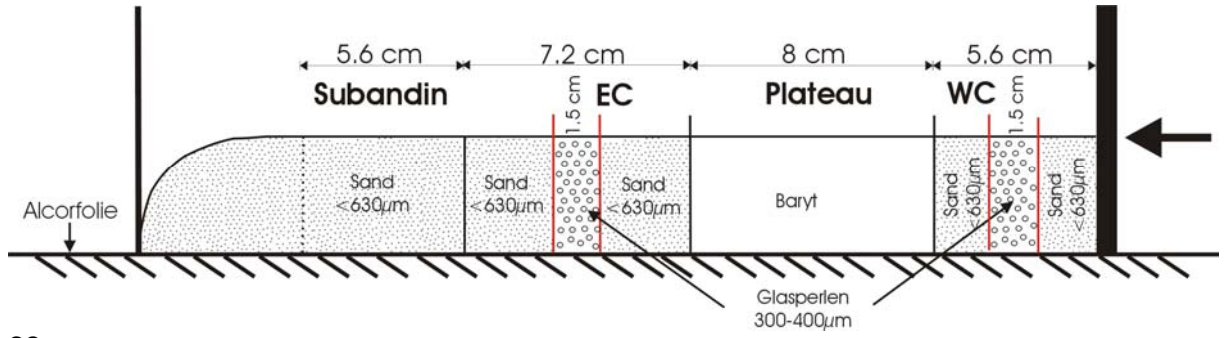


25

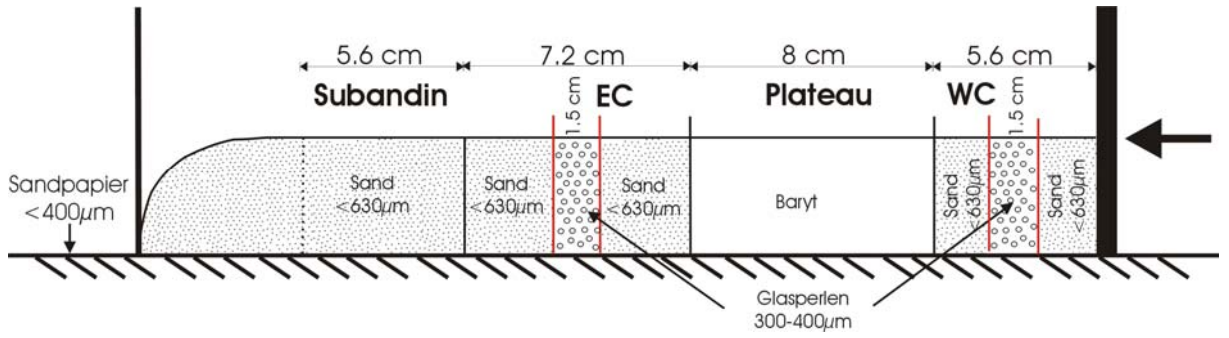




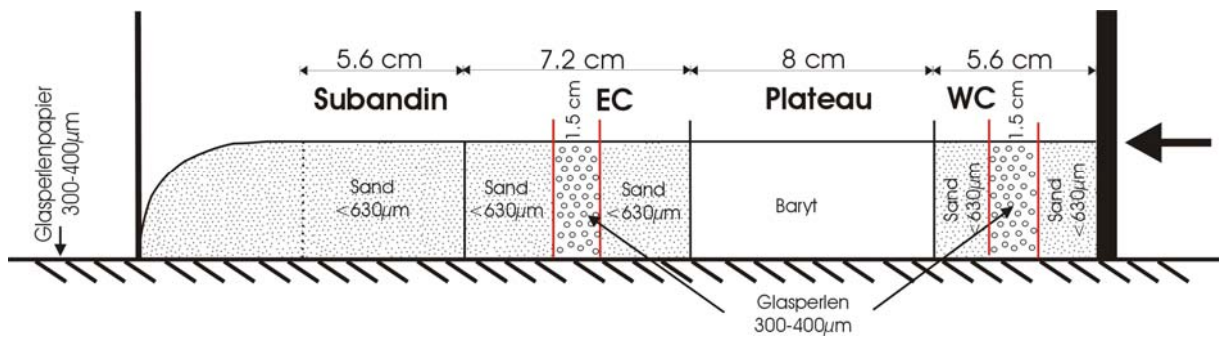
31



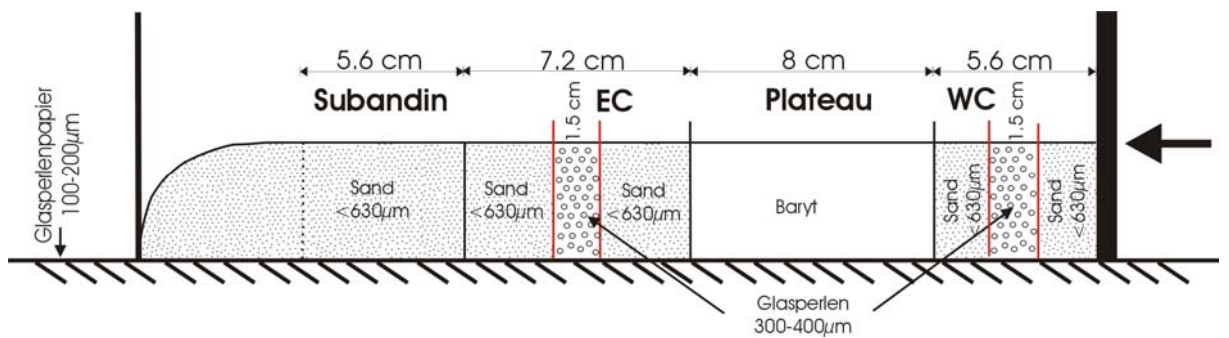
32



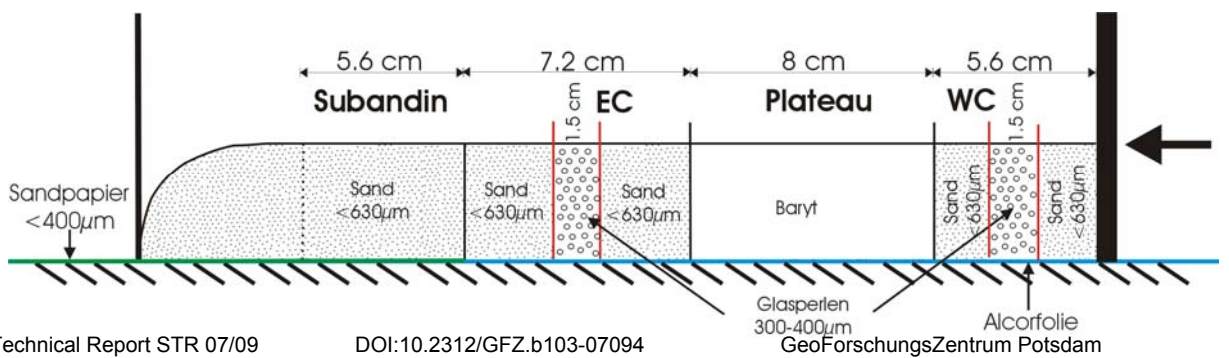
33



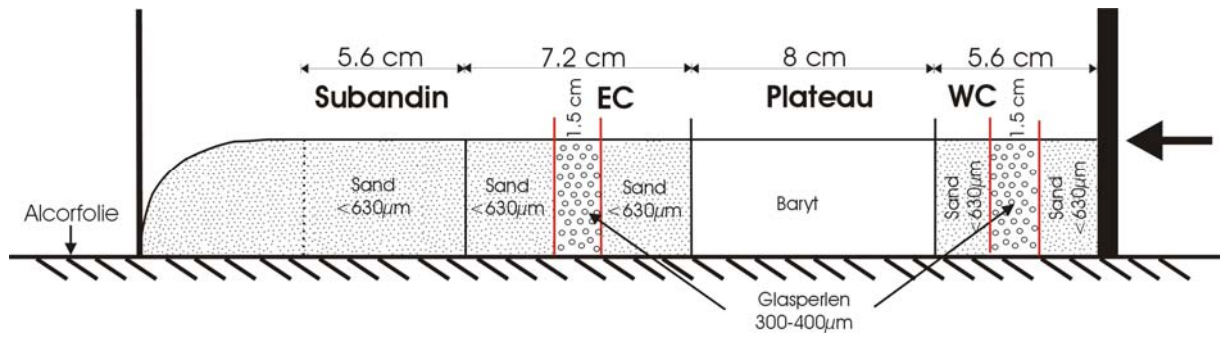
34



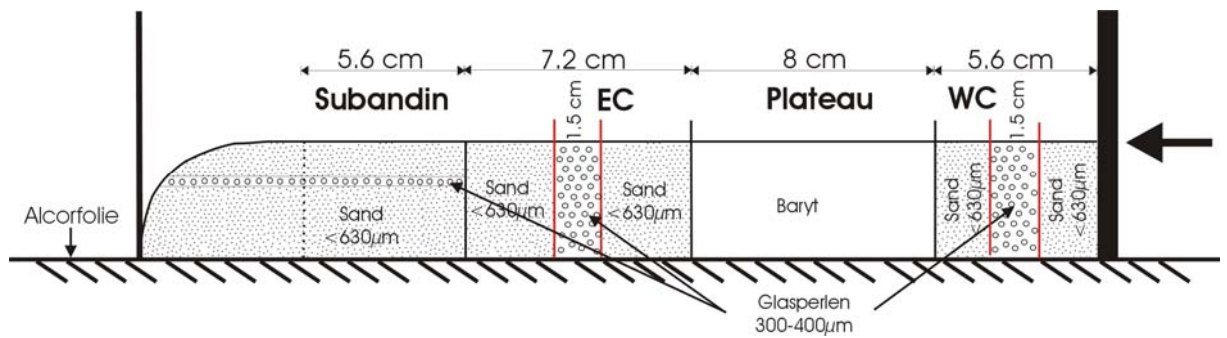
35



36



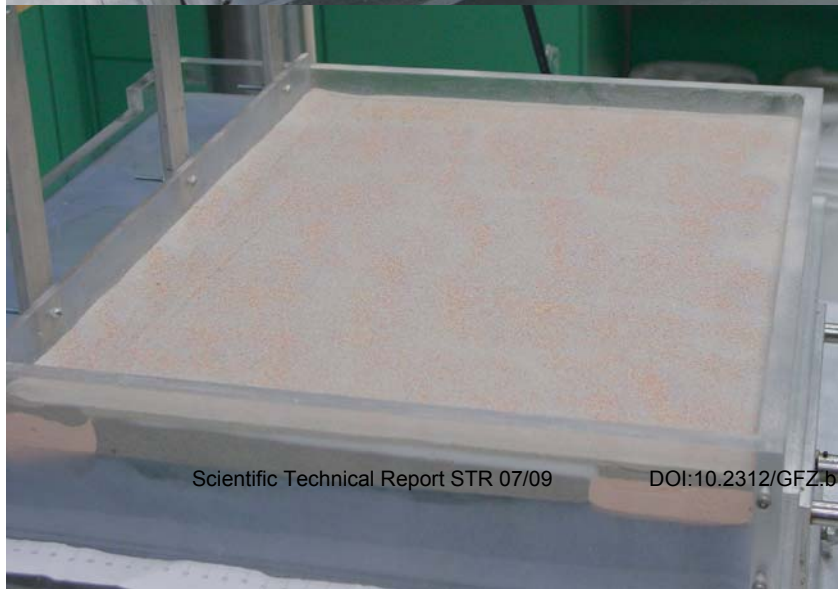
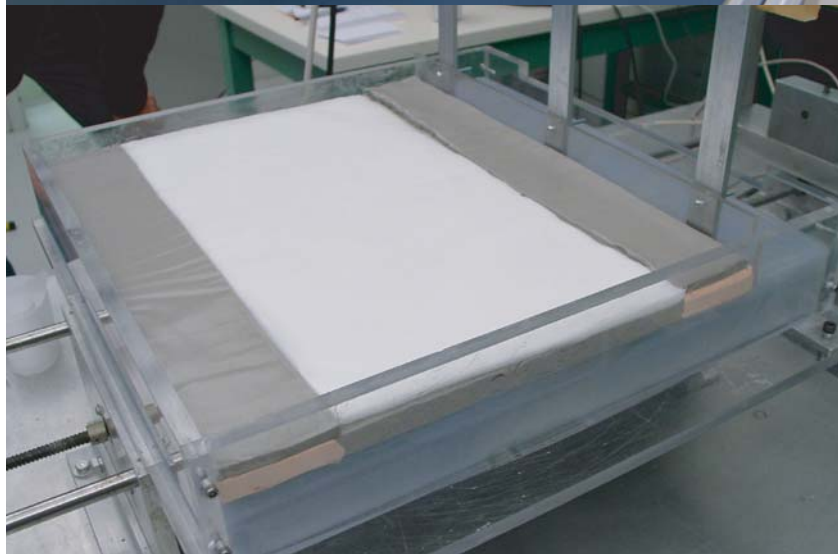
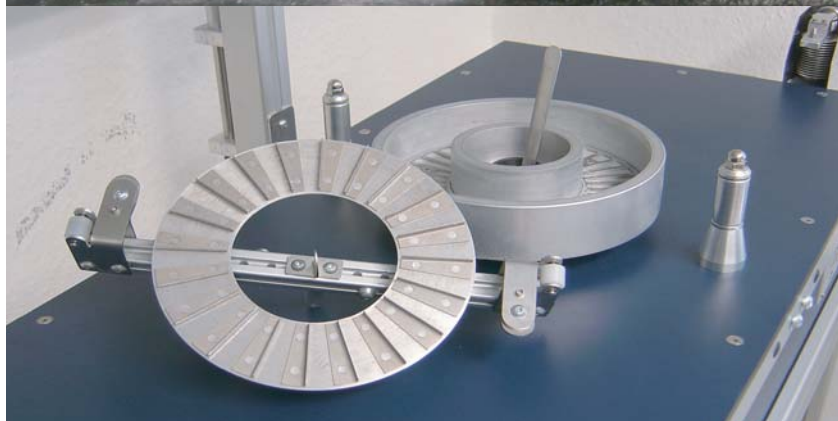
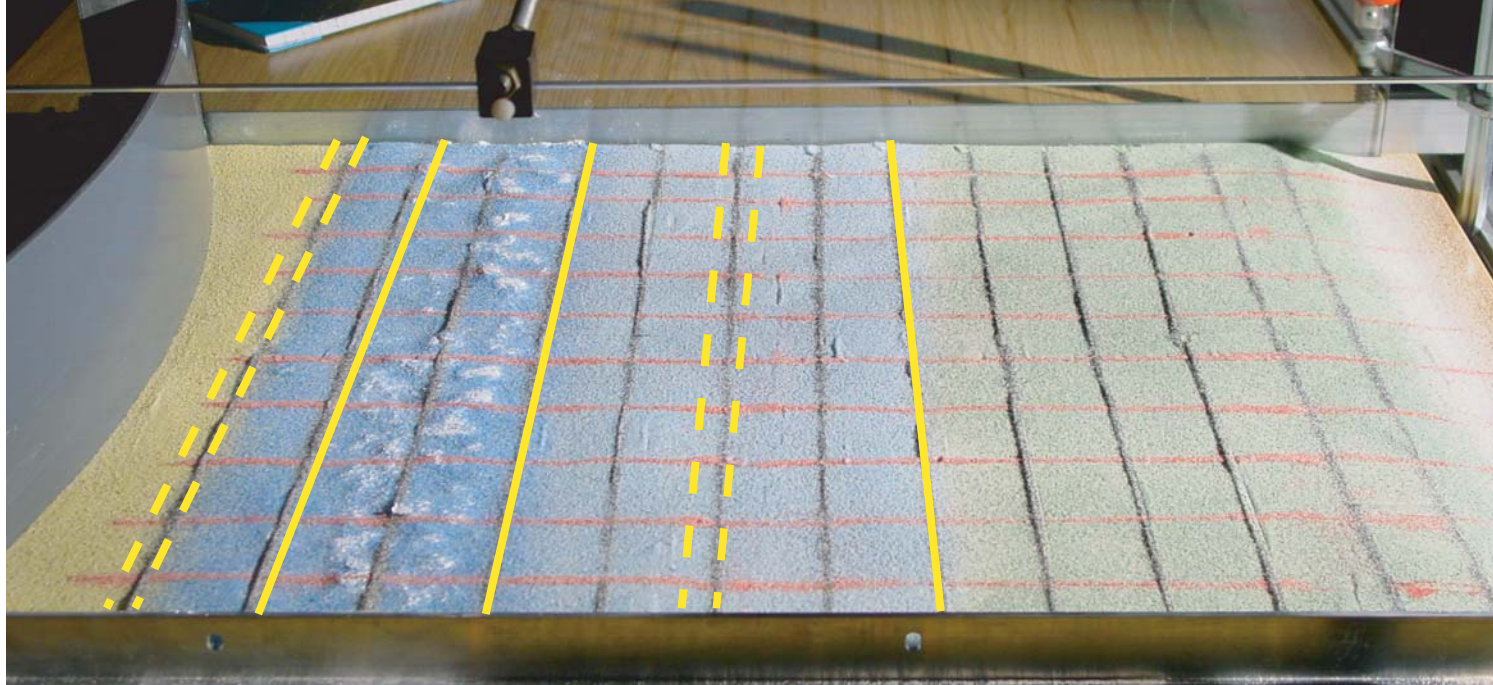
37



Experiments 38-44 have a similar set-up than Experiment 37, but with different dimensions (confer Appendix B, Details on initial experimental set-ups).

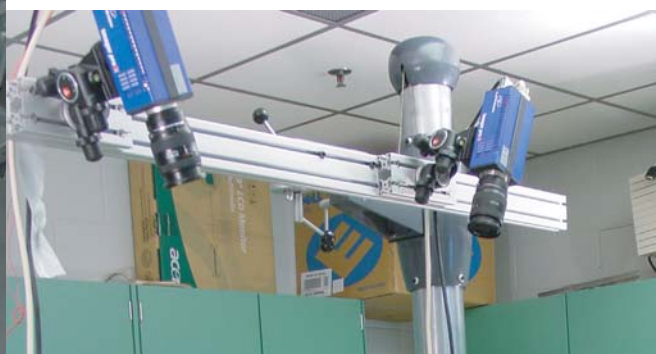
Appendix B-3

Photographs of Analogue Devices



Analogue devices

top: Granular experimental set-up
left (second from top): ring shear device
left (third from top): viscous layers in tank
left (bottom): vise model (here with viscous asthenosphere)
below: PIV cameras in stereoscopic view
bottom (right): PIV rack with PIV cameras (background), PIV computer (right), and digital cameras (front)



Appendix B-4

Material Parameters for Vise Experiments

	vice a	Exp. 1	Exp. 2	Exp. 3	vice b	Exp. 4	Exp. 5	Exp. 6	Exp. 7	Exp. 8	Exp. 9
upper crust	viscosity density	0,85 -	0,86 -	0,85 -	0,85 -	0,85 -	0,85 -	0,85 -	0,85 -	0,85 -	0,85 -
strong lower crust	viscosity density calc exponent	4,8*10E4 Pa*s 0,95 1,01772	4,8*10E4 Pa*s 0,95 1,01772	4,5*10E4 Pa*s 0,95 0,99652	4,5*10E4 Pa*s 0,95 0,99652	4,5*10E4 Pa*s 0,95 0,99652	3,68*10E4 Pa*s 0,95 0,99652	3,68*10E4 Pa*s 0,95 0,99652	3,68*10E4 Pa*s 0,95 0,99652	3,68*10E4 Pa*s 0,95 0,99652	3,68*10E4 Pa*s 0,95 0,99652
strong mantle	viscosity density calc exponent	8,61*10E4 Pa*s 0,968 1,05777	6,5*10E4 Pa*s 0,99 1,06024	1,83*10E5 Pa*s 0,99 1,10887	1,83*10E5 Pa*s 0,99 1,10887	1,83*10E5 Pa*s 0,99 1,10887	1,83*10E5 Pa*s 0,99 1,10887	1,83*10E5 Pa*s 0,99 1,10887	1,83*10E5 Pa*s 0,99 1,10887	1,83*10E5 Pa*s 0,99 1,10887	1,83*10E5 Pa*s 0,99 1,10887
weak lower crust	viscosity density calc exponent	assumed 4,28*10E4 0,91 1,00879	2,19*10E4 Pa*s 0,81 1,02945	1,46*10E4 Pa*s 0,81 1,02945	1,96*10E4 Pa*s 0,95 0,99905	2,14*10E4 Pa*s 0,95 0,99919	2,14*10E4 Pa*s 0,950,975 0,99919	2*10E4 Pa*s 0,94/0,975 1	2*10E4 Pa*s 0,94 1	2*10E4 Pa*s 0,94 1	2*10E4 Pa*s 0,94/0,81 1
weak mantle lithosphere	viscosity density calc exponent	5,07*10E4 Pa*s 0,964 1,02504	2,95*10E4 Pa*s 0,98 1,01733	2,95*10E4 Pa*s 0,98 1,01733	2,95*10E4 Pa*s 0,98 1,01733	2,95*10E4 Pa*s 0,98 1,01733	2,95*10E4 Pa*s 0,98 1,01733	2,95*10E4 Pa*s 0,98 1,01733	2,95*10E4 Pa*s 0,98 1,01733	2,95*10E4 Pa*s 0,98 1,01733	2,95*10E4 Pa*s 0,98 1,01733
mantle	viscosity density calc exponent	2,95*10E4 Pa*s 0,98 1,01733	water 1	water 1	water 1	water 1	water 1	water 1	water 1	water 1	water 1

Appendix B-5

Material mixtures for Vise Experiments

Mixtures

	upper crust	strong lower crust (for one vice)	strong mantle lithosphere (for one vice)	weak lower crust	weak mantle lithosphere	mantle
Vice a	514,24 g sand 269 g Z-lights	176,5 g PDMS 18 g black plasticene 37,5 g Z-lights	152 g pink putty 412 g PDMS 45,5 g Z-lights	8,16 g PDMS 24 g 3M glass bubbles S 46,5 g low-viscosity silicone	1922,15 g reused PDMS 186,9 g black plasticene 234,3 g Z-lights	reused PDMS
Exp. 1	514,24 g sand 269 g Z-lights	194 g PDMS 20,5 g black plasticene 25 g Z-lights	158 g pink putty 446,4 g PDMS 19,5 g Z-lights	750,7 g PDMS 4,2 g 3M glass bubbles S 67,3 g low-viscosity silicone	2381,4 g reused PDMS (27 cm frame)	water
Exp. 2	413,45 g sand 175,8 g Z-lights	194 g PDMS 20,5 g black plasticene 25 g Z-lights	158 g pink putty 446,4 g PDMS 19,5 g Z-lights	566,2 g PDMS 70 g glass bubbles S 55 g low-viscosity silicone of this 345,6 g and 76,8 PDMS 32 g 3M glass bubbles S 245,7 g low-viscosity silicone	1190,7 reused PDMS (24 cm frame)	water
Exp. 3	370 g sand 129 g Z-lights	for both vices 350 g PDMS 39 g black plasticene 47 g Z-lights	for both vices 393 g pink putty 665 g PDMS 78 g Z-lights	566,2 g PDMS 70 g glass bubbles S 55 g low-viscosity silicone of this 336,7 g and 76,8 g glass bubbles S 32 g 3M glass bubbles S 245,7 g low-viscosity silicone	1058,4 g reused PDMS (will be cut smaller)	water
vice b	370 g sand 129 g Z-lights	for both vices 350 g PDMS 39 g black plasticene 47 g Z-lights	548,5 g recovered 203,2 g pink putty 343,7 g PDMS 40,6 g Z-lights	328,7 g PDMS 248,9 g low-viscosity silicone 102,6 g iron filler 67,6 g 3M glass bubbles S	944,64 g reused PDMS	water
Exp. 4	370 g sand 129 g Z-lights	for both vices 350 g PDMS 39 g black plasticene 47 g Z-lights	847,8 g recovered 99,7 g pink putty 168,6 g PDMS 19,9 g Z-lights	328,7 g PDMS 248,9 g low-viscosity silicone 106,3 g barium sulphate filler 63,9 g 3M glass bubbles S	944,64 g reused PDMS	water
Exp. 5	370 g sand 129 g Z-lights	for both vices 370 g PDMS 31 g blue plasticene 36 g Z-lights	910,4 g recovered 78,2 g pink putty 132,2 g PDMS 15,6 g Z-lights	328,7 g PDMS 248,9 g low-viscosity silicone 106,3 g barium sulphate filler 63,9 g 3M glass bubbles S <i>low-viscosity silicone for LVZ</i>	944,64 g reused PDMS	water
Exp. 6	370 g sand 129 g Z-lights	for both vices 370 g PDMS 31 g blue plasticene	797 g recovered 117,3 g pink putty 198,3 g PDMS	304,1 g PDMS 230,3 g low-viscosity silicone 87,1 g barium sulphate filler	1889,3 g reused PDMS	water

Exp. 7	370 g sand 129 g Z-lights	36 g Z-lights	23,4 g Z-lights	63,1 g 3M glass bubbles S	944,64 g reused PDMS 150,92 g reused PDMS extra	water
	319,2 g from this: for both vices 370 g PDMS 31 g blue plasticene 36 g Z-lights	831,6 g recovered		383,9 PDMS 133,34 calcium sulphate 290,7g low-viscosity silicone 65,45 g 3M glass bubbles S		
Exp. 8	370 g sand 129 g Z-lights	287,6 g PDMS 24,1 g blue plasticene 28 g Z-lights	242 g recovered 222,5 g pink putty 376,2 g PDMS 44,4 g Z-lights	397,86 g PDMS 301,1 g low-viscosity silicone 138,2 g calcium sulphate 67,8 g 3M glass bubbles S	1167,18 g reused PDMS	water
Exp. 9	370 g sand 129 g Z-lights	117,8 g left from vice 9 270,3 g PDMS 22,6 g blue plasticene 26,3 g Z-lights	for both vices 393 g pink putty 665 g PDMS 78 g Z-lights	buoyant part (10 cm wide) 136,6 g PDMS 25,4 g 3M glass bubbles S 0,15 g calcium sulphate 103,4 g low-viscosity silicone non-buoyant part (2*7cm wide) 191,74 g PDMS 145,2 g low-viscosity silicone 66,6 g calcium sulphate 32,7 g 3M glass bubbles S	944,64 g reused PDMS	water

Acknowledgments

I'd like to express gratitude to my advisor Onno Oncken for supporting my scientific project and the application to the Studienstiftung, and for having me as a guest in his department at the GFZ Potsdam. He helped me on many occasions with inspiring and insightful discussion and ideas, but also gave me all the freedom I could imagine to follow my ideas and plans towards the final shape of my dissertation.

This project would not have been possible without the funding of the "Studienstiftung des deutschen Volkes". In addition to the PhD grant, they supported my research visit to the Tectonophysics Laboratory, University of Toronto. CSAG and the GFZ are hereby thanked for financing the attendance of several international conferences and a field-trip to the Andes.

All colleagues from the Geodynamics section 3.1 at the GFZ are thanked for good times together, discussing geoscience and other important things. Günter Tauscher definitely builds the nicest analogue boxes.

My fellow PhD students certainly understood best what it means to do a doctorate with all ups and downs, including the quest to find the right approach and the constant need for self-motivation: Maïke Buddensiek, who has become a close friend; Uli Micksch and Antje Kellner, with whom I shared the headquarters of tea consumption, invention of physical units, and certainly the most fun; and Tina Lohr and Raik Bachmann. Raik shared the experience of being a scholarship holder, so we could discuss all relevant matters.

Uli helped greatly by always finding the right computing tools for data transformation and preparation etc.

I am very grateful to David Boutelier and Christoph Schrank (of course not only for good times at Second Cup) and Sandy Cruden that I could be part of a top-of-the line analogue team. Thanks to you guys I had a wonderful and inspiring time in Toronto - it was here that I regained my motivation for idealistic science!

Thanks to Martina Böhme, who did an internship with me right at the beginning of my PhD. This made me think about everything especially careful. She was a great help, not only with checking my geostatistics and doing great plots (plots of which some are used and acknowledged in Chapter 5), but also with the analogue experiments and the protocols and figures. Best of all, she became a good friend.

I am thankful to Alan Levander who (had to) become enthusiastic about my data, had some good ideas to analyze them, and wrote the Matlab codes to extract the right details.

I would not be where I am now without the support of my family and friends, who helped to make the best out of my PhD time, constantly attended to my motivation level, and accepted my frequent stays abroad. My parents always incited my curiosity for science and sustained my work.

And hard to imagine what would have become of this thesis – "let alone life" – without Steffen.

Kerstin Schemmann

Born: April 11, 1980 In: Frankfurt/Main (Germany)

EDUCATION AND ACADEMIC HISTORY

11/2007 PhD in Geology

2005-2007 PhD, Freie Universität Berlin/ GFZ Potsdam

Thesis: Scale-related strain evolution at convergent margins and effects due to parameter changes – insights from nature and experiment

2006 Tectonophysics Laboratory, University of Toronto (Canada)

2004 Graduate research assistant, GFZ Potsdam, Collaborative Research Center 267: "Deformation Processes in the Andes"

07/2004 Diplom (Master's Degree) in Geology

Thesis: Geology of Mount Diablo and further constraints on the Coast Range Fault, California

2004 Geological Survey Namibia, Windhoek

1999-2004 Studies in Geology, Freie Universität Berlin

2002-2003 University of California, Davis (USA)

1999 Abitur

1994-1999 Sophie-Charlotte-Oberschule, Berlin

1992-1994 Walther-Rathenau-Oberschule, Berlin

1991-1992 Grunewald-Grundschule, Berlin

1990-1991 Eichwald-Gymnasium, Schwalbach im Taunus

1986-1990 Drei-Linden-Grundschule, Neuenhain im Taunus

AWARDS

2005-2007 PhD Scholarship of the German National Merit Foundation

2006 ISES Summer School on Rheology

2002-2003 Scholarship, FU Berlin and University of California, Davis

2002-2004 Scholarship of the German National Merit Foundation

2002 Scholarship holder of the "Ernst-Reuter-Stiftung", FU Berlin

2002 Grantee of the German-American Fulbright Commission